

Fluctuation X-ray scattering
for systems of particles obeying
arbitrary orientational distributions:
from theory to applications

Dissertation
zur Erlangung des Doktorgrades

an der Fakultät für Mathematik, Informatik und Naturwissenschaften

Fachbereich Physik

der Universität Hamburg

vorgelegt von

Tim Benedict Berberich

Hamburg

2024

Gutachter/innen der Dissertation:

Prof. Dr. Alexander Lichtenstein
Prof. Dr. Serguei Molodtsov

Zusammensetzung der Prüfungskommission:

Prof. Dr. Alexander Lichtenstein
Prof. Dr. Serguei Molodtsov
Dr. Ruslan Kurta
Prof. Dr. Christian Bressler
Prof. Dr. Michael Potthoff

Vorsitzende/r der Prüfungskommission:

Prof. Dr. Michael Potthoff

Datum der Disputation:

22.08.2024

Vorsitzender des Fach-Promotionsausschusses PHYSIK: Prof. Dr. Markus Drescher

Leiter des Fachbereichs PHYSIK:

Prof. Dr. Wolfgang J. Parak

Dekan der Fakultät MIN:

Prof. Dr.-Ing. Norbert Ritter

Dedicated to Lin, Anya and Yuxuan

Abstract

Random fluctuations and their representations are ubiquitous in our everyday life, some are mundane like the distribution of bubblegum on floor tiles at train stations, others are rare like a winning streak in your favorite board game and yet others are mesmerizing like the sudden gust of wind that swirls up leaves in autumn. In physics we have observed them in phenomena at all length scales, from the cosmic microwave background over the Brownian motion of dust grains down to decay rates of fundamental particles. Their study has been extremely influential and sparked the development of statistical mechanics as well as quantum physics. From a mathematical perspective statistics has taught us that there are different kinds of randomness which can be described by the probability distribution p_X assigned to a random variable X . Moreover the, knowledge about averages of the form $\langle X \rangle, \langle X^2 \rangle, \dots$, called moments of X , uniquely determines p_X , i.e. the kind of randomness of X .

In the field of single-particle imaging (SPI) randomness manifests itself in the distribution of rotation states of several instances of the particle to be imaged. The technique of *fluctuation X-ray scattering* (FXS) seeks to merge the concept of statistical moments with SPI and use randomness to its advantage. It can be understood as natural extension to the study of the averaged diffraction pattern $\langle I \rangle$, which is a common analysis method in Small- and Wide-angle X-ray scattering (SAXS/WAXS). Specifically, FXS aims to characterize the structural information that averages of the form $\langle I \rangle, \langle I^2 \rangle, \dots$ contain and therefore quite literally seeks structure in randomness. Despite its development in the late 1970s and early 1980s [1–3], applications of FXS have only recently become possible with the emergence of X-ray free-electron lasers (XFEL). Interestingly XFELs themselves rely on the use of fluctuations as they produce highly intense and coherent X-ray pulses via the process of self-amplified spontaneous emission (SASE), i.e. the amplification of X-ray noise. Their introduction made it possible to carry out “diffraction before destruction” experiments on individual bio-particles [4–10], which have been theorized before [11–13]. These measurements allow to record diffraction patterns from random orientation states of the studied particles. Alongside of *FXS* this lead to the development of the previously mentioned single-particle imaging (SPI) technique [14–18], which holds the prospect of providing high resolution structure recovery. FXS shares this prospect with SPI [19, 20], but it also allows for single-particle reconstructions from multi-particle scattering [21]. This makes FXS especially interesting for the study of particles in solution. It can also be used in a forward modeling approach to understand dynamical changes in optically excited particles, as has been recently demonstrated [22].

This thesis pursues three goals. Firstly it aims to provide a generalized theoretical description of fluctuation X-ray scattering. The second goal is, to report on the development of a software suite [23] for single-particle structure recovery from FXS data and its applications to experimental datasets. Finally, it describes an extension to the theoretical concepts of FXS, that allows the treatment of systems of particles following arbitrary nonuniform rotational probability distributions. The latter is relevant in the analysis of optically excited particles which are known to follow nonuniform distributions [22, 24–26], as well as in studies of molecular alignment [24].

Zusammenfassung

Zufällige Schwankungen und deren Auswirkungen sind in unserem Alltag allgegenwärtig. Einige sind banal, wie die Verteilung von Kaugummiflecken auf den Fliesen eines Bahnsteiges, andere sind selten, wie die Gewinnsträhne in Ihrem Lieblingsbrettspiel und wieder andere sind bezaubernd, wie der zufällige Windstoß, der im Herbst das Laub aufwirbelt. Wir beobachten sie in physikalischen Phänomenen aller Längenskalen, angefangen bei der kosmischen Hintergrundstrahlung über die Brownsche Bewegung von einzelnen Staubteilchen, bis hin zu den Zerfallsraten elementarer Teilchen. Die Erforschung zufälliger Schwankungen war von großer Bedeutung für die Entwicklung der statistischen Mechanik sowie der Quantenphysik. Aus dem Blickwinkel der Statistik betrachtet wissen wir, dass es unterschiedliche Arten von Zufälligkeit gibt, die wir mit Hilfe von einer Zufallsvariable X und ihrer Wahrscheinlichkeitsverteilung p_X beschreiben können. Ferner erlaubt das Wissen über Erwartungswerte der Form $\langle X \rangle, \langle X^2 \rangle, \dots$, welche auch Momente von X genannt werden, die eindeutige Bestimmung der Wahrscheinlichkeitsverteilung p_X und damit die Bestimmung der Art der Zufälligkeit von X .

Im Wissenschaftszweig des *single-particle imaging* (SPI) manifestiert sich Zufälligkeit in der Verteilung von Rotationszuständen einzelner Teilchen. Die Analysemethode der *Fluktuationsröntgenstreuung* (FXS) setzt sich zum Ziel, das Konzept von statistischen Momenten mit SPI zu Verbinden und die vorhandenen Schwankungen zu ihrem Vorteil zu nutzen. FXS kann als natürliche Erweiterung zur Untersuchung des gemittelten Beugungsbildes $\langle I \rangle$ verstanden werden, die eine übliche Analysemethode für Klein- und Weitwinkelröntgenstreuung (SAXS/WAXS) ist. Im Speziellen hat FXS zum Ziel, die in Erwartungswerten der Form $\langle I \rangle, \langle I^2 \rangle, \dots$ enthaltenen Informationen über die Teilchenstruktur sowohl zu charakterisieren als auch zu extrahieren und sucht damit im doppelten Sinne nach Struktur in der Zufälligkeit. Obwohl sie zwischen Ende der 1970er und Anfang der 1980er entwickelt wurde [1–3], sind Anwendungen von FXS erst kürzlich durch das Aufkommen von Freien Elektronen Laser im Röntgenbereich (XFEL) möglich geworden. Interessanterweise nutzen XFELs ebenfalls zufällige Schwankungen, da sie zur Erzeugung von kohärenten Röntgenpulsen extrem hoher Intensität auf den Prozess der selbstverstärkenden spontanen Emission (SASE), also die Verstärkung von Röntgenrauschen, zurückgreifen. Ihre Entwicklung machte es möglich *diffraction before destruction* Experimente mit einzelnen biologischen Teilchen durchzuführen [4–10], deren Möglichkeit zuvor prognostiziert wurde [11–13]. Experimente dieser Form erlauben die Messung von Beugungsbildern der zu untersuchenden Teilchen in einzelnen zufälligen Orientierungszuständen. Neben FXS führte dies auch zu der Entwicklung des zuvor erwähnten *single-particle imaging* (SPI) [14–18], welches hochauflösende Strukturbestimmung in Aussicht stellt. Fluktuationsröntgenstreuung teilt dieses Potential mit SPI [19, 20], ist jedoch zusätzlich in der Lage die Struktur einzelner Teilchen aus Beugungsbildern von Mehrteilchensystemen abzuleiten [21]. Diese Eigenschaft macht FXS besonderes interessant für die Untersuchung von in Lösungen vorliegenden Teilchen. Zudem kann FXS in modellierungsbasierten Analysemethoden eingesetzt werden, um dynamische Prozesse in optisch angeregten Molekülen zu untersuchen [22].

Die vorgelegte Dissertation verfolgt drei Ziele. Zu Beginn führt sie eine verallgemeinerte

theoretische Beschreibung von Fluktuationsröntgenstreuung ein. Daraufhin beschreibt sie die Entwicklung und Anwendung einer Softwaresuite [23], welche die Strukturbestimmung einzelner Teilchen basierend auf FXS Messungen ermöglicht. Es werden sowohl simulierte als auch experimentelle Datensätze untersucht. Zuletzt beschreibt sie eine Erweiterung von FXS, die es ermöglicht, Systeme von Teilchen zu betrachten, deren Rotationswahrscheinlichkeitsverteilungen keine Gleichverteilung ist. Dies ist zum Einen von Interesse für die Analyse von optisch angeregten Molekülen [22, 24–26] und zum Anderen für Untersuchungen von molekularer Ausrichtung [24].

Eidesstattliche Versicherung/Declaration on oath

Hiermit versichere ich an Eides statt, die vorliegende Dissertationsschrift selbst verfasst und keine anderen als die angegebenen Hilfsmittel und Quellen benutzt zu haben.

Sofern im Zuge der Erstellung der vorliegenden Dissertationsschrift generative Künstliche Intelligenz (gKI) basierte elektronische Hilfsmittel verwendet wurden, versichere ich, dass meine eigene Leistung im Vordergrund stand und dass eine vollständige Dokumentation aller verwendeten Hilfsmittel gemäß der Guten wissenschaftlichen Praxis vorliegt. Ich trage die Verantwortung für eventuell durch die gKI generierte fehlerhafte oder verzerrte Inhalte, fehlerhafte Referenzen, Verstöße gegen das Datenschutz- und Urheberrecht oder Plagiat

Hamburg September 11, 2024



Tim Benedict Berberich

Contents

Abstract/Zusammenfassung	iv
Declaration of oath/Eidesstattliche Versicherung	vii
List of Theorems	x
Structure and notation	xi
1. Introduction	1
1.1. Thomson scattering	1
1.2. The phase problem	6
1.3. Iterative phase retrieval	10
1.4. X-ray free-electron laser (XFEL)	13
1.5. Single-particle imaging (SPI)	15
1.6. Small and wide angle x-ray scattering (SAXS/WAXS)	17
1.7. Rotations and harmonic analysis	18
2. Fluctuation X-ray scattering (FXS)	23
2.1. Connection to invariant theory	28
2.1.1. Orbit-recovery problems	28
2.1.2. Orbit-recovery and invariant polynomials	30
2.1.3. Solutions to the orbit-recovery problem	33
2.1.4. Implications for FXS	35
2.2. Single-particle invariants	38
2.2.1. Degree 1 invariants	38
2.2.2. Degree 2 invariants	39
2.2.3. Degree 3 invariants	40
2.3. Information content of degree-2 invariants	41
2.4. FXS based phase retrieval via MTIP	46
2.5. FXS moments and single-particle invariants	47
2.5.1. FXS moments in the single-particle case	47
2.5.2. Extraction of single-particle invariants	52
2.5.3. Extension to multi-particle case	53
2.6. Summary	61
3. Single-particle structure reconstruction workflow	63
3.1. Calculation of FXS moments from masked data (d=1,2)	64
3.2. Degree-2 moments from difference patterns	65
3.3. Extraction and regularization of rotational invariants	66
3.4. Iterative phasing using MTIP	72
3.4.1. Fourier transforms	72
3.4.2. Discrete polar/spherical grids	74
3.4.3. Fourier transform stabilization	75
3.4.4. Generic iterative phase retrieval components	76
3.4.5. Reconstruction error metric	76

3.5. Alignment and Averaging	77
4. xFrame: A python implementation of the reconstruction-workflow	83
4.1. Usage of the FXS project	83
4.2. Dependencies	83
4.3. Multiprocessing scheme	84
4.4. Input/Output data formats	85
5. xFrame applications	86
5.1. Reconstructions from simulated data	86
5.1.1. Multi-particle reconstruction	91
5.1.2. Dependence on the harmonic cutoff	95
5.1.3. Performance of the phase retrieval routine	97
5.2. Reconstructions of PR772 from experimental XFEL data	98
5.2.1. Reconstructions for the AMO86615 experiment	100
5.2.2. Reconstructions for the AMO06516 experiment	106
6. FXS in the case of non-uniform orientational distributions	113
6.1. Rotational probability distributions and their characteristic functions . . .	114
6.2. FXS moments for arbitrary orientational distributions	116
6.2.1. Two-dimensional case	116
6.2.2. Three-dimensional case	118
6.3. Consequences for FXS	121
6.4. Analytic expressions of characteristic functions for selected distributions . .	123
6.4.1. Uniform distribution	123
6.4.2. Delta distribution (perfect alignment)	124
6.4.3. Effectively spherical distributions	125
6.4.4. Gaussian distribution	130
6.4.5. Analogs of distributions over \mathbb{R}	130
7. Summary	133
A. Fluctuation X-ray scattering invariants and moments	137
A.1. Geometric interpretation of degree-2 invariants	137
A.2. Proof of explicit form of degree-3 invariants	141
A.3. Proof of explicit form of the degree-3 moments	142
A.4. Derivation of Observation 2.19	143
B. Hankel transform approximations	147
B.1. Expansion via orthogonal polynomials	147
B.2. Cosine/sine series expansion approximation	150
B.3. Zernike polynomials expansion approximation	150
B.4. Direct approximation of the Hankel integrals using the midpoint rule . . .	153
B.5. Hankel transform of the radial part of the 3D Zernike polynomial	153
List of orthogonality and symmetry relations	156

List of Theorems

2.1. Definition (Fluctuation X-ray scattering in 3D)	24
2.2. Definition (Fluctuation X-ray scattering in 2D)	26
2.3. Observation (Single-particle 2D FXS is a general orbit-recovery problem)	30
2.4. Definition (Polynomials in harmonic coefficients)	31
2.5. Example (Polynomials in harmonic coefficients)	31
2.6. Example (Averaged polynomials in harmonic coefficients)	31
2.7. Definition (Invariant Polynomials)	32
2.8. Definition (orbit-recovery via invariant polynomials)	32
2.9. Theorem (Solution to orbit-recovery)	33
2.10. Theorem (Rotational average as Reynolds operator)	33
2.11. Theorem (Better solution to orbit-recovery)	34
2.12. Theorem (FXS version of theorem 2.11)	35
2.13. Observation (FXS moments are sums over invariants)	37
2.14. Observation (Information limit for FXS)	37
2.15. Observation (Properties of B_l and B_n)	40
2.16. Observation (Connection to degree 1 invariants)	40
2.17. Observation (Information content of B_n and B_l)	42
2.18. Observation (Invariant projection)	45
2.19. Observation (Reduction to single-particle moments)	58
2.20. Example ($d = 1, 2$ and 3)	58
6.1. Observation (FXS moments for arbitrary rotational distributions)	120
6.2. Remark (Averaged angular cross-correlations)	121

Structure and notation

Section 1 has the purpose of introducing all prerequisites necessary for the description of *fluctuation X-ray scattering* in section 2. A description of our workflow for FXS-based structure determination and the associated software suite can be found in sections 3 and 4, while its applications are covered in section 5. After discussing its applications, the concept of FXS is extended to cover nonuniform rotational distributions in section 6.

The reader may have noticed the list of theorems after the table of contents. Its presence reflects the attempt of this thesis to merge the strength of physics literature, which lies in its description of thought processes, with the strength of its mathematical counterpart, the clarity and conciseness of theorems and definitions. This thesis will however not contain proofs in the mathematical sense. Correspondingly, Theorems (which always require proofs) are only mentioned in conjunction with their corresponding reference. Instead of theorems we will use “observations”, their purpose is to summarize results that have been obtained in prior derivations. Irrespective of the type (definition, observation, example, ...), the statements are numbered consecutively within each section of this thesis. The purpose of the “list of theorems” is to provide the reader with an additional tool to locate specific statements.

1. Introduction

1.1. Thomson scattering

Throughout this thesis we will consider X-ray scattering processes, in which a fully coherent light pulse scatters elastically from a particle with electron density $\rho(\mathbf{r})$. For a single photon this scattering process is shown in figure 1.

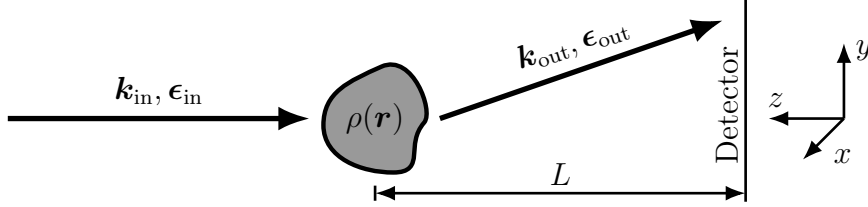


Figure 1: An incoming photon with wave vector \mathbf{k}_{in} and polarization direction $\boldsymbol{\epsilon}_{\text{in}}$, propagates along the z -axis of a local coordinate system and scatters from a collection of electrons given by their density $\rho(\mathbf{r})$. The outgoing photon has the new wave vector \mathbf{k}_{out} and new polarization direction $\boldsymbol{\epsilon}_{\text{out}}$. It propagates freely until it is recorded on a detector surface in the xy -plane, which is placed at a distance L from the scattering center (measured along the z axis).

We will further more restrict our considerations to the simplest type of such scattering processes, which is known as *Thomson scattering*. Its differential cross section is given by [27, equation 12.34]

$$\frac{d\sigma}{d\Omega} = \left(\frac{\alpha \hbar c}{m_e c^2} \right)^2 |\langle \boldsymbol{\epsilon}_{\text{in}}, \boldsymbol{\epsilon}_{\text{out}} \rangle|^2 |\widehat{\rho}(\mathbf{k}_{\text{out}} - \mathbf{k}_{\text{in}})|^2, \quad (1)$$

$$\widehat{\rho}(\mathbf{q}) = \int_{\mathbb{R}^3} d\mathbf{r} \rho(\mathbf{r}) e^{-i(\mathbf{q}, \mathbf{r})} = [\mathcal{F}\rho](\mathbf{q}), \quad (2)$$

where $\langle \boldsymbol{\epsilon}_{\text{in}}, \boldsymbol{\epsilon}_{\text{out}} \rangle$ denotes the scalar product between the incoming and outgoing polarization directions, $\alpha \approx \frac{1}{137}$ is the fine structure constant, m_e is the electron mass and c, \hbar denote the speed of light and the reduced Planck constant, respectively. We shall call $\widehat{\rho}(\mathbf{q})$ the *scattering amplitude*, which is given as the Fourier transform (symbolized by \mathcal{F}) of the electron density $\rho(\mathbf{r})$. In case the considered particle is an atom, $\widehat{\rho}(\mathbf{q})$ coincides with the atomic form factor. For linear polarized photons both $\boldsymbol{\epsilon}_{\text{in}}$ and $\boldsymbol{\epsilon}_{\text{out}}$ are real valued and the outgoing polarization direction is, up to normalization, given by the cross-products

$$\boldsymbol{\epsilon}_{\text{out}} = (\mathbf{k}_{\text{out}} \times \boldsymbol{\epsilon}_{\text{in}}) \times \mathbf{k}_{\text{out}}. \quad (3)$$

It is interesting to note that the above scattering cross section, equation (1), can be obtained from purely classical considerations as well as from perturbation theory in quantum physics.

In the former case, the incident plane electromagnetic wave exerts a periodic force on the electrons within the considered particle. This force causes each electron to oscillate and act as an oscillating electric dipole, which radiates a scattered electromagnetic wave.

In order for the intensity of the emitted dipole radiation to obey equation (1), it has to be measured in the *far field*, that is at large enough distances L from the scattering center such that $\frac{D^2|\mathbf{k}_{\text{in}}|}{L2\pi} \ll 1$, where D is the largest distance within the particle. More detailed derivations can be found in text books such as [28, chapter 1.2],[27, chapter 6.2] or [29, volume 2, part VI].

From a quantum theoretic perspective, equation (1) is well known for $\widehat{\rho}(\mathbf{q}) = 1$, i.e. in the case of a photon scattering from a single free electron. It is the result of considering the two lowest order Feynman diagrams, displayed in figure 2, while averaging over all possible spin states and demanding that the energy of the electron remains conserved throughout the scattering process. Detailed derivation of this result can be found, as low energy limit of *Compton scattering*, in many text books, such as [30–32]. A derivation

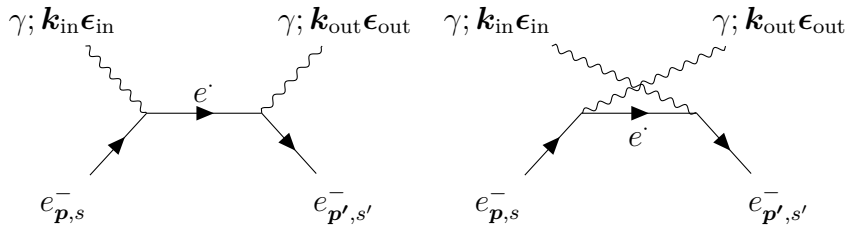


Figure 2: Feynman diagrams considered in Thomson scattering. (left) An electron $e_{\mathbf{p},s}^-$, with momentum \mathbf{p} and spin state s , first absorbs the incident photon $\gamma; \mathbf{k}_{\text{in}}\boldsymbol{\epsilon}_{\text{in}}$, then propagates as intermediate electron until it emits the outgoing photon. (right) The initial electron first emits the outgoing photon, then propagates as intermediate electron and finally absorbs the photon that has been present in the initial state.

considering multiple bound electrons, as encountered in atoms or molecules, is given in [27, chapter 12.5]. Here we shall loosely follow this derivation, to motivate the appearance of the *scattering amplitude* in equation (1). We may describe the interaction between charged particles and electromagnetic fields via the non-relativistic hamiltonian¹

$$H_{\text{int}} = \frac{e}{m_e} \langle \mathbf{p}, \mathbf{A} \rangle + \frac{e^2}{2m_e} \langle \mathbf{A}, \mathbf{A} \rangle, \quad (4)$$

$$\mathbf{A}(\mathbf{r}, t) = \sum_{\mathbf{k}} \sum_{l=0}^1 \mathcal{A}(\mathbf{k}) (\boldsymbol{\epsilon}_l \mathbf{a}_{l\mathbf{k}} e^{i(\langle \mathbf{k}, \mathbf{r} \rangle - \omega_{\mathbf{k}} t)} + \boldsymbol{\epsilon}_l^* \mathbf{a}_{l\mathbf{k}}^\dagger e^{-i(\langle \mathbf{k}, \mathbf{r} \rangle - \omega_{\mathbf{k}} t)}), \quad (5)$$

where \mathbf{A} is the quantized vector potential [27, equation 3.55], l is the quantum number associated to the two polarization states and $\mathbf{a}_{l\mathbf{k}}^\dagger, \mathbf{a}_{l\mathbf{k}}$ denote the bosonic creation and annihilation operators, respectively. The photon energy is given by $\hbar\omega_{\mathbf{k}} = \hbar c|\mathbf{k}|$ and $\mathcal{A}(\mathbf{k}) = \sqrt{\frac{\hbar}{2\epsilon_0 V \omega_{\mathbf{k}}}}$, whose precise form is not relevant for the following argument.² We now seek to treat the interaction given by H_{int} using the framework of perturbation theory. Let us assume, that the eigenstates of the non-interacting theory, represented by

¹ H_{int} as given in (4) neglects terms describing interaction between the electron spin and EM fields, for details see [27].

² V in the definition of $\mathcal{A}_{\mathbf{k}}$ is the quantization volume and ϵ_0 denotes the vacuum permittivity.

a Hamiltonian H_0 , are known. If the initial and final state, $|i\rangle$ and $|f\rangle$, of the scattering process are eigenstates of H_0 we may use Fermi's golden rule to describe the scattering rate $\Gamma_{i\rightarrow f}$ up to first order in H_{int} and find

$$\Gamma_{i\rightarrow f} \propto |\langle f|H_{\text{int}}|i\rangle|^2. \quad (6)$$

In order to describe *Thomson scattering* we only consider initial and final states that differ by a single occupation number, i.e.

$$|i\rangle = |\psi, n(\mathbf{k}_{\text{in}}, \boldsymbol{\epsilon}_{\text{in}}), 0\rangle, \quad (7)$$

$$|f\rangle = |\psi, (n-1)(\mathbf{k}_{\text{in}}, \boldsymbol{\epsilon}_{\text{in}}), 1(\mathbf{k}_{\text{out}}, \boldsymbol{\epsilon}_{\text{out}})\rangle. \quad (8)$$

In equations (7)-(8), $|\psi\rangle$ describes the electronic state, which remains unchanged during the scattering process, $|n(\mathbf{k}_{\text{in}}, \boldsymbol{\epsilon}_{\text{in}}), 0\rangle$ describes n free photons in the mode $(\mathbf{k}_{\text{in}}, \boldsymbol{\epsilon}_{\text{in}})$ and $|(n-1)(\mathbf{k}_{\text{in}}, \boldsymbol{\epsilon}_{\text{in}}), 1(\mathbf{k}_{\text{out}}, \boldsymbol{\epsilon}_{\text{out}})\rangle$ describes the state in which a single photon changed its mode to $(\mathbf{k}_{\text{out}}, \boldsymbol{\epsilon}_{\text{out}})$. It becomes immediately clear that only the term proportional $\langle \mathbf{A}, \mathbf{A} \rangle$ in H_{int} contributes to such a scattering process, since only it contains products of the form $\mathbf{a}_{l\mathbf{k}}\mathbf{a}_{l'\mathbf{k}'}$ or $\mathbf{a}_{l\mathbf{k}}^\dagger\mathbf{a}_{l'\mathbf{k}'}$, that conserve the total number of photons. In computing the matrix elements given in equation (6) one directly finds

$$\begin{aligned} \Gamma_{i\rightarrow f} &\propto \left| \langle \psi, (n-1)(\mathbf{k}_{\text{in}}, \boldsymbol{\epsilon}_{\text{in}}), 1(\mathbf{k}_{\text{out}}, \boldsymbol{\epsilon}_{\text{out}}) | \langle \mathbf{A}, \mathbf{A} \rangle | \psi, n(\mathbf{k}_{\text{in}}, \boldsymbol{\epsilon}_{\text{in}}), 0 \rangle \right|^2 \\ &\propto \left| \langle \psi | e^{-i\langle \mathbf{k}_{\text{out}} - \mathbf{k}_{\text{in}}, \mathbf{r} \rangle} | \psi \rangle \right|^2 = \left| \widehat{\rho}(\mathbf{k}_{\text{out}} - \mathbf{k}_{\text{in}}) \right|^2, \end{aligned} \quad (9)$$

where in the last step we used that, by definition, $\psi(\mathbf{r})\psi(\mathbf{r})^*$ describes the electron density $\rho(\mathbf{r})$ of the free state $|\psi\rangle$. This appearance of $\left| \widehat{\rho}(\mathbf{k}_{\text{out}} - \mathbf{k}_{\text{in}}) \right|^2$ in the transition rate for *Thomson scattering* ultimately leads to its presence in the differential cross section, shown in equation (1).

From now on, we shall assume that the polarization state of the incident X-ray pulse is known and that the intensity patterns I^M , for scattering geometries as described by figure 1, provide direct measurements of the differential cross section (1). Equivalently we can demand that the diffraction patterns I^M are simply given by ³

$$I^M = \left| \widehat{\rho}(\mathbf{k}_{\text{out}} - \mathbf{k}_{\text{in}}) \right|^2. \quad (10)$$

It is hard to overstate the importance of equation (10), as it constitutes the foundation on which many imaging techniques are build, including *single-particle imaging* (SPI) [11, 12, 33], *fluctuation X-ray scattering* (FXS) [1] and also *X-ray crystallography* [34, equation 3.27]. Equation (10) states that *Thompson scattering* from a particle can be used as probe for its electron density $\rho(\mathbf{r})$, albeit with a builtin limitation in form of the absolute value squared $|\cdot|^2$, which will be discussed in the next section. It is instructive to think of the *scattering amplitude* $\widehat{\rho}(\mathbf{q})$ as a complex valued three-dimensional function in

³The knowledge about $\boldsymbol{\epsilon}_{\text{in}}$ together with equation (3) allows one to compute the polarization factor in the Thompson cross section (1) and remove its contribution.

momentum space, whose absolute value squared $I(\mathbf{q}) = \widehat{\rho}(\mathbf{q})\widehat{\rho}(\mathbf{q})^*$ shall be called the *scattering intensity*. We may now connect the measured two-dimensional diffraction patterns I^M to portions of the three-dimensional intensity $I(\mathbf{q})$, using the energy conservation of elastic scattering. Specifically, elasticity implies that the wavelength λ of incident X-ray photons does not change during the scattering process and we find $|\mathbf{k}_{\text{out}}| = |\mathbf{k}_{\text{in}}| = \frac{2\pi}{\lambda}$. The vector $\mathbf{k}_{\text{out}} - \mathbf{k}_{\text{in}}$, present in equation (10), therefore lies on a sphere in momentum space, whose radius is given by $\frac{2\pi}{\lambda}$. This sphere is known as *Ewald's sphere* E_λ and it is convenient to denote all momentum transfer vectors lying on this sphere by \mathbf{q}^λ . The points $\mathbf{q}^\lambda = \mathbf{k}_{\text{out}} - \mathbf{k}_{\text{in}}$ have a particularly simple representation in spherical coordinates, if one assumes that \mathbf{k}_{in} points along the z -axis. In this case one finds

$$\mathbf{q}^\lambda = (q, \theta_\lambda(q), \phi), \quad (11)$$

$$\theta_\lambda(q) = \arccos\left(\frac{q}{2|\mathbf{k}_{\text{in}}|}\right) = \arccos\left(\frac{q\lambda}{4\pi}\right) \quad (12)$$

and we are able to express I^M through the *scattered intensity* I via

$$I^M(q, \phi) = I(\mathbf{q}^\lambda) = I(q, \theta_\lambda(q), \phi). \quad (13)$$

A graphical representation of this relationship is given in figure 3.

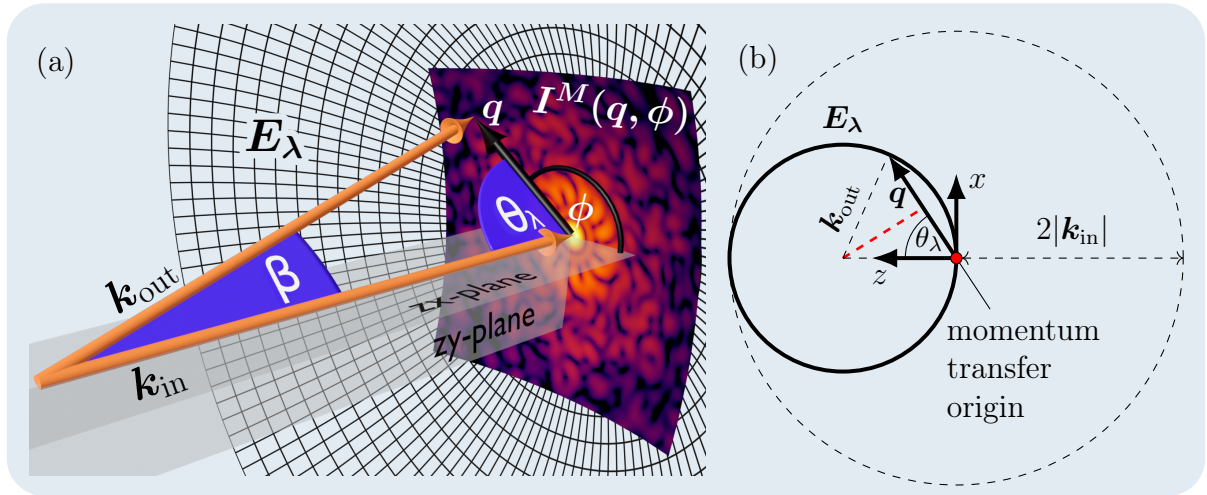


Figure 3: (a) 3D representation of the scattering geometry of figure 1 in momentum space. The origin of the spherical coordinate system lies at the end of the \mathbf{k}_{in} vector and the z -axis is directed along $-\mathbf{k}_{\text{in}}$, such that the momentum transfer vector \mathbf{q} has the coordinate representation (q, θ, ϕ) . Each momentum transfer vector \mathbf{q} has an associated scattering angle β . A portion of the Ewald's sphere E_λ is visualized as grid and the visible diffraction pattern lies on the part of E_λ associated with a square shaped detector plane in real space. (b) Two-dimensional representation of (a) for \mathbf{q} lying in the zx -plane. The Ewald's sphere is represented by the solid circle touching the red coordinate origin. The legs of the right triangle leading to equation (12) are given by $\mathbf{q}/2$ and the red dashed line.

The connection between θ_λ and the scattering angle β , visible in figure 3(b), is given by

$$\theta_\lambda = \frac{\pi - \beta}{2}. \quad (14)$$

In the limit of small scattering angles β , one finds $\theta_\lambda \approx \frac{\pi}{2}$ and the surface spanned by $(q, \theta_\lambda = \frac{\pi}{2}, \phi)$ is precisely the xy -plane in momentum space. For this reason, the small scattering angle limit is also known as the *flat Ewald's sphere limit*. In this case one can use the Fourier projection-slice theorem to directly connect the measured diffraction patterns, given by equation (10), to the absolute value squared of the 2D Fourier transform of the studied particle on to the xy -plane in real space, i.e.

$$I^M(q, \phi) = |[\mathcal{F}P_{xy}\rho](\mathbf{q}^\lambda)|^2, \quad (15)$$

where P_{xy} denotes the projection on to the xy -plane. Equation (15) is one example of how the Fourier transform relationship between the scattering amplitude $\widehat{\rho}(\mathbf{q})$ and the structure of the studied sample, encoded in $\rho(\mathbf{r})$, allows to draw conclusions on the observed scattering patterns. In general, any property of the Fourier transform translates directly into a specific relationship between the real space structure and the observed scattering pattern via the fundamental equation (10). Leaving the realm of small-angle scattering, we will discuss four basic properties that result in general symmetries and transformation properties of I^M .

1. (point inversion) Under point inversion ($\rho(\mathbf{r}) \rightarrow \rho(-\mathbf{r})$) the Fourier transform of a real function changes by a complex conjugation ($\widehat{\rho}(\mathbf{q}) \rightarrow \widehat{\rho}(\mathbf{q})^*$), i.e.

$$[\mathcal{F}\rho(-\mathbf{r})](\mathbf{q}) = \widehat{\rho}(\mathbf{q})^* = \widehat{\rho}(-\mathbf{q}) \quad (16)$$

On the level of intensities this implies $I(\mathbf{q}) = I(-\mathbf{q})$, which is known as *Friedel symmetry* in the context of X-ray scattering [35]. A direct consequence of this symmetry is that the measurement of Thompson scattering patterns does not allow to distinguish between a particle and its point inverse.

2. (shift theorem) Consider $\mathbf{T}_\mathbf{x}$ to describe translations by a vector \mathbf{x} such that $\mathbf{T}_\mathbf{x}\rho(\mathbf{r}) = \rho(\mathbf{r} - \mathbf{x})$. The shift theorem for the Fourier transform states

$$[\mathcal{F}\mathbf{T}_\mathbf{x}\rho](\mathbf{q}) = \widehat{\rho}(\mathbf{q})e^{-i\langle\mathbf{q},\mathbf{x}\rangle}. \quad (17)$$

Since the change is completely captured by the phase $e^{-i\langle\mathbf{q},\mathbf{x}\rangle}$ one finds that the scattered intensity I and by extension I^M , are independent under particle translation, that is

$$|[\mathcal{F}\mathbf{T}_\mathbf{x}\rho](\mathbf{q})|^2 = |\widehat{\rho}(\mathbf{q})e^{-i\langle\mathbf{q},\mathbf{x}\rangle}|^2 = |\widehat{\rho}(\mathbf{q})|^2 = I(\mathbf{q}) \quad (18)$$

3. (rotations) Let ω be an element of the rotation group $SO(3)$ and define its action, \mathbf{R}_ω , on a function, by applying the inverse rotation to its argument, i.e.

$$\mathbf{R}_\omega\rho(\mathbf{r}) = \rho(\mathbf{R}_{\omega^{-1}}\mathbf{r}). \quad (19)$$

Since the Fourier transform commutes with rotations [36, chapter IV theorem 1.1] we directly find that a rotation of the particle causes the scattering amplitude $\widehat{\rho}$ and its intensity I to transform according to the same rotation, i.e.

$$|[\mathcal{F}\mathbf{R}_\omega\rho](\mathbf{q})|^2 = |\mathbf{R}_\omega[\mathcal{F}\rho](\mathbf{q})|^2 = |\mathbf{R}_\omega\widehat{\rho}(\mathbf{q})|^2 = \mathbf{R}_\omega I(\mathbf{q}). \quad (20)$$

This relationship has deep implications on the amount of information that can be extracted from scattering patterns I^M . Equation (20) tells us, that rotating the sample in real space is equivalent to rotating the Ewald's sphere in momentum space, along which the intensities I^M are recorded. By measuring these 2D diffraction patterns for different orientation states of the particle, one can map out the values of the scattered intensity $I(\mathbf{q})$ in a 3D spherical volume. The extend of this volume is ultimately limited by the radius of the Ewald's sphere, i.e. the X-ray wavelength λ , and indicated by the big dashed circle in figure 3 (b).⁴

4. (convolution/cross-correlation theorem) Given two functions $f(\mathbf{r})$ and $g(\mathbf{r})$ the cross-correlation theorem states

$$\left[\mathcal{F} \int_{\mathbb{R}^3} d\mathbf{r}' f(\mathbf{r}' + \mathbf{r})g(\mathbf{r}') \right] = [\mathcal{F}f][\mathcal{F}g]^* \quad (21)$$

In our context this allows us to understand the scattered intensity I , by choosing $f(\mathbf{r}) = g(\mathbf{r}) = \rho(\mathbf{r})$, as Fourier transformed cross-correlation of the electron density ρ with itself, i.e. its auto-correlation

$$[\mathcal{F}^{-1}I](\mathbf{r}) = \int_{\mathbb{R}^3} d\mathbf{r}' \rho(\mathbf{r}' + \mathbf{r})\rho(\mathbf{r}') \quad (22)$$

1.2. The phase problem

If we seek to determine the structure of a particle from measurements of its X-ray *Thomson scattering* patterns I^M alone, we are faced with an ill defined inverse problem, that is caused by the absolute value squared in equation (10). Let us for a moment disregard the challenges associated with the measurement of 2D Ewald's sphere slices and assume full knowledge about the 3D scattered intensity $I(\mathbf{q})$. The structure recovery task can then be formulated as follows:

$$\textbf{Determine } \rho'(\mathbf{r}) \textbf{ such that } |[\mathcal{F}\rho'](\mathbf{q})|^2 = I(\mathbf{q}) \quad (23)$$

The ill definition of (23) relates to the fact, that different structures can have the same scattering intensity. In equation (16) we have already seen this for a structure and its point inverse. In general, any electron density ρ' whose Fourier transform differs from $\widehat{\rho}$ by a complex phase, will have the same scattering intensity. Consider $\rho'(\mathbf{r})$ to be given via

$$\mathcal{F}\rho'(\mathbf{r}) = \widehat{\rho}(\mathbf{q})e^{i\xi(\mathbf{q})},$$

⁴In practice the detector shape limits the accessible momentum space volume, as is indicated by the scattering pattern visible in figure 3(a).

for an arbitrary real valued function $\xi(\mathbf{q})$, then

$$I'(\mathbf{q}) = |\mathcal{F}\rho'(\mathbf{r})|^2 = |\widehat{\rho}(\mathbf{q})e^{i\xi(\mathbf{q})}|^2 = I(\mathbf{q}) \quad (24)$$

and the measured I^M will not allow us to differentiate between the “correct” structure $\rho(\mathbf{r})$ and $\rho'(\mathbf{r})$. One may equivalently think of this as a loss of information that occurs during the measurement process. The scattered electromagnetic wave has the complex scattering amplitude $\widehat{\rho}$, which using its intensity can be expressed via

$$\widehat{\rho}(\mathbf{q}) = \sqrt{I(\mathbf{q})}e^{i\xi(\mathbf{q})}. \quad (25)$$

Current detectors, such as charge coupled device (CCD) sensors, are not sensitive to the phase term $e^{i\xi(\mathbf{q})}$ in equation (25) and only the intensity can be observed. This loss of information is commonly referred to as the *phase problem* [27, 28, 38–40]. In real space the *phase problem* can be stated as the loss of information that occurs under substitution of an electron density $\rho(\mathbf{r})$ with its auto-correlation given by equation (22). These two equivalent perspectives on the phase problem are visualized in figure 4. A “solution” to the *phase problem* is knowledge about the missing information and consequently knowledge about the particle structure $\rho(\mathbf{r})$. Solving the *phase problem* therefore means to pick the “correct” electron density out of all densities ρ' characterized by (23). It is clear that such a choice requires some form of *a priori* information, which acts as additional constraint and allows one to differentiate between all possible ρ' . Depending on the strength of these constraints they may cause the structure recovery task to have a unique solution or even provide a concrete algorithm by which the optimal solution can be found. In the following we list examples of different fields of structure determination and the kind of *a priori* information they employ to provide solutions to the *phase problem*.

X-ray crystallography: Several different types of *a priori* information have been used to solve the *phase problem* in X-ray crystallography. The most prominent methods are based on *isomorphous replacement*, *molecular replacement* and *anomalous scattering* (resonant scattering) [34, 41, 42]. In *isomorphous replacement* one demands to measure diffraction from a crystal of interest as well as an isomorphic crystals, in which one atom is replaced with a heavier element without altering the atomic position in the unit cell. For *molecular replacement* one demands knowledge about the structure of a similar crystal, such that the search space for ρ can be restricted to small variations around this known structure. While these two techniques place constraints on the studied crystal, in *anomalous dispersion* one instead requires resonant scattering patterns to be recorded. The effect of resonant scattering can be understood by adding a complex-valued energy dependent term $f(\hbar\omega)$ to the scattering amplitude [28, equation 1.12], i.e.

$$\widehat{\rho}(\mathbf{q}, \hbar\omega) = \widehat{\rho}_0(\mathbf{q}) + f(\hbar\omega),$$

where $\widehat{\rho}_0(\mathbf{q})$ is the ordinary scattering amplitude from equation (2). Since $f(\hbar\omega)$ is complex the Friedel symmetry expressed in equation (16) is broken and phase information about $\widehat{\rho}_0(\mathbf{q})$ becomes accessible from the measured diffraction patterns $I^M(\mathbf{q}^\lambda, \hbar\omega) = |\widehat{\rho}(\mathbf{q}, \hbar\omega)|^2$.

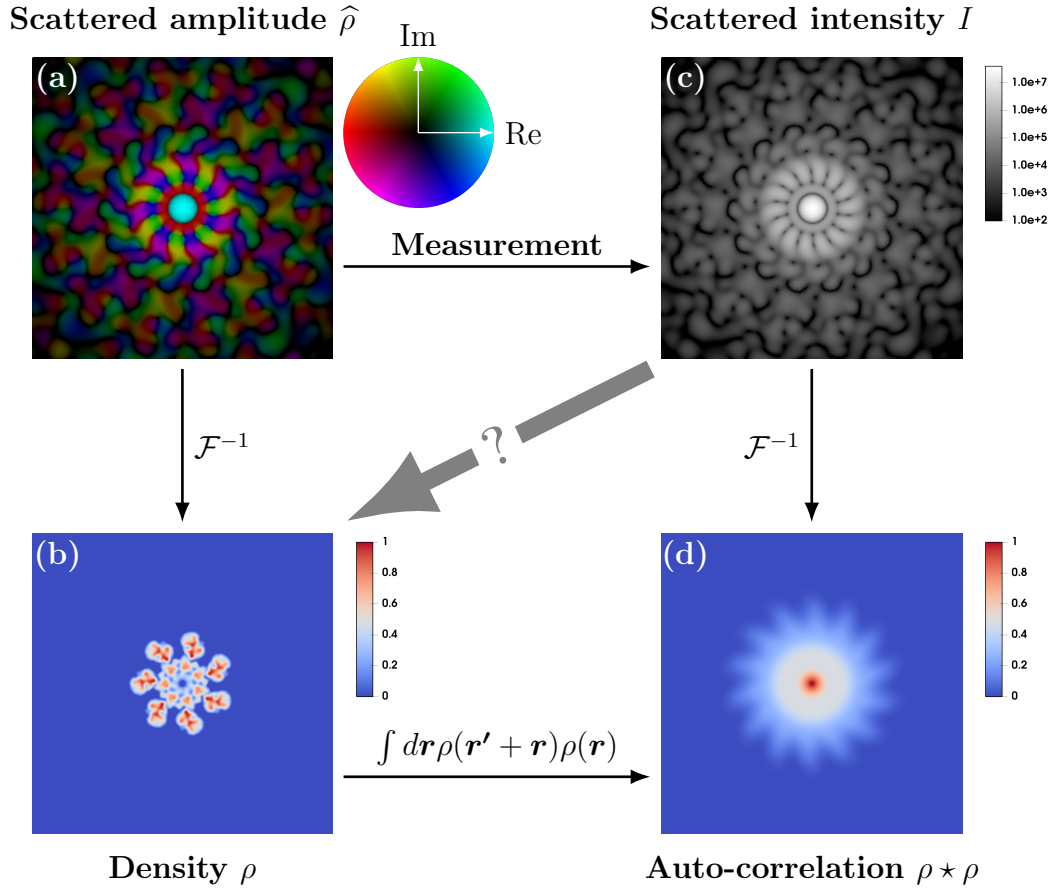


Figure 4: (a) Complex scattering amplitude $\widehat{\rho}(\mathbf{q})$ in the xy -plane of momentum space. Complex numbers $z = xe^{i\xi}$ are represented using the HSV color scheme. The phase ξ determines the color, i.e. the hue (H), the absolute value x determines the black level, i.e. the value (V), and the Saturation (S) remains fixed to its maximum value of 1. The corresponding color map is given by the circular inset to the right of (a). (b) Inverse Fourier transform of (a). By the projection-slice theorem (b) is the projection of the electron density $\rho(\mathbf{r})$ on to the xy -plane in real space. The visible structure belongs to the human apoptosome complex [PDB^a entry *3j2t* [37]]. (c) Scattered intensity $I(\mathbf{q}) = |\widehat{\rho}(\mathbf{q})|^2$ corresponding to (a), displayed in log scale. (d) Inverse Fourier transform of (c), or equivalently the auto-correlation of (b). The *phase problem* manifests itself as the loss of information that occurs in going from the left column of this figure, (a) and (b), to the right column, (c) and (d). The gray arrow symbolizes the problem of structure recovery (23).

^aProtein data bank <https://www.rcsb.org/>

Fourier transform Holography: Here one demands that the electron density $\tilde{\rho}(\mathbf{r})$, of which diffraction patterns are recorded, is the sum of a shifted known electron density $\mathbf{T}_x\rho_0(\mathbf{r})$ and the unknown structure of interest $\rho(\mathbf{r})$, i.e.

$$\tilde{\rho}(\mathbf{r}) = \mathbf{T}_x\rho_0(\mathbf{r}) + \rho(\mathbf{r}).$$

Using the cross correlation theorem from equations (21) and (22) one finds the inverse Fourier transform of the scattering intensity $\tilde{I}(\mathbf{q}) = |[\mathcal{F}\tilde{\rho}](\mathbf{q})|^2$ to contain four terms, that is

$$\left[\mathcal{F}^{-1}\tilde{I}\right](\mathbf{r}) = [\rho_0 \star \rho_0](\mathbf{r}) + [\rho \star \rho](\mathbf{r}) + \mathbf{T}_x[\rho \star \rho_0](\mathbf{r}) + \mathbf{T}_{-x}[\rho_0 \star \rho](\mathbf{r}),$$

where \star denotes cross correlations. If the shift length $|\mathbf{x}|$ is large enough the auto-correlations of ρ and ρ_0 do not overlap with the shifted cross correlations in real space. More over, if ρ_0 is small⁵ compared to ρ , then one finds $[\rho \star \rho_0] = [\rho_0 \star \rho] \approx \rho$ which allows direct access to the unknown structure, see [29, volume 2 part VI] for details.

Single-particle imaging: The phase problem in single-particle imaging (SPI) [9, 11–13, 15] is solved using *iterative phase retrieval* [39, 43]. Both *iterative phase retrieval* as well as SPI are discussed in more detail in 1.3 and 1.5, respectively. The main additional constraint used to solve the phase problem relies on knowledge about the finite support of the structure to be determined [44], i.e. the area where $\rho(\mathbf{r})$ does not vanish. Interestingly, this also places a lower boundary on the sampling rate of the momentum transfer value $|\mathbf{q}_{\max}|$ at which scattering patterns should optimally be measured. This can be seen as follows. The condition of finite support also implies that the scattering intensity $I(\mathbf{q})$ is band limited with “frequency” $2R_{\max}$, where R_{\max} is the largest absolute radial distance $|\mathbf{r}|$ for which $\rho(\mathbf{r}) \neq 0$ [45, 46]. Since we are only able to sample the diffraction patterns on a finite grid, the Shannon sampling theorem [47, theorem 3.2] states that, in order to avoid artifacts due to aliasing, $I^M(\mathbf{q})$ has to be sampled with sampling rates higher than $4R_{\max}$, i.e. momentum transfer steps $\Delta q \leq \frac{\pi}{2R_{\max}}$. Sampling conditions due to the finite support of ρ are usually referred to as *oversampling* constraints in the context of *iterative phase retrieval* [45, 46, 48–50] [51, chapter 5].

Ptychography: In ptychography [52–54] one employs a modified version of *iterative phase retrieval* to solve the *phase problem*. It demands that the sample is partially illuminated by coherent X-ray radiation, such that the recorded scattering patterns I^M correspond to overlapping regions on the sample. A single diffraction pattern is thus not a probe for the entire sample structure $\rho(\mathbf{r})$, but rather its product with a shifted illumination function $[\mathbf{T}_xP](\mathbf{r}) = P(\mathbf{r} - \mathbf{x})$, that takes values in the range $[0, 1]$ and is characterized by the beam shape of the incident X-ray pulse. The overlapping constraint is strong enough to allow for both the structure $\rho(\mathbf{r})$ as well as the illumination function $P(\mathbf{r})$ to be determined from the recorded diffraction patterns [54].

⁵Where, by ρ_0 is small compared to ρ , we mean, that the volume of space on which ρ_0 is non-zero, i.e. its support $\text{supp}(\rho_0)$, is small compared to $\text{supp}(\rho)$.

1.3. Iterative phase retrieval

As mentioned before, single-particle imaging employs a class of phase retrieval algorithms, known as *method of alternating projections* or just *iterative phase retrieval* [38, 55]. In fact, the algorithm implemented as part of this thesis and discussed in sections 2.4 and 3.4 also belongs to this class of algorithms. The main idea behind *iterative phase retrieval* may be formulated as follows.

In the presence of additional constraints, due to *prior* information, the description of the set of electron densities satisfying all constraints generally becomes extremely complicated. This is not surprising, since ideally this set should only contain a single element, i.e. the solution to the phase problem. It is however often possible to split all constraints into two parts, such that the set of densities satisfying either one of these collections of constraints becomes “simple” to describe. Let us call these sets of densities \mathcal{Q} and \mathcal{X} . By the phrase “*simple*” to describe we shall mean numerical access to projections $P_{\mathcal{Q}}$ and $P_{\mathcal{X}}$ that project any given density to the closest density belonging to \mathcal{Q} and \mathcal{X} , respectively.

As an example one may consider \mathcal{Q} to be described by constraints formulated in reciprocal space and \mathcal{X} by those formulated in real space. In the simplest case, the only reciprocal space constraints are given via the scattering intensity $I(\mathbf{q})$. The set \mathcal{Q} then contains densities satisfying $|\hat{\rho}(\mathbf{q})|^2 = I(\mathbf{q})$, i.e. solutions to (23), and the corresponding projection $P_{\mathcal{Q}}$ maps any given density ρ into \mathcal{Q} by substituting the absolute value of its associated scattering amplitude with the square root of I , that is

$$\mathcal{Q} = \{ \rho \mid |\hat{\rho}(\mathbf{q})|^2 = I(\mathbf{q}) \}, \quad (26)$$

$$P_{\mathcal{Q}}\rho = \mathcal{F}^{-1}P_I\mathcal{F}\rho = \mathcal{F}^{-1}P_I\hat{\rho}, \quad (27)$$

where \mathcal{F} is the Fourier transform and P_I is the intensity projection

$$P_I\hat{\rho} = \begin{cases} \frac{\hat{\rho}}{|\hat{\rho}|}\sqrt{I} & \text{if } \hat{\rho} \neq 0 \\ \sqrt{I} & \text{otw.} \end{cases}. \quad (28)$$

Assuming that the combined constraints are strong enough to make the structure determination problem well posed, one can use the sets \mathcal{Q} and \mathcal{X} , irrespective of their precise formulation, to reformulate the structure determination as the following feasibility problem

$$\begin{aligned} &\textbf{find } \rho \\ &\textbf{such that } \rho \textbf{ is in the intersection of } \mathcal{X} \textbf{ and } \mathcal{Q} \textbf{ (i.e. } \rho \in \mathcal{X} \cap \mathcal{Q} \textbf{).} \end{aligned} \quad (29)$$

Starting from an initial electron density guess ρ_0 , one may now try to find a solution by successive applications of the projections $P_{\mathcal{Q}}$ and $P_{\mathcal{X}}$ until a suitable stopping criterion is reached. If ρ_i is the density guess in the i -th step of this iterative process, then the next guess (ρ_{i+1}) is given by

$$\rho_{i+1} = P_{\mathcal{X}}P_{\mathcal{Q}}\rho_i. \quad (30)$$

Figure 5 illustrates this procedure in two examples, where both \mathcal{Q} and \mathcal{X} are simple one-dimensional sets. Alternating projection methods of this kind have a long history in

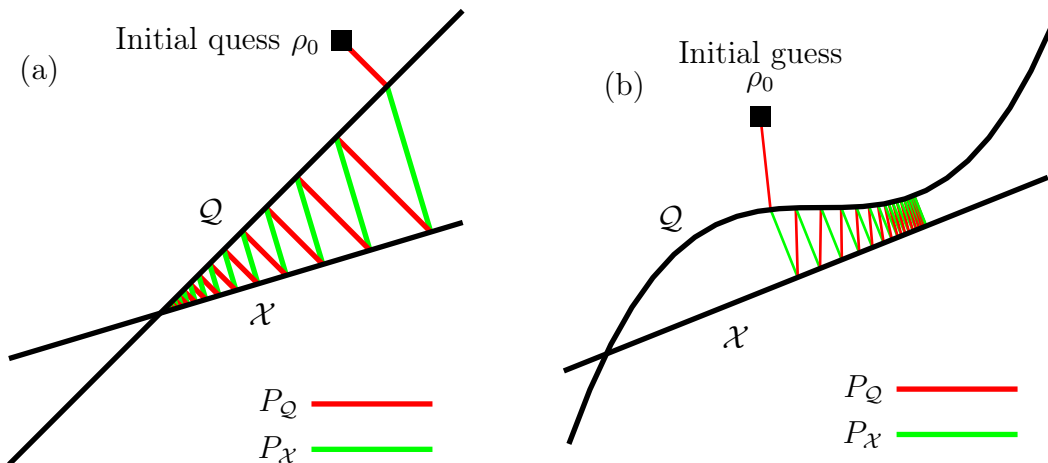


Figure 5: (a) illustrates how iterative projections allow two find the intersection between to lines. (b) serves as a warning that this method is not always guaranteed to work, even if a unique solution exists. The key difference between figure (a) and (b) is, that in the latter the set \mathcal{Q} is not convex.

convex optimization [56, section III] and their convergence properties are well understood [57]. Unfortunately, the set \mathcal{Q} representing our knowledge about the intensity profile $I(\mathbf{q})$ from equation (26) is not convex and many of the results obtained in the convex setting are lost, see figure 5 (b). Nevertheless, such algorithms have been applied with great success [15, 48] and, as already mentioned, form the foundation of single-particle imaging. Their first introduction into the field of electron microscopy is due to Gerchberg & Saxton [38], which used intensity measurements in the image plane as additional constraints. The well known *error-reduction* method (ER) [39] is a relaxation of the Gerchberg & Saxton algorithm. ER only employs the finite size of the studied particle, i.e. the finite support of its electron density, as additional constraint, which allowed its use in single-particle imaging. If S is the support of the studied particle, that is the region of space in which $\rho(\mathbf{r})$ takes non-zero values, then the corresponding real-space constraint is

$$\mathcal{X} = \{\rho \mid \rho(\mathbf{r}) = 0 \text{ for all } \mathbf{r} \notin S\} \quad (31)$$

$$[P_{\mathcal{X}}\rho](\mathbf{r}) = [P_S\rho](\mathbf{r}) = \begin{cases} \rho(\mathbf{r}) & \mathbf{r} \in S \\ 0 & \text{otw.} \end{cases}, \quad (32)$$

where $\mathbf{r} \in S$ denotes all points \mathbf{r} that belong to the support, conversely $\mathbf{r} \notin S$ stands for all points outside of it, and we defined P_S to be the support projection. A schematic representation of the *error-reduction* algorithm can be found in figure 6.

Since its initial development many modifications and adaptations of the *error-reduction* algorithm [43, 52, 58–62], as well as entirely different optimizations schemes [63] have been proposed. All of these variants target different shortcomings of the *ER* method, such as slow convergence [43, 59–62], high dependence on the given support S [58] or the lack of convergence guaranties [63]. In the following we shall highlight some of these variants, as

well as other extensions, that will be part of the phase retrieval algorithm described in section 3.4.

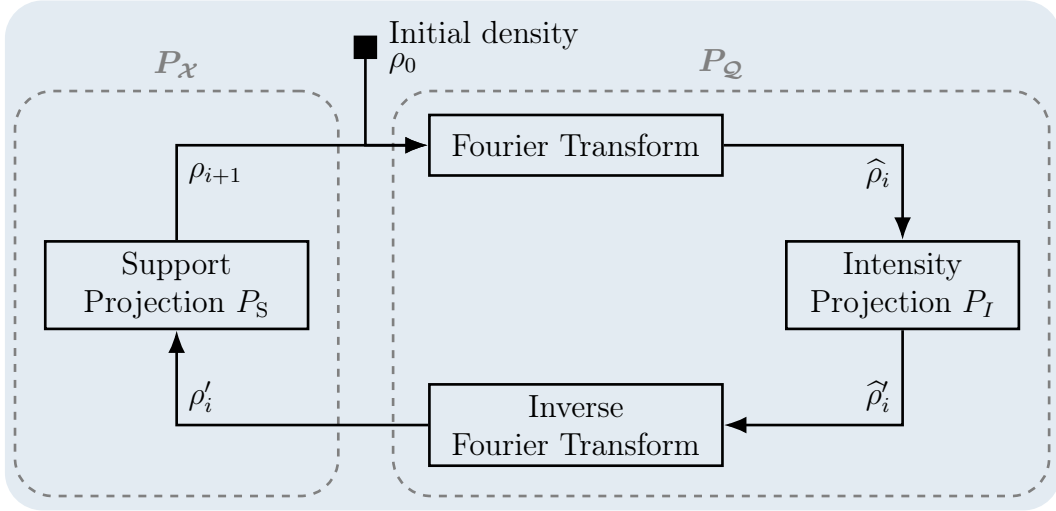


Figure 6: Schematic illustration of the *error-reduction* algorithm.

Additional real-space constraints: Common additions to the support constraint of ER include the realness and positivity of the electron density. In general, constraints of this type can be represented by a “value” projection P_V that places bounds on the real and imaginary values of a density ρ , via

$$P_V \rho'(\mathbf{r}) = \rho_{\text{Re}}(\mathbf{r}) + i\rho_{\text{Im}}(\mathbf{r}), \quad (33a)$$

with

$$\rho_{\text{Re}}(\mathbf{r}) = \begin{cases} V_{\text{Re}}^{\min} & \text{if } \text{Re}[\rho'(\mathbf{r})] < V_{\text{Re}}^{\min} \\ V_{\text{Re}}^{\max} & \text{if } \text{Re}[\rho'(\mathbf{r})] > V_{\text{Re}}^{\max} \\ \text{Re}[\rho'(\mathbf{r})] & \text{otherwise} \end{cases} \quad (33b)$$

and

$$\rho_{\text{Im}}(\mathbf{r}) = \begin{cases} V_{\text{Im}}^{\min} & \text{if } \text{Im}[\rho'(\mathbf{r})] < V_{\text{Im}}^{\min} \\ V_{\text{Im}}^{\max} & \text{if } \text{Im}[\rho'(\mathbf{r})] > V_{\text{Im}}^{\max} \\ \text{Im}[\rho'(\mathbf{r})] & \text{otherwise} \end{cases}, \quad (33c)$$

where $\text{Re}(\cdot)$ and $\text{Im}(\cdot)$ define the real and imaginary parts of the corresponding arguments, and V_{Re}^{\min} , V_{Re}^{\max} , V_{Im}^{\min} and V_{Im}^{\max} are free parameters.

Hybrid input-output method: One of the mayor short comings of the *error-reduction* algorithm is its tendency to stagnate in local minima [43]. To combat this behavior the hybrid input-output (HIO) scheme for optimizing the feasibility problem given in (29), was proposed [43]. It changes the update rule presented in equation (30) to

$$\rho_{i+1}(\mathbf{r}) = \begin{cases} \rho'_i(\mathbf{r}) & \text{if } \rho'_i(\mathbf{r}) = P_{\mathcal{X}}[\rho'_i(\mathbf{r})] \\ \rho_i(\mathbf{r}) - \beta(\rho'_i(\mathbf{r}) - P_{\mathcal{X}}[\rho'_i(\mathbf{r})]) & \text{otw.} \end{cases}, \quad (34)$$

where $\rho'_i(\mathbf{r}) = P_{\mathcal{Q}}[\rho_i(\mathbf{r})]$, as shown in figure 6. One can show that for $\beta = 1$ this method coincides with the Douglas-Rachford splitting method known in convex optimization [44, 64]. Douglas-Rachford splitting is connected to proximal algorithms [65, 66], around which some interesting alternatives to HIO have been proposed [62].

Shrinkwrap: The Shrinkwrap (SW) algorithm [58], seeks to remove the necessity to have precise *a priori* information about the support of $\rho(\mathbf{r})$. It does so via periodic updates of the support constraint. Given the electron density candidate at the i -th step of iterative phase retrieval, $\rho_i(\mathbf{r})$. Shrinkwrap then defines the updated support, as the area inside an isosurface of the convolution of ρ_i with a Gaussian, i.e. via the isosurface of a blurred version of the current electron density guess. If S' denotes the updated support then we may formalize its connection to ρ_i via

$$S' = \left\{ \mathbf{r} \mid \left[|\rho'_i(\mathbf{r})| \star \left(\frac{1}{\sigma\sqrt{2\pi}} e^{-\frac{|\mathbf{r}|^2}{2\sigma^2}} \right) \right] > \gamma \right\}, \quad (35)$$

where \star denotes convolution and the free parameters σ and γ define the standard deviation of the Gaussian function and the isosurface threshold value, respectively.

1.4. X-ray free-electron laser (XFEL)

Free-electron lasers (FEL) are devices in which an electron bunch propagates colinearly with an electromagnetic wave through a sinusoidally alternating magnetic field [29], that is typically generated by an undulator. The alternating magnetic field of the undulator forces the electrons to move along a sinusoidal trajectory. This forced oscillation has two effects, it causes the electron to spontaneously emit electromagnetic radiation and allows electrons to interact with the already co-propagating electromagnetic wave. This interaction depends on the combined phase of the sinusoidal electron motion and the phase of the electromagnetic wave, it is known as the *ponderomotive phase* [67]. Depending on it electrons either loose or gain kinetic energy, which results in a density modulation of the electron bunch itself, known as *micro bunching*. The periodicity of this longitudinal density modulation is equal to the wavelength of the co-propagating electromagnetic wave and causes the electrons to emit radiation in phase with the existing EM field. A positive feedback loop is formed, in which the emitted electromagnetic field grows exponentially [68]. In this period of exponential growth, the relative phase between the density modulation and the emitted EM field is such, that the electrons in a bunch predominantly

loose kinetic energy. This energy-loss in turn continuously changes the relative phase of the density modulation, until it causes the electrons to start absorbing energy from the EM field and saturation is reached [69]. This process can also be started from spontaneously emitted photons without an initially present EM wave, in this case it is known as *self-amplified spontaneous emission* (SASE) [69, 70]. SASE is currently the standard operation mode for FELs in the X-ray regime (XFELs). During the exponential growth phase of the SASE process, one can describe the power of the EM wave $P(z)$, as function of the longitudinal travel distance z , via [67, equation 7.7]

$$P(z) \propto \rho_{\text{FEL}}^2 \sqrt{\frac{L_g}{z}} e^{\frac{z}{L_g}}, \quad (36)$$

where L_g is the *FEL gain length* and ρ_{FEL} is the dimensionless *FEL parameter* that also appears in the saturation power [67, equation 5.16], which is roughly approximated by

$$P_{\text{sat}} \approx \rho_{\text{FEL}} P_{\text{beam}}, \quad (37)$$

where P_{beam} denotes the electron beam power. Typical XFEL gain length are on the order of 1-10 m [71, 72], while the saturation power is approximately reached after 10-20 gain length [72]. The SASE process thus requires undulator length on the order of 100 m which is roughly a factor of 100 longer than typical undulators used in synchrotron facilities [73]. Moreover, the SASE process places strong requirements on the electron beam properties in form of low emittance, high charge density and low energy spread, which can currently only be satisfied by linear accelerators [67, 74]. In such an accelerator electron bunches with charges around 1 nC are typically created by a photoemission radio frequency gun [72, 74] and subsequently accelerated using several super-conducting or normal-conducting acceleration modules up to bunch energies of 5 to 20 GeV. Table 1 lists key parameters of several operational XFEL facilities, it is a modified version of [75, Table 1].

Parameter	LCLS	SACLA	PAL-XFEL	SwissFEL	EuXFEL
Beam energy [GeV]	13.6	8.5	10	5.8	17.5
Bunch charge [nC]	0.25	0.2-0.3	0.2	0.2	1
Slice emittance [μm]	0.4	1.8	0.5	0.4	0.4-1
Peak current [kA]	2.5-3.5	3	3	3	5
User operation	2009	2012	2017	2018	2017
Reference	[71]	[76]	[77]	[78, 79]	[72, 75, 80]

Table 1: Parameters of operational XFEL facilities.

The important property of XFELs, in the scope of this thesis, is their ability to produce coherent X-ray radiation with pulse durations shorter than 100 fs and a peak brightness that is 10 orders of magnitudes larger compared to the brightness achievable at synchrotron light sources.

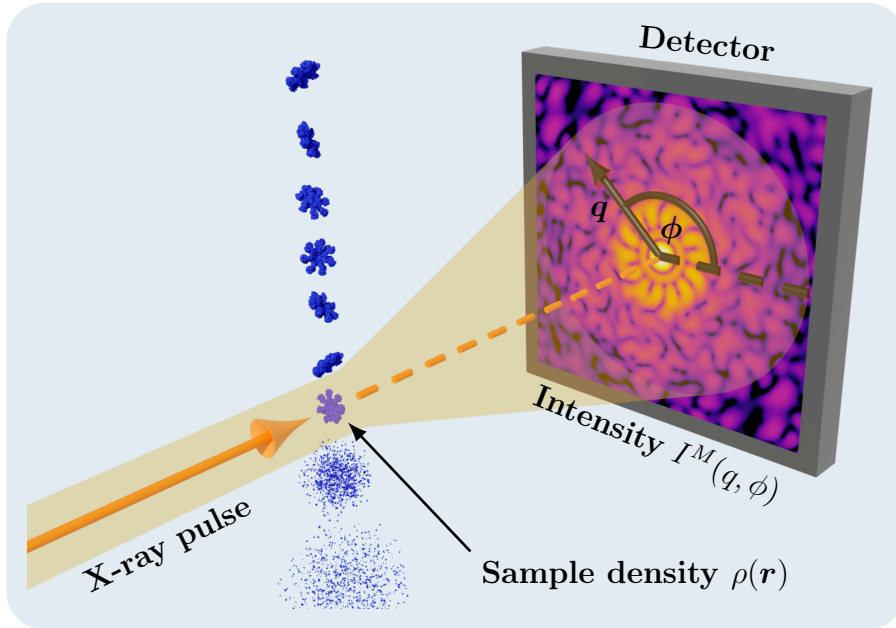


Figure 7: SPI scattering geometry. An incident X-ray pulse diffracts from a single randomly oriented particle with electron density $\rho(\mathbf{r})$. The corresponding intensity pattern $I^M(q, \phi)$ is recorded on a 2D pixel detector.

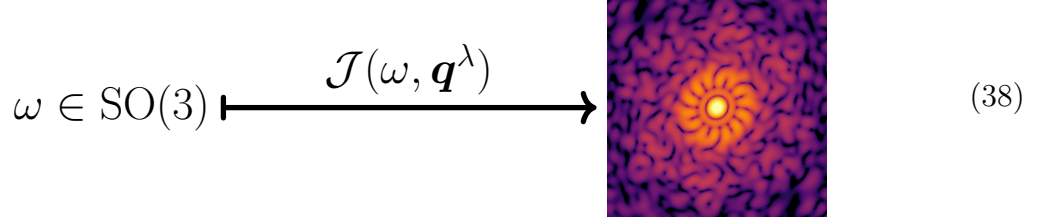
1.5. Single-particle imaging (SPI)

That short coherent pulses of X-ray radiation may enable diffraction limited structure determination under biologically relevant conditions, has been theorized since the 1980's [11]. The potential of sidestepping the need to crystalize biological samples for imaging has ever since been a major driving force and lead to the first descriptions of *diffraction before destruction* experiments [12]. In such experiments ultra short X-ray pulses, with pulse durations below 100 fs, are used [81] in order to “outrun” radiation damage and preserve structural information in scattering patterns. Single-particle imaging, in similarity to FXS, represents a concrete scattering technique based on *diffraction before destruction* experiments and has been made possible by X-ray free-electron lasers [9, 15, 18]. Figure 7 depicts a typical experimental setup within SPI. As the name suggests, SPI relies on the measurement of diffraction patterns from individual reproducible randomly oriented particles. Its structure reconstruction workflow can be understood as a two step process. Initially the recorded single-particle scattering patterns $I^M(\mathbf{q}^\lambda)$ are used to construct a model of the full 3D scattered intensity $I(\mathbf{q})$. This step is usually [9, 15, 18] performed using the “expand-maximize-compress” (EMC) algorithm [33], which is a derivative of the maximum likelihood algorithm [82]. With access to the full 3D scattered intensity $I(\mathbf{q})$ one is able to apply iterative phase retrieval in the second step and reconstruct the electron density $\rho(\mathbf{r})$ of the studied particle, as described in section 1.3.

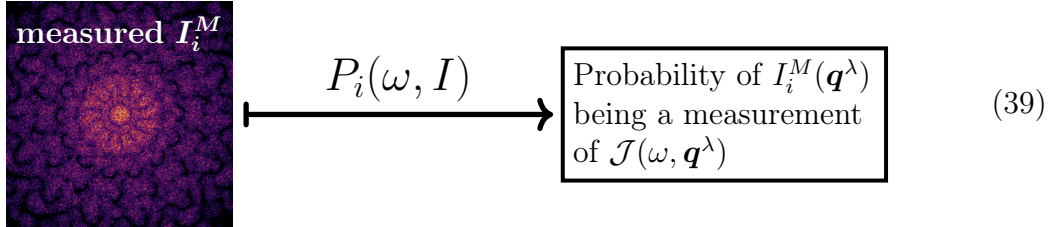
One of the main differences between FXS and SPI is how they use the measured diffraction patterns $I^M(\mathbf{q}^\lambda)$ to access information about $I(\mathbf{q})$. It is therefore interesting to

understand the principles behind the *EMC* algorithm [33].

At its core EMC is an iterative optimization algorithm build around the following two observations. Assume, we are given a candidate 3D scattering intensity $I(\mathbf{q})$. By applying a rotation ω to this intensity and restricting \mathbf{q} to the Ewald's sphere, it is possible to simulate diffraction patterns corresponding to arbitrary particle rotations. One may think of this process as the function, $\mathcal{J}(\omega, \mathbf{q}^\lambda) = \mathbf{R}_\omega I(\mathbf{q}^\lambda)$, that maps a rotation ω to its scattering pattern under the intensity candidate I , i.e.

$$\omega \in \text{SO}(3) \xrightarrow{\mathcal{J}(\omega, \mathbf{q}^\lambda)} \text{Image} \quad (38)$$


The second observation is that the probability of measuring photons on a detector pixel follows Poisson statistics. For any measured diffraction pattern $I_i^M(\mathbf{q}^\lambda)$ we are then able to compute the probability $P_i(\omega, I)$ of it being a measurement of the simulated patterns $\mathcal{J}(\omega, \mathbf{q}^\lambda)$, which are based on our current guess for $I(\mathbf{q})$, i.e.

$$\text{measured } I_i^M \xrightarrow{P_i(\omega, I)} \text{Probability of } I_i^M(\mathbf{q}^\lambda) \text{ being a measurement of } \mathcal{J}(\omega, \mathbf{q}^\lambda) \quad (39)$$


The probability $P_i(\omega, I)$ takes the form [33, equation 9]

$$\begin{aligned} P_i(\omega, I) &= \frac{R_i(\omega, I)}{\int_{\text{SO}(3)} d\omega R_i(\omega, I)} \\ R_i(\omega, I) &= \prod_k \mathcal{J}(\omega, \mathbf{q}_k^\lambda)^{I_i^M(\mathbf{q}_k^\lambda)} \exp(-\mathcal{J}(\omega, \mathbf{q}_k^\lambda)) \\ &= \exp\left(\sum_k I_i^M(\mathbf{q}_k^\lambda) \ln(\mathcal{J}(\omega, \mathbf{q}_k^\lambda)) - \mathcal{J}(\omega, \mathbf{q}_k^\lambda)\right), \end{aligned}$$

where k indexes the pixels of the detector and \mathbf{q}_k^λ is the Ewald's sphere point corresponding to the k 'th detector pixel. The probabilities $P_i(\omega, I)$ together with the set of diffraction patterns $I_i^M(\mathbf{q}^\lambda)$, indexed by i , now allow us to obtain an updated guess for the function \mathcal{J} from (38) by simply computing the probability weighted sum of all I_i^M [33, equation 11],

$$\mathcal{J}'(\omega, \mathbf{q}_k^\lambda) = \frac{\sum_i P_i(\omega, I) I_i^M(\mathbf{q}_k^\lambda)}{\sum_i P_i(\omega, I)}. \quad (40)$$

This new function \mathcal{J}' does, in general, not have the form $\mathcal{J}'(\omega, \mathbf{q}^\lambda) = \mathbf{R}_\omega I'(\mathbf{q}^\lambda)$ for some new candidate intensity I' . Physically we know that such a function has to exist⁶, so we may use this knowledge as additional constraint and compute our new candidate intensity I' such that $\mathbf{R}_\omega I'(\mathbf{q}^\lambda)$ is as close as possible to \mathcal{J}' . This can be done by defining $I'(\mathbf{q})$ for each fixed \mathbf{q} as the average over all values of $\mathcal{J}'(\omega, \mathbf{q}_k^\lambda)$ that satisfy $\mathbf{q} = \mathbf{R}_{\omega^{-1}} \mathbf{q}_k^\lambda$ [33, equation 14]⁷. This last step is called “condensation/compression” step. We may summarize the EMC algorithm as the following iterative procedure

1. Choose a starting guess for $I(\mathbf{q})$ called I_0 .
2. In the j -th step of the algorithm: Compute $\mathcal{J}_j(\omega, \mathbf{q}^\lambda) = \mathbf{R}_\omega I_j(\mathbf{q}^\lambda)$ and the associated probabilities $P_i(\omega, I_j)$.
3. Compute the updated map \mathcal{J}'_j via equation (40).
4. “Condensate/Compress” $\mathcal{J}'_j(\omega, \mathbf{q}^\lambda)$ into an updated intensity I_{j+1}
5. Repeat steps 2-4 until a suitable convergence criterion is reached.

In summary one can say that EMC uses an assumption about photon statistics⁸ to compute $I(\mathbf{q})$ directly from the measured $I^M(\mathbf{q}^\lambda)$, while, as we shall see in section 2, FXS uses an assumption about the rotational statistics of the measured particles and extracts information about $I(\mathbf{q})$ from certain averages over all collected diffraction patterns.

1.6. Small and wide angle x-ray scattering (SAXS/WAXS)

Small and wide angle X-ray scattering is the study of the averaged scattering pattern of a sample, where the average is taken over all possible realizations of the studied sample [83–85]. The difference between SAXS and WAXS lies purely in the range of momentum transfer values for which this average is measured (or computed), i.e. if the *flat Ewald’s sphere limit* applies or not. In *diffraction before destruction* experiments the SAXS/WAXS intensity I^{SAXS} simply has the form

$$I^{\text{SAXS}}(q, \phi) = \langle I^M(q, \phi) \rangle_M, \quad (41)$$

where $\langle \cdot \rangle_M$ denotes the average over all measured diffraction patterns. In many cases $I^{\text{SAXS}}(q, \phi)$ is angularly isotropic, if experimental factors, such as the polarization contribution [equation (1)], have been compensated. Under these conditions one may further reduce $I^{\text{SAXS}}(q, \phi)$ to a 1D profile [see figure 8], i.e.

$$I^{\text{SAXS}}(q) = \frac{1}{2\pi} \int_0^{2\pi} d\phi I^{\text{SAXS}}(q, \phi) = I^{\text{SAXS}}(q, 0). \quad (42)$$

⁶In form of the correct scattering intensity $I(\mathbf{q})$ corresponding to the electron density $\rho(\mathbf{r})$ of the measured particle.

⁷In practice this average becomes an interpolation task since \mathbf{q} and $\mathbf{R}_{\omega^{-1}} \mathbf{q}_k^\lambda$ are most likely correspond to different samplings of momentum space.

⁸The assumption, that the probability of a photon being measured on a detector pixel follows a Poisson distribution.

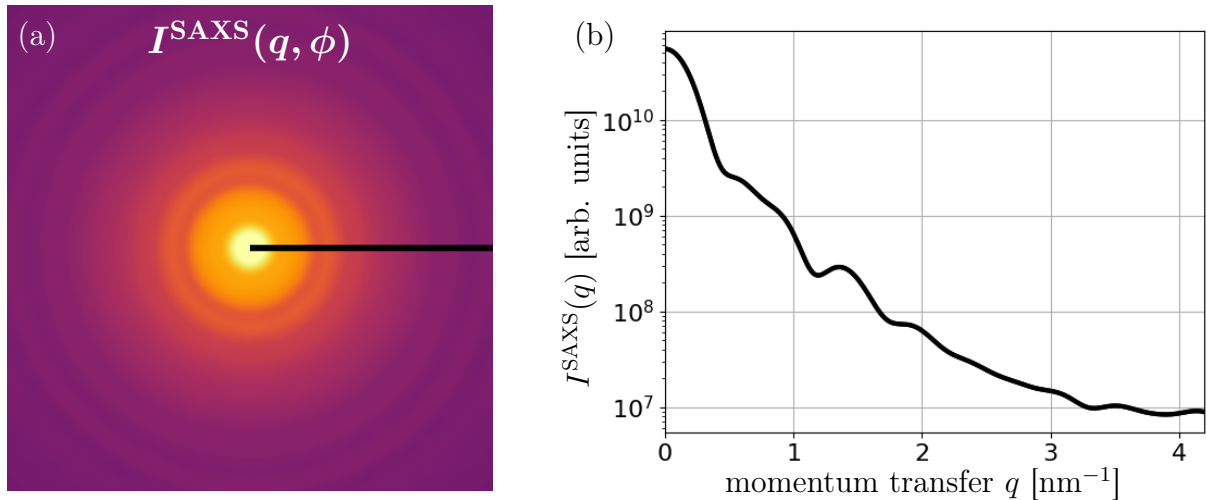


Figure 8: (a) Isotropic SAXS pattern (b) Line cut of (a) along the black line or equivalently its azimuthal average as defined in equation (42).

In general, I^{SAXS} is not angularly isotropic and the reduction to its azimuthal average, as depicted in figure 8 (b), unnecessarily hides some of the structural information contained in the averaged scattering signal. This will become especially important in section 6, where we discuss systems of particles whose rotation states are not uniformly distributed. For this reason we will always regard I^{SAXS} in its 2D form, unless explicitly written as $I^{\text{SAXS}}(q)$.

We shall see in section 2 that, if the considered sample is a dilute solution of randomly oriented particles obeying a uniform orientational distribution, I^{SAXS} is proportional to the rotational average of the single-particle scattering intensity $\int_{\text{SO}(3)} d\omega \mathbf{R}_\omega I(\mathbf{q}) = \langle \mathbf{R}_\omega I(\mathbf{q}) \rangle_{\text{SO}(3)}$. While this average hides much of the information contained in $I(\mathbf{q})$, it allows to estimate the size and low-resolution shape of the studied particle [84, 85]. The process of averaging is at the same time the greatest strength of SAXS/WAXS since it makes the analysis method comparatively simple and inherently robust to noise.

1.7. Rotations and harmonic analysis

Rotations and their actions on functions will play an important role in the formulation of *fluctuation X-ray scattering*. Moreover, they are tightly connected to harmonic analysis in polar and spherical coordinates. This section is dedicated to introduce basic statements and conventions that will be used throughout the thesis. All the presented results are readily available in text books, such as [36, 86–89].

We shall follow the standard conventions for polar and spherical coordinate systems. In polar coordinates a vector \mathbf{v} is specified by the pair (r, ϕ) where $r = \|\mathbf{v}\|$ denotes its norm and ϕ is its angle with the x -axis. In spherical coordinates a vector is described by the triple (r, θ, ϕ) , where r is defined as before, θ represents its angle to the z -axis and ϕ

denotes the angle between the x -axis and the projection of \mathbf{v} to the xy -plane, see figure 9 (a).

A two-dimensional rotation, i.e. an element of the group $SO(2)$, will be denoted by its rotation angle α . Conversely, an element of the three-dimensional rotation group $SO(3)$ will be either symbolically represented by ω , or through its associated Euler angles (α, β, γ) . We shall follow the zyz convention for Euler angles. One may either think of (α, β, γ) as defining rotation angles around the z and y axes of a rotating reference frame, or with respect to the fixed coordinate system. Let $(\mathbf{x}, \mathbf{y}, \mathbf{z})$ denote the axis directions

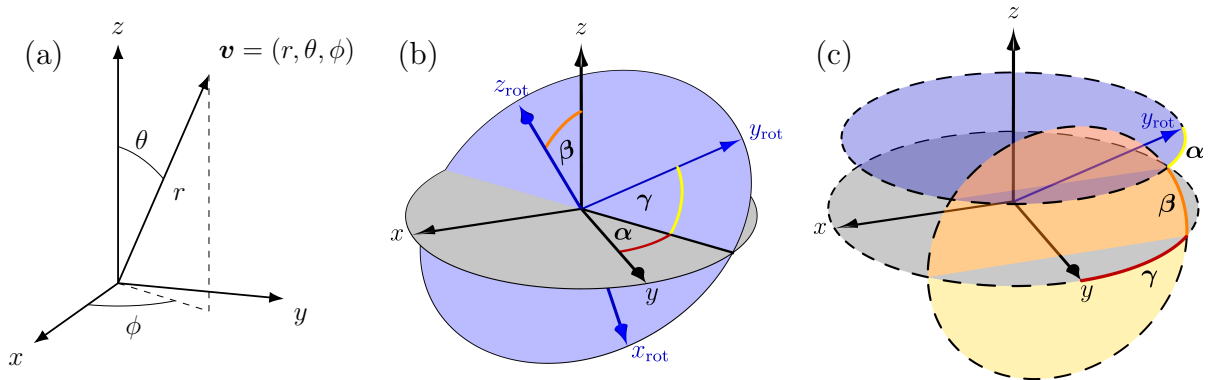


Figure 9: (a) Representation of a vector \mathbf{v} in spherical coordinates. (b) Depiction of a rotation by (α, β, γ) using the zyz Euler angle convention interpreted with respect to a rotating coordinate frame. The vectors \mathbf{x}_{rot} , \mathbf{y}_{rot} and \mathbf{z}_{rot} are rotated by (α, β, γ) with respect to \mathbf{x} , \mathbf{y} and \mathbf{z} . (c) The same rotation as in (b), that transforms \mathbf{y} to \mathbf{y}_{rot} , but executed in a fixed coordinate system.

of the original coordinate system. In the co-rotating interpretation (α, β, γ) acts, as represented in figure 9 (b), via

1. Rotate by α around \mathbf{z} , which results in a new coordinate frame $(\mathbf{x}', \mathbf{y}', \mathbf{z})$.
2. Rotate by β around \mathbf{y}' , which yields the coordinate frame $(\mathbf{x}'', \mathbf{y}', \mathbf{z}')$.
3. Rotate by γ around \mathbf{z}' .

The same rotation can be described in a fixed coordinate system via [see figure 9 (c)]

1. Rotate by γ around \mathbf{z} .
2. Rotate by β around \mathbf{y} .
3. Rotate by α around \mathbf{z} .

The action of a rotation α , ω or (α, β, γ) on a point in space will be denoted by \mathbf{R}_α , \mathbf{R}_ω or $\mathbf{R}_{(\alpha, \beta, \gamma)}$ respectively. This definition can be extended to the rotation action on a scalar function $f(\mathbf{r})$, by applying the inverse rotation to its argument vector. We will write $\mathbf{R}_\alpha f(\mathbf{r})$, $\mathbf{R}_\omega f(\mathbf{r})$ or $\mathbf{R}_{(\alpha, \beta, \gamma)} f(\mathbf{r})$ to denote the rotated function, that is

$$\mathbf{R}_\alpha f(\mathbf{r}) = f(\mathbf{R}_{-\alpha} \mathbf{r}) \quad \text{and} \quad \mathbf{R}_\omega f(\mathbf{r}) = f(\mathbf{R}_{\omega^{-1}} \mathbf{r}) = f(\mathbf{R}_{(-\gamma, -\beta, -\alpha)} \mathbf{r}). \quad (43)$$

Using the above conventions we will now introduce basic concepts from *harmonic analysis* starting in two-dimensions. Consider a sufficiently smooth complex valued function $f(r, \phi)$. By definition this implies, that f is periodic in its angular variable and we may expand $f(r, \phi)$, for constant r , in a Fourier series

$$f(r, \phi) = \sum_{n=-\infty}^{\infty} f_n(r) e^{in\phi} \quad \text{with} \quad f_n = \frac{1}{2\pi} \int_0^{2\pi} d\phi f(r, \phi) e^{-in\phi}, \quad (44)$$

where we call $f_n(r)$ the harmonic coefficients or Fourier coefficients of f . This notion can be generalized from a circle to a sphere using spherical harmonics

$$Y_m^l(\theta, \phi) = \sqrt{\frac{2l+1}{4\pi} \frac{(l-m)!}{(l+m)!}} P_l^{|m|}(\cos(\theta)) e^{im\phi} \quad \text{with} \quad \begin{matrix} l = 0, \dots, \infty \\ m = -l, \dots, l \end{matrix}, \quad (45)$$

with $P_l^{|m|}$ being associated Legendre polynomials where l and m are called the degree and order of Y_m^l respectively. It will be convenient to introduce the following notation for spherical harmonics

$$Y_m^l(\theta, \phi) = \tilde{P}_l^m(\theta) e^{im\phi} \quad \text{with} \quad \tilde{P}_l^m(\theta) = \sqrt{\frac{2l+1}{4\pi} \frac{(l-m)!}{(l+m)!}} P_l^{|m|}(\cos(\theta)). \quad (46)$$

Given a complex valued function $f(r, \theta, \phi)$ in spherical coordinates, which for fixed r is defined on a sphere, one may consider its spherical harmonic expansion

$$f(r, \theta, \phi) = \sum_{l=0}^{\infty} \sum_{m=-l}^l f_m^l(r) Y_m^l(\theta, \phi) \quad (47)$$

$$f_m^l(r) = \int_{S^2} d\Omega f(r, \theta, \phi) Y_m^l(\theta, \phi)^* = \int_0^\pi d\theta \sin(\theta) \int_0^{2\pi} d\phi f(r, \theta, \phi) Y_m^l(\theta, \phi)^*, \quad (48)$$

here * indicates complex conjugation. The $f_m^l(r)$ are typically called spherical harmonic coefficients of f . In case f is a real valued function it is important to note that not all of its harmonic coefficients are independent, but rather obey the symmetry relations

$$f_n(r)^* = f_{-n}(r) \quad \text{and} \quad f_m^l(r)^* = (-1)^m f_{-m}^l(r), \quad (49)$$

which are a direct consequences of analogue symmetries in the expansion functions $e^{in\phi}$ and $Y_m^l(\theta, \phi)$, respectively.

It will be useful to extend the notion of a Fourier series even further to the spaces of rotations $\text{SO}(2)$ and $\text{SO}(3)$ ⁹. For functions $f(\alpha)$, that take two-dimensional rotations as argument, we already encountered the proper notion of a Fourier transform in eq. (44). This is because two-dimensional rotations are completely specified by a single angle and

⁹In fact, the notion of Fourier series can be defined on any compact Lie group [88] of which the rotation group $\text{SO}(3)$ is an example.

thus $SO(2)$ itself behaves like a circle¹⁰. For $SO(3)$ a Fourier series analogue can be defined using Wigner D-matrices [87, equation 19.15]

$$D_{nm}^l(\alpha, \beta, \gamma) = e^{-in\alpha} d_{n,m}^l(\beta) e^{-im\gamma} \quad (50)$$

$$d_{nm}^l(\beta) = \sqrt{(l+m)!(l-m)!(l+n)!(l-n)!} \times \sum_{\kappa=\min(0,m-n)}^{\min(l+m,l-n)} (-1)^\kappa \frac{\cos(\beta/2)^{2l+m-n-2\kappa} \sin(\beta/2)^{n-m+2\kappa}}{(l-n-\kappa)!(l+m-\kappa)!(\kappa+n-m)!\kappa!}, \quad (51)$$

where $l = 0, \dots, \infty$ and $n, m = -l, \dots, l$ and $d_{n,m}^l$ are called small Wigner D-matrices. A possibly complex valued function $f(\alpha, \beta, \gamma)$ on $SO(3)$ may then be expanded via [90]

$$f(\alpha, \beta, \gamma) = \sum_{l=0}^{\infty} \sum_{n=-l}^l \sum_{m=-l}^l (2l+1) f_{nm}^l D_{nm}^l(\alpha, \beta, \gamma) \quad (52)$$

$$f_{nm}^l = \frac{1}{8\pi^2} \int_{SO(3)} d\omega f(\omega) = \frac{1}{8\pi^2} \int_0^{2\pi} d\alpha \int_0^\pi d\beta \sin(\beta) \int_0^{2\pi} d\gamma f(\alpha, \beta, \gamma) D_{nm}^l(\alpha, \beta, \gamma)^*, \quad (53)$$

with f_{nm}^l denoting the Fourier transform of f . We will see in section 3.5 and 6 that this Fourier series will allow us to efficiently align functions that differ by a rotation and further more plays a major role in an extension of the FXS formalism. The most important use case of Wigner D-matrices, in the context of FXS, is however the description of rotations acting on spherical harmonics. A rotated spherical harmonic $\mathbf{R}_{(\alpha,\beta,\gamma)} Y_m^l(\theta, \phi)$ is a linear combination of all spherical harmonics of the same degree l whose coefficients are determined by the Wigner D-matrices associated to the rotation (α, β, γ) , i.e.

$$\mathbf{R}_{(\alpha,\beta,\gamma)} Y_m^l(\theta, \phi) = \sum_{n=-l}^l Y_n^l(\theta, \phi) D_{nm}^l(\alpha, \beta, \gamma)^*. \quad (54)$$

In combining equation (54) with the spherical harmonic series in equation(47) we obtain an expression for the rotation action on an arbitrary function $f(r, \theta, \phi)$, given in spherical coordinates, that is

$$\begin{aligned} \mathbf{R}_{(\alpha,\beta,\gamma)} f(r, \theta, \phi) &= \sum_{l,m} f_m^l(r) \sum_n D_{nm}^l(\alpha, \beta, \gamma)^* Y_n^l(\theta, \phi) \\ &= \sum_{l,n} \left(\sum_m f_m^l(r) D_{nm}^l(\alpha, \beta, \gamma)^* \right) Y_n^l(\theta, \phi) \\ &= \sum_{l,m} \left(\sum_n f_n^l(r) D_{mn}^l(\alpha, \beta, \gamma)^* \right) Y_m^l(\theta, \phi), \end{aligned} \quad (55)$$

¹⁰ $SO(2)$ and the circle group \mathbb{S}^1 are isomorphic as groups.

where in the last line the roles of the indices n and m have been swapped. Note, that the last equality in eq. (55) has again the form of a spherical harmonic series with coefficients $\sum_n f_n^l(r) D_{mn}^l(\alpha, \beta, \gamma)^*$. This allows us to identify the rotation action on the level of spherical harmonic coefficients and we may write

$$\mathbf{R}_{(\alpha, \beta, \gamma)} f_m^l(r) = \sum_n f_n^l(r) D_{mn}^l(\alpha, \beta, \gamma)^*. \quad (56)$$

Similarly one can realize that the action of a two-dimensional rotation α on a polar function, i.e. $\mathbf{R}_\alpha f(r, \phi) = f(r, \phi - \alpha)$, multiplies its Fourier series coefficients by a constant phase and we arrive at

$$\mathbf{R}_\alpha f_n(r) = f_n(r) e^{-in\alpha}. \quad (57)$$

Equation (56) and (57) are the rotational analogues of the Fourier shift theorem from equation (17) and represent the main takeaways from our introduction to harmonic analysis.

2. Fluctuation X-ray scattering (FXS)

The goal behind the invention of *fluctuation X-ray scattering* [1] was to access structural information of particles in solution, that goes beyond the rotationally averaged information extractable from SAXS or WAXS measurements. To do so FXS demands to measure diffraction patterns using coherent X-ray pulses on time scales shorter than the rotational diffusion times of the considered particles. An instantaneous diffraction pattern of this kind can be thought of as the sum between the ensemble averaged SAXS pattern and *fluctuations* around this average, see figure 10. These fluctuations and their study via av-

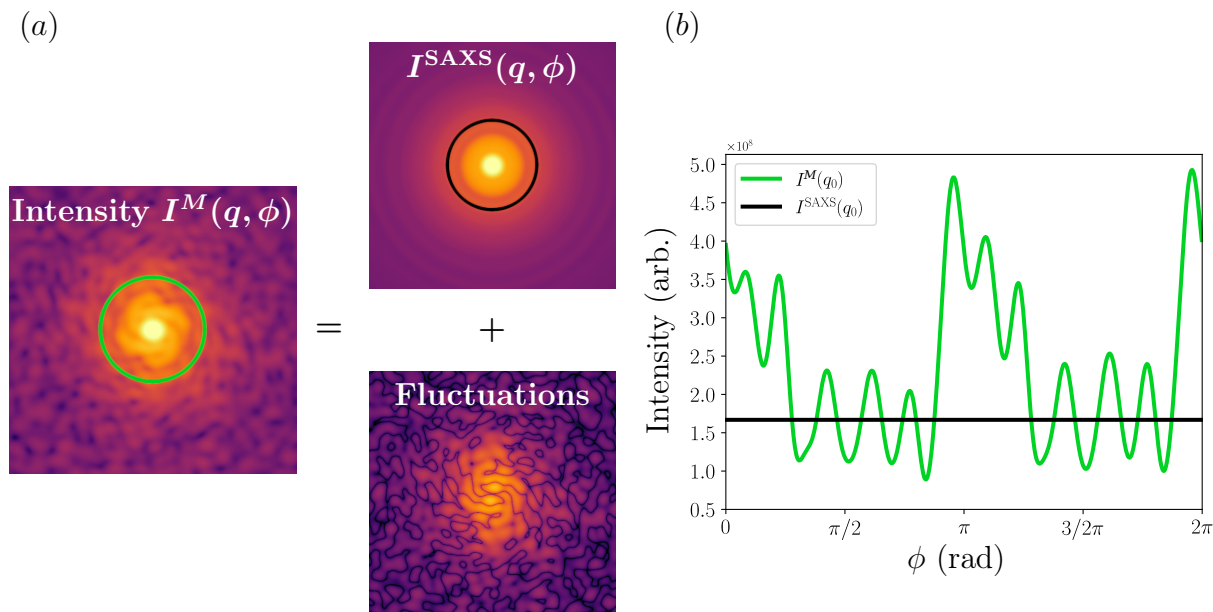


Figure 10: (a) The left hand side depicts a simulated instantaneous scattering pattern $I^M(q, \phi)$ for a cluster of four proteins (PDB 6B3R [91]), while the right hand side displays its decomposition into a SAXS pattern, corresponding to the average over many realizations of such 4 particle clusters, plus *fluctuations* around this average. (b) Shows line cuts of $I^M(q, \phi)$ and $I^{\text{SAXS}}(q, \phi)$ along the circles visible in (a) at $q = q_0$, where *fluctuations* become visible as differences between the two curves.

erages, as proposed by Kam [1–3], are what ultimately coined the term *fluctuation X-ray scattering*. It however turned out, that the X-ray pulses available at the time where neither short enough nor intense enough to measure diffraction patterns of the needed quality, despite efforts such as freezing particles prior to their illumination [3]. In particular for biological samples, e.g. proteins or viruses, it turned out, that the observation of a sufficient scattering signal necessitates X-ray pulses of such brightness that the sample is destroyed after a single exposure, due to coulomb explosion. In this case the limiting timescale for the pulse duration became the time scale at which radiation damage occurs within samples, which is on the order of 1-100fs [12]. As we have seen in sections 1.4 and 1.5, such measurements became possible [4–8, 15] and are called *diffraction before destruction* experiments. With the availability of experimental data, interest in FXS resurged. This

gave rise to the first phase retrieval algorithm modified to fit FXS [19] and also sparked important adjacent fields such as X-ray cross-correlation analysis (XCCA) [92–94], the use of triple and higher correlations [95–97], as well as methods targeting the local order of liquids and glasses using the *pair-angle distribution function* (PADF) [98]. XCCA, in particular, is centered around the computation of the angular cross-correlation function $C(q_1, q_2, \Delta)$ for each individual scattering pattern $I^M(q, \phi)$ and subsequent analysis of its statistical average.

$$C(q_1, q_2, \Delta) = \int_0^{2\pi} d\phi I(q_1, \phi + \Delta) I(q_2, \phi) \quad (58)$$

Sometimes XCCA is used synonymously with FXS. While the concept of the cross-correlation function is numerically useful within FXS, as we shall see in section 3.1, it is not necessary for its definition and in some ways also distracts from the core principle behind FXS, which lies in the use of averages. Because of this we prefer to differentiate between the two techniques.

In the following we shall provide a rather general definition of *fluctuation X-ray scattering*, including the studied objects as well as the assumptions necessary for their interpretation. Its goal is to provide a center around which the remainder of this thesis will be structured.

Definition 2.1 (Fluctuation X-ray scattering in 3D) *Let $\rho(\mathbf{r})$ be the electron density of a particle and consider $\rho^M(\mathbf{r})$ to be a sample configuration containing a random number N of randomly oriented realizations of ρ , that are randomly distributed inside an interaction volume V_{int} , i.e.*

$$\rho^M(\mathbf{r}) = \sum_{i=1}^N \mathbf{T}_{\mathbf{x}_i} \mathbf{R}_{\omega_i} \rho(\mathbf{r}) = \sum_{i=1}^N \rho(\mathbf{R}_{\omega_i}^{-1} \mathbf{r} - \mathbf{x}_i), \quad (59)$$

where ω_i are elements of the rotation group $\text{SO}(3)$ and \mathbf{x}_i are vectors pointing to the origin of the i -th particle within V_{int} . Furthermore, let $\widehat{\rho}^M(\mathbf{q})$ and $\widehat{\rho}(\mathbf{q})$ be the scattering amplitudes with corresponding intensities $I^M(\mathbf{q}) = |\widehat{\rho}^M(\mathbf{q})|^2$ and $I(\mathbf{q}) = |\widehat{\rho}(\mathbf{q})|^2$ of the electron densities ρ^M and ρ at momentum transfer vector \mathbf{q} , respectively. We will write $I^M(\mathbf{q}^\lambda)$ or $I^M(q, \phi)$ for a recorded two-dimensional scattering pattern¹¹ of the sample ρ^M and introduce the FXS moments of degree $d \geq 1$ as ensemble averages of the form

$$\mathcal{M}_N^d(q_1, \dots, q_d, \phi_1, \dots, \phi_d) = \left\langle \prod_{i=1}^d I^M(q_i, \phi_i) \right\rangle_M \quad (60)$$

or, using the harmonic coefficients $I_n^M(q_i)$ of a scattering pattern $I^M(q, \phi)$, as

$$\mathcal{M}_N^d(q_1, \dots, q_d, n_1, \dots, n_d) = \left\langle \prod_{\substack{i=1 \\ \text{odd } i}}^d I_{n_i}^M(q_i) \prod_{\substack{i=2 \\ \text{even } i}}^d I_{n_i}^M(q_i)^* \right\rangle_M = \langle I_{n_1}^M(q_1) I_{n_2}^M(q_2)^* \dots \rangle_M \quad (61)$$

Fluctuation X-ray scattering is the study of the moments \mathcal{M}_N^d , with the goal of obtaining structural information about the considered particle, if the following assumptions hold.

¹¹As introduced in section 1.1, \mathbf{q}^λ denotes a point on the Ewald's sphere, see equations (12) and (13).

1. (*diffraction before destruction*) The measured intensity patterns are the result of Thompson scattering, see section 1.1, and are created on time scales shorter than any dynamical processes within a sample that would alter its electron density, including radiation damage. That is, we can assume the measured intensity pattern of an individual particle to be given by

$$I^M(q, \phi) = |\widehat{\rho}(\mathbf{q}^\lambda)|^2 = \left| \int d\mathbf{r} \rho(\mathbf{r}) e^{-i\langle \mathbf{q}^\lambda, \mathbf{r} \rangle} \right|^2. \quad (62)$$

2. (*nature of randomness*)

- a) The rotational random variables $\{\omega_0, \omega_1, \dots\}$ are independently and identically distributed as well as independent from the random variable N describing the number of particles.
- b) Particle rotations ω_i follow a uniform distribution.

3. (*dilute limit*) The transverse coherence length L_t of the X-ray pulse is much shorter than the average distance between particles, and we may approximate the scattering intensity of a sample realization I^M by the incoherent sum over scattering intensities of its constituents

$$I^M(\mathbf{q}^\lambda) = \sum_{i=1}^N \mathbf{R}_{\omega_i} I(\mathbf{q}^\lambda), \quad (63)$$

Figure 11 shows a typical FXS experimental setup for single-particle structure determination from solution scattering. It is worth to explain some of the peculiarities in the above definition. For $d = 2$ the moment $\mathcal{M}_N^2(q_1, q_2, \phi_1, \phi_2)$ coincides precisely with the function $C(\boldsymbol{\kappa}_1, \boldsymbol{\kappa}_2)$ that was considered in the founding paper of FXS [1]. In case of $d = 1$ one retrieves the average over the diffraction patterns themselves, which is the object studied in SAXS or WAXS experiments, see section 1.6, whereas for $d \geq 3$ one is in the realm studied by triple and higher correlations. The letter \mathcal{M} was chosen to reserve C for the *angular cross-correlation function*, as well as for the similarity of the right hand side of equation 60 to statistical moments ($\langle X \rangle, \langle X^2 \rangle, \langle X^3 \rangle, \dots$) of some random variable X .

While assumption 2 b) is usually explicitly mentioned in descriptions of FXS [1, 19, 99], assumption 2 a) is often only implied indirectly and the number of particles is restricted to be constant. We shall see, in section 2.5, that especially in the case of the number of particles, its treatment as fluctuating random variable, N , affects the equations connecting the multi-particle moments \mathcal{M}_N^d to the single-particle structural information and opens up new possibilities. In section 6 we will drop assumption 2 b) and explore the connection between the moments \mathcal{M}_N^d and the single-particle scattered intensity $I(\mathbf{q})$ in case of arbitrary rotational probability distributions. As special case, for $d = 1$, this also includes the study of SAXS/WAXS patterns under these conditions.

The main reason behind the presence of the *dilute-limit* limit condition in the above definition, is that it allows to generalize many results within FXS from the case of a single particle per sample, that is $N = 1$, to the case of N being a random variable with arbitrary mean value. We will give a detailed derivation of this result in subsection 2.5.3.

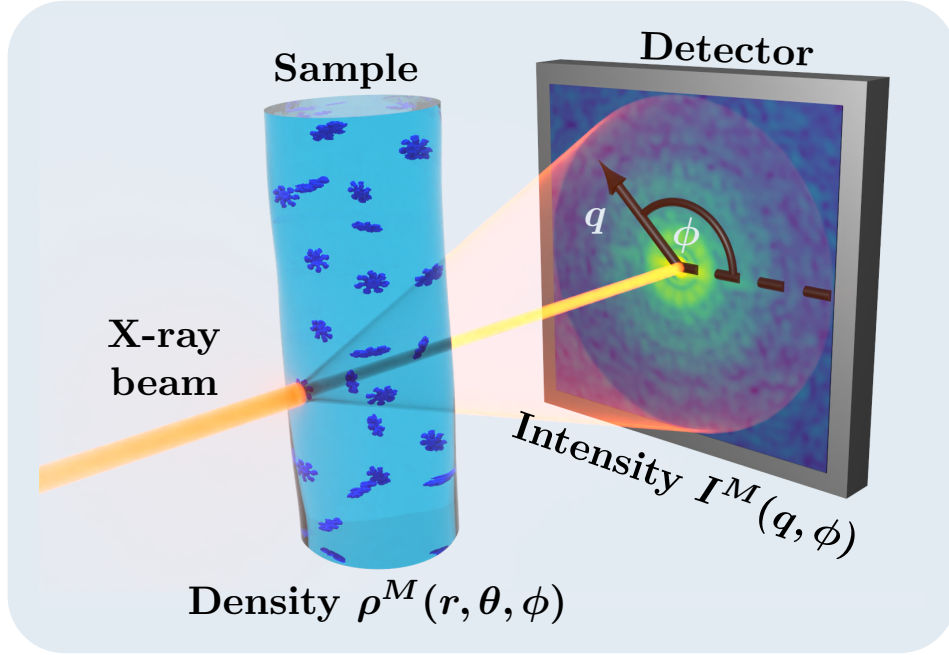


Figure 11: Typical scattering geometry within FXS. An incident X-ray pulse is diffracted from a sample solution or aerosol with density ρ^M , that contains multiple randomly oriented but otherwise identical particles. The corresponding diffraction pattern I^M is recorded in the far-field on a two-dimensional detector.

Before we continue with the description of the formalism of *fluctuation X-ray scattering* let us introduce a simplified version of the general three-dimensional problem which we shall call the *two-dimensional* case.

Definition 2.2 (Fluctuation X-ray scattering in 2D) Consider the setting and assumptions as described in the general 3D case of definition 2.1 and add the following constraints.

1. Assume small scattering angles, i.e. use the flat Ewald's sphere approximation.
2. Allow particle rotations only around axes parallel to the incoming X-ray pulse. That means, only two-dimensional rotations are allowed.

Together these two assumptions imply that only intensity values along the xy -plane, $I(q, \frac{\pi}{2}, \phi)$, can be measured and the considered rotations preserve this plane.

Note, that *two-dimensional* here does not stand for two-dimensional samples but rather two-dimensional rotations or two-dimensional projection. Since the measurable momentum transfer vectors \mathbf{q}^λ are confined to the xy -plane, we can use the Fourier projection-slice theorem to conclude that the measured diffraction patterns $I^M(\mathbf{q}^\lambda)$, correspond to projections of the electron density $\rho(\mathbf{r})$ to the aforementioned plane, see equation (15). Hence, in 2D FXS one seeks to recover the projected density $P_{xy}\rho$. This model has found

applications in the imaging of proteins bound to membranes [100], at the same time many concepts are easier to introduce within this 2D setting. This stems from the fact that the rotation group $SO(2)$ is in many aspects simpler than $SO(3)$, which has to be used in the general case. Sample configurations of these two cases can be seen in Figure 12.

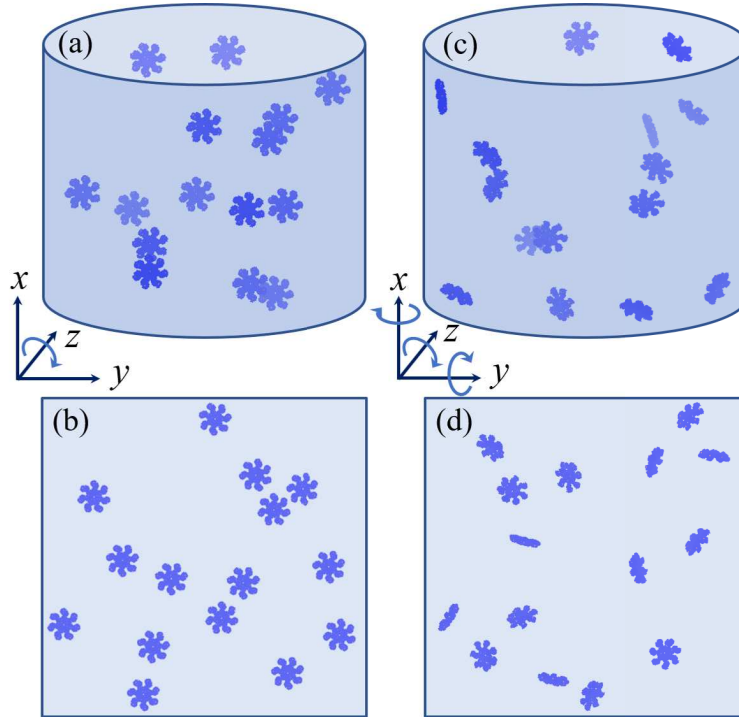


Figure 12: Sample configurations for two-dimensional FXS (a), (b) and three-dimensional FXS (c), (d). Here the incident X-ray pulse is assumed to propagate along the z -axis. In accordance with definition 2.2 particles in (a) and (b) only vary by two-dimensional rotations around axes parallel to the z -axis, while particles in (c) and (d) can vary by arbitrary rotations in $SO(3)$. (a) and (c) symbolize bulk three-dimensional samples, while (b) and (d) represent planar samples, for both cases of FXS respectively. Planar samples are for example encountered if particles are deposited on a membrane [100]

The approach we shall follow in the remainder of this section, is to strip away all complicated details of definition 2.1, such as multiple-particles per diffraction pattern or the restriction of measurements to the Ewald's sphere, analyze the resulting situation and reintroduce the details, one at a time.

Initially we will take a dive into mathematical invariant theory and study *orbit-recovery* problems, which assume measurements of randomly rotated versions of the full 3D intensity $I(\mathbf{q})$ in the case of a single particle, i.e. $N = 1$. This will allow us to understand what type of information about the single-particle intensity $I(\mathbf{q})$ we may hope to obtain within FXS. We shall see, that this information takes the form of rotational invariants formulated in terms of harmonic coefficients of the single-particle intensity $I(\mathbf{q})$. In section 2.2 we will derive explicit forms for these single-particle invariants. This will be followed by a discussion of how these invariants can be used for structure determination in sections 2.3

and 2.4. Finally, in section 2.5 we will first discuss how the single-particle invariants can be extracted from the FXS moments \mathcal{M}_N^d for $N = 1$, i.e. for one particle per sample ρ^M , and then describe how the general multi-particle moments \mathcal{M}_N^d can be represented using their single-particle counterparts.

2.1. Connection to invariant theory

Invariant theory is a sub-field of mathematical algebra, that is concerned with the study of polynomials that are invariant under the action of some group G . For FXS we are especially interested in the case where G is one of the two rotation groups $\text{SO}(3)$ or $\text{SO}(2)$. It turns out, that invariant theory has deep connections to a set of mathematical problems called *orbit-recovery* problems, which are almost equivalent to the problem encountered in FXS. In this section we shall summarize some of the results presented in [101] and [102]. Despite the fact that FXS is not explicitly mentioned in these works and they are not well known within our field, their disposition represent an alternative view on *fluctuation X-ray scattering* that is extremely powerful and provides a good intuition for its core principles. Given that the target audience of [101] are mathematicians, while this thesis belongs to the field of physics, we shall neglect some mathematical details in favor of presenting the underlying ideas.

The following list represents a quick summary of the results discussed in this section.

1. FXS is equivalent to the study of rotation invariant polynomials whose variables are the harmonic coefficients $I_m^l(q)$ or $I_n(q)$ of the single-particle intensity $I(\mathbf{q})$.
2. The rotational invariants can be computed by averages from noisy measurements of $I_m^l(q)$ (3D case)¹² or $I_n(q)$ (2D case). (theorem 2.10)
3. Knowledge about a small finite number of invariant polynomials uniquely determines the single-particle intensity, up to a global rotation. (theorem 2.11)
4. In case of three-dimensional FXS we may only access sums over the invariant polynomials of points 2 and 3 directly. More concretely, the moments \mathcal{M}_N^d , from definition 2.1, are sums over invariant polynomials of degree $\leq d$ given below in equations (73a) and (73b). Special cases of this statement include the ensemble average of angular cross-correlations (eq. (58)) for $d=2$, as well as triple correlations studied in [95, 96] ($d=3$) and even higher correlations for $d > 3$.

2.1.1. Orbit-recovery problems

Consider a space of functions, e.g. the space of all possible single-particle scattered intensities $I(\mathbf{q})$, on which we can act with a group G . In our case G acts by rotating a given intensity. This action then divides the space of all possible scattering intensities into orbits of intensities that are connected by rotations, i.e. the group action. A schematic representation of this can be seen in figure 13.

¹²In 3D FXS such measurements are not possible since they would require experimental access to noisy version of the 3D intensity $I(\mathbf{q})$.

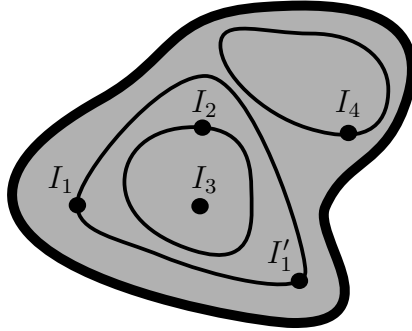


Figure 13: Visualization of orbits. Consider the entire displayed set to be the space of single-particle intensities $I(\mathbf{q})$. Points in this set, e.g. I_1, \dots, I_4 and I'_1 , correspond to different intensities. For example, you may think of I_1 as the 3D scattering intensity of a solid cube with a particular density and size, while I_2 is the intensity corresponding to a particular protein. Each point in this abstract set is connected to other points by the group action, indicated by the thin black loops. These loops are the orbits of all intensities that lie within them. For example I_1 and I'_1 belong to the same orbit while I_1 and I_2 do not. Roughly speaking this means, our protein is not a cube. To be more precise it means, that the intensity I'_1 is a rotated version of I_1 , but I_2 is not. Since each point has to lie in a unique orbit, this causes the entire space of intensities to decompose into a collection of orbits. The orbits that only contain a single point, such as the orbit of I_3 , are orbits of isotropic intensities, i.e. orbits of intensities that are them selves invariant under rotations.

The *orbit-recovery* problem can be formulated as follows [101, problem 2.1]. Identify the orbit of a function $I(\mathbf{q})$ from a given set of noisy measurements of the form

$$\eta_i(\mathbf{q}) = \mathbf{R}_{\omega_i} I(\mathbf{q}) + \xi_i(\mathbf{q}), \quad (64)$$

where the rotations ω_i are uniformly distributed as random variables and ξ_i denotes a normal distributed noise term with mean 0. Hence, solving the *orbit-recovery* problem means to determine the function $I(\mathbf{q})$ up to a global rotation, from the randomly rotated and noisy measurements $\eta_i(\mathbf{q})$.

Note that the problem we are faced with in FXS, concerning the single-particle scattered intensity $I(\mathbf{q})$, can be formulated in complete analogy if one considers a single-particle per sample, i.e. $N = 1$, and we may call it a *sliced orbit-recovery* problem. Given a set of possibly noisy measurements I^M of the form

$$I^M(\mathbf{q}^\lambda) = \mathbf{R}_{\omega_i} I(\mathbf{q}^\lambda) + \xi_i(\mathbf{q}^\lambda) \quad (65)$$

that is

$$I^M(q, \phi) = \mathbf{R}_{\omega_i} I(q, \theta_\lambda(q), \phi) + \xi_i(q, \phi),$$

we want to determine $I(\mathbf{q})$ up to a global rotation, in other words we want to determine the orbit of $I(\mathbf{q})$ under the action of rotations. The term *sliced* reflects the fact that in FXS we can only access noisy Ewald's sphere slices $I(\mathbf{q}^\lambda)$ directly, but not the full intensity as demanded in equation (64).

In the flat Ewald's sphere limit, where \mathbf{q}^λ simply describes the xy -plane in momentum space, there exists an interesting connection between FXS and *cryo-electron microscopy*. The case of an additional restriction to the xy -plane is directly studied in [101], as the special case of *orbit-recovery* for *cryo-electron microscopy*. The observables in *cryo-electron microscopy* are given by noisy projections, on to the xy -plane, of randomly rotated versions of the electron density $\rho(\mathbf{r})$ of the studied particle. By virtue of the Fourier projection-slice theorem, these are equivalent to slices of the scattered amplitude $\widehat{\rho}(\mathbf{q}) = [\mathcal{F}\rho](\mathbf{q})$ along the xy -plane. Therefore, one finds that, in the limit of small-scattering angles, the *sliced orbit-recovery* problem of FXS (eq. (65)) transforms into the *cryo-electron microscopy* problem under substitution of $I(\mathbf{q})$ with the Fourier transform of the electron density $\widehat{\rho}(\mathbf{q})$.

Observation 2.3 (Single-particle 2D FXS is a general orbit-recovery problem)

The single-particle ($N = 1$) case of two-dimensional FXS as defined in 2.2 is an *orbit-recovery* problem over $\text{SO}(2)$, with regard to information obtainable about the scattering Intensity $I(q, \frac{\pi}{2}, \phi)$ on the xy -plane. To see this, observe that in definition 2.2 both measurements as well as rotations are limited to the xy -plane. Moreover, each measured diffraction pattern I^M corresponds to a randomly oriented, possibly noisy, version of the target intensity $I(q, \frac{\pi}{2}, \phi)$, via

$$\begin{aligned} I^M(q, \phi) &= \widehat{\rho}(\mathbf{R}_{\alpha_1}^{-1}(\mathbf{q}^\lambda) - \mathbf{x}_1)\widehat{\rho}(\mathbf{R}_{\alpha_1}^{-1}(\mathbf{q}^\lambda) - \mathbf{x}_1)^* = \widehat{\rho}(\mathbf{R}_{\alpha_1}^{-1}(\mathbf{q}^\lambda))\widehat{\rho}(\mathbf{R}_{\alpha_1}^{-1}(\mathbf{q}^\lambda))^* \\ &= \mathbf{R}_{\alpha_1}I(\mathbf{q}^\lambda) = \mathbf{R}_{\alpha_1}I(q, \frac{\pi}{2}, \phi) = I(q, \frac{\pi}{2}, \phi - \alpha), \end{aligned} \quad (66)$$

where the second equality is due to the Fourier shift theorem, see (17). Hence two-dimensional FXS measurements are of the form given in equation (64).

2.1.2. Orbit-recovery and invariant polynomials

In order to avoid the troubles associated with infinite dimensional spaces of functions, as well as to make numerical solutions possible, we have to restrict our considerations to a finite dimensional space of functions. We shall do so, by considering functions whose harmonic expansions are band limited up to some finite maximal degree L , i.e. functions that are given by finite versions of equations (44) and (47) for the two and three dimensional cases

$$I(q, \phi) = \sum_{n=-L}^L I_n(q)e^{in\phi} \quad f_n = \frac{1}{2\pi} \int_0^{2\pi} d\phi f(q, \phi)e^{-in\phi} \quad (67a)$$

$$I(q, \theta, \phi) = \sum_{l=0}^L \sum_{m=-l}^l I_m^l(q)Y_m^l(\theta, \phi) \quad f_m^l(q) = \int_{S^2} d\Omega I(q, \theta, \phi)Y_m^l(\theta, \phi)^*. \quad (67b)$$

Additionally, we have to consider a finite number of radial sampling points given by q_1, \dots, q_S , also called shells. Thus, a three dimensional function is now fully specified by $S(L + 1)^2$ complex numbers $I_m^l(q_i)$, similarly a two dimensional function is specified by

the $S(2L+1)$ complex values given by its harmonic coefficients¹³ $I_n(q_i)$. We may think of our space of functions as a $D = S(L+1)^2$ or $D = S(2L+1)$ dimensional complex vector space $V = \mathbb{C}^D$ with $SO(2)$ or $SO(3)$ actions as defined in equations (57) and (56).

Note that for any fixed point (q_i, θ, ϕ) , in spherical coordinates, we can interpret equation (67b) as a simple¹⁴ polynomial whose variables are the harmonic coefficients $I_m^l(q_i)$ and the values of $Y_m^l(\theta, \phi)$ represent the corresponding complex coefficients.¹⁵ From this viewpoint any concrete scattering intensity, say I , is obtained by evaluating the above polynomial on a particular choice of its variables $I_m^l(q_i)$. In the *orbit-recovery* problem we have direct access to noisy estimates of randomly rotated versions of these variables in form of the spherical harmonic coefficients $\eta_m^l(q_i)$ of $\eta(\mathbf{q})$, as defined in equation (64). At the same time this implies, that we are able to compute, possibly noisy, values of arbitrary polynomials in $I_m^l(q_i)$ and not just the ones corresponding to equation (67).

Definition 2.4 (Polynomials in harmonic coefficients) *By $\mathbb{C}[I_m^l(q_i)]$ we shall mean the set of polynomials in $I_m^l(q_i)$ with complex coefficients. Correspondingly we define $\mathbb{C}[I_n(q_i)]$ to be the set of polynomials in $I_n(q_i)$ with complex coefficients¹⁶.*

Example 2.5 (Polynomials in harmonic coefficients) *Examples of such polynomials are :*

- $\sum_{m=-l}^l I_m^l(q_i) I_m^l(q_j)$ for any triple of indices l, i, j . Here each term is a product of two of the polynomial variables and all coefficients are just 1.
- An example with coefficients different from 1 would be: $2I_0^2(q_i) + i(I_0^0(q_i))^6$.

Since we have defined the notion of a rotation action on the level of harmonic coefficients, see equations (57) and (56), this action now naturally extends to an action on the polynomials in $\mathbb{C}[I_m^l(q_i)]$ and $\mathbb{C}[I_n(q_i)]$. While most of these polynomials can not be estimated with increasing precision as the number of observed patterns in the form of $\eta(\mathbf{q})$ from eq. (64) increases, there is a subset of polynomials for which this is the case. This subset is given by polynomials that are invariant under the group action, i.e. rotations. In the simplified case where the noise term in $\eta(\mathbf{q})$ is neglected this becomes evident since a rotation invariant polynomial f , by definition, has to have the same values $f(\eta)$ when evaluated on observations that differ by rotations. Let us give an example.

Example 2.6 (Averaged polynomials in harmonic coefficients) *Consider the following polynomials in the 2D case,*

$$\begin{aligned} A &= 2I_1(q_i) + I_4(q_i)I_2(q_i)^* \\ B &= 2I_0(q_i) + I_4(q_i)I_2(q_i)^* \\ C &= 2I_0(q_i) + I_2(q_i)I_2(q_i)^* . \end{aligned}$$

¹³Since intensities have to be real valued functions, the actual number of independent harmonic coefficients is lower. Using the symmetry relations (49) one finds the number of independent variables to be $S(L+1)(L+2)/2$ and $S(L+1)$ for the two cases, but we shall ignore this for the moment.

¹⁴Simple in the sense that this polynomial is linear in all of its variables.

¹⁵In the same way one may interpret (67a) as a polynomial whose variables are $I_n(q_i)$

¹⁶Mathematically $\mathbb{C}[I_m^l(q_i)]$ is the ring of polynomials whose variables are given by a basis $\mathbf{x}_1, \dots, \mathbf{x}_D$ of the dual vector space, V^*

We shall later see, using equations (78a) and (80a), that their averages under rotations are given by

$$\begin{aligned}\langle A \rangle_{\text{SO}(2)} &= 0 \neq A \\ \langle B \rangle_{\text{SO}(2)} &= 2I_0(q_i) \neq B \\ \langle C \rangle_{\text{SO}(2)} &= 2I_0(q_i) + I_2(q_i)I_2(q_i)^* = C.\end{aligned}$$

Clearly polynomials A and B can not be estimated with increasing precision by averaging over more and more observations. For C this is possible.

In the general case, including the noise term in (64), it was shown [101, lemma 6.5] that for any rotation invariant polynomial f one can define an estimator polynomial \tilde{f} , such that in the limit of an infinite set M of observations in the form of eq (64), we find

$$\left\langle \tilde{f}(\eta) \right\rangle_M = f(I), \quad (68)$$

where $\tilde{f}(\eta)$ and $f(I)$ denote the evaluation¹⁷ of the corresponding polynomials on the harmonic coefficients of an observation η and the single-particle intensity I , respectively. This implies that we can access invariant polynomials in the target quantity I , i.e. the single-particle intensity I , from noisy observables η by means of averages.

Definition 2.7 (Invariant Polynomials) *Let us denote by $\mathbb{C}[I_m^l(q_i)]^{\text{SO}(3)}$ the subset of polynomials in $\mathbb{C}[I_m^l(q_i)]$ that are invariant under rotations in $\text{SO}(3)$. That is, all polynomials $f(I_m^l(q_i))$ such that $f(\mathbf{R}_\omega I_m^l(q_i)) = f(I_m^l(q_i))$ for any rotation ω in $\text{SO}(3)$. Similarly let $\mathbb{C}[I_n(q_i)]^{\text{SO}(2)}$ be the subset of polynomials in $\mathbb{C}[I_n(q_i)]$ invariant under the action of $\text{SO}(2)$.*

Using the notion of invariant polynomials, we can now reformulate what solving the orbit-recovery problem means. First, observe that invariant polynomials by definition have the same value when evaluated on scattering intensities I belonging to the same orbit, i.e. when evaluated on intensities that differ by a rotation. If f is an invariant polynomial and \mathfrak{o}_1 is an orbit of intensities, we may write $f(\mathfrak{o}_1)$ for the unique value that f attains when evaluated on any intensity belonging to \mathfrak{o}_1 .

Definition 2.8 (orbit-recovery via invariant polynomials) *A subset U_{inv} of the invariant polynomials represents a solution to the orbit-recovery problem if it can uniquely identify (resolve) each orbit. That is, if for any intensity $I(\mathbf{q})$ there exists a single unique orbit \mathfrak{o} such that*

$$f(\mathfrak{o}) = f(I) \quad \text{for all polynomials } f \text{ in } U_{\text{inv}}. \quad (69)$$

This definition is the analog to [101, definition 2.12]. One may equivalently demand that for any pair of different orbits \mathfrak{o}_1 and \mathfrak{o}_2 , with $\mathfrak{o}_1 \neq \mathfrak{o}_2$, there has to exist at least one invariant polynomial f in U_{inv} , such that

$$f(\mathfrak{o}_1) \neq f(\mathfrak{o}_2).$$

¹⁷Evaluating a polynomial whose variables are $I_m^l(q_i)$ on a specific intensity, e.g. $J(\mathbf{q})$, simply means substituting the variables $I_m^l(q_i)$ with their corresponding value for $J(\mathbf{q})$, which in this case are the complex numbers $J_m^l(q_i)$.

Note that if U_{inv} is such a solution, it is possible to recover the single-particle intensity I , up to a global rotation, from evaluations of the polynomials in U_{inv} on the measurements defined in equation (64).

2.1.3. Solutions to the orbit-recovery problem

It turns out that the set of all invariant polynomials, is a solution to the *orbit-recovery* problem [101, theorem A.32] and we may formulate the following theorem.

Theorem 2.9 (Solution to orbit-recovery) *The sets $\mathbb{C}[I_m^l(q_i)]^{\text{SO}(3)}$ and $\mathbb{C}[I_n(q_i)]^{\text{SO}(2)}$ are solutions, in the sense of definition 2.8, to their corresponding orbit-recovery problems for $\text{SO}(3)$ and $\text{SO}(2)$.*

We can however find much smaller sets of polynomials that are solutions. To do so we need the following statement about the behavior of polynomials if they are averaged over rotations [101, definition 3.11].

Theorem 2.10 (Rotational average as Reynolds operator) *The rotational average $\langle \mathbf{R}_\omega \cdot \rangle_{\text{SO}(3)}$ maps each polynomial f in $\mathbb{C}[I_m^l(q_i)]$ to an invariant polynomial $\langle \mathbf{R}_\omega f \rangle_{\text{SO}(3)}$ in $\mathbb{C}[I_m^l(q_i)]^{\text{SO}(3)}$ and this map is surjective. The same statement holds for the two-dimensional case with group $\text{SO}(2)$.*

In our example 2.6 the above theorem 2.10 merely states that, while A and B are not invariant under rotations the new polynomials $\langle A \rangle_{\text{SO}(2)}$ and $\langle B \rangle_{\text{SO}(2)}$ are.

Since averages are linear, they preserve the degree of polynomials. We can use this to obtain a generating set for all invariant polynomials as follows. Consider monomials of degree- d defined by

$$\prod_{j=1}^d I_{n_j}(q_{i_j}) \quad \text{and} \quad \prod_{j=1}^d I_{m_j}^{l_j}(q_{i_j}) \quad (70)$$

for all possible values of n_j and i_j in the two-dimensional case and all triples l_j, m_j, i_j for the three-dimensional case. Since any polynomial is a linear combination of monomials of arbitrary degree d we find that any invariant polynomial must be given by a linear combination over the averaged monomials of degree- d , i.e.

$$\left\langle \mathbf{R}_\alpha \prod_{j=1}^d I_{n_j}(q_{i_j}) \right\rangle_{\text{SO}(2)} = \left\langle \prod_{j=1}^d \mathbf{R}_\alpha I_{n_j}(q_{i_j}) \right\rangle_{\text{SO}(2)} = \frac{1}{2\pi} \int_0^{2\pi} d\alpha \prod_{j=1}^d \mathbf{R}_\alpha I_{n_j}(q_{i_j}) \quad (71a)$$

$$\left\langle \mathbf{R}_\omega \prod_{j=1}^d I_{m_j}^{l_j}(q_{i_j}) \right\rangle_{\text{SO}(3)} = \left\langle \prod_{j=1}^d \mathbf{R}_\omega I_{m_j}^{l_j}(q_{i_j}) \right\rangle_{\text{SO}(3)} = \frac{1}{8\pi^2} \int_{\text{SO}(3)} d\omega \prod_{j=1}^d \mathbf{R}_\omega I_{m_j}^{l_j}(q_{i_j}). \quad (71b)$$

We shall call the polynomials from equation (71) *invariant generators* of degree- d and can use them to formulate the main result of this section, the analog of [101, theorem 4.19]

Theorem 2.11 (Better solution to orbit-recovery) *Consider the orbit-recovery problem formulated in eq. (64) over the space V of functions with finite maximal harmonic degree L and S different momentum transfer values q_1, \dots, q_S , such that $L \geq 1$ and $S \geq 3$. Then, the sets consisting of invariant generators with degree $d \leq 3$ solve the orbit-recovery problem. That is, the sets containing*

$$\left\langle \mathbf{R}_\alpha I_{n_0}(q_{i_0}) \right\rangle_{\text{SO}(2)}, \quad \left\langle \mathbf{R}_\alpha I_{n_1}(q_{i_1}) I_{n_2}(q_{i_2}) \right\rangle_{\text{SO}(2)}, \quad \left\langle \mathbf{R}_\alpha I_{n_3}(q_{i_3}) I_{n_4}(q_{i_4}) I_{n_5}(q_{i_5}) \right\rangle_{\text{SO}(2)}$$

and

$$\left\langle \mathbf{R}_\omega I_{m_0}^{l_0}(q_{i_0}) \right\rangle_{\text{SO}(3)}, \quad \left\langle \mathbf{R}_\omega I_{m_1}^{l_1}(q_{i_1}) I_{m_2}^{l_2}(q_{i_2}) \right\rangle_{\text{SO}(3)}, \quad \left\langle \mathbf{R}_\omega I_{m_3}^{l_3}(q_{i_3}) I_{m_4}^{l_4}(q_{i_4}) I_{m_5}^{l_5}(q_{i_5}) \right\rangle_{\text{SO}(3)},$$

for all possible indices $i_j \leq S$, $|n_j| \leq L$, $l_j \leq L$ and $|m_j| \leq l_j$ with $j = 0, \dots, 5$ are solutions to the orbit-recovery problem for the cases of $\text{SO}(2)$ and $\text{SO}(3)$, respectively.

At this point we shall deviate slightly from the exposition in [101]. Instead of monomials as defined in (70) we will, for the remainder of the thesis, use monomials where each second variable is complex conjugated, i.e.

$$\prod_{\substack{j=1 \\ \text{odd } j}}^d I_{m_j}^{l_j}(q_{i_j}) \prod_{\substack{j=2 \\ \text{even } j}}^d I_{m_j}^{l_j}(q_{i_j})^* = I_{m_1}^{l_1}(q_{i_1}) I_{m_2}^{l_2}(q_{i_2})^* I_{m_3}^{l_3}(q_{i_3}) \dots \quad (72)$$

for all possible values of l_j, m_j and i_j . Using the fact that we are interested in real valued functions, i.e. single-particle intensities $I(\mathbf{q})$, we may use equation (49) to see that these monomials are identical to the ones from equation (70) up to a constant prefactor.

$$\prod_{\substack{j=1 \\ \text{odd } j}}^d I_{m_j}^{l_j}(q_{i_j}) \prod_{\substack{j=2 \\ \text{even } j}}^d I_{m_j}^{l_j}(q_{i_j})^* = \left(\prod_{\substack{j=2 \\ \text{even } j}}^d (-1)^{m_j} \right) \prod_{\substack{j=1 \\ \text{odd } j}}^d I_{m_j}^{l_j}(q_{i_j}) \prod_{\substack{j=2 \\ \text{even } j}}^d I_{-m_j}^{l_j}(q_{i_j}).$$

Since all of the results derived from the monomials given in (70) (the equation (71) and theorem 2.12) only depend on the set of possible linear combinations of monomials for a fixed degree d , they can be directly generalized to monomials in the form of (72).

The invariant generators for the two-dimensional and three-dimensional case, thus take

the form

$$\begin{aligned}\mathcal{I}_{\text{SO}(2)}^d &= \left\langle \mathbf{R}_\alpha \prod_{\substack{j=1 \\ \text{odd } j}}^d I_{n_j}(q_{i_j}) \prod_{\substack{j=2 \\ \text{even } j}}^d I_{n_j}(q_{i_j})^* \right\rangle_{\text{SO}(2)} \\ &= \frac{1}{2\pi} \int_0^{2\pi} d\alpha \prod_{\substack{j=1 \\ \text{odd } j}}^d \mathbf{R}_\alpha I_{n_j}(q_{i_j}) \prod_{\substack{j=2 \\ \text{even } j}}^d [\mathbf{R}_\alpha I_{n_j}(q_{i_j})]^*\end{aligned}\quad (73a)$$

$$\begin{aligned}\mathcal{I}_{\text{SO}(3)}^d &= \left\langle \mathbf{R}_\omega \prod_{\substack{j=1 \\ \text{odd } j}}^d I_{m_j}^{l_j}(q_{i_j}) \prod_{\substack{j=2 \\ \text{even } j}}^d I_{m_j}^{l_j}(q_{i_j})^* \right\rangle_{\text{SO}(3)} \\ &= \frac{1}{8\pi^2} \int_{\text{SO}(3)} d\omega \prod_{\substack{j=1 \\ \text{odd } j}}^d \mathbf{R}_\omega I_{m_j}^{l_j}(q_{i_j}) \prod_{\substack{j=2 \\ \text{even } j}}^d [\mathbf{R}_\omega I_{m_j}^{l_j}(q_{i_j})]^*\end{aligned}\quad (73b)$$

and theorem 2.11 may be restated via

Theorem 2.12 (FXS version of theorem 2.11) *Consider the general orbit-recovery problem formulated in eq. (64) over the space V of functions with finite maximal harmonic degree L and S different momentum transfer values q_1, \dots, q_S , such that $L \geq 1$ and $S \geq 3$. Then, the sets consisting of invariant generators with degree $d \leq 3$ solve the orbit-recovery problem. That is, the sets containing*

$$\left\langle \mathbf{R}_\alpha I_{n_0}(q_{i_0}) \right\rangle_{\text{SO}(2)}, \left\langle \mathbf{R}_\alpha I_{n_1}(q_{i_1}) I_{n_2}(q_{i_2})^* \right\rangle_{\text{SO}(2)}, \left\langle \mathbf{R}_\alpha I_{n_3}(q_{i_3}) I_{n_4}(q_{i_4})^* I_{n_5}(q_{i_5}) \right\rangle_{\text{SO}(2)} \quad (74)$$

and

$$\left\langle \mathbf{R}_\omega I_{m_0}^{l_0}(q_{i_0}) \right\rangle_{\text{SO}(3)}, \left\langle \mathbf{R}_\omega I_{m_1}^{l_1}(q_{i_1}) I_{m_2}^{l_2}(q_{i_2})^* \right\rangle_{\text{SO}(3)}, \left\langle \mathbf{R}_\omega I_{m_3}^{l_3}(q_{i_3}) I_{m_4}^{l_4}(q_{i_4})^* I_{m_5}^{l_5}(q_{i_5}) \right\rangle_{\text{SO}(3)}, \quad (75)$$

for all possible indices $i_j \leq S$, $|n_j| \leq L$, $l_j \leq L$ and $|m_j| \leq l_j$ with $j = 0, \dots, 5$ are solutions to the orbit-recovery problem for the cases of $\text{SO}(2)$ and $\text{SO}(3)$, respectively.

The motivation for this deviation is to keep the explicit expressions for the invariant polynomials consistent with the ones commonly used in FXS [1, 19, 23, 94, 99]. Other wise they would differ by constant prefactors of the form $(-1)^{\sum_{j=1}^d g_j m_j}$, where the g_j are either 0 or one 1 and only depend on the degree of the considered invariant polynomial.

2.1.4. Implications for FXS

Two dimensional FXS In observation 2.3 we have seen that the two dimensional version of FXS, as defined in 2.2, has the form of an *orbit-recovery* problem, if one assumes that each sample ρ^M only consist of single particle, i.e. $N = 1$. By virtue of theorem 2.12 we can expect that the single particle intensity $I(q, \pi/2, \phi)$, restricted to the xy -plane, is

recoverable¹⁸ from the invariant generators of degree smaller than 4. This is precisely the result given in [95] where triple correlations, i.e. degree-3 invariant polynomials, are used to determine $I(q, \pi/2, \phi)$. In particular [95] shows how to determine the single-particle intensity in case of an arbitrary but fixed number of particles N . Moreover the algorithm outlined in [95] is conceptually very similar to the *frequency-marching* algorithm presented in [101, 102] for the *orbit-recovery* problem on $SO(3)$. We want to additionally point out that, in the two-dimensional case with $N = 1$, the moments \mathcal{M}_N^d in the definition of FXS 2.1 for $d \leq 3$ exactly correspond to evaluations of the invariant generators listed in equation (74).

Three dimensional FXS As outlined in section 2.1.1 the three dimensional FXS problem is not given by an *orbit-recovery* problem. That is because, even for $N = 1$, we only have access to Ewald's sphere slices of the single-particle intensity in form of eq. (65), but the considered rotations act on the full three-dimensional single-particle intensity. Another invocation of this is, that the measurements considered in *orbit-recovery* would allow us to compute noisy versions (η_m^l) of the spherical harmonic coefficients I_m^l of the single-particle intensity. Note that by their definition in equation (48), this involves an integration over both angles, θ and ϕ , of the spherical coordinate system. The same computation can not be done in FXS, since the restriction to the Ewald's sphere links the measurable θ values via equation (12) to the momentum transfer value q and thus prevents an integration over θ . However, we may perform the integration over ϕ , which motivates the second version of the moments \mathcal{M}_N^d given in our definition of *fluctuation X-ray scattering*, see equation (61). The intuition behind their introduction is to use quantities that are as close as possible to the natural formulation of the *orbit-recovery* problem in terms of spherical harmonic coefficients. We shall see in section 2.5, that this second version results in a simpler connection between \mathcal{M}_N^2 and the single-particle invariants of degree-2 from equation (73b).

Despite the fundamental limitation in the general FXS case, we may use theorem 2.10 to gain a general understanding about the form of \mathcal{M}_N^d which is valid for both of its definitions. To keep the following derivations simple, let us restrict to the case $N = 1$. All subsequent statements remain valid in the case of N being a random variable. The measured quantities I^M of FXS are slices along E_λ of randomly rotated versions of the single-particle intensity I , that is

$$\begin{aligned} I^M(q, \phi) &= \mathbf{R}_\omega I(\mathbf{q}^\lambda) = \mathbf{R}_\omega \sum_{l,m} I_m^l(q) Y_m^l(\theta_\lambda(q), \phi) \\ &= \sum_{l,n} I_n^l(q) \sum_m D_{mn}^l(\omega)^* Y_m^l(\theta_\lambda(q), \phi), \end{aligned} \quad (76)$$

where in the second equality we used the spherical harmonic expansion (equation (47)) of I and in the third equality we used the action of rotations on spherical harmonic coefficients from equation (56). We may observe using equation (76), that $I^M(q, \phi)$ itself is a degree-1 polynomial in the harmonic coefficients $I_m^l(q)$. Consequently k -fold products,

¹⁸up to a global rotation.

such as $I^M(q_1, \phi_1) \dots I^M(q_k, \phi_k)$, are simply given by sums over the monomials specified in equation (72) with degree- $d \leq k$ and complex coefficients.¹⁹ The same statement holds for products of the form $I_{n_1}^M(q_1) \dots I_{n_d}^M(q_d)$ since the computation of the polar harmonic coefficients $I_n^M(q)$ only involves an integration over ϕ which preserves the property of equation (76) being a degree 1 polynomial in spherical harmonic coefficients. By the same reasoning one may observe that the angular cross-correlations calculated from $I^M(q, \phi)$, i.e. $\frac{1}{2\pi} \int_0^{2\pi} d\phi I^M(q_1, \phi + \Delta) I^M(q_2, \phi)$, have to be sums over the corresponding monomials with $d \leq 2$. Angular triple correlations consequently are sums over monomials with $d \leq 3$, with an equivalent extension to higher angular correlations and higher degree monomials. Since the ensemble average is linear and, by theorem 2.10, maps monomials to the corresponding invariant generators given in equations (73a)-(73b), we arrive at the following observation

Observation 2.13 (FXS moments are sums over invariants) The moments \mathcal{M}_N^d of FXS, as defined in equations (60) and (61), are given by sums over the invariant generators with degree smaller or equal to d , that are evaluated on the single-particle intensity $I(\mathbf{q})$. The same is true for ensemble averaged angular cross-correlations, angular triple correlations as well as higher angular correlations.

In fact, this result is true for ensemble averages of products of arbitrary polynomials in spherical harmonic coefficients evaluated on the measured scattering patterns $I^M(q, \phi)$. A direct consequence of the above observation is the following

Observation 2.14 (Information limit for FXS) Within FXS we may at most gain access to all single-particle invariants given in equation (73b), that is

$$\left\langle \mathbf{R}_\omega \prod_{\substack{j=1 \\ \text{odd } j}}^d I_{m_j}^{l_j}(q_{i_j}) \prod_{\substack{j=2 \\ \text{even } j}}^d I_{m_j}^{l_j}(q_{i_j})^* \right\rangle_{\text{SO}(3)} \quad \text{for arbitrary degree } d$$

By theorem 2.12 this is equivalent to knowing the single-particle intensity $I(\mathbf{q})$ up to an overall rotation.

We shall see in the following sections and chapters that the invariants $\langle I_m^l(q_1) I_m^l(q_2)^* \rangle_{\text{SO}(3)}$, as well as their extraction from the moments \mathcal{M}_N^2 , form the backbone of practical applications of FXS. Combining this with observations 2.13 and 2.14 it is no overstatement to conclude that FXS itself is the study of invariant polynomials, which was stated as point 1 in the summary presented at the beginning of this section.

¹⁹Since the scattering patterns $I^M(q, \phi)$ are real valued we may conveniently place complex conjugations without altering the product, i.e. $I^M(q_1, \phi_1) I^M(q_2, \phi_2) I^M(q_3, \phi_3) \dots = I^M(q_1, \phi_1) I^M(q_2, \phi_2)^* I^M(q_3, \phi_3) \dots$, which yield the necessary complex conjugations on $I_{m_j}^{l_j}(q)$ for this statement to be true. Otherwise one would obtain monomials in form of equation (70).

2.2. Single-particle invariants

This section is devoted to the derivation of explicit forms for the single-particle invariants given in theorem 2.12. Many of the following expressions are already well known in the literature under various names [2, 19, 99] and presented here as part of an overview of *fluctuation X-ray scattering*. We want to briefly mention, that from this section onward by the terms *single-particle invariants* or just *invariants* of degree- d , we shall mean evaluations of the invariant generators given in equation (73a) or (73b) on the single-particle intensity $I(\mathbf{q})$, depending on whether they are mentioned in the context of two-dimensional FXS or three-dimensional FXS. By slight abuse of notation we will also denote them by $\mathcal{I}_{\text{SO}(2)}^d$ and $\mathcal{I}_{\text{SO}(3)}^d$ or just \mathcal{I}^d if the dimensionality of the rotation group does not matter.

2.2.1. Degree 1 invariants

The degree-1 invariants are given as simple averages over the harmonic coefficients themselves, that is

$$\mathcal{I}_{\text{SO}(2)}^1 = \langle \mathbf{R}_\alpha I_n(q) \rangle_{\text{SO}(2)} \quad \text{and} \quad \mathcal{I}_{\text{SO}(3)}^1 = \langle \mathbf{R}_\omega I_m^l(q) \rangle_{\text{SO}(3)}. \quad (77)$$

We can now explicitly evaluate these averages by expanding the rotation action, given in equations (56) and (57). In the 2D case this results in

$$\begin{aligned} \langle \mathbf{R}_\alpha I_n(q) \rangle_{\text{SO}(2)} &= \langle I_n(q) e^{-in\alpha} \rangle_{\text{SO}(2)} = I_n(q) \langle e^{-in\alpha} \rangle_{\text{SO}(2)} = I_n(q) \frac{1}{2\pi} \int_0^{2\pi} d\alpha e^{-in\alpha} \\ &= \delta_{n,0} I_0(q), \end{aligned}$$

where $\delta_{n,0}$ is the standard Kronecker delta. Similarly we find

$$\begin{aligned} \langle \mathbf{R}_\omega I_m^l(q) \rangle_{\text{SO}(3)} &= \left\langle \sum_{n=-l}^l I_n^l(q) D_{mn}^l(\alpha, \beta, \gamma)^* \right\rangle_{\text{SO}(3)} = \sum_{n=-l}^l I_n^l(q) \langle D_{mn}^l(\alpha, \beta, \gamma)^* \rangle_{\text{SO}(3)} \\ &= \sum_{n=-l}^l \frac{I_n^l(q)}{8\pi^2} \int_0^{2\pi} d\alpha \int_0^\pi d\beta \sin(\beta) \int_0^{2\pi} d\gamma D_{mn}^l(\alpha, \beta, \gamma)^* \\ &= \delta_{l,0} \delta_{m,0} I_0^0(q), \end{aligned}$$

where in the last equality we used the orthogonality relation for Wigner D-matrices over $\text{SO}(3)$, given in equation (264), together with the fact that $D_{0,0}^0(\alpha, \beta, \gamma) = 1$.

The invariants for both cases can be related to the SAXS profiles $I^{\text{SAXS}}(q)$, as defined in section 1.6. One may intuitively understand this by realizing that the harmonic coefficient of degree 0 is, by definition in (44) or (48), simply the average of the intensity I over its angular coordinates. That this average is the same as I^{SAXS} , i.e. the degree-1 moments $\mathcal{M}_{N=1}^1$, will be shown in section 2.5.1 and we may summarize our findings as follows

$$\mathcal{I}_{\text{SO}(2)}^1(q) = \langle \mathbf{R}_\alpha I_n(q) \rangle_{\text{SO}(2)} = \delta_{n,0} I_0(q) = \delta_{n,0} I^{\text{SAXS}}(q) \quad (78a)$$

$$\mathcal{I}_{\text{SO}(3)}^1(q) = \langle \mathbf{R}_\omega I_m^l(q) \rangle_{\text{SO}(3)} = \delta_{l,0} \delta_{m,0} I_0^0(q) = \delta_{l,0} \delta_{m,0} \sqrt{4\pi} I^{\text{SAXS}}(q). \quad (78b)$$

The coefficient $\sqrt{4\pi}$ in the three-dimensional case is due to our convention for the spherical harmonics from equation (45), which implies $Y_0^0(\theta, \phi) = \frac{1}{\sqrt{4\pi}}$.

2.2.2. Degree 2 invariants

Single-particle invariants of degree-2 have been defined via

$$\mathcal{I}_{\text{SO}(2)}^2 = \left\langle \mathbf{R}_\alpha I_n(q) I_{n'}(q')^* \right\rangle_{\text{SO}(2)} \quad \text{and} \quad \mathcal{I}_{\text{SO}(3)}^2 = \left\langle \mathbf{R}_\omega I_m^l(q) I_{m'}^{l'}(q')^* \right\rangle_{\text{SO}(3)},$$

for the two FXS cases. Let us again derive their explicit form starting with the two-dimensional case.

$$\begin{aligned} \left\langle \mathbf{R}_\alpha I_n(q) I_{n'}(q')^* \right\rangle_{\text{SO}(2)} &= \left\langle \mathbf{R}_\alpha I_n(q) [\mathbf{R}_\alpha I_{n'}(q')]^* \right\rangle_{\text{SO}(2)} = I_n(q) I_{n'}(q')^* \left\langle e^{i(n'-n)\alpha} \right\rangle_{\text{SO}(2)} \\ &= \frac{I_n(q) I_{n'}(q')^*}{2\pi} \int_0^{2\pi} d\alpha e^{i(n'-n)\alpha} = \delta_{n,n'} I_n(q) I_n(q')^*. \end{aligned}$$

In the interest of readability we will suppress summation ranges for the three-dimensional case, where one may find

$$\begin{aligned} \left\langle \mathbf{R}_\omega I_m^l(q) I_{m'}^{l'}(q')^* \right\rangle_{\text{SO}(3)} &= \left\langle \left[\sum_n I_n^l(q) D_{mn}^l(\omega)^* \right] \left[\sum_{n'} I_{n'}^{l'}(q') D_{m'n'}^{l'}(\omega)^* \right]^* \right\rangle_{\text{SO}(3)} \\ &= \sum_{n,n'} I_n^l(q) I_{n'}^{l'}(q')^* \left\langle D_{mn}^l(\omega)^* D_{m'n'}^{l'}(\omega) \right\rangle_{\text{SO}(3)}. \end{aligned} \quad (79)$$

One may recognize the remaining average over Wigner-D matrices to be, up to a constant prefactor of $\frac{1}{8\pi^2}$, the orthogonality relation from equation (264), that has already been used in the computation of the degree-1 invariants. Substituting this relation into equation (79) results in

$$\left\langle \mathbf{R}_\omega I_m^l(q) I_{m'}^{l'}(q')^* \right\rangle_{\text{SO}(3)} = \frac{\delta_{l,l'} \delta_{m,m'}}{2l+1} \sum_n I_n^l(q) I_n^l(q')^*.$$

In summary we found the degree-2 invariants to be given by

$$\mathcal{I}_{\text{SO}(2)}^2(q, q') = \left\langle \mathbf{R}_\alpha I_n(q) I_{n'}(q')^* \right\rangle_{\text{SO}(2)} = \delta_{n,n'} I_n(q) I_n(q')^* \quad (80a)$$

$$\mathcal{I}_{\text{SO}(3)}^2(q, q') = \left\langle \mathbf{R}_\omega I_m^l(q) I_{m'}^{l'}(q')^* \right\rangle_{\text{SO}(3)} = \frac{\delta_{l,l'} \delta_{m,m'}}{2l+1} \sum_n I_n^l(q) I_n^l(q')^* \quad (80b)$$

For the three-dimensional case it is common to denote the non-vanishing invariants, at $m = m'$ and $l = l'$, as B_l coefficients [19, 23, 99], i.e.

$$B_l(q, q') = \sum_n I_n^l(q) I_n^l(q')^* \quad (81)$$

Adopting a similar naming convention in the two-dimensional case yields

$$B_n(q, q') = I_n(q) I_n(q')^* \quad (82)$$

The reader may verify that the equations (80a)-(82) are indeed invariant under the action of rotations. In the two-dimensional case this directly follows from the rotation action whereas in the three-dimensional case it is convenient to additionally use the Wigner D-matrix property presented in equation (265). A geometric interpretation of their invariance under rotations can be found in appendix A.1. The remainder of this section will be devoted to show the following two useful observations

Observation 2.15 (Properties of B_l and B_n)

1. The quantities $B_l(q, q')$ from equations (81) are real valued and symmetric, that is

$$B_l(q, q') = B_l(q, q')^* \quad \text{and} \quad B_l(q, q') = B_l(q', q)$$

2. In the two-dimensional case $B_n(q, q')$, as specified in equation (82), are self-adjoint and satisfy

$$B_n(q, q') = B_{-n}(q, q')^*$$

Observation 2.16 (Connection to degree 1 invariants) The invariants $B_{l=0}(q, q')$ and $B_{n=0}(q, q')$ are in fact given by the degree-1 invariants from equation (78) via

$$\begin{aligned} B_{n=0}(q, q') &= I_0(q)I_0(q') = I^{\text{SAXS}}(q)I^{\text{SAXS}}(q') \\ B_{l=0}(q, q') &= I_0^0(q)I_0^0(q') = 4\pi I^{\text{SAXS}}(q)I^{\text{SAXS}}(q') \end{aligned}$$

Consequently they are proportional to the “square” of the SAXS intensity.

Observation 2.15 is a direct consequence of the real valuedness of the single-particle intensity which allows us to use the symmetry relations from equation (49) and show

$$\begin{aligned} B_n(q, q') &= I_n(q)I_n(q')^* = I_{-n}(q)^*I_{-n}(q') = B_{-n}(q', q) \\ B_l(q, q') &= \sum_n I_n^l(q)I_n^l(q')^* = \sum_n (-1)^{2n}I_{-n}^l(q)^*I_{-n}^l(q') = B_l(q', q), \end{aligned}$$

which together with

$$B_n(q, q') = I_n(q)I_n(q')^* = B_n(q', q)^* \quad \text{and} \quad B_l(q', q) = \sum_n I_n^l(q')I_n^l(q)^* = B_l(q, q')^*$$

completes our derivation.

2.2.3. Degree 3 invariants

While studied less than their degree 2 and degree 1 counterparts one can readily find explicit forms of the degree 3 invariants in the literature [95, 96, 101]. At this point we

simply want to mention their form and shall refer any interested reader to appendix A.2 for the corresponding derivation.

$$\begin{aligned}\mathcal{I}_{\text{SO}(2)}^3(q_1, q_2, q_3) &= \left\langle \mathbf{R}_\alpha I_{n_1}(q_1) I_{n_2}(q_2)^* I_{n_3}(q_3) \right\rangle_{\text{SO}(2)} \\ &= \delta_{n_2, (n_1+n_3)} I_{n_1+n_3}(q_2)^* I_{n_1}(q_1) I_{n_3}(q_3)\end{aligned}\quad (83a)$$

$$\begin{aligned}\mathcal{I}_{\text{SO}(3)}^3(q_1, q_2, q_3) &= \left\langle \mathbf{R}_\omega I_{m_1}^{l_1}(q_1) I_{m_2}^{l_2}(q_2)^* I_{m_3}^{l_3}(q_3) \right\rangle_{\text{SO}(3)} \\ &= \delta_{m_2, (m_1+m_3)} \frac{C_{m_1, m_3}^{l_1, l_3, l_2}}{2l_2 + 1} \sum_{n_1, n_3} I_{n_1+n_3}^{l_2}(q_2)^* I_{n_1}^{l_1}(q_1) I_{n_3}^{l_3}(q_3) C_{n_1, n_3}^{l_1, l_3, l_2},\end{aligned}\quad (83b)$$

where symbols of type $C_{m, m'}^{l, l', L}$ are a shorthand notation for the Clebsch-Gordan coefficients $\langle l m l' m' | L(m + m') \rangle$. In analogy to the degree 2 case one may define

$$B_{n_1, n_3}(q_1, q_2, q_3) = I_{n_1+n_3}(q_2)^* I_{n_1}(q_1) I_{n_3}(q_3) \quad (84)$$

$$B_{l_1, l_2, l_3}(q_1, q_2, q_3) = \sum_{n_1, n_3} I_{n_1+n_3}^{l_2}(q_2)^* I_{n_1}^{l_1}(q_1) I_{n_3}^{l_3}(q_3) C_{n_1, n_3}^{l_1, l_3, l_2} \quad (85)$$

2.3. Information content of degree-2 invariants

So far we have seen that rotational invariants \mathcal{I}^d in general and especially the invariants with degree- d smaller than 4 are of fundamental importance in FXS, since they specify the single-particle intensity up to a global rotation (theorem 2.12). One might already suspect that the same does not hold if we restrict ourselves to degree-1 and degree-2 invariants exclusively, or for that matter, just to degree-2 invariants. This is because the positivity of the single-particle intensity $I(\mathbf{q})$ implies together with observation 2.16 that the degree-1 invariants can be obtained from their degree-2 counterparts.²⁰, i.e.

$$\langle I_n(q) \rangle_{\text{SO}(2)} = \sqrt{B_{n=0}(q, q)} \quad \text{and} \quad \langle I_m^l(q) \rangle_{\text{SO}(3)} = \sqrt{B_{l=0}(q, q)}$$

In accordance with this suspicion one may formulate the following questions, which shall be the topic of this section.

- How much does $B_l(q, q')$ "know" about the single-particle intensity $I(\mathbf{q})$?
- How can the information contained in $B_l(q, q')$ be used ?

The answer to the first questions was provided in [2, appendix A] and hence goes back to the very beginning of *fluctuation X-ray scattering*. Let us again consider our discrete set of single-particle harmonic coefficients $I_n(q_i)$ and $I_m^l(q_i)$ with S momentum transfer

²⁰Using these relations to actually compute the degree-1 invariants, i.e. the SAXS curves, if one has access to measurements of either one of $I_n(q), I_m^l(q), I(q, \pi/2, \phi)$ or $I(q, \theta_\lambda(q), \phi)$ is numerically always inferior to their direct computation, as in equation (41). For more details on the numerical challenges encountered in computing the degree-2 invariants we refer the reader to section 3.3.

points q_i . For fixed harmonic degrees n and l one can then represent $I_n(q_i)$ and $I_m^l(q_i)$ as matrices of size $(S \times 1)$ (i.e. a column vector) and $S \times (2l + 1)$, respectively

$$(\mathbf{I}_n)_{i,1} = I_n(q_i) \quad \text{and} \quad (\mathbf{I}_l)_{i,m} = I_m^l(q_i), \quad (86)$$

where bold symbols represent matrices (or vectors) and the bracket notation $(\mathbf{A})_{i,j}$ denotes the matrix coefficient in the i -th row and j -th column of \mathbf{A} . Correspondingly, one can interpret the invariants $B_n(q_i, q_j)$ and $B_l(q_i, q_j)$ as $(S \times S)$ matrices which take the form of simple matrix products

$$\mathbf{B}_n = \mathbf{I}_n \mathbf{I}_n^\dagger \quad \text{and} \quad \mathbf{B}_l = \mathbf{I}_l \mathbf{I}_l^\dagger, \quad (87)$$

where “ \dagger ” denotes the conjugate transpose. From observation 2.15 we already know that the matrix \mathbf{B}_n is self-adjoint and \mathbf{B}_l is symmetric, therefore they have to be diagonalizable by a unitary matrix and an orthogonal matrix, respectively. The form of eq. (87), which identifies the invariants as positive semidefinite matrices, furthermore enforces their eigenvalues to be positive. By construction the maximal rank of \mathbf{B}_n is the maximal rank of \mathbf{I}_n , which is 1. Similarly one finds the maximal rank of \mathbf{B}_l to be given by $S_l = \min(S, 2l + 1)$. Together this means that there exist a complex vector \mathbf{v}_n of length S , a positive eigenvalue λ_n , as well as a real $S \times S_l$ matrix \mathbf{V}_l together with a diagonal matrix $\mathbf{\Lambda}_l$ of eigenvalues $\lambda_{l,1}, \dots, \lambda_{l,S_l} > 0$, such that

$$\mathbf{B}_n = \mathbf{v}_n \lambda_n \mathbf{v}_n^\dagger = \tilde{\mathbf{v}}_n \tilde{\mathbf{v}}_n^\dagger \quad \text{and} \quad \mathbf{B}_l = \mathbf{V}_l \mathbf{\Lambda}_l \mathbf{V}_l^T = \tilde{\mathbf{V}}_l \tilde{\mathbf{V}}_l^T, \quad (88)$$

where for brevity we defined $\tilde{\mathbf{v}}_n = \mathbf{v}_n \sqrt{\lambda_n}$ and $\tilde{\mathbf{V}}_l = \mathbf{V}_l \sqrt{\mathbf{\Lambda}_l}$. Equations (87) and (88) show two different decompositions of the same positive semidefinite matrices \mathbf{B}_n and \mathbf{B}_l . Since such decompositions are unique up to unitary transformations [103, theorem 7.3.11] there exist a (1×1) unitary matrix u_n (i.e. a complex phase) as well as a complex matrix \mathbf{U}_l of size $(S_l \times 2l + 1)$ such that $\mathbf{U}_l \mathbf{U}_l^\dagger = \mathbf{id}$ (here \mathbf{id} stands for the identity matrix), which satisfy

$$\mathbf{I}_n = \tilde{\mathbf{v}}_n u_n \quad \text{and} \quad \mathbf{I}_l = \tilde{\mathbf{V}}_l \mathbf{U}_l. \quad (89)$$

This equation formulates an answer to our first question about how much knowledge the invariants of degree-2 contain about the single-particle intensity $I(\mathbf{q})$. To be precise, $\tilde{\mathbf{v}}_n$ and $\tilde{\mathbf{V}}_l$ correspond to the information contained in the degree-2 invariants while u_n and \mathbf{U}_l represent the missing information.

Observation 2.17 (Information content of \mathbf{B}_n and \mathbf{B}_l) The invariants \mathbf{B}_n and \mathbf{B}_l specify the harmonic coefficients of the single-particle intensity \mathbf{I}_n and \mathbf{I}_l for each corresponding harmonic degree n and l up to an unknown (semi-)unitary²¹ matrix u_n or \mathbf{U}_l of shapes (1×1) and $(\min(S, 2l + 1) \times 2l + 1)$ respectively. Hence, the unknowns u_n are elements of $U(1)$ while the \mathbf{U}_l are in general elements of $U(S_l, 2l + 1)$.

²¹For harmonic degrees l such that $S < 2l + 1$ the matrix \mathbf{U}_l is non-square and hence can not be unitary. We shall call a possibly non-square (n, m) matrix \mathbf{U} semi-unitary if it satisfies $\mathbf{U} \mathbf{U}^\dagger = \mathbf{id}$ and $n \leq m$. We will denote the set of semi-unitary matrices of shape (n, m) by $U(n, m)$.

At this point we want to make two side remarks on the above result.

- Notice that the reasoning leading from the eigen-decomposition in equation (88) to equation (89) remains valid if we substitute $\tilde{\mathbf{v}}_n$ and $\tilde{\mathbf{V}}_l$ with arbitrary matrices of the same shape, say \mathbf{w}_n and \mathbf{W}_l , as long as they provide decompositions of the form

$$\mathbf{B}_n = \mathbf{w}_n \mathbf{w}_n^\dagger \quad \text{and} \quad \mathbf{B}_l = \mathbf{W}_l \mathbf{W}_l^\dagger$$

and we would find

$$\mathbf{I}_n = \mathbf{w}_n u_n \quad \text{and} \quad \mathbf{I}_l = \mathbf{W}_l \mathbf{U}_l.$$

In section 3.3 we will use this fact to propose a regularization scheme that circumvents some of the difficulties encountered in the computation of $\tilde{\mathbf{V}}_l$ from experimental data.

- The second remark concerns the total maximal number of real unknown parameters contained in u_n or \mathbf{U}_l . This number does not depend on S , the number of momentum transfer values q_i , and instead only depends on the maximal considered harmonic order L . Informally one could say that the degree-2 invariants contain the complete radial information about $I(\mathbf{q})$ and only lack part of its angular information. This is easy to see in the two-dimensional case, where we only have a single unknown phase u_n per harmonic degree n . Therefore the total number of unknown parameters is given by the maximal harmonic degree L (for $l = 0$ one has $u_0 = 1$ since $\mathbf{I}_{n=0}$ has to be real).²² In the three-dimensional case one finds the maximal number of real unknowns to be given by $\sum_{l=1}^L \dim_{\mathbb{R}}(U(2l+1)) = \sum_{l=1}^L (2l+1)^2 = \frac{1}{3}(11L + 12L^2 + 4L^3)$, where $\dim_{\mathbb{R}}(U(2l+1)) = (2l+1)^2$ is the real dimension²³ of the group of unitary matrices of size $2l+1$.

With the first question answered we may now turn to the second and investigate how the information in form of $\tilde{\mathbf{v}}_n$ and $\tilde{\mathbf{V}}_l$ from equation (89) may be used. One possible use case has been proposed in [19] and centers around the following question.

Given the degree-2 invariant matrix \mathbf{B}_l of a single-particle intensity I and an arbitrary function $f(\mathbf{q}_i)$ with harmonic coefficient matrix \mathbf{f}_l . What is the "closest" function $f'(\mathbf{q}_i)$ to $f(\mathbf{q}_i)$ such that it has the same degree-2 invariants as the considered single-particle intensity, i.e. such that $\mathbf{f}'_l \mathbf{f}'_l{}^\dagger = \mathbf{B}_l$?

Before answering that question we first have to agree on a notion of "closest" discrete function. Here we want to borrow the definition of "closest", that is induced by the scalar product of square integrable functions²⁴ and formulate a discrete version of it. For paris

²²Because of Friedel's symmetry, $I(\mathbf{q}) = I(-\mathbf{q})$, all harmonic coefficients of the single-particle intensity with odd degrees vanish and the number of free parameters is even lower than L . The fact that odd harmonic degrees vanish is valid in the three-dimensional case as well.

²³ $\dim_{\mathbb{R}}(U(2l+1))$ denotes the dimension of $U(2l+1)$ as vector space over the field of real numbers \mathbb{R} .

²⁴The Hilbert space of square integrable functions over K , with K being real or complex numbers, is commonly denoted by $L^2(K^d)$, where d is the dimension of the vector space on which functions are formulated.

of functions in polar and spherical coordinates, $f(q, \phi)$, $g(q, \phi)$ and $f(q, \theta, \phi)$, $g(q, \theta, \phi)$, the L^2 scalar product is given by

$$\begin{aligned} \langle f(q, \phi), g(q, \phi) \rangle_{L^2} &= \int_0^\infty dq q \int_0^{2\pi} d\phi f(q, \phi) g(q, \phi)^* \\ &= \sum_{n=-\infty}^\infty \int_0^\infty dq q f_n(q) g_n(q)^* \end{aligned} \quad (90a)$$

$$\begin{aligned} \langle f(q, \theta, \phi), g(q, \theta, \phi) \rangle_{L^2} &= \int_0^\infty dq q^2 \int_0^\pi d\theta \sin(\theta) \int_0^{2\pi} d\phi f(q, \theta, \phi) g(q, \theta, \phi)^* \\ &= \sum_{l=0}^\infty \sum_{m=-l}^l \int_0^\infty dq q^2 f_m^l(q) g_m^l(q)^*, \end{aligned} \quad (90b)$$

where in each case the second equation is obtained by expanding f in its harmonic series and subsequently using the orthogonality relation for the respective expansion functions. We shall discretize this scalar product by replacing the remaining integral with a sum as well as introducing a maximal harmonic degree L , i.e.

$$\left\langle \sum_n f_n(q_i) e^{in\phi}, \sum_n g_n(q_i) e^{in\phi} \right\rangle_{L^2} = \sum_{n=-L}^L \sum_{i=1}^S q_i f_n(q_i) g_n(q_i)^* \quad (91)$$

$$\left\langle \sum_{l,m} f_m^l(q) Y_m^l(\theta, \phi), \sum_{l,m} g_m^l(q) Y_m^l(\theta, \phi) \right\rangle_{L^2} = \sum_{l=0}^L \sum_{m=-l}^l \sum_{i=1}^S q_i^2 f_m^l(q_i) g_m^l(q_i)^* \quad (92)$$

Correspondingly we will define the discrete L^2 norm via

$$\left\| \sum_n f_n(q_i) e^{in\phi} \right\|_{L^2} = \sqrt{\left\langle \sum_n f_n(q_i) e^{in\phi}, \sum_n f_n(q_i) e^{in\phi} \right\rangle_{L^2}} \quad (93)$$

$$\left\| \sum_{l,m} f_m^l(q) Y_m^l(\theta, \phi) \right\|_{L^2} = \sqrt{\left\langle \sum_{l,m} f_m^l(q) Y_m^l(\theta, \phi), \sum_{l,m} f_m^l(q) Y_m^l(\theta, \phi) \right\rangle_{L^2}}. \quad (94)$$

For a single harmonic matrix(or vector) \mathbf{f}_l or \mathbf{f}_n we find

$$\|\mathbf{f}_n\|_{L^2}^2 = \sum_{i=1}^S q_i |(\mathbf{f}_n)_{i,1}|^2 \quad \|\mathbf{f}_l\|_{L^2}^2 = \sum_{m=-l}^l \sum_{i=1}^S q_i^2 |(\mathbf{f}_l)_{i,m}|^2 \quad (95)$$

Note that in this case the discrete L^2 norm is equivalent²⁵ to the well known Frobenius norm [104] of matrices, $\|\mathbf{A}\|_F^2 = \sum_{i,j} |A_{i,j}|^2$. The closeness of two functions f and f' can now be quantified via the norm of their difference $\|f - f'\|_{L^2}$.

²⁵Up to scaling factors depending on the radial points q_i .

Observe, that a function f' has the same degree-2 invariant as the considered single-particle intensity $I(\mathbf{q}_i)$ if and only if its harmonic coefficients have the form

$$\mathbf{f}'_n = \tilde{\mathbf{v}}_n \mathbf{u}_n \quad \text{and} \quad \mathbf{f}'_l = \tilde{\mathbf{V}}_l \mathbf{u}_l,$$

where $\tilde{\mathbf{v}}_n$ and $\tilde{\mathbf{V}}_l$ are the same as in equation (89), \mathbf{u}_n is a phase and \mathbf{u}_l a complex $(S_l \times 2l + 1)$ semi-unitary matrix (see observaiton 2.17). We are now able to reformulate the question of finding the closest function f' as the following optimization problems in the free parameters \mathbf{u}_n and \mathbf{u}_l ,

$$\mathbf{u}_n = \underset{\mathbf{u}_n \text{ in } U(1)}{\operatorname{argmin}} \|\mathbf{f}_n - \tilde{\mathbf{v}}_n \mathbf{u}_n\|_{L^2} \quad \text{and} \quad \mathbf{u}_l = \underset{\mathbf{u}_l \text{ in } U(S_l, 2l+1)}{\operatorname{argmin}} \|\mathbf{f}_l - \tilde{\mathbf{V}}_l \mathbf{u}_l\|_{L^2}. \quad (96)$$

Both of these optimization problems have unique solutions [19]. In the two-dimensional case one may derive

$$\begin{aligned} \mathbf{u}_n &= \underset{\mathbf{u}_n \text{ in } U(1)}{\operatorname{argmin}} \|\mathbf{f}_n - \tilde{\mathbf{v}}_n \mathbf{u}_n\|_{L^2} = \underset{\mathbf{u}_n \text{ in } U(1)}{\operatorname{argmax}} \operatorname{Re} [\langle \mathbf{f}_n, \tilde{\mathbf{v}}_n \mathbf{u}_n \rangle_{L^2}] \\ &= \frac{\langle \mathbf{f}_n, \tilde{\mathbf{v}}_n \rangle_{L^2}}{|\langle \mathbf{f}_n, \tilde{\mathbf{v}}_n \rangle_{L^2}|} = \frac{\sum_{i=1}^S f_n(q_i) (\tilde{\mathbf{v}}_n)_i^* q_i}{\left| \sum_{i=1}^S f_n(q_i) (\tilde{\mathbf{v}}_n)_i^* q_i \right|}, \end{aligned}$$

here $\operatorname{Re}[\cdot]$ means projection to the real part. In the third step we used the fact that the real part of $\langle \mathbf{f}_n, \tilde{\mathbf{v}}_n \mathbf{u}_n \rangle_{L^2}$ becomes maximal for the phase \mathbf{u}_n that causes the entire scalar product to become real, as well as $\langle \mathbf{f}_n, \tilde{\mathbf{v}}_n \mathbf{u}_n \rangle_{L^2} = \langle \mathbf{f}_n, \tilde{\mathbf{v}}_n \rangle_{L^2} \mathbf{u}_n^*$. For the three-dimensional case it has been realized that the optimization problem given on the right hand side of equation (96) is, for $S_l = 2l + 1$, equivalent to a scaled unitary version of the orthogonal procrustes problem which is well known in linear algebra [105]. The solution to which can be given, following [19], as

$$\mathbf{u}_l = \mathbf{v}_l \mathbf{u}_l^\dagger,$$

where \mathbf{u}_l and \mathbf{v}_l are the unitary matrices given by a singular value decomposition of the $(S_l \times 2l + 1)$ matrix $\tilde{\mathbf{V}}_l^\dagger \mathbf{D} \mathbf{f}_l$. The matrix \mathbf{D} in this expression is the diagonal $(S \times S)$ matrix with elements $(\mathbf{D})_{i,i} = q_i^2$, that incorporate the scaling factors present in our definition of the discrete L^2 norm. Together this means

$$\operatorname{SVD}[\tilde{\mathbf{V}}_l^\dagger \mathbf{D} \mathbf{f}_l] = \mathbf{v}_l \mathbf{\Sigma}_l \mathbf{u}_l^\dagger, \quad (97)$$

where $\mathbf{\Sigma}_l$ is the diagonal matrix of singular values. This solution directly generalizes to the case where $S_l < 2l + 1$ using the compact version of the singular value decomposition, in which \mathbf{v}_l is a unitary $(S_l \times S_l)$ and \mathbf{u}_l^\dagger a semi-unitary matrices of shape $(S_l \times 2l + 1)$ [23]. In conclusion of this chapter let us formulate the answer to our second question, regarding the possible uses of the information contained in the degree-2 invariants, as the following observation.

Observation 2.18 (Invariant projection) Given the degree-2 invariants of a single-particle intensity $I(\mathbf{q}_i)$ with associated matrix $\tilde{\mathbf{v}}_n$ or $\tilde{\mathbf{V}}_l$ (see equations (88)-(89)) and an

arbitrary complex function $f(\mathbf{q}_i)$. Then, the closest function f' to f , in the discrete L^2 norm, that has the same degree-2 invariants as I is given by the harmonic coefficient matrices

$$P_{\text{inv}}[\mathbf{f}_n] = \mathbf{f}'_n = \tilde{\mathbf{v}}_n \frac{\langle \mathbf{f}_n, \tilde{\mathbf{v}}_n \rangle_{L^2}}{|\langle \mathbf{f}_n, \tilde{\mathbf{v}}_n \rangle_{L^2}|} \quad \text{and} \quad P_{\text{inv}}[\mathbf{f}_l] = \mathbf{f}'_l = \tilde{\mathbf{V}}_l \mathbf{V}_l \mathbf{U}_l^\dagger \quad (98)$$

for the two-dimensional and three-dimensional case respectively. Here we have introduced the symbol P_{inv} to denote the corresponding projection on the level of the harmonic coefficients, which we shall call the *invariant* projection. The matrices \mathbf{V}_l and \mathbf{U}_l^\dagger in (98) are given by the singular value decomposition specified in equation (97).

While this observation might seem a bit vague, it has major practical implications. As we shall see in the following section it enables one to formulate a phase retrieval algorithm, that is solely based on the invariants accessible within FXS.

2.4. FXS based phase retrieval via MTIP

The basic idea is to use observation 2.18 to modify the iterative phase retrieval algorithm presented in section 1.3, such that full knowledge about the single-particle intensity I may be substituted with the degree-2 and degree-1 invariants of FXS. In each phasing loop iteration the intensity projection, as defined in equation (28), is split into three steps

1. In the i -th iteration use the current estimate of the scattering-amplitude to compute its corresponding intensity $I_i = \hat{\rho}_i \hat{\rho}_i^*$
2. Apply observation 2.18 to find the closest intensity for given degree-2 and degree-1 invariants, $I'_i = P_{\text{inv}}(I_i)$.
3. Use I'_i to perform the intensity projection as in standard iterative phase retrieval, i.e. $\hat{\rho}'_i = P_{I'_i}[\hat{\rho}_i]$ with $P_{I'_i}$ as defined in (28).

Apart from the change in the reciprocal space constraint the rest of the phasing loop and associated methods such as shrink wrap [58] or the *hybrid input-output* method [39], stay the same with one exception. Since the algorithm relies on frequent applications of observation 2.18 it has to frequently compute the polar or spherical harmonic decomposition of the current intensity candidate, necessitating access to a description of this quantity in polar or spherical coordinates. As consequence the entire phasing loop is formulated in polar or spherical coordinates. The resulting algorithm is called *multi-tiered iterative phase retrieval (MTIP)* and was first proposed in [19, 106]. A schematic representation of the discussed MTIP phasing loop can be found in figure 14. As part of this thesis a structure reconstruction workflow has been developed, that is based on a modified version of the MTIP algorithm. Details about the modifications and the precise implementation will be discussed in section 3.4.

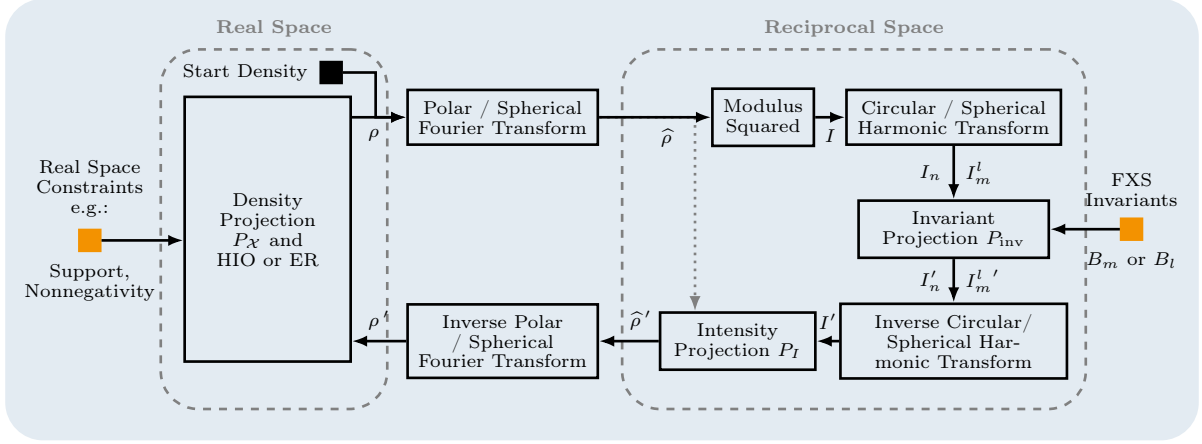


Figure 14: Representation of the MTIP loop. The filled orange squares mark the entry points for constraints, and the black square denotes the initial density guess. The quantities labeled by $(\rho, I, I_n$ and $I_m^l)$ should be interpreted as iterative estimates of the corresponding theoretical quantities.

2.5. FXS moments and single-particle invariants

While we have now learned a lot about the single-particle invariants \mathcal{I}^d of various degrees, starting from their role in FXS (theorem 2.12 and observation 2.13) over their concrete form (section 2.2) to their information content and possible usage for structure recovery (observations 2.17-2.18 and section 2.4), there remains a missing link in our presentation. We have not yet fully connected the single-particle invariants with the moments \mathcal{M}_N^d from equations (60)-(61), that can be directly computed within *fluctuation X-ray scattering*.

In the two-dimensional version of FXS we identified \mathcal{M}_N^d with the single-particle invariants directly (section 2.1.4), but only in the case of $N = 1$. That is, in the case in which each sample $\rho^M(\mathbf{r})$ consists precisely of a single randomly oriented and positioned copy of the studied particle. In the three-dimensional case we know even less. The only connection, so far, was given in observation 2.13, which tells us that the moments \mathcal{M}_N^d have to be sums over single-particle invariants. The precise characterization of those sums for $d \leq 3$ as well as the description of methods by which one can recover the degree-2 single-particle invariants $B_l(q_1, q_2)$ will be the topic of this section. While some of the corresponding results are well known [1, 2, 99], the disposition in this section will contain original contributions. They mostly center around the presentation of a new approach to the extraction of the single-particle degree-2 invariants from the moments \mathcal{M}_N^2 in the three-dimensional case and the treatment of the multi-particle case, in which the number of particles N is allowed to be a random variable.

2.5.1. FXS moments in the single-particle case

Let us for now assume, that the number of particles per scattering pattern N is constant and equal to 1. We will denote the corresponding moments $\mathcal{M}_{N=1}^d$ simply by \mathcal{M}^d . As

stated, in the two-dimensional version of FXS we already found that the moments \mathcal{M}^d are directly given by the single-particle invariants $\mathcal{I}_{\text{SO}(2)}^d$ from equation (73a), that is

$$\mathcal{M}^d(q_1, \dots, q_d, n_1, \dots, n_d) = \mathcal{I}_{\text{SO}(2)}^d = \left\langle \mathbf{R}_\alpha \prod_{\substack{j=1 \\ \text{odd } j}}^d I_{n_j}(q_{i_j}) \prod_{\substack{j=2 \\ \text{even } j}}^d I_{n_j}(q_{i_j})^* \right\rangle_{\text{SO}(2)} \quad (99)$$

We shall now derive the corresponding relationships in the general three-dimensional case for degrees smaller than 4. Note that for $N = 1$ the dilute limit assumption 3 is always true, since there are no other particles in the interaction volume. By the Fourier shift theorem (18) the diffraction patterns I^M have to be independent on the position \mathbf{x}_1 of the corresponding particle and the ensemble average $\langle \cdot \rangle_M$, present in the definition of the moments \mathcal{M}^d in equations (60) and (61), reduces to a simple average over the uniformly distributed rotation states of the considered particle $\langle \cdot \rangle_{\text{SO}(3)}$.

Expansion of moments: The general procedure of obtaining explicit expressions for \mathcal{M}^d will be as follows.

1. Expand the definition of \mathcal{M}^d using the spherical harmonic series expression of I^M , that is

$$I^M(q, \phi) = \mathbf{R}_\omega I(q, \theta_\lambda(q), \phi) = \sum_{l=1}^L \sum_{m=-l}^l [\mathbf{R}_\omega I_m^l(q)] Y_m^l(\theta_\lambda(q), \phi),$$

where $\theta_\lambda(q)$ represents the restriction to the Ewald's sphere. This allows one to recognize \mathcal{M}^d as a sum over the single-particle invariants \mathcal{I}^d .

2. Use the known expressions for \mathcal{I}^d from section 2.2 and simplify the resulting equation.

$d = 1$: In this case we find

$$\mathcal{M}^1(q, \phi) = \langle I^M(q, \phi) \rangle_{\text{SO}(3)} = \sum_{l=0}^L \sum_{m=-l}^l \langle \mathbf{R}_\omega I_m^l(q) \rangle_{\text{SO}(3)} Y_m^l(\theta_\lambda(q), \phi) \quad (100)$$

and we can use equation (78b) for the single-particle invariant $\mathcal{I}_{\text{SO}(3)}^1(q)$ to obtain

$$\mathcal{M}^1(q, \phi) = I^{\text{SAXS}}(q) = I_0^0(q) Y_0^0(\theta_\lambda(q), \phi). \quad (101)$$

Equation (101) simply states that the degree-1 moments are, up to a constant prefactor, precisely the single-particle invariants of the same degree. Note that using the second version of the moments $\mathcal{M}^1(q, n)$, given in equation (61), yields almost the same result

$$\mathcal{M}^1(q, n) = \langle I_n^M(q, \phi) \rangle_{\text{SO}(3)} = \sum_{l=0}^L \sum_{m=-l}^l \langle \mathbf{R}_\omega I_m^l(q) \rangle_{\text{SO}(3)} (Y_m^l(\theta_\lambda(q), \phi))_n.$$

Using equations (46) and (44) one can find the Fourier series coefficient of a spherical harmonic $(Y_m^l(\theta_\lambda(q), \phi))_n$ to be given by

$$\begin{aligned} (Y_m^l(\theta_\lambda(q), \phi))_n &= \frac{1}{2\pi} \int_0^{2\pi} d\phi \tilde{P}_l^m(\theta_\lambda(q)) e^{im\phi} e^{-in\phi} \\ &= \delta_{n,m} \tilde{P}_l^n(\theta_\lambda(q)) \end{aligned} \quad (102)$$

and hence

$$\mathcal{M}^1(q, n) = \sum_{l=0}^L \langle \mathbf{R}_\omega I_m^l(q) \rangle_{\text{SO}(3)} \tilde{P}_l^n(\theta_\lambda(q)) = \delta_{n,0} I_0^0(q) \tilde{P}_0^0(\theta_\lambda(q)) = \delta_{n,0} I^{\text{SAXS}}(q), \quad (103)$$

where in the second step we used that by equation (46) $\tilde{P}_0^0(\theta_\lambda(q)) = \frac{1}{\sqrt{4\pi}}$. Comparing the right hand side of equation (100) for $\mathcal{M}^1(q, \phi)$ with the first step in equation (103) for $\mathcal{M}^1(q, n)$, one can see that the latter is simpler, in the sense that it lacked the sum over the harmonic order m . Ultimately this resulted in no significant difference²⁶ for the degree-1 moments, for higher degrees it will however affect the final results and give an advantage to moments in their second form, $\mathcal{M}^d(q_1, \dots, q_d, n_1, \dots, n_d)$, introduced in equation (61).

$d = 2$: Let us begin deriving an explicit expression for $\mathcal{M}^2(q_1, q_2, \phi_1, \phi_2)$. In order to keep the resulting equations as concise as possible we shall omit the summation ranges of all indices. Indices l_i will always correspond to a spherical harmonic degree and take values from 0 to L , correspondingly m_i and n_i represent spherical harmonic orders with values between $-l_i$ and l_i .

$$\begin{aligned} \mathcal{M}^2(q_1, q_2, \phi_1, \phi_2) &= \langle I^M(q_1, \phi_1) I^M(q_2, \phi_2)^* \rangle_{\text{SO}(3)} \\ &= \sum_{\substack{l_1, l_2 \\ m_1, m_2}} \langle \mathbf{R}_\omega I_{m_1}^{l_1}(q_1) I_{m_2}^{l_2}(q_2)^* \rangle_{\text{SO}(3)} Y_{m_1}^{l_1}(\theta_\lambda(q_1), \phi_1) Y_{m_2}^{l_2}(\theta_\lambda(q_2), \phi_2)^* \\ &= \sum_{l, m, n} I_n^l(q_1) I_n^l(q_2)^* \frac{Y_m^l(\theta_\lambda(q_1), \phi_1) Y_m^l(\theta_\lambda(q_2), \phi_2)^*}{2l+1}, \end{aligned}$$

where the simplification in the last step is due to equation (80b) that specifies the single-particle invariant $\mathcal{I}_{\text{SO}(3)}^2(q_1, q_2)$ of degree-2. Using the addition theorem for spherical harmonics, given in equation (263) and the definition of $B_l(q_1, q_2)$ from equation (81), this results in

$$\mathcal{M}^2(q_1, q_2, \phi_1, \phi_2) = \sum_{l=0}^L F^l(q_1, q_2, \phi_1 - \phi_2) B_l(q_1, q_2), \quad (104)$$

with

$$F^l(q_1, q_2, \phi_1 - \phi_2) = \frac{P^l(\cos(\theta_\lambda(q_1)) \cos(\theta_\lambda(q_2)) + \sin(\theta_\lambda(q_1)) \sin(\theta_\lambda(q_2)) \cos(\phi_1 - \phi_2))}{4\pi},$$

²⁶The difference for $d = 1$ lies in the Kronecker delta $\delta_{n,0}$ present in (103), whereas (101) is independent on ϕ .

where P^l are Legendre polynomials and we simply wrote $F^l(q_1, q_2, \phi_1 - \phi_2)$ instead of $F^l(\theta_\lambda(q_1), \theta_\lambda(q_1), \phi_1 - \phi_2)$. We want to point out that $\mathcal{M}^2(q_1, q_2, \phi_1, \phi_2)$ as given in the above equation is the most common expression in the literature, that is used to access the invariants $B_l(q_1, q_2)$. It corresponds precisely to the function $J(q, \phi; q', \phi')$ in [99, equation 7] as well as $C(\boldsymbol{\kappa}_1, \boldsymbol{\kappa}_2)$ in [1, equation 17]. Another well known variant of it is given by the ensemble averaged angular cross-correlation function used in XCCA [92–94],

$$\mathcal{C}(q_1, q_2, \Delta) = \langle C(q_1, q_2, \Delta) \rangle_{\text{SO}(3)} = \frac{1}{2\pi} \int_0^{2\pi} d\phi \langle I^M(q_1, \phi + \Delta) I^M(q_2, \phi) \rangle_{\text{SO}(3)}, \quad (105)$$

which is the result of choosing $\phi_1 = \phi + \Delta$ and $\phi_2 = \phi$ in $\mathcal{M}^2(q_1, q_2, \phi_1, \phi_2)$, i.e.

$$\mathcal{C}(q_1, q_2, \Delta) = \mathcal{M}^2(q_1, q_2, \phi + \Delta, \phi) = \sum_{l=0}^L F^l(q_1, q_2, \Delta) B_l(q_1, q_2). \quad (106)$$

Let us continue by computing the moments in their second form $\mathcal{M}^2(q_1, q_2, n_1, n_2)$. Similarly to the $d = 1$ case we can use equation (102) to connect \mathcal{M}^2 to the single-particle invariants as follows

$$\begin{aligned} \mathcal{M}^2(q_1, q_2, n_1, n_2) &= \langle I_{n_1}^M(q_1) I_{n_2}^M(q_2)^* \rangle_{\text{SO}(3)} \\ &= \sum_{l_1, l_2} \langle \mathbf{R}_\omega I_{n_1}^{l_1}(q_1) I_{n_2}^{l_2}(q_2)^* \rangle_{\text{SO}(3)} \tilde{P}_l^{n_1}(\theta_\lambda(q_1)) \tilde{P}_l^{n_2}(\theta_\lambda(q_2)), \end{aligned}$$

which under application of equations (80b) and (81) transforms to

$$\begin{aligned} \mathcal{M}^2(q_1, q_2, n_1, n_2) &= \delta_{n_1, n_2} \sum_{l=|n_1|}^L \tilde{F}_{n_1}^l(q_1, q_2) B_l(q_1, q_2) \\ \tilde{F}_n^l(q_1, q_2) &= \frac{1}{2l+1} \tilde{P}_l^n(\theta_\lambda(q_1)) \tilde{P}_l^n(\theta_\lambda(q_2)) \end{aligned} \quad (107)$$

The reason that the summation over l does not start at zero in (107), as opposed to equation (104), is due to the fact that the associated Legendre polynomials $P_l^{|n|}$ contained in \tilde{F}_n^l are identically zero for $l < |n|$. It is interesting to note that the non-zero contributions in equation (107) can be associated with the averaged cross-correlation \mathcal{C} via its harmonic coefficients, i.e.

$$\mathcal{C}_n(q_1, q_2) = \sum_{l=|n|}^L \tilde{F}_n^l(q_1, q_2) B_l(q_1, q_2) \quad (108)$$

The simplest way to see this, is via the cross-correlation theorem for the Fourier transform which implies, that the harmonic coefficients of the angular cross-correlation $C(q_1, q_2, \Delta)$ are given by $C_n(q_1, q_2) = I_n^M(q_1) I_n^M(q_2)^*$ and hence

$$\mathcal{M}^2(q_1, q_2, n, n) = \langle I_n^M(q_1) I_n^M(q_2)^* \rangle_{\text{SO}(3)} = \langle C_n(q_1, q_2) \rangle_{\text{SO}(3)} = \mathcal{C}_n(q_1, q_2) \quad (109)$$

Note that this equation also holds in the two-dimensional case, since its derivation did not use any specific form for the average correlation \mathcal{C}_n nor for the moments \mathcal{M}^2 . The crucial simplification of equation (108) over (106) lies precisely in the start of the summation over the harmonic degree l . While the invariants B_l of a fixed degree l contribute to values of $\mathcal{C}(q_1, q_2, \Delta)$ for all angles Δ , they only contribute to values of $\mathcal{C}_n(q_1, q_2)$ for $|n| \leq l$. Stated differently this means, that the information about B_l is completely contained in the first l non-zero harmonic coefficients $\mathcal{C}_n(q_1, q_2)$ with $0 \leq n \leq l$, as opposed to being spread out over all of the possible angular values Δ in $\mathcal{C}(q_1, q_2, \Delta)$.²⁷ Note that since we assumed band limited functions with a maximal harmonic degree L we also find that $\mathcal{C}_n = 0$ for $n > L$ and one may neglect all of these coefficients in the data analysis. Conversely, if a given experimental dataset does not allow to compute \mathcal{C}_n for $n > n_{\max}$ reliably, then one may at most gain information about the single-particle invariants B_l with $l \leq n_{\max}$ and assume $L = n_{\max}$, which acts as resolution constraint within FXS. As we shall see in 2.5.2 the link between the harmonic degrees n and l will also allow for simpler and faster methods to extract the invariants B_l from the moment \mathcal{M}^2 .

$d = 3$: For the degree-3 moments we shall again only list the results and refer the interested reader to their derivation in appendix A.3

$$\begin{aligned} \mathcal{M}^3(q_1, q_2, q_3, \phi_1, \phi_2, \phi_3) &= \sum_{l_1, l_2, l_3}^L F^{l_1, l_2, l_3}(q_1, q_2, q_3, \phi_1, \phi_2, \phi_3) B_{l_1, l_2, l_3}(q_1, q_2, q_3) \quad (110) \\ F^{l_1, l_2, l_3}(q_1, q_2, q_3, \phi_1, \phi_2, \phi_3) &= \sum_{m_1, m_3} \frac{2Y_{m_1+m_3}^{l_2}(\theta_\lambda(q_2), \phi_2)^*}{2l_2+1} \\ &\quad \times Y_{m_1}^{l_1}(\theta_\lambda(q_1), \phi_1) Y_{m_3}^{l_3}(\theta_\lambda(q_3), \phi_3) C_{m_1, m_3}^{l_1, l_3, l_2} \\ \mathcal{M}^3(q_1, q_2, q_3, n_1, n_2, n_3) &= \delta_{n_2, n_1+n_3} \sum_{\substack{l_1 \geq |n_1|, l_3 \geq |n_3| \\ l_2 \geq |n_1+n_3|}}^L \tilde{F}_{n_1, n_3}^{l_1, l_2, l_3}(q_1, q_2, q_3) B_{l_1, l_2, l_3}(q_1, q_2, q_3) \quad (111) \\ \tilde{F}_{n_1, n_3}^{l_1, l_2, l_3}(q_1, q_2, q_3) &= \frac{2C_{n_1, n_3}^{l_1, l_3, l_2}}{2l_2+1} \tilde{P}_{l_1}^{n_1}(\theta_\lambda(q_1)) \tilde{P}_{l_2}^{n_1+n_3}(\theta_\lambda(q_2)) \tilde{P}_{l_3}^{n_3}(\theta_\lambda(q_3)) \end{aligned}$$

Here B_{l_1, l_2, l_3} are the single-particle invariants given in (85). Versions of equation (110) are known and can for example be found in [107, equation 16.7]²⁸, the second equation (111) has not been published so far. Note that the summation over the triple l_1, l_2 and l_3 in the latter equation is again restricted by the harmonic degrees n_1, n_2 and n_3 . Additionally the summation coefficients $\tilde{F}_{n_1, n_3}^{l_1, l_2, l_3}(q_1, q_2, q_3)$ are simpler compared to $\tilde{F}^{l_1, l_2, l_3}(q_1, q_2, q_3, \phi_1, \phi_2, \phi_3)$, in the sense that they do not contain large sums.

²⁷Since $B_l(q, q')$ is real so is $\mathcal{M}^2(q_1, q_2, n, n)$ and one finds $\mathcal{M}^2(q_1, q_2, n, n) = \mathcal{M}^2(q_1, q_2, -n, -n)^*$. Hence, we can restrict our considerations to positive values of n .

²⁸The formula given [107, equation 16.7] corresponds the case where $\phi_1 = 0$

2.5.2. Extraction of single-particle invariants

Staying in the setting of the previous subsection, in which we consider each sample configuration $\rho^M(\mathbf{r})$ to contain exactly one particle ($N = 1$), we may now discuss methods by which to extract the single-single particle invariants \mathcal{I}^d given in section 2.2 from the moments \mathcal{M}^d of the previous subsection 2.5.1.

In the two-dimensional case there is nothing to show since the single-particle invariants exactly correspond to the FXS moments by equation (99). The same holds for degree-1 invariants, i.e. SAXS curves, in the three dimensional case via equations (101) and (103). Whether the degree-3 or any higher invariants can be extracted from the moments \mathcal{M}^d is an open question and will not be solved in this thesis. Our main topic of discussion are therefore extraction methods for the degree-2 invariants $B_l(q_1, q_2)$ as specified in equation (81). For their description we shall use a similar strategy as adopted in section 2.3, where we applied tools from linear algebra to analyze the information content of the degree-2 invariants. A well known realization of such a method was proposed in [99] and can be summarized as follows. Recall equation (106), that linked the averaged angular cross correlation to the B_l coefficients, via

$$\mathcal{C}(q_1, q_2, \Delta) = \mathcal{M}^2(q_1, q_2, \Delta, 0) = \sum_{l=1}^L F^l(q_1, q_2, \Delta) B_l(q_1, q_2)$$

and consider a discretization of the angular variable Δ into N_Δ different values. For each fixed pair of momentum transfer values q_1 and q_2 the above equations take the form a system of N_Δ linear equations in the $L + 1$ invariants B_l . Let us drop the constant arguments q_1 and q_2 from our notation and view $\mathcal{C}(\Delta)$ as a vector \mathbf{C} of size N_Δ , B_l as vector \mathbf{B} ²⁹ size $L + 1$ and $F^l(\Delta)$ as $(N_\Delta \times L + 1)$ matrix \mathbf{F} whose coefficients we will call $F_{\Delta,l}$. With this we may reformulate the linear system as follows

$$\mathbf{C} = \mathbf{F}\mathbf{B} = \begin{bmatrix} F_{1,0} & \cdots & F_{1,L} \\ \vdots & \ddots & \vdots \\ F_{N_\Delta,0} & \cdots & F_{N_\Delta,L} \end{bmatrix} \begin{bmatrix} B_0 \\ \vdots \\ B_L \end{bmatrix} \quad (112)$$

In practical applications one typically has $N_\Delta > L$ causing the matrix \mathbf{F} to be non-square. This implies the system of linear equations is over-determined and may only be solved approximately. Usually least squares methods such as the pseudo-inverse [108], based on a singular value decomposition of \mathbf{F} , are used to solve such linear systems. Applications of this procedure on experimental data can be found in [20] and [21].

Tangent on $N_\Delta > L$: A justification for why $N_\Delta > L$ holds in practical applications can be found by realizing that N_Δ is linked to the angular resolution at which the diffraction patterns I^M are recorded. In the single-particle case ($N = 1$) these diffraction patterns are Ewald's sphere slices of the target single particle intensity, i.e. $I(q, \theta_\lambda(q), \phi)$, and

²⁹Note the difference between vector \mathbf{B} and the $(S \times S)$ matrix \mathbf{B}_l from section 2.3. The former is a vector in l for fixed values of q_1, q_2 while the latter is a matrix in q_1, q_2 for a fixed harmonic degree l .

one can argue that the obtainable information about the unprojected intensity $I(q, \theta, \phi)$ has to be limited in the same way as the diffraction patterns, i.e. its maximal angular resolution is tied to the angular sampling N_Δ . On the other hand discrete computations of the spherical harmonic coefficients link the spherical grid size to the maximal harmonic degree L for which coefficients can be computed.³⁰ Typical algorithms to compute spherical harmonic coefficients, such as [109], require at least $2l + 1$ sampling points in ϕ to reliably compute the l -th harmonic coefficient and hence $N_\Delta > L$.

We can now turn to the extraction method proposed in [23] which is based on the second variant of the FXS moments $\mathcal{M}^2(q_1, q_2, n_1, n_2)$. To do so, let us give a matrix representation of equation (107) for $n_1 = n_2 = n$ and fixed momentum transfer values q_1 and q_2 . Here we may interpret $\mathcal{M}^2(q_1, q_2, n, n)$ as vector \mathcal{M}^2 of size $(L + 1)$ ³¹ and $\tilde{F}_n^l(q_1, q_2)$ as $(L + 1) \times (L + 1)$ matrix $\tilde{\mathbf{F}}$ with coefficients $\tilde{F}_{n,l}$. Together this allows us to restate equation (107) as

$$\mathcal{M}^2 = \tilde{\mathbf{F}}\mathbf{B} = \begin{bmatrix} \tilde{F}_{0,0} & \cdots & \tilde{F}_{0,L} \\ & \ddots & \vdots \\ 0 & & \tilde{F}_{L,L} \end{bmatrix} \begin{bmatrix} B_0 \\ \vdots \\ B_L \end{bmatrix}. \quad (113)$$

The linear system defined by the matrix $\tilde{\mathbf{F}}$ is therefore not only square but upper-triangular as well. This allows to solve equation (113) via back-substitution. Similar to many SVD algorithms back-substitution is backwards stable [108, chapter 8], which in particular means that it does not amplify errors in the input parameters. Moreover, the statistical complexity of back-substitution is $O((L + 1)^2)$ which is much lower than $O(N_\Delta^2(L + 1))$, the complexity of calculating the *singular value decomposition* (SVD) of \mathbf{F} required to solve equation (112).³² Even in the case where $\mathcal{M}^2(q_1, q_2, n, n)$ are computed from the averaged cross correlation via its Fourier series coefficients (see equation (109)) one finds that the combined complexity of the harmonic decomposition plus back-substitution, being $O(N_\Delta \log(N_\Delta) + (L + 1)^2)$, is still lower than the SVD counterpart. All results that will be presented in section 5 where obtained using back-substitution in the computation of the invariants B_l .

2.5.3. Extension to multi-particle case

We may now drop our assumption that each sample ρ^M contains exactly one particle. Instead, let the number of particles per sample be a discrete positive random variable N , such that the probability to find $\eta = N$ particles in a sample is given by $P(\eta)$. For our derivations in the remainder of this section the notion of *set partitions* will be very useful. They will allow us to express the formulas connecting the single-particle moments \mathcal{M}^d to the multi-particle moments \mathcal{M}_N^d in a graphical way. Let us therefore start with an introduction to set partitions.

³⁰The same phenomenon may be observed for fast Fourier transforms in which the highest accessible frequency and the real space sampling share a similar connection.

³¹Neglecting all negative values of n since $\mathcal{M}^2(q_1, q_2, n, n) = \mathcal{M}^2(q_1, q_2, -n, -n)$.

³²Assuming $N_\Delta > l$, other wise the complexity of the SVD is $O(N_\Delta(L + 1)^2)$.

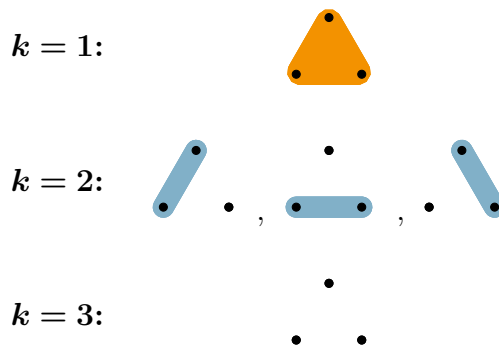
Set partitions: Consider a set with d elements, e.g. $d = 3$



A partition of this set, is a subdivision of its elements into a sequence of non-empty subsets. For example, a possible partition of the above set into two subsets is given by



where the lower two points from one subset and the other one is given by the set that contains the single upper point. One may now ask, how many possible partitions into k subsets does a set with d elements have. The answer for $d = 3$ is given by the following diagram

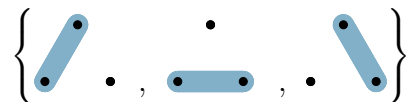


As before, the colored regions denote subsets that contain at least two elements while isolated points simply denote one-element subsets.

In general the total number of set partitions of a set with d elements is called *Bell number* $B(d)$ [110, chapter 1.9], whereas the number number of partitions that have k subsets is known as *Stirling number of the second kind* [110] $\left\{ \begin{smallmatrix} d \\ k \end{smallmatrix} \right\}$, they satisfy

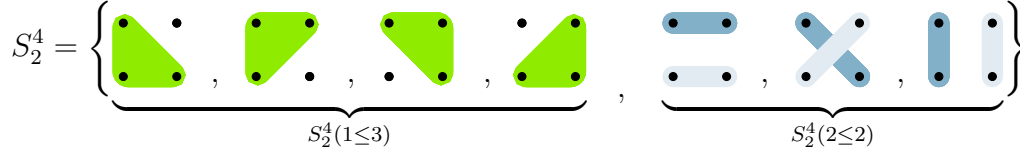
$$B(d) = \sum_{k=1}^d \left\{ \begin{smallmatrix} d \\ k \end{smallmatrix} \right\} \quad \text{and} \quad \left\{ \begin{smallmatrix} d \\ k \end{smallmatrix} \right\} = \sum_{i=1}^k \frac{(-1)^{k-i} i^n}{(k-i)! i!} \quad (114)$$

Let us denote the space³³ of partitions of a set with d elements into k subsets by S_k^d . For example S_2^3 contains 3 partitions and is given by



³³ S_k^d is a set of partitions, i.e. a set containing partitions of another set. In order to not confuse the different sets with each other we call S_k^d a space.

The number of partitions in S_k^d is given by $|S_k^d| = \binom{d}{k}$ from equation (114).³⁴ In order to systematically list all possible partitions in S_k^d , it is useful to subdivide it further into the spaces $S_k^d(o_1 \leq \dots \leq o_k)$ of partitions, whose k subsets have known sizes o_1, \dots, o_k . As example consider a set with 4 elements, then the space S_2^4 has two subspaces, $S_2^4(1 \leq 3)$ and $S_2^4(2 \leq 2)$, i.e.



These subspaces of S_k^d are completely characterized by the conditions $o_1 \leq \dots \leq o_k$ and $o_1 + \dots + o_k = d$, since it makes no sense to consider different orders of subset sizes and the number of elements in all parts of a partition have to add up to d . Furthermore, the number of partitions in $S_k^d(o_1 \leq \dots \leq o_k)$ is given by the number of possibilities to successively draw o_1, \dots, o_k elements, which is given by the multinomial $\binom{d}{o_1, \dots, o_k} = \binom{d}{o_1} \binom{d-o_1}{o_2} \dots \binom{o_k}{o_k}$, divided by the number of ways to order o_j that have the same value³⁵, i.e.

$$|S_k^d(o_1 \leq \dots \leq o_k)| = \frac{\binom{d}{o_1, \dots, o_k}}{\prod_{i=1}^d n(i, o_1, \dots, o_k)!}, \quad (115)$$

where $n(i, o_1, \dots, o_k)$ simply counts the number of times the value i appears in the sizes o_1, \dots, o_k .

In summary this means that all partitions in S_k^d are characterized by a tuple of the form $(o_1 \leq \dots \leq o_k, \sigma)$, in short (\mathbf{o}, σ) , where $o_1 \leq \dots \leq o_k$ are the subset sizes and σ represents one of the elements of $S_k^d(o_1, \dots, o_k)$. For $d = 1, 2$ and 3 this leads to the classification shown in figure 15.

$d = 1$			$d = 2$				$d = 3$				
k	o_1	$ S_k^1(o_1) $	k	o_1	o_2	$ S_k^2(o_1, o_2) $	k	o_1	o_2	o_3	$ S_k^3(o_1, o_2, o_3) $
1	1	1	1	2		1	1	3			1
			2	1	1	1	2	1	2		3
							3	1	1	1	1

Figure 15: Example of the classification of all possible subdivisions of sets with 1,2 or 3 elements

³⁴Here we introduced the notation $|A|$ to denote the number of elements of a set A .

³⁵Since we do not care about the order with which they are drawn.

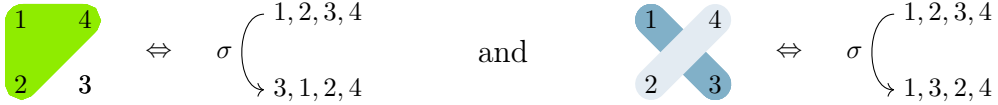
The last ingredient we need, is a way to formalize the partition σ in our tuples (\mathbf{o}, σ) . For this, note that one may associate a permutation, conveniently called σ , of the sequence $1, 2, \dots, d$ to each partition of a set with d elements as follows

1. Assign numbers $1, \dots, d$ to the elements of set to be partitioned (previously called set with d elements).
2. Order the subsets of a partition $(\mathbf{o}, \sigma) \in S_k^d$ increasingly by their size. Subsets of equal size are ordered increasingly by the lowest number they contain.
3. Demand that the permutation σ maps $1, 2, \dots, d$ to $\sigma(1), \sigma(2), \dots, \sigma(d)$ such that
 - a) $\{\sigma(1), \dots, \sigma(o_1)\}$ is the first subset of the partition and in general the p -th subset is given by $\{\sigma(1 + \sum_{l=1}^{p-1} o_l), \dots, \sigma(o_p + \sum_{l=1}^{p-1} o_l)\}$ and we introduce the shorthand notation

$$\sigma(p, a) = \sigma \left(a + \sum_{l=1}^{p-1} o_l \right) \quad \text{for } a \in \{1, \dots, o_p\} \quad (116)$$

- b) Numbers within a subset are increasingly ordered.

For example consider the following cases of a partitions in $S_2^4(1 \leq 3)$ and $S_2^4(2 \leq 2)$



This concludes our discussion of set partitions and we can return to the question of how to represent the multi-particle moments \mathcal{M}_N^d via their single particle counterparts \mathcal{M}^d . Before stating the main result in observation 2.19 we shall give a simplified motivation in the case of an arbitrary but fixed number of particles $N = \eta$, the full derivation in the general case can be found in appendix A.4.

Motivation for fixed $N = \eta$: By the [dilute-limit assumption](#) we find that each scattering pattern I^M is given by a sum over the η scattering contributions I_j^M corresponding to the η individual particles a sample ρ^M contains. Using the form of \mathcal{M}_N^d given in equation (60), representing coordinate pairs (q, ϕ) by their Ewald's sphere point \mathbf{q}^λ and applying the dilute-limit assumption yields

$$\mathcal{M}_{N=\eta}^d = \langle I^M(\mathbf{q}_1^\lambda) \cdot \dots \cdot I^M(\mathbf{q}_d^\lambda) \rangle_M = \sum_{j_1, \dots, j_d=1}^{\eta} \langle I_{j_1}^M(\mathbf{q}_1^\lambda) \cdot \dots \cdot I_{j_d}^M(\mathbf{q}_d^\lambda) \rangle_M,$$

which is a sum over all possible d -fold products of single-particle intensity contributions. Since we assumed a fixed number of particles and the I_j^M are invariant under translations

of the corresponding particles, we can substitute the ensemble average over M with the average over the rotational random variables of all particles $\omega_1, \dots, \omega_\eta$ and obtain

$$\mathcal{M}_{N=\eta}^d = \sum_{j_1, \dots, j_d=1}^{\eta} \langle I_{j_1}^M(\mathbf{q}_1^\lambda) \cdot \dots \cdot I_{j_d}^M(\mathbf{q}_d^\lambda) \rangle_{\omega_1, \dots, \omega_\eta}.$$

We may now use the independence of the random variables $\omega_1, \dots, \omega_\eta$ to simplify each summand. For example, if all particle indices $1 \leq j_1, \dots, j_d \leq \eta$ are different, then the corresponding summands simplify to

$$\langle I_{j_1}^M(\mathbf{q}_1^\lambda) \rangle_{\omega_{j_1}} \cdot \dots \cdot \langle I_{j_d}^M(\mathbf{q}_d^\lambda) \rangle_{\omega_{j_d}} = \mathcal{M}_{N=1}^1(\mathbf{q}_1^\lambda) \cdot \dots \cdot \mathcal{M}_{N=1}^1(\mathbf{q}_d^\lambda). \quad (117)$$

Note that the right hand side of (117) does not depend on the single particle indices j_i anymore and there are exactly $\eta(\eta-1) \cdot \dots \cdot (\eta-d+1) = \frac{\eta!}{(\eta-d)!}$ different ways to choose the indices $1 \leq j_1, \dots, j_d \leq \eta$ such that they are all different. This means that the above factor occurs $\frac{\eta!}{(\eta-d)!}$ times in $\mathcal{M}_{N=\eta}^d$.

In general we can use set partitions to classify all summands in $\mathcal{M}_{N=\eta}^d$. To see this observe, that any summand contains $k \leq d$ different particle indices and is characterized by a possible way to distribute these k particle indices over the d intensity contributions in the product $I_{j_1}^M \cdot \dots \cdot I_{j_d}^M$, i.e. by one possible way to split the d intensity contributions into k subsets, each of which representing one of the k different particle indices. In this way we have identified each summand as a product of single-particle averages of the form

$$\underbrace{\langle I_i^M \cdot \dots \cdot I_i^M \rangle}_{o \text{ times}} = \mathcal{M}^o,$$

which are our single-particle moments and o is the size of one of the k subsets. These products are again independent from the k different single-particle indices³⁶ and therefore occur $\frac{\eta!}{(\eta-k)!}$ times in $\mathcal{M}_{N=\eta}^d$. Remembering that set partitions in S_k^d are characterized by tuples (\mathbf{o}, σ) , with $\mathbf{o} = (o_1 \leq \dots \leq o_k)$, one arrives at

$$\mathcal{M}_{N=\eta}^d = \sum_{k=1}^d \frac{\eta!}{(\eta-k)!} \sum_{(\mathbf{o}, \sigma) \in S_k^d} \prod_{p=1}^k \mathcal{M}^{o_p}, \quad (118)$$

where the permutation σ regulates the distribution of the d arguments $\mathbf{q}_1^\lambda, \dots, \mathbf{q}_d^\lambda$ of $\mathcal{M}_{N=\eta}^d$ over the products of single particle moments. While this formula seems quite complicated, it simply means that the distinct summands of $\mathcal{M}_{N=\eta}^d$ correspond to set partitions of a set with d elements whose multiplicative prefactor $\eta!/(\eta-k)!$ depends on the number of subsets k of a given partition. This interpretation allows for a nice graphical formulation of equation (118) based on set-partition diagrams, like the ones presented in figure 15, as we shall see in later examples.

We are now able state the main result of this section for the case in which the number of particles, N , is a random variable. The full derivation of this result can be found in appendix A.4.

³⁶Since the products only contain single-particle moments and all particles are assumed to be identical up to rotations, i.e. they have the same moments.

Observation 2.19 (Reduction to single-particle moments)

Consider FXS as defined in 2.1 and let \mathcal{M}_N^d be one of the two types of multi-particle moments as defined in equation (60) or (61), e.g.

$$\mathcal{M}_N^d = \mathcal{M}_N^d(q_1, \dots, q_d, \phi_1, \dots, \phi_d) \text{ or } \mathcal{M}_N^d(q_1, \dots, q_d, n_1, \dots, n_d)$$

Consider $\mathcal{M}_{|i_1, \dots, i_o}^o$ to denote the corresponding single-particle moment of the same type, that has degree $1 \leq o \leq d$ and is evaluated on the coordinate pairs with indices $1 \leq i_1, \dots, i_o \leq d$ of the multi particle moment \mathcal{M}_N^d , e.g.

$$\mathcal{M}_{|i_1, \dots, i_o}^o = \mathcal{M}^o(q_{i_1}, \dots, q_{i_o}, \phi_{i_1}, \dots, \phi_{i_o}) \text{ or } \mathcal{M}^o(q_{i_1}, \dots, q_{i_o}, n_{i_1}, \dots, n_{i_o})$$

For a set partition $(\mathbf{o}, \sigma) \in S_k^d$ with $\mathbf{o} = (o_1 \leq \dots \leq o_k)$ we define

$$\mathcal{M}_{||\sigma}^{o_p} = \mathcal{M}_{|\sigma(p,1), \dots, \sigma(p,o_p)}^{o_p},$$

where $\sigma(p, a)$ is the shorthand from equation (116).³⁷ Using this notation one finds that \mathcal{M}_N^d is given by

$$\mathcal{M}_N^d = \sum_{k=1}^d \left\langle \frac{N!}{(N-k)!} \right\rangle \sum_{(\mathbf{o}, \sigma) \in S_k^d} \prod_{p=1}^k \mathcal{M}_{||\sigma}^{o_p}, \quad (119)$$

where $\langle \cdot \rangle$ is the average with respect to the random variable N . With $P(\eta)$ being the probability to observe a sample consisting of η particles this means

$$\left\langle \frac{N!}{(N-k)!} \right\rangle = \sum_{\eta=k}^{\infty} P(\eta) \frac{\eta!}{(\eta-k)!} = \sum_{\eta=k}^{\infty} P(\eta) \eta(\eta-1) \cdot \dots \cdot (\eta-k+1). \quad (120)$$

Example 2.20 ($d = 1, 2$ and 3) *The classification of set partitions from figure 15 allows us to directly compute the multi-particle moments with degree smaller than 4. To do so, identify each black dot in 15 with a single particle intensity I evaluated at q_i and place averages according to the partitions. For $d = 3$ this means for example³⁸*

$$\begin{array}{ccc}
 I(q_2) & & \\
 & \color{orange}{\triangle} & \\
 I(q_1) & \bullet & I(q_3) \\
 & \color{orange}{\bullet} & \\
 & = \langle I(q_1)I(q_2)I(q_3) \rangle = \mathcal{M}_{|1,2,3}^3 & \color{blue}{\text{rod}} = \langle I(q_1)I(q_2) \rangle \langle I(q_3) \rangle \\
 & & \bullet = \mathcal{M}_{|1,2}^2 \mathcal{M}_3^1
 \end{array}$$

³⁷This means $\mathcal{M}_{\sigma}^{o_p}$ defines the single particle moment whose argument indices correspond to the p -th part of the partition (\mathbf{o}, σ) , that subdivides the argument indices $1, \dots, d$ of the multi-particle moment.

³⁸In order to make these examples as clear as possible we are suppressing the additional arguments ϕ_i or n_i depending on whether equation (60) or (61) is considered.

With this the multi-particle moments take the form

$$\begin{aligned}
\mathcal{M}_N^1 &= \langle N \rangle (\bullet) \\
\mathcal{M}_N^2 &= \langle N \rangle (\bullet \text{---} \bullet) + \langle N(N-1) \rangle (\bullet \quad \bullet) \\
\mathcal{M}_N^3 &= \langle N \rangle \left(\text{triangle} \right) + \langle N(N-1) \rangle \left(\text{diag1} + \text{diag2} + \text{diag3} \right) \\
&\quad + \langle N(N-1)(N-2) \rangle \left(\begin{array}{c} \bullet \\ \bullet \quad \bullet \end{array} \right)
\end{aligned}$$

which using the corresponding single-particle moments results in

$$\mathcal{M}_N^1 = \langle N \rangle_N \mathcal{M}_{|1}^1 = \langle N \rangle I^{\text{SAXS}} \quad (121)$$

$$\mathcal{M}_N^2 = \langle N \rangle_N \mathcal{M}_{|1,2}^2 + \langle N(N-1) \rangle_N \mathcal{M}_{|1}^1 \mathcal{M}_{|2}^1 \quad (122)$$

$$\begin{aligned}
\mathcal{M}_N^3 &= \langle N \rangle_N \mathcal{M}_{|1,2,3}^3 + \langle N(N-1) \rangle_N \left(\mathcal{M}_{|1,2}^2 \mathcal{M}_{|3}^1 + \mathcal{M}_{|1,3}^2 \mathcal{M}_{|2}^1 + \mathcal{M}_{|2,3}^2 \mathcal{M}_{|1}^1 \right) \\
&\quad + \langle N(N-1)(N-2) \rangle_N \mathcal{M}_{|1}^1 \mathcal{M}_{|2}^1 \mathcal{M}_{|3}^1.
\end{aligned} \quad (123)$$

In particular we see, that the degree-1 multi-particle moment is simply the single-particle SAXS intensity I^{SAXS} scaled by the average number of particles.

A direct consequence of observation 2.19 is that knowledge about the first D multi-particle moments together with the first D statistical moments $\langle N^{d \leq D} \rangle$ of the particle number gives access to all single-particle moments of the same degrees. The cause of this is that, by equation (119), \mathcal{M}_N^D in general has the form

$$\mathcal{M}_N^D = \langle N \rangle \mathcal{M}_{|1, \dots, D}^D + V,$$

where the function V only depends on single-particle moments \mathcal{M}^d with $d < D$ and averages of the form $\langle N^d \rangle$ with $d \leq D$. Stated differently this simply means that within *fluctuation X-ray scattering* one is able to use scattering patterns from multi-particle samples to retrieve single particle structural-information, provided one has knowledge about the probability distribution of the number of particles per sample.

In practice knowledge about N is of fundamental importance if one is interested in obtaining structural information that goes beyond pure SAXS analysis, i.e. if one seeks to use multi-particle moments of degrees higher than 1. To illustrate this, let us take a closer look at the degree-2 case. Using the explicit formulas for the single-particle moments given in equations (101) and (104) we find

$$\begin{aligned}
\mathcal{M}_N^2(q_1, q_2, \phi_1, \phi_2) &= \langle N \rangle \sum_{l=0}^L F^l(q_1, q_2, \phi_1 - \phi_2) B_l(q_1, q_2) \\
&\quad + (\langle N^2 \rangle - \langle N \rangle) I^{\text{SAXS}}(q_1) I^{\text{SAXS}}(q_2) \\
&= \sum_{l=0}^L F^l(q_1, q_2, \phi_1 - \phi_2) B_l(q_1, q_2) \begin{cases} \langle N^2 \rangle & l = 0 \\ \langle N \rangle & \text{otw.} \end{cases}, \quad (124)
\end{aligned}$$

where the last equality is due to observation 2.16 which identified $B_0(q_1, q_2)$ as product of SAXS intensities. In the two-dimensional case we can use the equivalence of the FXS moments \mathcal{M}^d and the single-particle invariants given in equations (78) and (80a) to similarly obtain.

$$\begin{aligned} \mathcal{M}_N^2(q_1, q_2, n, n) &= \langle N \rangle \mathcal{M}^2(q_1, q_2, n, n) + \langle N(N-1) \rangle \mathcal{M}^1(q_1, n) \mathcal{M}^1(q_2, n) \\ &= B_n(q_1, q_2) \begin{cases} \langle N^2 \rangle & n = 0 \\ \langle N \rangle & \text{otw.} \end{cases} \end{aligned} \quad (125)$$

The versions of this equation for a fixed number of particles $N = \eta$, such that $\langle N \rangle = \eta$ and $\langle N^2 \rangle = \eta^2$, have been widely studied [19, 95, 100] and, for the three-dimensional case, are already contained in the founding paper of the field [1, equation 11]³⁹.

Let us keep the assumption $N = \eta$ for a moment and continue considering three-dimensional FXS. If one would directly apply the methods described in section 2.5.2 to equation (124) and attempt to extract the invariants $B_l(q_1, q_2)$ one would instead obtain the scaled versions $\eta^2 B_0(q_0, q_1)$ and $\eta B_{l>0}(q_1, q_2)$ of the single-particle invariants. Remember that B_l contains information about the harmonic coefficient of the single-particle intensity $I(q, \theta, \phi)$, that can be retrieved by essentially computing the matrix “square root”

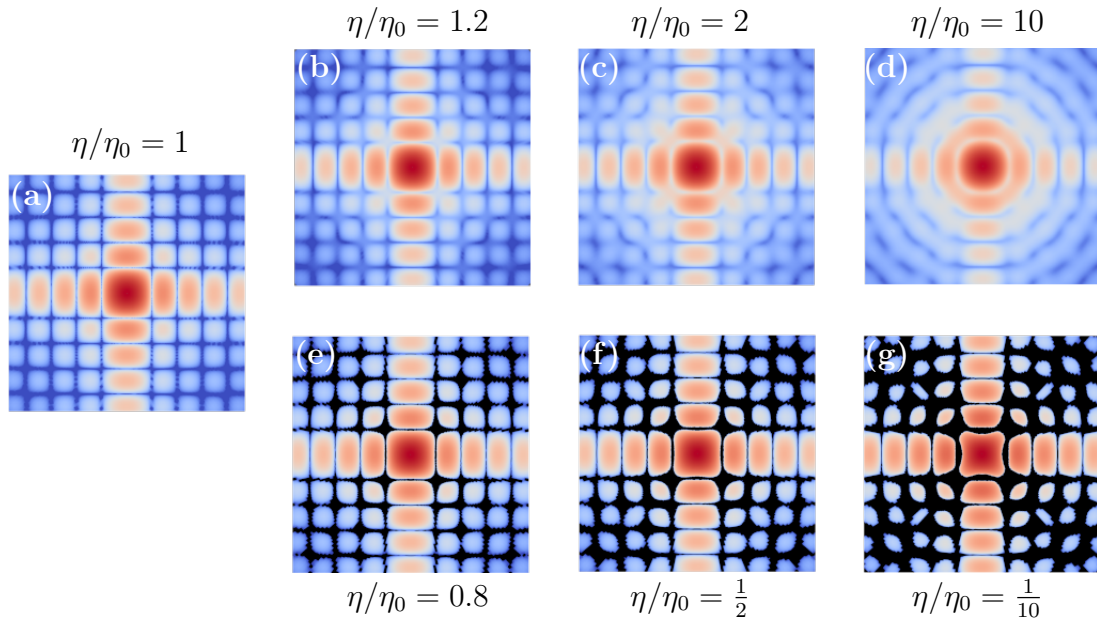


Figure 16: Effect of scaling the I_0^0 coefficients of the simulated noise-free scattered intensity of a solid cube. Consider η_0 to be the estimated number of particles which may differ from the actual number n . (a) depicts the correct single-particle intensity I . (b)-(d) depict I' for an underestimated number of particles, such that η/η_0 takes the values 1.2, 2 and 10. Conversely (e)-(f) depict cases in which the $n_0 > n$ and η/η_0 is given by 0.8, $\frac{1}{2}$ and $\frac{1}{10}$. The black areas in figures (e)-(f) indicate areas with negative values.

³⁹Although with the factor of $n^2 + n$ for $l = 0$ instead of the correct n^2 .

of B_l as described in section 2.3. This means that if the scaled versions of B_l are used, one does not extract information about I but rather about

$$I'(q, \theta, \phi) = \sqrt{\eta} (I(q, \theta, \phi) + (\sqrt{\eta} - 1)I_0^0(q)) \propto I(q, \theta, \phi) + (\sqrt{\eta} - 1)I_0^0(q) \quad (126)$$

whose isotropic part $I_0^0 \propto \sqrt{\eta}I_0^0$ is overemphasized by a factor of $\sqrt{\eta}$ in comparison to its single-particle analogue I_0^0 . This can cause I' to significantly deviate from the correct intensity profile I . An example can be seen in figure 16, which displays the effect of differently scaled isotropic parts I_0^0 on cuts through the simulated scattered intensity of a solid cube.

This problem is further complicated by the fact that there is no known way of estimating the number of particles directly from the moments \mathcal{M}_N^d , despite their dependence on η . One might suspect that the situation does not improve when one considers the number of particles to be a random variable, but in fact this is precisely what happens. Let us write $B_l^N(q_1, q_2)$ for the scaled invariants that can be obtained by directly using the multi-particle moments \mathcal{M}_N^2 , that is

$$B_l^N(q_1, q_2) = B_l(q_1, q_2) \begin{cases} \langle N^2 \rangle & l = 0 \\ \langle N \rangle & \text{otw.} \end{cases} \quad (127)$$

and we find

$$\frac{B_0^N(q_1, q_2)}{\mathcal{M}_N^1(q_1)\mathcal{M}_N^1(q_2)} - 1 = \frac{\langle N^2 \rangle}{\langle N \rangle^2} - 1 = \frac{\text{Var}(N)}{\langle N \rangle^2}. \quad (128)$$

That means, we can compute the normalized variance of the number of particles, whose square root is also known as *coefficient of variation*. Depending on the probability distribution of N , this can allow us to compute all moments $\langle N^d \rangle$, that are necessary to access the single-particle moments.

For example, if one can assume the particles to be uniformly distributed in space, then the Poisson distribution becomes a valid model for N , that is $P(\eta) = \frac{\zeta^\eta e^{-\zeta}}{\eta!}$. In this case the statistical moments of N take the form $\langle N \rangle = \zeta$, $\langle N^2 \rangle = \zeta^2 + \zeta$ and equation (128) reduces to

$$\frac{B_0^N(q_1, q_2)}{\mathcal{M}_N^1(q_1)\mathcal{M}_N^1(q_2)} - 1 = \frac{1}{\zeta}, \quad (129)$$

which allows direct access to the average number of particles ζ and therefore all higher moments of the Poisson distribution. While it remains to be seen if equation (129) can be used to estimate the average number of particles with good enough accuracy to be of practical value, it shows that FXS in principle provides access to the average number of particles.

2.6. Summary

We have started this chapter with a generalized definition of *fluctuation X-ray scattering*, see 2.1, that includes moments of arbitrary degree and allows for a fluctuating number

of particles N . Based on connections to mathematical invariant theory we were able to derive general statements about the information content of the FXS moments in form of observations 2.12 and 2.13, which told us, that moments are sums over rotational invariants and that knowledge about a finite number of these invariants is in principle enough to specify the single-particle intensity up to a global rotation. Subsequently we derived explicit forms for the important invariants of degree smaller than 4 (equations (78), (80) and (83)) and discussed the information content of degree-2 invariants, which are known to specify the single particle intensity up to a set of unitary matrices, see observation 2.17. Building on this fact, we saw how to use degree-2 moments to find the closest single-particle intensity that is compatible with their information content (observation 2.18) which then allowed us to introduce the well known MTIP algorithm for structure determination in section 2.4. In the final subsection we progressively connected the single particle invariants to the FXS moments of increasing complexity. Starting in the single-particle case we derived explicit expression of the moments \mathcal{M}^d for degrees lower than 4. We realized that the second version of the FXS moments, defined in (61), leads to simpler connections to the single-particle invariants, which are given in equations (103), (107) and (111). This fact allowed us to introduce a new approach for the extraction of the single-particle invariants via the linear system given by equation (113). Last but not least, we have derived the general connection between multi-particle and single-particle moments of arbitrary degrees, using the language of set partitions, which resulted in observation 2.19. As consequence of this observation we have found that FXS is sensitive to the coefficient of variation in the number of particles N , which holds the potential of giving access to all statistical moments $\langle N^d \rangle$ via equation (129) and thereby solving the scaling issue described in figure 16.

Contributions: All results based on the second version of the FXS moments, given in equation (61), have been developed as part of this Thesis. This includes the new approach to invariant extraction via equation (113), that has been published in [23]. Section 2.1 can be regarded as a contribution, insofar as the connection to *orbit-recovery* problems and mathematical invariant theory has previously not been known in the Field of *fluctuation X-ray scattering*, nor have the general insights it provided via observations 2.3, 2.12, 2.13 and 2.14. To be clear, the underlying statements about *orbit-recovery* problems belong to the authors of [101], this thesis merely realized their connection to FXS and translated them accordingly. The link between single and multi-particle moments of arbitrary degrees, under consideration of the number of particles as fluctuating random variable, has been introduced as part of this thesis via observation 2.19. This connection was previously only known for a fixed number of particles and degrees smaller than 3. Finally this thesis showed that FXS provides direct access to the coefficient of variation in the number of particles.

3. Single-particle structure reconstruction workflow

With the principles of fluctuation X-ray scattering covered, let us proceed to its practical applications. This section describes the numerical details of a single-particle reconstruction workflow that was created as part of this thesis and published in [23]. There are many interesting aspects that the presented workflow addresses, such as:

- The treatment of missing data.
- A Regularization scheme for the degree-2 invariants, that takes their natural decaying behavior for increasing momentum transfer values.
- Modifications to the MTIP routine that improve its convergence.
- Alignment schemes for both 3D and 2D reconstructions. In the 2D case, they allow for comparison free rotational alignment.

Most of these topics center around the treatment of real imperfect data as well as the numerical stability of the phasing loop itself and are therefore of major importance for practical applications of FXS. As shown in figure 17 one can think of the presented reconstruction workflow can be seen as a four step process consisting of the following parts

1. Computation of the FXS moments of degree-1 and degree-2 from masked diffraction patterns using cross-correlations.
2. The extraction and regularization of the degree-2 invariants.
3. Reconstruction of several candidates for the single-particle density $\rho(\mathbf{r})$ as well as its intensity $I(\mathbf{q})$ via a modified MTIP algorithm.
4. Alignment and subsequent averaging of all computed reconstructions as well as the computation of resolution metrics.

Each of these steps will be addressed individually, starting with the computation of the degree-1 and degree-2 moments.

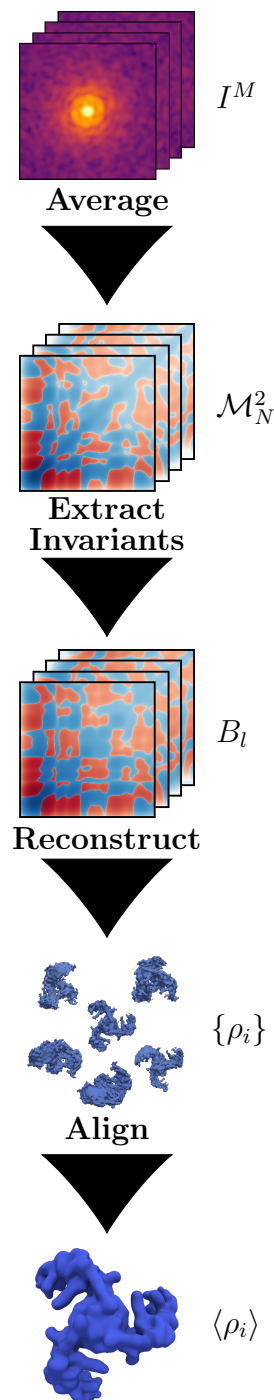


Figure 17: Sketch of the single-particle reconstruction workflow.

3.1. Calculation of FXS moments from masked data (d=1,2)

Figure 18 displays typical experimental scattering patterns $I^M(q, \phi)$ which feature missing data in detector gaps as well as areas of bad detector pixels that have to be masked. This is

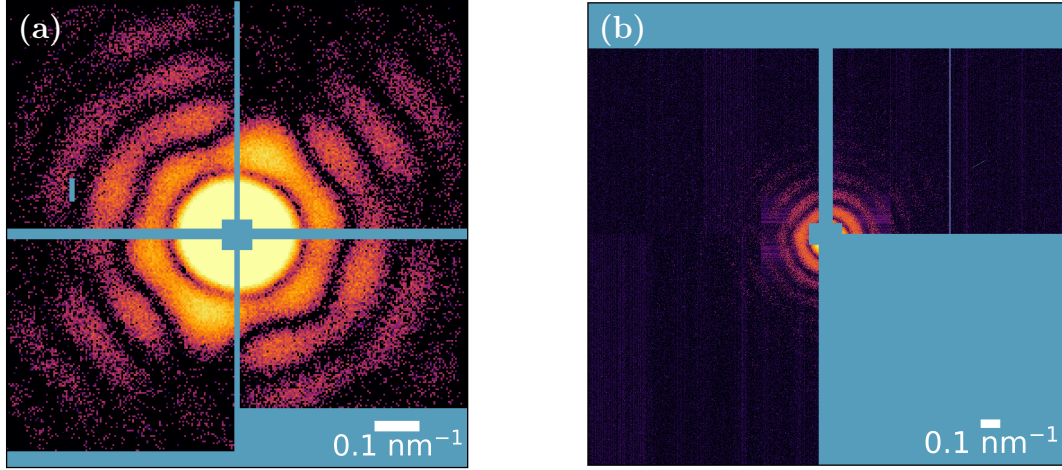


Figure 18: Example single-particle diffraction patterns of the PR772 virus collected during the experiments, (a) amo86615 [111] and (b) amo06516 [112], at the Linac coherent light source (LCLS). Light blue areas correspond to masked detector regions.

less critical for the determination of the SAXS intensity I^{SAXS} , i.e. the degree-1 moments. They can be computed by averaging the discretized scattering patterns $I^M(q_i, \phi_j)$, for any fixed momentum transfer value q_i , over their unmasked angular values followed by a subsequent average over all measured diffraction patterns. Let us write $m^M(q_i, \phi_j)$ for the mask associated with the diffraction pattern $I^M(q_i, \phi_j)$, such that for masked coordinate pairs $m^M(q_i, \phi_j) = 0$, then we may formalize the above as

$$\mathcal{M}_N^1(q_i) = \left\langle \frac{1}{\sum_{j=0}^{N_\phi-1} m^M(q_i, \phi_j)} \sum_{j=0}^{N_\phi-1} I^M(q_i, \phi_j) m^M(q_i, \phi_j) \right\rangle_M, \quad (130)$$

where N_ϕ is the number of angular grid points ϕ_j . The fact that data may be missing or unusable is however challenging in the computation of the degree-2 moments \mathcal{M}_N^2 , since neither of its two definitions in equations (60) and (61) handle masked data. This is exactly where angular cross-correlations become useful. In equation (109) we have seen that the harmonic coefficients of the averaged *angular cross-correlation* correspond to the non-zero values of the degree-2 moments, i.e.

$$\mathcal{M}_N^2(q_1, q_2, n_1, n_2) = \delta_{n_1, n} \delta_{n_2, n} \left\langle C_n(q_1, q_2) \right\rangle_M.$$

Moreover, it is possible to compute cross-correlations for masked data [23, 113][114, supporting information]. Consider a discretization of the arguments (q, ϕ) into a uniform polar grid (q_i, ϕ_j) with S momentum transfer values and N_ϕ angular grid points. In the

following we will use both ϕ_j and Δ_j to denote the angular grid points $\phi_j = \Delta_j = 2\pi j/N_\phi$. It is then possible to compute the angular cross-correlation either directly or in Fourier space. The direct approach is given by the formula

$$C(q_i, q_k, \Delta_j) = \frac{\sum_{t=0}^{N_\phi-1} I^M(q_i, \phi_t) m^M(q_i, \phi_t) I^M(q_k, \phi_t + \Delta_j) m^M(q_k, \phi_t + \Delta_j)}{\sum_{t=0}^{N_\phi-1} m^M(q_i, \phi_t) m^M(q_k, \phi_t + \Delta_j)}, \quad (131)$$

which simply is the angular cross-correlation of the measured intensity, whose masked area is set to zero, divided by the angular cross-correlation of the mask itself. Using the cross-correlation theorem for the discrete Fourier transform \mathcal{F} applied to the angular coordinate yields the second version of this equation

$$C(q_i, q_k, \Delta_j) = \frac{\mathcal{F}^{-1} \left[\mathcal{F} [I^M m^M] (q_i, n) \mathcal{F} [I^M m^M] (q_k, n)^* \right] (q_i, q_k, \Delta_j)}{\mathcal{F}^{-1} \left[\mathcal{F} [m^M] (q_i, n) \mathcal{F} [m^M] (q_k, n)^* \right] (q_i, q_k, \Delta_j)}, \quad (132)$$

where, as usual, \mathcal{F} denotes the Fourier transform and \mathcal{F}^{-1} is its inverse. This second version has an advantage in terms of computational complexity and is the preferred computation method in our implementation. Using *fast Fourier transforms* (FFT) it requires $O(S^2 N_\phi \log(N_\phi))$ operations, which is less than the $O(S^2 N_\phi^2)$ operations needed to determine the angular cross-correlation via equation (131).

Finally, in the three-dimensional case we know from equation (106) that the averaged *angular cross-correlation* has to be an even function in Δ and therefore needs to satisfy

$$\mathcal{C}(q_1, q_2, \Delta) = \frac{1}{2} (\mathcal{C}(q_1, q_2, \Delta) + \mathcal{C}(q_1, q_2, -\Delta)) \quad (133)$$

This allows us to perform an additional average over pairs of angular values $(\Delta, -\Delta)$ in the computation of the final averaged angular cross correlation. This property of the *angular cross-correlation* does not hold in the two-dimensional case. In the two-dimensional case the averaged *angular cross-correlation* does not satisfy this property⁴⁰ and no further processing can be done.

3.2. Degree-2 moments from difference patterns

Another interesting feature of FXS is, that it allows to compute the degree-2 moments $\mathcal{M}^2(q_1, q_2, n, n')$ for $n, n' > 0$, from pairwise differences between diffraction patterns, which significantly reduces the effect of a constant background signal. The following derivation shows that this computation method preserves the FXS moments⁴¹ for all harmonic degrees other than $n = 0$. Let us consider the difference between two intensity patterns $I^M = I^{M;1} - I^{M;2}$. Using the linearity in the definition of the harmonic coefficients

⁴⁰In the 2D case one can use equation (109) to find $\mathcal{C}(q_1, q_2, \Delta) = \sum_{n=-\infty}^{\infty} B_n(q_1, q_2) e^{in\Delta}$, which in general is not even in Δ .

⁴¹Upto the multiplication with a constant factor of 2.

we directly find $I_n^M = I_n^{M;1} - I_n^{M;2}$. Substituting this result into the definition of the FXS moments from equation (61) yields

$$\begin{aligned}
\mathcal{M}_{\text{diff}}^2(q, q', n, n') &= \left\langle \left(I_n^{M;1}(q) - I_n^{M;2}(q) \right) \left(I_{n'}^{M;1}(q') - I_{n'}^{M;2}(q') \right)^* \right\rangle_M \\
&= \left\langle I_n^{M;1}(q) I_{n'}^{M;1}(q')^* \right\rangle_M + \left\langle I_n^{M;2}(q) I_{n'}^{M;2}(q')^* \right\rangle_M \\
&\quad - \left\langle I_n^{M;1}(q) \right\rangle_M \left\langle I_{n'}^{M;2}(q')^* \right\rangle_M - \left\langle I_n^{M;2}(q) \right\rangle_M \left\langle I_{n'}^{M;1}(q')^* \right\rangle_M \\
&= 2\mathcal{M}^2(q, q', n, n') - 2\mathcal{M}^1(q, n)\mathcal{M}^1(q', n')^* \\
&= 2\mathcal{M}^2(q, q', n, n') - 2\delta_{n,0}\delta_{n',0}I^{\text{SAXS}}(q)I^{\text{SAXS}}(q') \tag{134}
\end{aligned}$$

In the second equality we used the linearity of averages and the statistical independence between different diffraction patterns, i.e. different samples, to expand the average. The third equality is a simple application of the definition of the FXS moments and in the final step we used equation (103) which relates the degree-1 moments to the SAXS intensity. The additional factors for $n = n' = 0$ do not play a significant role since they will only affect the extracted single particle invariants $B_n(q, q')$ and $B_l(q, q')$ at $n = l = 0$ and we have already seen in observation 2.16, that B_0 can be independently obtained from the SAXS profiles.⁴² A version of equation (134), formulated in terms of harmonic coefficients of the *angular cross-correlation function* can be found in [22, Supplementary equation S17] and has been developed as part of this thesis.

3.3. Extraction and regularization of rotational invariants

With access to the degree-2 moments $\mathcal{M}^2(q_1, q_2, n, n)$ we may now proceed to compute the scaled degree-2 invariants

$$B_n^N(q_1, q_2) = B_n(q_1, q_2) \begin{cases} \langle N^2 \rangle & n = 0 \\ \langle N \rangle & \text{otw.} \end{cases} \quad B_l^N(q_1, q_2) = B_l(q_1, q_2) \begin{cases} \langle N^2 \rangle & l = 0 \\ \langle N \rangle & \text{otw.} \end{cases}, \tag{135}$$

as described in section 2.5.2. In the three-dimensional case this is achieved by solving the linear system presented in equation (113) via back-substitution, whereas in the two-dimensional case equations (125) can be used to directly identify the invariants with the degree-2 moments, that is $\mathcal{M}^2(q_1, q_2, n, n) = B_n^N(q_1, q_2)$.

The constraint on the averaged cross-correlation from equation (133), together with the definition of the cross-correlation itself, ensure that the extracted degree-2 invariants have the symmetry properties given in observation 2.15. The extraction routine does however not enforce other important properties of the invariants such as their rank, which we know from section 2.3 to be

$$\text{rank}(\mathbf{B}_n^N) = 1 \quad \text{and} \quad \text{rank}(\mathbf{B}_l^N) = \min(S, 2l + 1) = S_l,$$

⁴²That $B_l(q, q')$ will only change for $l = 0$ is directly evident from the triangular shape of the system of linear equation in equation (113).

as well as their positive semi-definiteness, which is a direct consequence of their connection to the harmonic coefficients of the single-particle intensity, given in equation (87). In the regularization step we therefore seek to find the optimal projection matrices $\tilde{\mathbf{v}}_n$ and $\tilde{\mathbf{V}}_l$ such that equation (88) holds ,i.e.

$$\mathbf{B}_n^N = \tilde{\mathbf{v}}_n \tilde{\mathbf{v}}_n^\dagger \qquad \mathbf{B}_l^N = \tilde{\mathbf{V}}_l \tilde{\mathbf{V}}_l^T \qquad (136)$$

and the matrices $\tilde{\mathbf{v}}_n$ and $\tilde{\mathbf{V}}_l$ have the theoretical rank of their corresponding invariants. This decomposition enforces the previous mentioned properties and is a necessary prerequisite for the application of the MTIP phasing routine. As outlined in section 2.3 one approach to their computation, as presented in [19], uses an eigenvalue decomposition of the corresponding invariants $B_n^N(q_1, q_2)$ and $B_l^N(q_1, q_2)$, seen as matrices in their arguments q_1 and q_2 . The columns of $\tilde{\mathbf{v}}_n$ and $\tilde{\mathbf{V}}_l$ are then identified with eigenvectors scaled by the square root of their respective nonzero eigenvalue. We have seen, in section 2.3, that there should be exactly $1 = \text{rank}(\mathbf{B}_n^N)$ nonzero eigenvalue per harmonic degree n in the two dimensional case and $S_l = \text{rank}(\mathbf{B}_l^N)$ nonzero eigenvalues at degree l for the 3D case. When computing eigenvalues of \mathbf{B}_n^N and \mathbf{B}_l^N in the presence of noise, this is unfortunately not the case. Both matrices are then almost guaranteed to have full rank

$$S = \text{rank}(\mathbf{B}_n^N) = \text{rank}(\mathbf{B}_l^N)$$

and one is faced with the problem of selecting the eigenvalue-eigenvector pairs out of which the projection matrices should be formed.

One possible solution to this problem is to choose the highest nonzero eigenvalues, until as many are selected as the theoretical rank of the invariants permit. We shall call this the *direct* regularization approach. Following this procedure can however lead to quite substantial differences between the input invariants and their decomposition in terms of $\tilde{\mathbf{v}}_n$ and $\tilde{\mathbf{V}}_l$, especially at higher momentum-transfer values q_1 and q_2 . Intuitively one may understand the problem by realizing that the eigenvectors multiplied with the largest eigenvalues are connected to the first principal components of the invariant matrices and thus represent their dominant features.⁴³ At the same time we know that the absolute value of the invariants have to decrease fast for increasing momentum transfer values.⁴⁴ Together these two facts imply that the *direct* approach tends to maximize the agreement between the input invariants and $\tilde{\mathbf{v}}_n \tilde{\mathbf{v}}_n^\dagger$ or $\tilde{\mathbf{V}}_l \tilde{\mathbf{V}}_l^T$ at low momentum transfer values, i.e. in regions that contain their largest values, while neglecting higher parameter ranges.

Here we propose an alternative way of computing the projection matrices, which we call the *rescaled* approach. An example of the bad behavior of the *direct* method in comparison to our *rescaled* computation can be seen in Figure 19. As already mentioned in a remark

⁴³Independent from noise or any artifacts, contained in the scattering data, both \mathbf{B}_n^N and \mathbf{B}_l^N have to be self-adjoint by their construction. Their eigenvalue decomposition is therefore connected to their singular-value decomposition by separating the signs of the eigenvalues. The products between eigenvectors and the absolute value of their eigenvalues thus form the principal components.

⁴⁴For example if the considered particle is a sphere, Porods law [28, equation 4.27] tells us that its intensity decays like $\frac{1}{q^4}$ in the limit $q \rightarrow \infty$, correspondingly $B_n(q, q)$ and $B_l(q, q)$ may decay as fast as $\frac{1}{q^8}$.

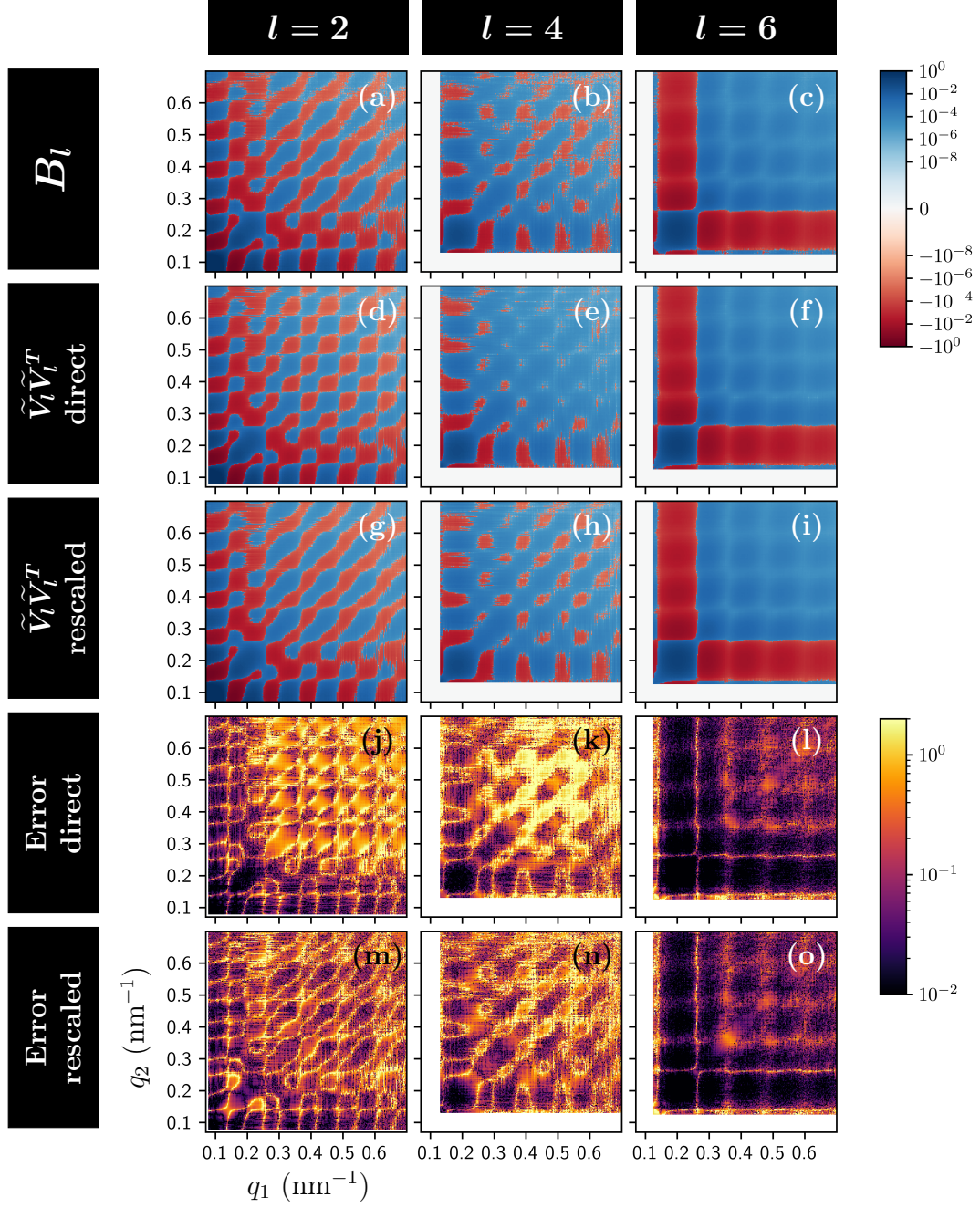


Figure 19: (a)-(c) show extracted B_l coefficients for $l = 2, 4, 6$. (d)-(f) display $\tilde{V}_l \tilde{V}_l^T$ where \tilde{V}_l is computed using the $2l + 1$ highest eigenvalues. (g)-(i) represent $\tilde{V}_l \tilde{V}_l^T$ in which \tilde{V}_l is computed via the proposed rescaling method. (j)-(l) and (m)-(o) display the relative error $\frac{|\tilde{V}_l \tilde{V}_l^T - B_l|}{|B_l|}$ for both versions of \tilde{V}_l , respectively. It can be seen that the direct approach causes $\tilde{V}_l \tilde{V}_l^T$ to differ significantly from B_l for all $q_1, q_2 > 0.2 \text{nm}^{-1}$. The proposed rescaled approach results in error values that are more evenly spread across the argument range and crucially yield a significantly better agreement between the phases (signs) of B_l and its decomposition $\tilde{V}_l \tilde{V}_l^T$. The graphs are computed using the experimental dataset discussed in 5.2.

to observation 2.17 the matrices $\tilde{\mathbf{v}}_n$ and $\tilde{\mathbf{V}}_l$ do not have to be created from eigenvalues of the invariants. In general the problem may be rephrased as finding the matrices $\tilde{\mathbf{v}}_n$ and $\tilde{\mathbf{V}}_l$ that satisfy equation (136) in an “optimal” way, where the chosen optimality condition has to take the natural decay behavior of the invariants into account. We achieve this by rescaling the invariant matrices \mathbf{B}_n and \mathbf{B}_l in an “optimal” way before selecting its highest eigenvalues-eigenvector pairs. In detail the computation routine for the three-dimensional case is as follows.

1. Compute the eigenvalues and eigenvectors of \mathbf{B}_l .
2. Let λ be the highest eigenvalue with the associated eigenvector \mathbf{V}_λ and define $(\mathbf{s}_\sigma)_j = (\sqrt{\lambda} |(\mathbf{V}_\lambda)_i| \star \frac{1}{\sqrt{2\pi}\sigma} e^{-i^2/(2\sigma^2)})_j$. That is \mathbf{s}_σ is given by applying a Gaussian filter with standard deviation σ to the component-wise absolute value of $\sqrt{\lambda}(\mathbf{V}_\lambda)_i$.
3. Scale \mathbf{B}_l by $\mathbf{s}_\sigma \mathbf{s}_\sigma^T$, i.e. consider the component-wise division $\mathbf{B}'_l = \frac{\mathbf{B}_l}{\mathbf{s}_\sigma \mathbf{s}_\sigma^T}$.
4. Create a matrix $\tilde{\mathbf{V}}_l^\sigma$ by choosing the S_l highest eigenvalue-eigenvector pairs of \mathbf{B}'_l that are multiplied with \mathbf{s}_σ component-wise. That is $(\tilde{\mathbf{V}}_l^\sigma)_{i,j} = \sqrt{\lambda'_j} |(\mathbf{V}'_j)_i| (\mathbf{s}_\sigma)_i$, where λ'_j is the j -th highest nonzero eigenvalue of \mathbf{B}'_l with associated eigenvector \mathbf{V}'_j .
5. Consider the one dimensional loss function given by the Frobenius norm

$$\begin{aligned} L(\sigma) &= \|\text{sign}(\mathbf{B}_l) - \text{sign}(\tilde{\mathbf{V}}_l^\sigma \tilde{\mathbf{V}}_l^{\sigma T})\|_F \\ &= \sqrt{\sum_{i,j} (\text{sign}(\mathbf{B}_l) - \text{sign}(\tilde{\mathbf{V}}_l^\sigma \tilde{\mathbf{V}}_l^{\sigma T}))_{i,j}^2}. \end{aligned} \quad (137)$$

Determine the optimal standard deviation σ_{opt} , i.e. the value of σ that minimizes the above loss function and set $\tilde{\mathbf{V}}_l = \tilde{\mathbf{V}}_l^{\sigma_{\text{opt}}}$.

In the two-dimensional case one can proceed in complete analogy by simply exchanging \mathbf{B}_l with \mathbf{B}_n and its corresponding rank condition. In step 3 we use that the highest principal component of \mathbf{B}_l has to capture its decay property. Rescaling by its absolute value should therefore put all remaining features in \mathbf{B}_l on the same absolute scale and hence remove the imbalance between high and low momentum transfer values. The Gaussian filter is necessary to avoid zeros in the absolute value of the highest principal component that occur due to sign changes in \mathbf{B}_l . Finally the loss-function (137) allows one to chose the parameter of the Gaussian filter such that the phase boundaries (signs in the three-dimensional case) are optimally preserved by the resulting decomposition $\tilde{\mathbf{V}}_l \tilde{\mathbf{V}}_l^T$. This is desirable since it is known that the phase boundaries of \mathcal{C}_n or by extension the phase boundaries of $B_l(q_1, q_2)$ contain important structural information [20, 22].

Masking: Another noise related issue in the computation of the projection matrices is, that masking high- q regions in the extracted invariants affects the computed projection matrices $\tilde{\mathbf{v}}_n$ and $\tilde{\mathbf{V}}_l$ in a non-trivial way. Figure 20 shows that including noisy high- q regions in the computation of the projection matrices leads to worse results in the entire q -range. This means, that one has to be careful in the selection of the momentum transfer range that is used for the computation of the projection matrices and it is beneficial to choose this area independently for each considered harmonic order n or l . In the following we describe a procedure that is able to partially compensate the information loss in the projection matrices \mathbf{B}_l with \mathbf{B}_n , that is caused by the application of masks during their computation. Again we shall present the result only in the tree-dimensional case, its two-dimensional version can be obtained in complete analogy.

Consider the ideal noise free case in which $\mathbf{B}_l = \tilde{\mathbf{V}}_l \tilde{\mathbf{V}}_l^T$. Splitting the momentum transfer points into a low- q and a high- q region introduces a splitting of the invariant \mathbf{B}_l via⁴⁵

$$\mathbf{B}_l = \begin{array}{c} \begin{array}{|c|} \hline q_1 \\ \hline \end{array} \begin{array}{|c|c|} \hline & q_2 \\ \hline \end{array} \left[\begin{array}{c|c} \mathbf{B}_l^1 & \mathbf{A}_l \\ \hline \mathbf{A}_l^T & \mathbf{B}_l^2 \end{array} \right], \end{array} \quad (138)$$

as well as a splitting of $\tilde{\mathbf{V}}_l$ in its q -dependent dimension via $\tilde{\mathbf{V}}_l = [\tilde{\mathbf{V}}_l^1, \tilde{\mathbf{V}}_l^2]$, where $\tilde{\mathbf{V}}_l^1$ corresponds to the low- q region of $\tilde{\mathbf{V}}_l$. Using the decomposition property one finds

$$\mathbf{B}_l = \tilde{\mathbf{V}}_l \tilde{\mathbf{V}}_l^T = \begin{bmatrix} \tilde{\mathbf{V}}_l^1 \\ \hline \tilde{\mathbf{V}}_l^2 \end{bmatrix} \left[\begin{array}{c|c} \tilde{\mathbf{V}}_l^{1T} & \tilde{\mathbf{V}}_l^{2T} \end{array} \right] = \begin{bmatrix} \tilde{\mathbf{V}}_l^1 \tilde{\mathbf{V}}_l^{1T} & \tilde{\mathbf{V}}_l^1 \tilde{\mathbf{V}}_l^{2T} \\ \hline \tilde{\mathbf{V}}_l^2 \tilde{\mathbf{V}}_l^{1T} & \tilde{\mathbf{V}}_l^2 \tilde{\mathbf{V}}_l^{2T} \end{bmatrix} \quad (139)$$

Moreover the matrix $\tilde{\mathbf{V}}_l^1$ can always be assumed to have full rank, since they were created from scaled versions of distinct eigenvectors. As long as the number of momentum transfer points in the low- q area is larger than $2l + 1$ one can therefore assume that the matrix $\tilde{\mathbf{V}}_l^1$ has linearly independent columns. This implies that it has a left-inverse, i.e there is a matrix $\tilde{\mathbf{V}}_l^{1^{-1}}$ such that $\tilde{\mathbf{V}}_l^{1^{-1}} \tilde{\mathbf{V}}_l^1 = \mathbf{id}$ is the identity matrix. Combining this with equations (138) and (139) one can see that the decomposition matrix $\tilde{\mathbf{V}}_l^2$ in the high- q area may be reconstructed from the values of \mathbf{B}_l together with the decomposition matrix

⁴⁵Note that in matrix notation the q -values increase starting from the upper left corner downwards in the q_1 -direction and to the right in the q_2 -direction while in image representations of \mathbf{B}_l , see e.g. figure 20, the directions of the axes are swapped and they start in the lower left corner.

$\tilde{\mathbf{V}}_l^1$ in the low- q area, that is

$$\tilde{\mathbf{V}}_l^{1^{-1}} \mathbf{A}_l = \tilde{\mathbf{V}}_l^{1^{-1}} \tilde{\mathbf{V}}_l^1 \tilde{\mathbf{V}}_l^{2^T} = \tilde{\mathbf{V}}_l^{2^T} \quad (140)$$

In the presence of noise this relation can be used to optimally extend a decomposition calculated within a low- q area to higher momentum transfer values. The images labeled by *masked extended* in figure 20 show an example of this method applied to experimental data.

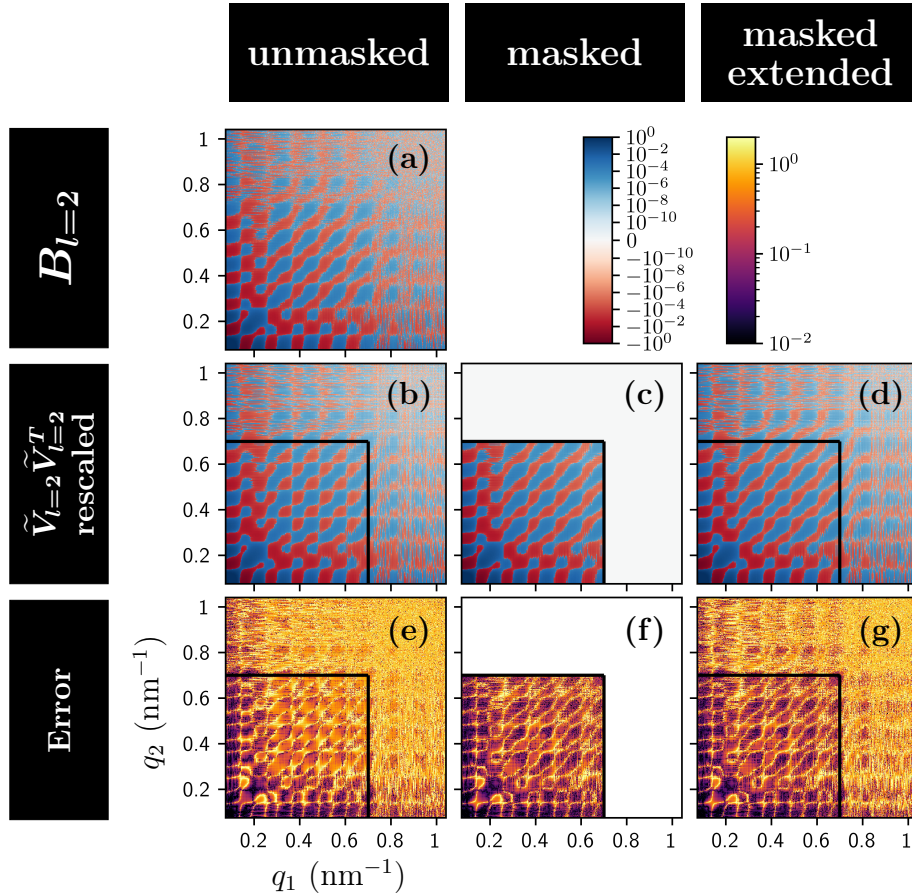


Figure 20: (a) displays the extracted invariants in degree $l = 2$. Images (b) and (c) display the decomposition $\tilde{\mathbf{V}}_l \tilde{\mathbf{V}}_l^T$ computed using the *rescaled* method on the entire dataset and the limited data range with $q \leq 0.7 \text{ nm}^{-1}$ indicated by the black square, respectively. (d) corresponds to the extension of the decomposition given in (c) by the proposed extension algorithm. Finally, (e)-(g) display the relative deviation of the decompositions (b)-(d) from the extracted invariants given in (a), i.e. $\frac{|\tilde{\mathbf{V}}_l \tilde{\mathbf{V}}_l^T - \mathbf{B}_l|}{|\mathbf{B}_l|}$. It can be seen that the unmasked computation results in larger deviations from the input invariants within the low- q area as compared to the masked computation. Additionally it can be seen that the extension process allows to obtain at least comparable, in some areas slightly better, agreement in the high- q area in comparison to the unmasked approach.

3.4. Iterative phasing using MTIP

Knowledge about the decomposition matrices $\tilde{\mathbf{V}}_l$ or $\tilde{\mathbf{v}}_n$ allows us to implement the invariant projection operator P_{inv} (98), which lies at the heart of the MTIP phasing routine described in section 2.4. The next step in our workflow therefore consists of using MTIP to obtain several candidate electron densities for the single-particle structure ρ . In this section we focus on the implementation of the individual subroutines within the phasing loop. The main differences between our implementation and the original approach proposed in [19], lies in the computation of the Fourier transforms and an iterative stabilization routine that reduces the impact of unavoidable numerical inaccuracies in their computation. These modifications will be the topic of sections 3.4.1-3.4.3 and have been published in [23]. Other aspects of the presented phasing routine, such as the used real-space constraints, the employed optimization schemes (ER/HIO) or the phasing error metrics are mostly based on known approaches in conventional X-ray imaging and will be discussed in sections 3.4.4 and 3.4.5.

3.4.1. Fourier transforms

The computation of the Fourier transforms within MTIP constitutes a major numerical challenge that is directly connected to the formulation of the invariant projection P_{inv} in terms of harmonic coefficients. Computations of these harmonic coefficients require access to the current single-particle intensity guess in polar / spherical coordinates. In order to avoid the inaccuracies and performance limitations that would arise from repeated interpolations between Cartesian and polar / spherical coordinates it is desirable to formulate the entire phasing loop, including the Fourier Transforms, in polar / spherical coordinates. The downside of this is, that there is no analog of the Cartesian discrete Fourier transform (DFT)[47], which acts as a unitary transformation, in polar / spherical coordinates. The approach applied here is similar to the one provided by [19], in the sense that both rely on numerical approximations of the Hankel transforms, which connects the harmonic expansion of a function to the harmonic expansion of its Fourier transform. Consider $\rho_n(r)$ and $\rho_m^l(r)$ to be the harmonic expansion coefficients of an electron density in polar and spherical coordinates, and let $\hat{\rho}_n(r)$ and $\hat{\rho}_m^l(r)$ be the expansion coefficients of the respective scattered amplitudes (Fourier transformed densities). The Hankel transform then connects $\rho_n(r)$ and $\hat{\rho}_n(r)$ in the 2D case via

$$\hat{\rho}_n(q) = (-i)^n \int_0^\infty \rho_n(r) J_n(qr) r dr \quad (141a)$$

$$\rho_n(r) = (i)^n \int_0^\infty \hat{\rho}_n(q) J_n(qr) q dq, \quad (141b)$$

where J_n are Bessel functions of the first kind. For spherical harmonics the corresponding connection is given by the three-dimensional Hankel transform

$$\hat{\rho}_m^l(q) = \sqrt{\frac{2}{\pi}} (-i)^l \int_0^\infty \rho_m^l(r) j_l(qr) r^2 dr \quad (142a)$$

$$\rho_m^l(r) = \sqrt{\frac{2}{\pi}} (i)^l \int_0^\infty \hat{\rho}_m^l(q) j_l(qr) q^2 dq, \quad (142b)$$

where j_l are spherical Bessel functions. These integrals are in general difficult to approximate due to the highly oscillatory behavior of the Bessel integral kernels. In the original version of MTIP [19], it was proposed to approximate the continuous Hankel transforms given in (141) and (142) by expanding the harmonic coefficients $\rho_m(r)$ or $\rho_m^l(r)$ (and their reciprocal space counterparts) in some orthogonal basis, thereby shifting the Hankel integral to the chosen expansion functions [see Appendix B]. The idea was, that the Hankel transforms of these known expansion functions can be numerically approximated to high precision and stored as weights. Approximation of the Hankel transform of any function could then be reduced to the approximation of its orthogonal expansion coefficients. In [19] this was accomplished using the cosine/sine series expansions [see Appendix B.2]. As part of this thesis we developed another approximation based on Zernike polynomial expansions, which allowed us to obtain closed-form expressions for the remaining Hankel integrals, and hence eliminate the need of their numerical approximation [see Appendix B.3]. Further investigation however showed, that both approaches converge to direct approximations of the integrals in equations (141) and (142) using simple Riemann sums. Moreover we could show, that any approximation based on orthogonal expansions is less accurate than the corresponding direct approximations of the continuous Hankel transforms, using the numerical method that would be used to estimate the orthogonal expansion coefficients [see Appendix B.1 and B.4]. We therefore employ the midpoint rule as default approximation scheme for the Hankel integrals in our reconstruction workflow [see Appendix B.4]. In the 2D case, the Hankel transform (141) can thus be approximated on a discrete polar grid as

$$\widehat{\rho}_n(q_k) \approx \frac{(-i)^n}{Q_{\max}^2} \sum_{p=0}^{N-1} \rho_n(r_p) w_n(p, k) \quad (143a)$$

$$\rho_n(r_p) \approx \frac{i^n}{R_{\max}^2} \sum_{k=0}^{N-1} \widehat{\rho}_n(q_k) w_n(k, p), \quad (143b)$$

with the quadrature weights $w_n(p, k)$ being defined by

$$w_n(p, k) = \frac{\pi^2(1+2p)}{2} J_n \left[\frac{\pi}{4N}(1+2p)(1+2k) \right]. \quad (143c)$$

In the 3D case, the spherical Hankel transform (142) is approximated by

$$\widehat{\rho}_m^l(q_k) \approx \frac{(-i)^l}{Q_{\max}^3} \sum_{p=0}^{N-1} \rho_m^l(r_p) w_l(p, k), \quad (144a)$$

$$\rho_m^l(r_p) \approx \frac{i^l}{R_{\max}^3} \sum_{k=0}^{N-1} \widehat{\rho}_m^l(q_k) w_l(k, p), \quad (144b)$$

using the quadrature weights

$$w_l(p, k) = \frac{\pi^2 \sqrt{\pi}}{2\sqrt{2}} (1+2p)^2 j_l \left[\frac{\pi}{4N}(1+2p)(1+2k) \right]. \quad (144c)$$

Notice, that the weights in the inverse transforms (143b) and (144b) are determined by transposing the parameters p and k in the weight functions specified for the forward transforms in equations (143c) and (144c), respectively.

For the computation of the polar harmonic expansion coefficients themselves we employ a fast Fourier transform (FFT) over the angular coordinates for each fixed momentum transfer value q_i , that is

$$\rho_n(q_i) = \frac{1}{N_\phi} \text{FFT}[\rho(q_i, \phi_j)] \quad \text{and} \quad \rho(q_i, \phi_j) = N_\phi \text{FFT}^{-1}[\rho_n(q_i)]. \quad (145)$$

In the 3D case we use the Gauss-Legendre quadrature based methods provided by the software package `shtns` [109] to compute the spherical harmonic coefficients.

3.4.2. Discrete polar/spherical grids

Our choice of using the midpoint rule to approximate the Hankel transform implies that the radial sampling used throughout the phasing loop has to be uniform and can be specified as follows

$$r_p = (p + \frac{1}{2})R_{\max}/S \quad q_k = (k + \frac{1}{2})Q_{\max}/S \quad p, k = 0, \dots, S - 1, \quad (146)$$

where R_{\max} and Q_{\max} represent the maximal extend of the real and reciprocal space, respectively, while S denotes the number of considered radial sampling points. In practice Q_{\max} is determined by the maximum momentum transfer value for which diffraction patterns I^M have been recorded or the quality of the extracted degree-2 invariants. For the approximation of polar/spherical Fourier transforms in general we found it beneficial to link R_{\max} to Q_{\max} and the number of sampling points S via an analogue of the reciprocity relation employed in FFTs [47, equation 2.5], i.e.:

$$2R_{\max}2\frac{Q_{\max}}{2\pi} = 2S \Rightarrow R_{\max}Q_{\max} = \pi S, \quad (147)$$

where the division by 2π is due to the convention of representing the momentum transfer values as angular wavenumbers in unit of radians per length scale, e.g. in units of $\frac{2\pi}{\text{nm}}$. Within the phase retrieval routine we however only need to consider a small fraction of the real-space sampling points r_p given in equation (146). The oversampling constraint of iterative phase retrieval (see section 1.3) demands that the maximal radius R_ρ , that is contained in the support of the target electron density, has to be several times smaller than R_{\max} for a given maximal data extend Q_{\max} in reciprocal space. This means that, without loss of numerical precision, we can restrict all computations within the phasing loop to those radial sampling points r_p that are smaller than R_ρ . For example in terms of the Hankel transforms this means that the sums in equations (143a) and (144a) only have to be computed for a small subset of all indices p . In our phasing routine it is therefore possible to specify the maximal particle radius R_ρ .

The angular grids are completely specified by the routines that compute the harmonic decompositions and the maximal considered harmonic degree L for which degree-2 invariants have been computed. In the two-dimensional case the use of FFTs translates into a

uniform angular grid with N_ϕ points given by

$$\phi_j = 2\pi \frac{j}{N_\phi} \quad \text{with } 0 \leq j < N_\phi. \quad (148)$$

In the 3D case the angular grid is given by

$$\phi_j = 2\pi \frac{j}{2L+1} \quad j = 0, \dots, 2L \quad \theta_k = \frac{\pi}{2} x_k \quad k = 0, \dots, L, \quad (149)$$

where x_k are the Gauss-Legendre quadrature notes, i.e. the roots of the Legendre polynomial with degree $L + 1$.

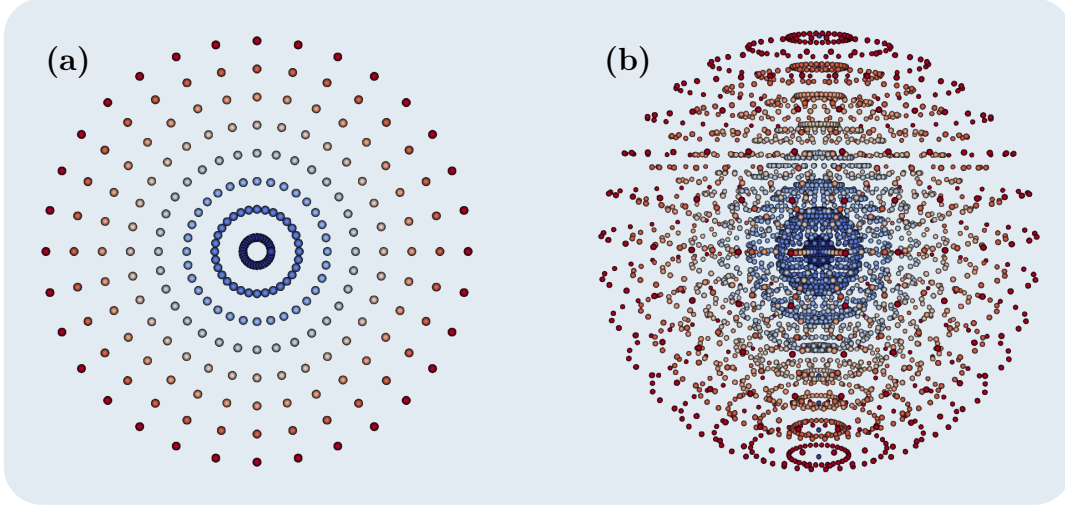


Figure 21: (a) Discrete polar grid, (b) discrete spherical grid, both for $L = 16$ and $N = 8$.

3.4.3. Fourier transform stabilization

One consequence of the approximation schemes for the analytic Fourier transform in polar or spherical coordinates is, that applying the forward and backwards transform in direct sequence is not numerically equivalent to the identity transformation. There are two main sources of error, firstly any features in the input density that correspond to harmonic orders higher than the considered cutoff L are lost and secondly the errors induced by the approximation of the Hankel integral as well as the integrals encountered in the computation of the harmonic coefficients. We empirically found that stabilizing the Fourier transforms in the iterative phasing loop by the following procedure helps to reduce those errors and improves the convergence of reconstructions. Using the notation in Fig. 14 this correction can be expressed by modifying the definition of $\rho' = \mathcal{F}^{-1}\hat{\rho}'$ as

$$\rho' = \mathcal{F}^{-1}\hat{\rho}' + [\rho - \mathcal{F}^{-1}\hat{\rho}]. \quad (150)$$

In the limit of a completely converged MTIP reconstruction, i.e. when $\hat{\rho} = \hat{\rho}'$, meaning that the reciprocal space projections do not change the intensity anymore, this definition ensures that the modified density ρ' coincides with the input density ρ of the current iteration. Without this procedure ρ' and ρ would differ due to the initially described error sources.

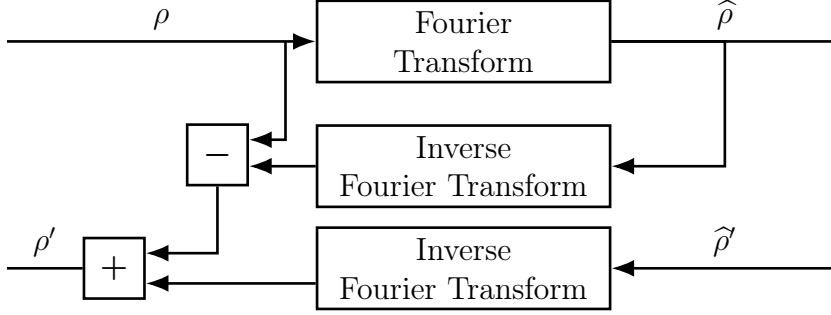


Figure 22: Flow chart of the proposed Fourier transform stabilization procedure.

3.4.4. Generic iterative phase retrieval components

Apart from the Fourier transforms and the reciprocal-space constraint our implementation of the phasing loop follows the common iterative phasing scheme discussed in section 1.3. It incorporates the possibility to iterate between the ER and HIO optimization schemes as well as shrinkwrap steps in which the real space support is updated according to equation (35). Both the feedback parameter β of the HIO routine as well as the Gaussian standard deviation σ of shrinkwrap steps can be chosen to depend on the iteration number during the phasing process. In addition to the support projection P_S it is possible to use the value projection P_V , as defined in equation (33), to enforce that electron-densities are real valued and positive. In our implementation the real-space density projection $P_{\mathcal{X}}$ (see figure 14) is therefore given by

$$P_{\mathcal{X}}[\rho'] = P_V[P_S[\rho']]. \quad (151)$$

Finally each reconstruction is started from a random spherical electron density guess ρ_0 whose support can be optimally chosen to fit the expected size of the reconstruction target. The support of ρ_0 also corresponds to the support used in P_S until it is changed during applications of the shrinkwrap method.

3.4.5. Reconstruction error metric

The evolution of the iterative phasing process can be tracked using several metrics, which may serve as convergence and error estimates. In analogy to error metrics commonly used in conventional X-ray imaging [39, 43] we define the relative normalized errors in reciprocal and real space as [see Fig. 14]

$$E_{\text{reciprocal}} = \frac{\|I(\mathbf{q}) - I'(\mathbf{q})\|_{L^2}}{\|I(\mathbf{q})\|_{L^2}}, \quad (152a)$$

$$E_{\text{real}} = \frac{\|\rho'(\mathbf{r}) - P_{\mathcal{X}}[\rho'](\mathbf{r})\|_{L^2}}{\|\rho'(\mathbf{r})\|_{L^2}}, \quad (152b)$$

where $P_{\mathcal{X}}$ is the density projection defined in equation (151). Since the single-particle scattered intensity I is initially unknown in FXS and reconstructed during the phasing

process, the metrics $E_{\text{reciprocal}}$ and E_{real} can only serve as convergence indicators and do not directly estimate the deviation of the current solution from experimental observables given by the decomposition matrices $\tilde{\mathbf{V}}_l$ or $\tilde{\mathbf{v}}_n$. For this reason we also define metrics for determining the relative difference in the L^2 norm on the level of the invariants as

$$E_n = \frac{\int \int q q' |B_n(q, q') - B_n^I(q, q')|^2 dq dq'}{\int \int q q' |B_n(q, q')|^2 dq dq'}, \quad (153a)$$

$$E_l = \frac{\int \int q^2 (q')^2 |B_l(q, q') - B_l^I(q, q')|^2 dq dq'}{\int \int q^2 (q')^2 |B_l(q, q')|^2 dq dq'}, \quad (153b)$$

where $B_n(q, q') = (\tilde{\mathbf{v}}_n \tilde{\mathbf{v}}_n^\dagger)_{q, q'}$ and $B_l(q, q') = (\tilde{\mathbf{V}}_l \tilde{\mathbf{V}}_l^\dagger)_{q, q'}$ denote the input invariants employed as constraints, while $B_n^I(q, q')$ and $B_l^I(q, q')$ are the invariants directly calculated from the harmonic coefficients $I_n(q)$ and $I_m^l(q)$ corresponding to the current phasing loop iteration [see figure 14].

3.5. Alignment and Averaging

The last step in our reconstruction workflow consists of aligning and averaging the electron density candidates, that have been obtained in the previous step. In conventional iterative phasing this requires the individual reconstructions to be aligned with respect to point inversion and translations, since these properties remain unconstrained during phasing. The same freedoms exist within *fluctuation X-ray scattering* and need to be addressed during averaging. Additionally FXS, by its definition, only allows access to rotation invariant information about the single-particle structure. Consequently, individual MTIP reconstructions, initiated from random density guesses, also vary in their rotation states. This implies that additionally a rotational alignment is required during averaging.

At the same time it is clear that the global rotation states of individual reconstructions do not contain any scientifically interesting information. In particular this means that, without loss of generality, we may try to reconstruct $\mathbf{R}_\alpha \rho$ or $\mathbf{R}_\omega \rho$ instead of ρ , for an arbitrary choice of the rotation α or ω . This free global rotation does not allow us to completely fix the rotation states of possible reconstructions. Instead, it allows us to place an additional constraint on the unknown unitary matrices given in equation (89). To characterize the possible restrictions, we may use the action of rotations on harmonic coefficients given in equations (56)-(57) and apply it to (89), which results in

$$\mathbf{R}_\alpha (\mathbf{I}_n) = \mathbf{I}_n e^{in\alpha} = \tilde{\mathbf{v}}_n u_n e^{in\alpha} \quad (154a)$$

$$\mathbf{R}_{(\alpha, \beta, \gamma)} (\mathbf{I}^l) = \mathbf{I}^l \mathbf{D}^l(\alpha, \beta, \gamma) = \tilde{\mathbf{V}}_l \mathbf{U}_l \mathbf{D}^l(\alpha, \beta, \gamma). \quad (154b)$$

In equation (154b) we interpret $\mathbf{D}^l(\alpha, \beta, \gamma)$ for each l as a $(2l + 1) \times (2l + 1)$ matrix whose coefficients are the Wigner D-matrix elements $D_{n,m}^l(\alpha, \beta, \gamma)$. The free rotations specified by α and (α, β, γ) allow us to change the unknowns by multiplication with a phase factor $e^{in\alpha}$ and a matrix multiplication with $\mathbf{D}^l(\alpha, \beta, \gamma)$ for the two-dimensional and three-dimensional cases, respectively.

In two-dimensional FXS the unknowns u_n , themselves, are phase factors and for a single fixed harmonic order n_0 one can always find a rotation α_0 such that the product $u_{n_0}e^{in_0\alpha_0}$ is equal to any desired complex number of norm 1, e.g. such that $u_{n_0}e^{in_0\alpha_0} = 1$. Stated differently this means, that the global rotation freedom allows us to choose a single harmonic order n_0 and add the restriction $\mathbf{I}_{n_0} = \tilde{\mathbf{v}}_{n_0}$ during the iterative phasing process. As we shall see later in this section, this results in a finite number of possible orientation states for all reconstruction⁴⁶, which enables *a posteriori* algebraic orientation determination on the level of individual 2D reconstructions. Therefore eliminating the need for comparative rotational alignment.

In the three-dimensional case, the restriction posed by equation (154b) is not strong enough to fix any of the unknown matrices \mathbf{U}_i during the reconstruction process and does not allow for orientation determination of single reconstructions. Instead we perform comparative rotational alignment with respect to the reconstruction $\rho_{\text{ref}}(r, \theta, \phi)$ with the lowest phasing error metric. For this comparative alignment we use the Fast Fourier Transform on the special orthogonal group SO(3) (equation (53)), in conjunction with the methods described in [90], to rotationally align all reconstructions with respect to the selected reference. The Fast Fourier Transform on SO(3) enable efficient calculations of the rotational cross-correlation $C(\omega)$ between the reference $\rho_{\text{ref}}(r, \theta, \phi)$ and any other reconstructed density $\rho(r, \theta, \phi)$, which is given by

$$C(\omega) = \int_{r_{\min}}^{r_{\max}} dr \int_0^\pi \sin \theta d\theta \int_0^{2\pi} d\phi \rho_{\text{ref}}(r, \theta, \phi) \mathbf{R}_\omega(\rho(r, \theta, \phi)), \quad (155)$$

where, as described in section 1.7, ω is a rotation in SO(3) and $\mathbf{R}_\omega(\rho(r, \theta, \phi))$ is a rotated version of the reconstructed density $\rho(r, \theta, \phi)$. The cross-correlation $C(\omega)$ is maximal at the rotation $\omega = \omega_{\text{opt}}$ for which the rotated density $\omega_{\text{opt}}(\rho)$ optimally matches the corresponding reference ρ_{ref} . To facilitate structure alignment it is helpful to limit the radial range (r_{\min}, r_{\max}) to regions of the reconstructed densities which are not spherically symmetric.

In order to account for point inversion of a reconstruction with respect to the reference we apply this alignment procedure to each 3D reconstruction ρ , as well as its point-inverse ρ_{inv} , resulting in two aligned candidates, $\bar{\rho}$ and $\bar{\rho}_{\text{inv}}$ per reconstruction. In the 2D case we obtain two aligned candidates $\bar{\rho}$ and $\bar{\rho}_{\text{inv}}$ per reconstruction by simply point inverting the result of the orientation determination step. The general alignment and averaging procedure can then, for both cases, be described as a four step process

1. (position) Shift all reconstructions, such that their respective center of density lies at the origin of the coordinate system.
2. (rotation) Perform rotational alignment, algebraically in 2D and comparatively in 3D.
3. (point inversion) Correct for point inversion.

⁴⁶Intuitively one may see this by realizing that due to the periodicity of $e^{in_0\alpha_0}$, there are always exactly n_0 possible rotation angles α_0 that satisfy $u_{n_0}e^{in_0\alpha_0} = 1$, these angles correspond the remaining free rotation states any reconstruction can attain.

4. Average the aligned densities and compute resolution metrics.

In the point inversion step we determine the relative distance of each of the aligned candidates $\rho_{\text{rot}} \in \{\bar{\rho}, \bar{\rho}_{\text{inv}}\}$ to the reference density ρ_{ref} using the L^2 norm derived from equation 90b,

$$L(\rho_{\text{rot}}, \rho_{\text{ref}}) = \frac{\|\rho_{\text{rot}} - \rho_{\text{ref}}\|_{L^2}}{\|\rho_{\text{ref}}\|_{L^2}}, \quad (156)$$

and select the candidate ρ_{rot} with the lowest distance for subsequent averaging. In the 2D this requires the selection of a reference, which is again done using the phasing error metric. Note, that the selection of a reference at this point is less critical since the only remaining freedom lies in the selection of $\bar{\rho}$ or $\bar{\rho}_{\text{inv}}$, which is less sensitive to structural differences between reconstructions than their rotational alignment.

In the last step the presented algorithm allows to select the reconstructions to be used in the final average based on their error metrics (152) and (153), as well as their distance (156) to the reference structure computed in step 3. Finally a resolution estimate of the average can be computed using a generalized version of the phase retrieval transfer function (PRTF) [20],

$$\text{PRTF}(\mathbf{q}) = \frac{|\langle \mathcal{F}[\rho_i(\mathbf{q})] \rangle_i|}{\langle |\hat{\rho}'_i(\mathbf{q})| \rangle_i}, \quad (157)$$

where $\langle \cdot \rangle_i$ denotes averaging over the selected collection of *aligned* reconstructions, and $\mathcal{F}[\rho_i(\mathbf{q})]$ is the Fourier transform of the i -th aligned electron density [see figure 14]. If we assume that $|\hat{\rho}'_i(\mathbf{q})|$ are identical in all individual reconstructions, as is the case in conventional SPI (where $|\hat{\rho}'_i(\mathbf{q})| = \sqrt{I(\mathbf{q})}$, and $I(\mathbf{q})$ is the experimentally determined intensity), the expression (157) reduces to the conventional PRTF formula [see e.g. [48]].

The remainder of this section focuses on the algebraic orientation determination algorithm that can be used in 2D FXS. Here we are in the fortunate situation that the freedom of choosing a global rotation poses a significant constraint. We have already seen, that via equation (154a) this freedom can be used to add the following constraint during the reconstruction stage.

- Choose a single harmonic order n_0 and demand $\mathbf{I}_{n_0} = \tilde{\mathbf{v}}_n$ during reconstructions.

Equivalently this means that we can use the rotational freedom together with the degree-2 invariants to completely determine the single-particle intensity harmonic coefficient $I_{n_0}(q)$ at order n_0 . This causes the space of possible rotation states of any reconstruction to become finite, since only those rotations remain allowed that leave the now completely known coefficient $I_{n_0}(q)$ unchanged. Consequently, the number of possible values for the remaining unknown phase factors u_n also becomes finite. After completing a particular reconstruction the determined values of u_n can be used to formulate a finite iterative process that successively reduces the remaining rotational freedom until each reconstruction reaches a common global rotation state. This method has the advantage that no choice of a reference structure is needed for rotational alignment and thus avoids potential biases introduced in the selection of such a reference. We shall now describe the iterative process in detail.

After the phase retrieval step the intensities associated with any reconstruction can only differ in their values for the unknown phases factors u_n , which encode their corresponding rotation states. Consequently, the different sets of possible unknowns u_n are connected by the action of rotations given in equation (154a). The constancy of I_{n_0} and hence u_{n_0} then demands

$$u_{n_0} e^{in_0\alpha_j} = u_{n_0} \quad \Rightarrow \quad \alpha_j = j \frac{2\pi}{n_0}, \quad j = 0, \dots, n_0 - 1. \quad (158)$$

Thus, there are n_0 distinct rotation angles α_j that leave u_{n_0} invariant upon the rotation action. Since all of these rotations are integer multiples of φ_1 , they lead to n_0 possible global rotation states attainable by each individual reconstruction. The remaining task is to rotate all individual reconstructions such that they have matching phase factors u_n and hence have the same global rotation state.

Given any other harmonic order $n_1 \neq n_0$, we can apply one of the remaining rotations φ_j that transforms u_{n_1} to some unique value, while leaving u_{n_0} unchanged. For example, we may request $\arg(u_{n_1})$ to take the minimum possible value after wrapping it into the interval $(0, 2\pi)$, that is

$$\arg \min_{\alpha \in \{\alpha_j\}} \left(\text{mod}[\arg(u_{n_1}) + n_1\alpha, 2\pi] \right), \quad (159)$$

and apply any of the rotations α_j that solve the minimization problem (159). In equation (159) “ $\text{mod}(\cdot, 2\pi)$ ” stands for the modulo operation with respect to 2π that is used for phase wrapping.

After aligning the phase for the harmonic order n_1 , only those rotations states α_j remain possible, which leave both u_{n_0} and u_{n_1} invariant under rotation. The invariance condition for order n_1 takes a form similar to equation (158), that is

$$u_{n_1} e^{in_1\alpha_k} = u_{n_1} \quad \Rightarrow \quad \alpha_k = k \frac{2\pi}{n_1}, \quad k = 0, \dots, n_1 - 1. \quad (160)$$

Clearly, only those rotations α_j leave both u_{n_0} and u_{n_1} invariant, which are present in both sets of rotations, $\{\alpha_j\}$ and $\{\alpha_k\}$, defined in equations (158) and (160), correspondingly. The set A of such rotations can be determined as a result of intersection of the two sets of rotations, e.g. $A = \{\alpha_j\} \cap \{\alpha_k\}$. The number of rotations g_1 in the set A is equal to the greatest common divisor of n_1 and n_0 , i.e. $g_1 = \text{gcd}(n_1, n_0)$. These g_1 rotation states can be considered in the following steps to align the remaining harmonic orders. Notice, that if (in the example above) n_1 would be a multiple of n_0 , then $g_1 = n_0$, and there are no rotation states in the set $\{\alpha_j\}$ that may alter u_{n_1} . Hence, all orders n that are multiples of n_0 may be excluded from the alignment procedure.

This allows us to define an algebraic alignment procedure, in which we successively choose harmonic orders n , and use the remaining rotational states to project $\arg(u_n)$ to its lowest possible value. The complete alignment algorithm can be formulated in steps as follows (see an example of its application in Fig. 23 for $n_0 = 12$, $n_1 = 8$, and $n_2 = 6$):

1. (Before reconstruction process) Define a sorted set of harmonic orders $O = \{n_t\}$, with $t \leq t_{\max}$, where t_{\max} is the total number of harmonic coefficients considered in the reconstructions. Set $u_{n_0} = 1$ during the iterative phasing.

2. (After completing the reconstruction) Do the following for each reconstructed electron density $\rho(\mathbf{r})$. In the 0-th alignment iteration ($i = 0$), compose a set A with possible global rotation states $\{\alpha_j\}$, where α_j are defined in equation (158), and set $g_0 = n_0$.
3. Remove all multiples of g_i from the set O . If O is empty (or $g_i = 2$) the alignment is finished, otherwise start the next iteration ($i \rightarrow i + 1$) in the next step.
4. Choose n_i to be the first remaining element of O . Choose one of the rotations α_j from the set A that solves the minimization problem (159) for n_i , and apply this rotation to all harmonic orders n_t present in the current set O , so that the updated phases are determined as $\arg(u_{n_t}) = \text{mod}[\arg(u_{n_t}) + n_t\alpha_j, 2\pi]$. Apply the same rotation to the considered reconstruction $\rho(\mathbf{r})$.
5. Compose a set B with rotation states $\{\alpha_k\}$ determined for the harmonic order n_i according to equation (160).
6. Update the set of remaining free rotations A by intersecting it with the set B , that is $A = A \cap B = \{\alpha_j\} \cap \{\alpha_k\}$. The updated set A contains $g_i = \text{gcd}(n_i, g_{i-1})$ rotation angles. Go to step 3.

Requiring the removal of all multiples of g_i (step 3) removes all orders whose phase factors can not be changed by the remaining rotations in A . Stated differently, this condition ensures that $g_i < g_{i-1}$, which means that the number of free rotations decreases after each alignment iteration. This causes the algorithm to stop after a finite (and typically small) number of iterations.

For robust performance of the algorithm it is important to sort the orders n_t in the set O according to the magnitude of the harmonic coefficients $|I_{n_t}|$ so that the most significant orders correspond to low indices t . To achieve this we ordered the intensity harmonic coefficients in descending order of their L^2 -norms determined as

$$\|I_n\| = \sqrt{\sum_k |I_n(q_k)|^2 q_k} = \sqrt{\sum_k |\tilde{\mathbf{v}}_n(q_k)|^2 q_k}, \quad (161)$$

where $\tilde{\mathbf{v}}_n(q_k)$ are the elements of the matrices $\tilde{\mathbf{v}}_n$ introduced in equation (88). The matrices $\tilde{\mathbf{v}}_n$ for small momentum transfer values q_k tend to be noisy, therefore it might be appropriate to exclude the low- q area from the summation in equation (161).

After completing the alignment process, individual aligned reconstructions are unique up to point inversion. This final ambiguity is resolved comparatively under usage of equation (156) in the same way as for the three-dimensional case.

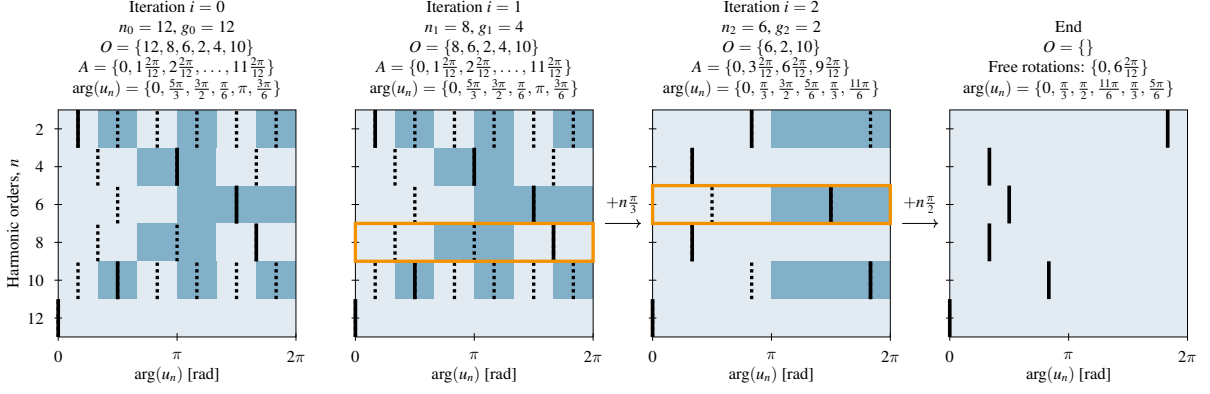
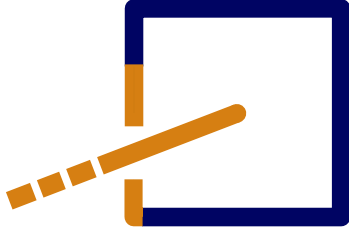


Figure 23: Illustration of the alignment algorithm, where the specified values of parameters correspond to the beginning of each alignment iteration. The values of phases $\arg(u_n)$ (corresponding to the beginning of each alignment iteration) are specified for the respective orders n provided in the original set O at $i = 0$. They are shown in the plots as solid black vertical lines, while the dashed lines signify all other possible values permitted by the set of rotations A in a particular iteration. The orange rectangles highlight the harmonic order whose phase is constrained in a particular iteration. The left most figure displays iteration $i = 0$ directly after the reconstruction, in which we enforced $u_{12} = 1$ for $n_0 = 12$. In iteration $i = 1$ we identified, for harmonic order $n_1 = 8$, the rotation $\frac{\pi}{3}$ in the set A as the one producing the minimal phase of u_8 , that is $\arg(u_8) = \text{mod}[\frac{5}{3}\pi + 8\frac{1}{3}\pi, 2\pi] = \frac{\pi}{3}$. This rotation is then applied to all orders present in the list O for the current iteration. The set A is then reduced according to step 6 of the algorithm, so that the updated set A contains only $g_1 = 4$ rotation angles at the beginning of iteration $i = 2$. We then fix the phase of $n_2 = 6$, and since $g_2 = 2$ the alignment process is completed after rotating the phases of the remaining harmonic orders in O by $\frac{\pi}{2}$. The final phases $\arg(u_n)$ for the aligned reconstruction are displayed in the right most figure.

4.



xFrame

A framework for scientific algorithms targeting X-ray scattering

As part of this thesis the open source software suite *xFrame* with its accompanying *fxs* project have been developed [23]. *xFrame* itself serves as a backbone for the development of scientific algorithms and takes care of common technical details such as multiprocessing, GPU access, data storage, settings management, command line interfaces and more. Specific algorithms can be implemented as projects within *xFrame*. An example of this is the *fxs* project that implements the reconstruction workflow presented in section 3 and is distributed alongside *xFrame*. The source code of *xFrame* is available at github.com/European-XFEL/xFrame and its documentation is hosted on xframe-fxs.readthedocs.io. Further more the software suite is distributed via the python package index PyPi and can be installed in a unix shell via the command:

```
$ pip install 'xframe[fxs]'
```

4.1. Usage of the FXS project

A typical reconstruction pipeline using the command-line interface of *xFrame* can be seen in figure 24. All four workflow steps are accessible via separate commands. Running *xframe fxs correlate* allows to compute the degree-1 and degree-2 moments $\mathcal{M}_N^{1,2}$ from a set of input diffraction patterns, as described in section 3.1. The extraction and regularization of the rotational invariants $B_n(q_1, q_2)$ or $B_l(q_1, q_2)$ (section 3.3) is available via the command *xframe fxs extract*. Reconstructions can be started using *xframe fxs reconstruct* and the final alignment and averaging step is available via *xframe fxs average*. Apart from the command-line interface it is also possible to use the routines provided by *xframe* as well as those part of the *fxs* project directly as Python modules. For further details on the usage of the *fxs* project we want to refer the interested reader to the corresponding documentation at xframe-fxs.readthedocs.io/en/latest/fxs/getting_started/. Among details on the settings files for the different workflow commands, the documentation also includes a simple self-contained workflow tutorial that can be run directly after installing *xframe* without the need for additional input data.

4.2. Dependencies

A list of the dependencies of *xFrame* and their use is provided in table 2. The general strategy is to employ existing software that references to C or Fortran code for as many computational expensive operations as possible. This includes, for example, fast Fourier transforms and the spherical harmonic decompositions. In all other cases we rely on *numpy* vectorization and GPU acceleration.

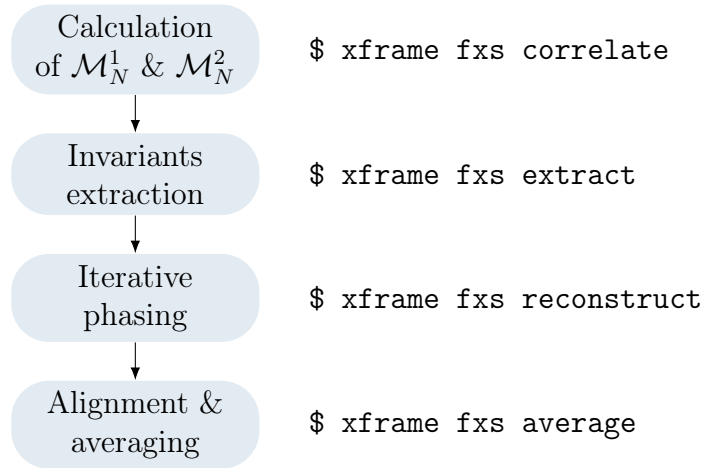


Figure 24: Schematic representation of the reconstruction workflow (left) associated command line tools (right). Each command line tool takes the filename of a human readable settings file as input parameter.

Package	Usage	Package	Usage
numpy [115]	All parts of <i>xFrame</i>	openCV [116]	2D plots
scipy [117]	Invariants extraction	vtk [118]	3D plots
pyOpenCL	GPU access	h5py [119]	Data storage
shtns [109]	Spherical harmonic transforms	ruamel.yaml	Software settings
pysofft (SOFT) [90]	3D alignment of reconstructions	click	Command line interface
matplotlib [120]	2D plots	psutil	Hardware info

Table 2: List of dependencies of *xFrame*.

4.3. Multiprocessing scheme

xFrame is designed to enable the use of multiple GPUs alongside CPU multi-processing. In its current state *xFrame* implements multiprocessing using the python *multiprocessing* module, while access to graphics cards is realized via *OpenCL* in order to be independent on graphics card manufacturers and to allow the software to be executable on as many platforms as possible.

A good example of combining both CPU and GPU processing is given by the reconstruction routine that can be started via *xframe fxs reconstruct*. Here several phasing loops are executed in parallel, if multiple CPU cores are available. At the same time GPU acceleration can be used to speed up the computation of the Fourier transforms within each individual phasing loop. A graphical representation of this multiprocessing scheme is given in figure 25. Notably access to the GPUs is controlled by separate CPU processes called *GPU workers*, this allows to decrease the overall GPU memory requirements and

enables performant phase retrieval on larger grid sizes and harmonic order limits.⁴⁷ A possible downside of the combined use of CPU and GPU parallelization is that calls to a single graphics card have to occur sequentially, which slightly breaks the independence between the different CPU processes. In our example this can cause the phasing workers to compete for GPU time. Since, however, the individual GPU workloads are quite small compared to the rest of the phasing loop, we found this effect to be negligible. A detailed runtime analysis of the phasing routine will be shown in section 5.1.

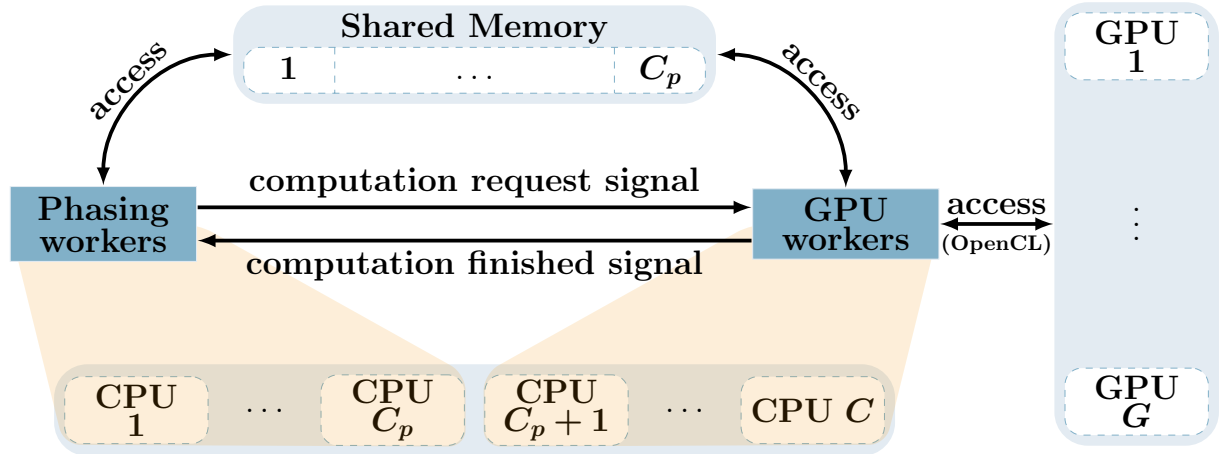


Figure 25: During iterative phasing step the available CPU cores are divided into phasing and GPU workers. Each phasing worker is running an individual reconstruction, while a smaller number of GPU workers are accepting requests from the phasing workers to perform parts of the MTIP loop (Hankel transforms) on the available GPUs. The phasing and GPU workers communicate via simple Boolean signals, while the data transfer is handled indirectly via shared memory.

4.4. Input/Output data formats

Within *xframe* the HDF5 format is used for general purpose data storage, e.g. to save calculated metrics and reconstruction results. Settings of projects, like the presented *fxs* workflow, are handled via human readable YAML files. Finally, VTK files and PNG images target visualization of reconstruction results. Specifically, the open-source VTK file format allows to examine the reconstructed densities on their native spherical or polar coordinate grid without any further post-processing. All reconstructions displayed in section 5 were generated using the VTK viewer [ParaView](#).

⁴⁷The concrete problem that is solved by the GPU workers is, that GPU memory, i.e. openCL contexts, can not be shared across several python processes (CPU workers). If a GPU computation requires some constant input data, e.g. the Hankel weights w_n and w_l from equations (143c) and (144c), this data needs to be stored in GPU memory separately for each CPU process that directly request the GPU computation.

5. xFrame applications

This chapter is dedicated to explore the capabilities and limitations of the presented reconstruction workflow. Initially we will consider simulated noise free datasets to test invariant based reconstructions under optimal conditions. Within this setting we will also test the dependence of reconstructions on important FXS specific variables, such as the harmonic degree cutoff L and the scaling introduced by considering multi-particle scattering (i.e. $N > 1$). In the second part of this chapter we will investigate two experimental single-particle diffraction datasets [111, 112] for the bacteriophage PR772, that have been measured at an XFEL. The first of these datasets has been studied in several publications, using SPI [9, 121] and MTIP based reconstructions [20]. We will be able to replicate the results obtained in [20] and expand on them by identifying deviations of the virus structure from its ideal icosahedral symmetry. The second dataset has not been explored in imaging so far. We shall see that, while the overall data quality is worse, this second dataset also clearly shows deviations from the icosahedral symmetry. The reconstruction results on simulated datasets have been reported in [23], while a publication of the presented reconstructions for the PR772 virus is currently in preparation [122].

5.1. Reconstructions from simulated data

We considered three different model structures, see figure 26, in the test of our workflow. Two of these models are protein structures given by the PDB entries *3j2t* [37] and *6b3r* [91], while the remaining structure is an artificial particle consisting of six spheres.

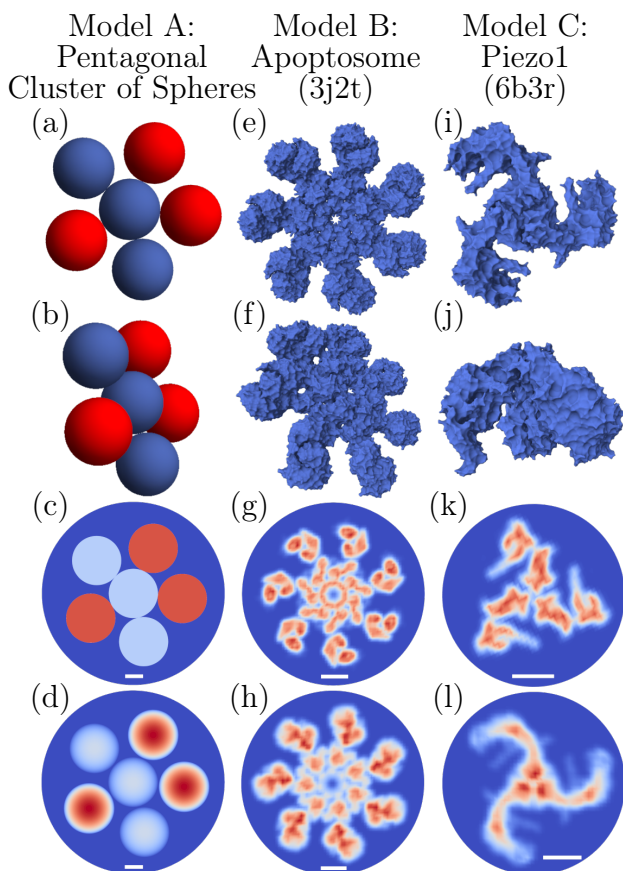


Figure 26: Three considered model structures (model A - model C): (a)-(d) a pentagonal cluster consisting of spheres of uniform density with a diameter of 14 nm, where the red spheres are of doubled density compared to the blue spheres; (e)-(h) the human apoptosome complex [PDB entry *3j2t* [37]]; (i)-(l) the mechanosensitive ion channel Piezo1 [PDB entry *6b3r* [91]]. The two upper rows show different views of the 3D structures. Two-dimensional slices through their centers are given in the third row, while the bottom row displays their 2D projections on to the image plane. The projections were computed using the electron density maps generated in UCSF Chimera [123] for the corresponding 3D models. The white scale bars shown in the two bottom rows correspond to 5 nm.

For each of these models two diffraction datasets were simulated, using rotation states in accordance with the 2D and 3D definitions of FXS (see figure 12). Each dataset consists of 10^5 noise-free single-particle diffraction patterns that were generated under the assumption of ideal Thomson scattering (equation (10)), examples of which can be found in figure 27.

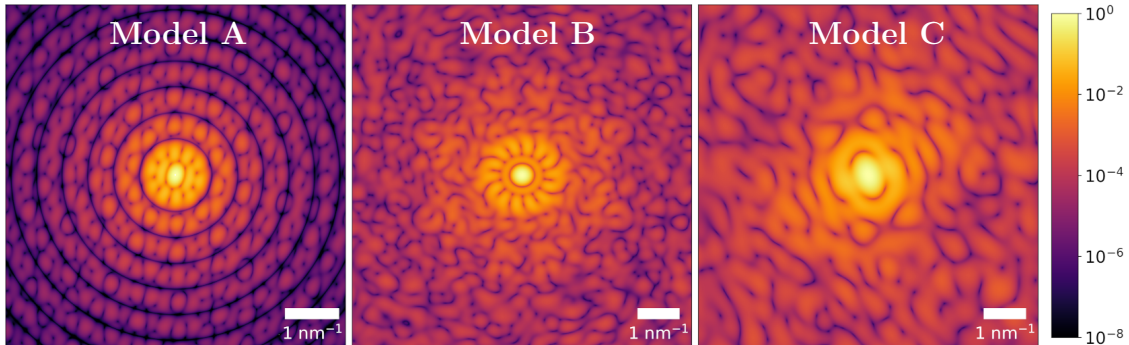


Figure 27: (Log scale, arb. units) Representative diffraction patterns for the different models. Diffraction patterns for model A were computed up to a maximum momentum transfer $Q_{\max} = 3.2 \text{ nm}^{-1}$, whereas for models B and C the diffraction patterns were limited to $Q_{\max} = 4.2 \text{ nm}^{-1}$.

Each set of diffraction patterns was then processed according to the workflow described in chapter 3. Examples of the extracted FXS moments and the corresponding single particle invariants $B_n(q_1, q_2)$ and $B_l(q_1, q_2)$ can be seen in figure 28. Following the extraction and regularization of the degree-2 invariants we performed iterative phase retrieval using the command `xframe fxs reconstruct`. This command allows one to perform phasing loops composed of custom sequences of ER, HIO and shrinkwrap (SW) steps, based on our MTIP modification (see section 3.4). The settings were chosen such that the complete iterative phasing process was divided into a main and a refinement stage. The purpose of the latter is to refine the electron density with the lowest error metric obtained during the main stage. For 3D reconstructions the main stage was assembled out of blocks consisting of $60 \times$ HIO steps, followed by a shrinkwrap application and $40 \times$ ER steps. The number of blocks in the main stage varied from 5 in the case of model A to 30 for model B and model C. All models shared the same refinement stage, which consisted of a shrinkwrap application followed by $200 \times$ ER steps. For reconstructions using the 2D FXS datasets the main stage consisted of 10 blocks of $500 \times$ HIO steps followed by a shrinkwrap application and $200 \times$ ER iterations, while the refinement part consisted of a shrinkwrap step followed by $200 \times$ ER iterations. The HIO parameter β [equation (34)] was determined in the i -th iteration as $\beta(i) = ae^{bi} + c$, with parameters a , b and c chosen such that $\beta(i)$ decreased exponentially during the reconstruction process from 0.5 down to 0.14 for the 3D reconstructions, and from 0.1 down to 0.01 for 2D reconstructions. The SW threshold value γ [equation (35)] was set to 0.11, and the standard deviation σ was linearly decreasing from 2 nm to 1.5 nm during the reconstruction for all models. The density value projection [equation (33)] was parameterized as, $V_{\text{Re}}^{\min} = 0$, $V_{\text{Re}}^{\max} = \infty$, $V_{\text{Im}}^{\min} = -2$ and $V_{\text{Im}}^{\max} = 2$. We empirically found that allowing small non-zero values of V_{Im}^{\min} and V_{Im}^{\max}

results in improved convergence rates of reconstructions. The Fourier transform stabilization has been applied as described in Section 3.4.3. All 3D reconstructions were obtained considering a spherical harmonic cutoff degree of $L = 127$, while the 2D reconstructions employed circular harmonic orders up to $L = 255$. The invariant projection P_{inv} [equation (98)] used degree-2 invariants upto the same maximal degree, while setting all odd order invariants to 0. The considered number of radial steps was $N = 256$ for all models, and the angular sampling was chosen such that the maximal harmonic order could be resolved (see section 3.4.2). To follow the reconstruction progress we used the error metric E_{real} defined in equation (152b). Individual reconstructions were classified as *converged* or *not converged* based on the histograms of the final values of the error metric E_{real} (see Fig. 29 and Table 3). Notice the different convergence rates for different structures in Table 3.

Model	Reconstructions performed	Reconstructions converged (% of total)
3D Model A	113	110 (97)
3D Model B	168	111 (66)
3D Model C	340	116 (34)
2D Model A	120	120 (100)
2D Model B	120	113 (94)
2D Model C	120	103 (86)

Table 3: Reconstruction statistics using *xFrame*

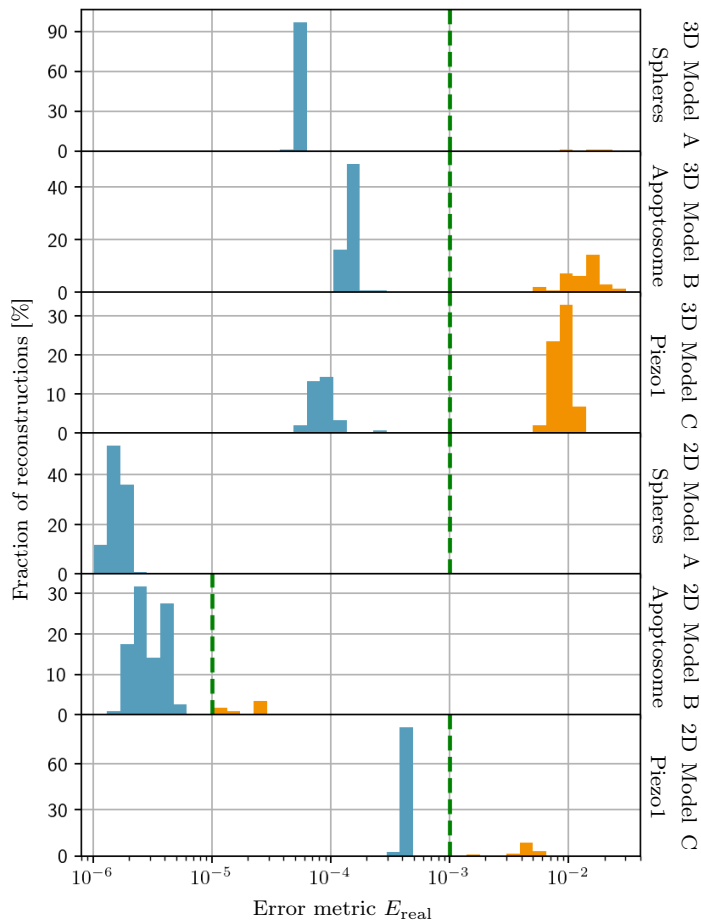


Figure 29: Normalized histograms of the final error metric values E_{real} [equation (152b)] shown for all individual reconstructions listed in Table 3. A clustering of reconstructions into two groups can be observed for most of the models. These groups are separated by at least half an order of magnitude in their final error value and allow us to identify converged reconstructions by introducing a threshold. The thresholds for each model are represented by the dashed green lines, placed at 10^{-5} for the 2D Model B, and at 10^{-3} for all other models. Light-blue and orange parts of the histogram signify converged and not converged reconstructions, respectively. For the 2D Model A all computed reconstructions have approximately similar values of E_{real} and were all identified as converged. The 3D model A has a total of 3 reconstructions with error values around 10^{-2} that did not converge.

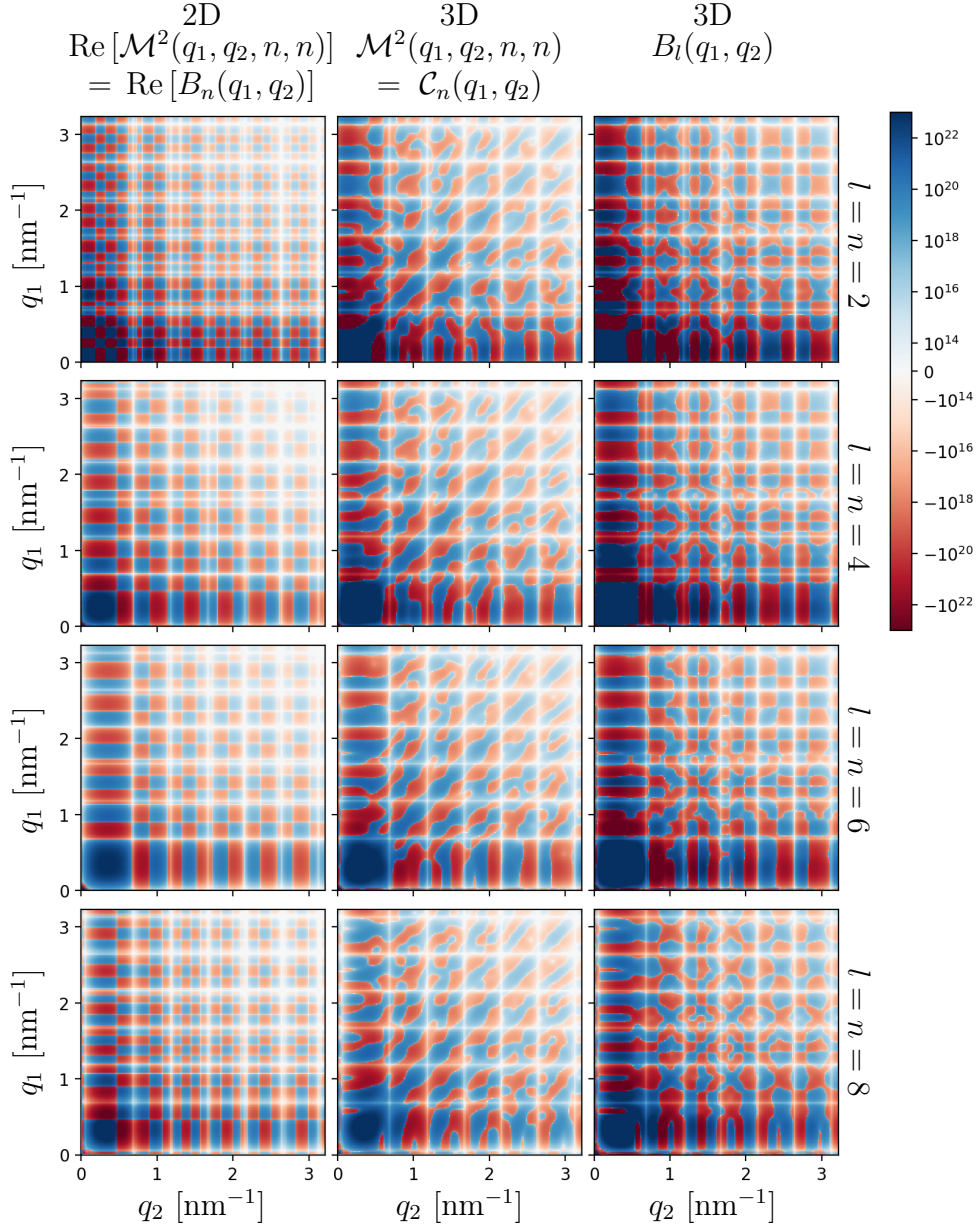


Figure 28: (Log scale, arb.units) Values of the rotational invariants $B_n(q_1, q_2)$ and $B_l(q_1, q_2)$ as well as the FXS *moments* \mathcal{M}^2 of orders $n, l = 2, 4, 6$ and 8 , determined for model A in the 2D case (left) and in the 3D case (middle, right). In the 2D case, the real part of the complex valued invariants $B_n(q_1, q_2)$ is shown, while the 3D moments and invariants are themselves real valued [see observation 2.15]. The connection between the moments, displayed in the middle column, and the invariants in the right column is given by equation (108). Notice, that the 2D invariants $B_n(q_1, q_2)$ only contain features in the form of vertical and horizontal stripes. This is no coincidence, but rather a direct consequence of \mathbf{B}_n being a rank 1 matrix in the form of equation (88). The 3D invariants $B_l(q_1, q_2)$ display more complex features since the respective matrices \mathbf{B}_l are of higher rank for $l > 0$, i.e. $\text{rank}(\mathbf{B}_l) = \min(S, 2l + 1)$ [see Section 2.3].

In the final workflow step, the command *xframe fxs average* was used to align and average a set of 100 converged reconstructions for each considered model. The resulting averaged reconstruction can be seen in figure 30. All 2D reconstructions were aligned using the algebraic method described at the end of section 3.5.

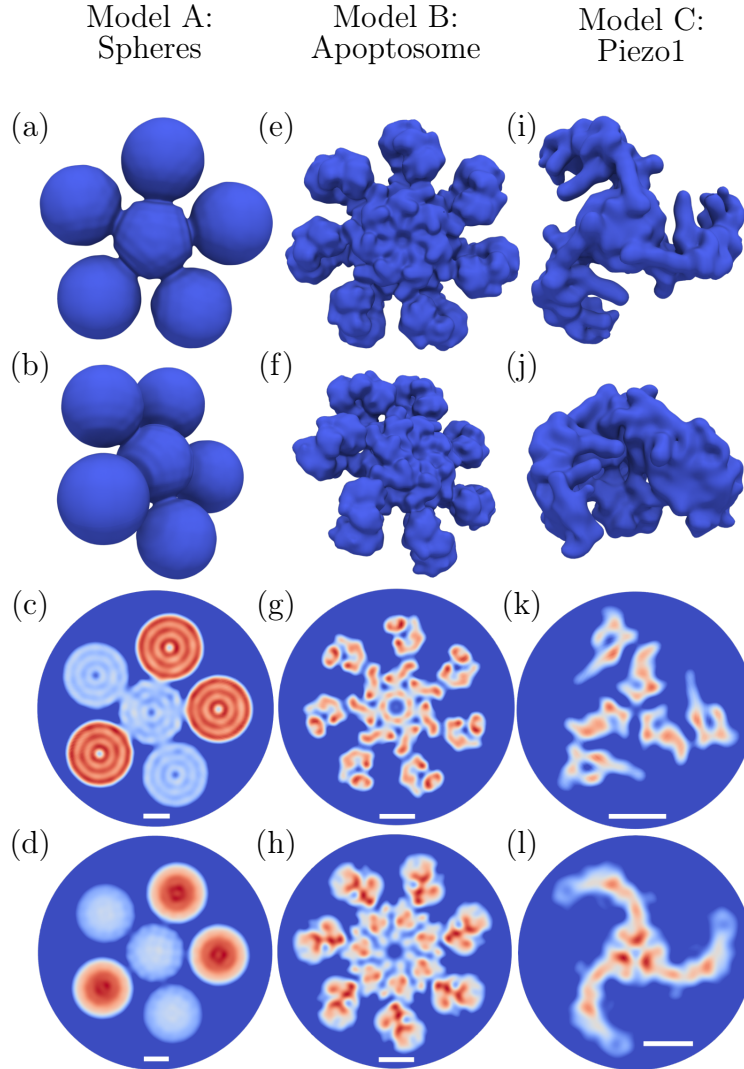


Figure 30: Averaged 2D and 3D reconstructions for the models shown in figure 26, using the same figure layout. The two upper rows contain different views of the reconstructed 3D structures, while the third row contains slices through their density distributions. Averaged 2D reconstructions are shown in the bottom row and correspond to the projections displayed in the bottom row of figure 26. All isosurfaces are taken at 15% of the maximal value of the reconstructed electron density and the two bottom rows display density values higher than this threshold. The 2D slices in (c), (g) and (k) are taken at approximately the same regions of the electron density as given for the model structures in (c), (g) and (k) of figure 26, respectively. The visible white scale bars correspond to 5 nm. (c) and (d) contain ring like density fluctuations, which are manifestations of the Gibbs phenomenon. All visible averages are displayed on their native spherical or polar grid, used during phasing.

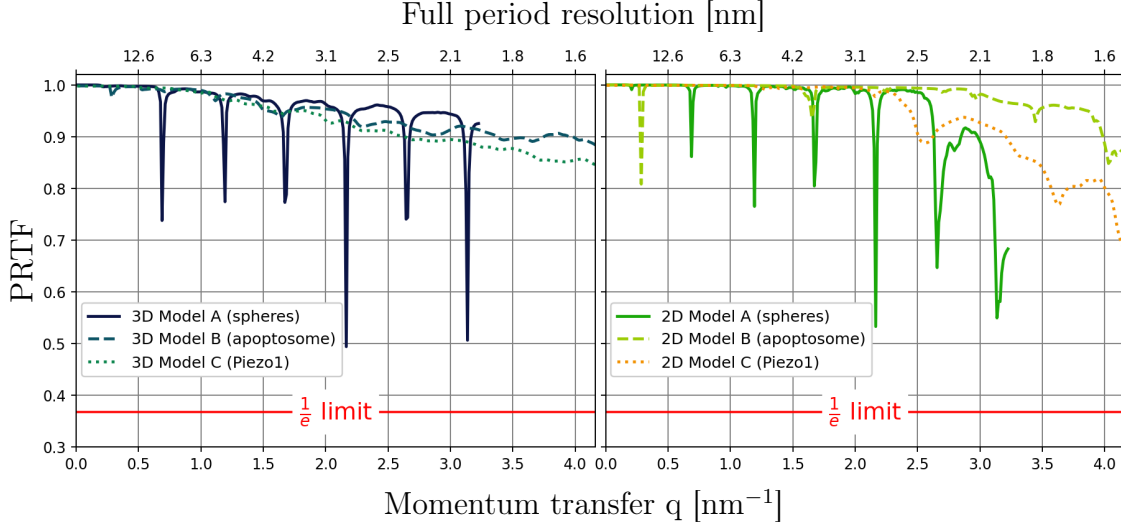


Figure 31: PRTF curves, computed according to equation (157), for the averaged 3D (left) and 2D (right) reconstructions shown in figure 30. The red lines represent the cutoff value $1/e$, used to estimate the reconstruction resolution.

The corresponding PRTF resolution metrics [equation (157)] are shown in figure 31. It can be seen that none of the resolution metrics come close to the standard cutoff value of $1/e$ [20], therefore indicating that the obtained resolution is Fourier limited for all obtained reconstructions, i.e. limited by the extend of the simulated diffraction patterns in reciprocal space. With this we could show that, under ideal conditions, invariant based phase retrieval allows to access the maximal amount of structural information contained in the used diffraction patterns. At least for the investigated models this implies that FXS is equivalent to SPI in terms of the obtainable structural information.

The remainder of this chapter will be divided into three parts investigating different aspects of the reconstruction pipeline. Initially, we will discuss multi-particle reconstructions. This will be followed by an investigation of the impact that different harmonic order cutoffs L have on the obtained averaged reconstructions, as well as a review about the computational performance of the implemented phasing routine itself.

5.1.1. Multi-particle reconstruction

Above, we have considered the ideal case, whose practical application would demand X-ray scattering measurements of individual particles ($N = 1$). In practice, this might be challenging to archive for weakly scattering bio-particles. We have seen in section 2.5.3 that FXS is not limited to these conditions and opens the possibility to perform single-particle reconstructions based on multi-particle X-ray scattering measurements, whose total scattering signal increases approximately linear with the number of particles N . The practical viability of such reconstructions has been shown in [21]. Within this section we will verify that our reconstruction workflow is able to perform single-particle reconstructions from multi-particle scattering patterns. Our discussion will start under

idealized conditions, in the form of noise-free diffraction patterns obtained from exactly 10 particles per sample ($N = 10$), that scatter according to the dilute limit assumption (63). After this, we will turn our attention to the fact that the number of particles affects the extractable invariants differently depending on their harmonic degree, see equations (124)-(125). In figure 16 we have seen the change in the effective single-particle intensity if this scaling is estimated incorrectly. As part of this section we will explore this effect on the level of averaged reconstructions.

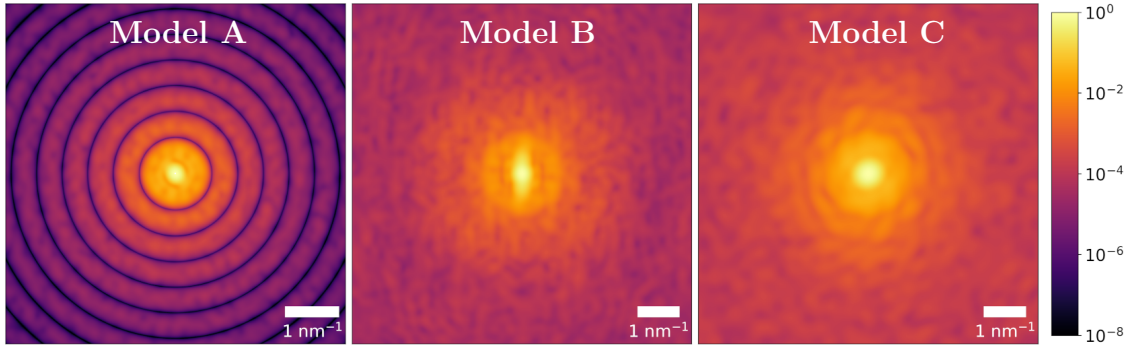


Figure 32: (Log scale, arb. units) Examples of the simulated 10-particle diffraction patterns for the three considered model structures. According to the dilute-limit assumption, given in definition 2.1, each of the shown patterns is the incoherent sum over 10 single-particle diffraction patterns, see (63).

We have simulated a total of 10^5 multi-particle diffraction patterns per model structure shown in figure 26, i.e. the same number of patterns as considered for the single-particle reconstructions. Examples of these simulated multi-particle diffraction patterns can be seen in figure 32. These diffraction patterns were then processed using the same workflow steps and parameters as described above for the single-particle reconstructions, with the exception of an additional scaling that is applied during the iterative phasing process. The decomposition matrices $\tilde{\mathbf{v}}_n$ and $\tilde{\mathbf{V}}_l$, that are used in the invariant projection P_{inv} during phasing, were multiplied by $1/\sqrt{N} = 1/\sqrt{10}$ for $n = l = 0$, to correct for the relative scaling introduced by the multi-particle diffraction patterns, see equations (124) and (125). The resulting averaged reconstructions can be found in figure 33 and are almost identical to their single-particle counterparts from figure 30. That the obtained reconstructions are of comparable quality, to those obtained in the single-particle case, is further indicated by their associated PRTF resolution metrics, presented in figure 34. All PRTF curves are close to their single-particle analogs, given in figure 31, and show that the resolution of the reconstructed densities are Fourier limited. In conclusion, we could show that our reconstruction workflow allows to compute single-particle reconstructions from multi-particle scattering data without loss of resolution compared to the single-particle case, if one has knowledge about the number of particles per sample.

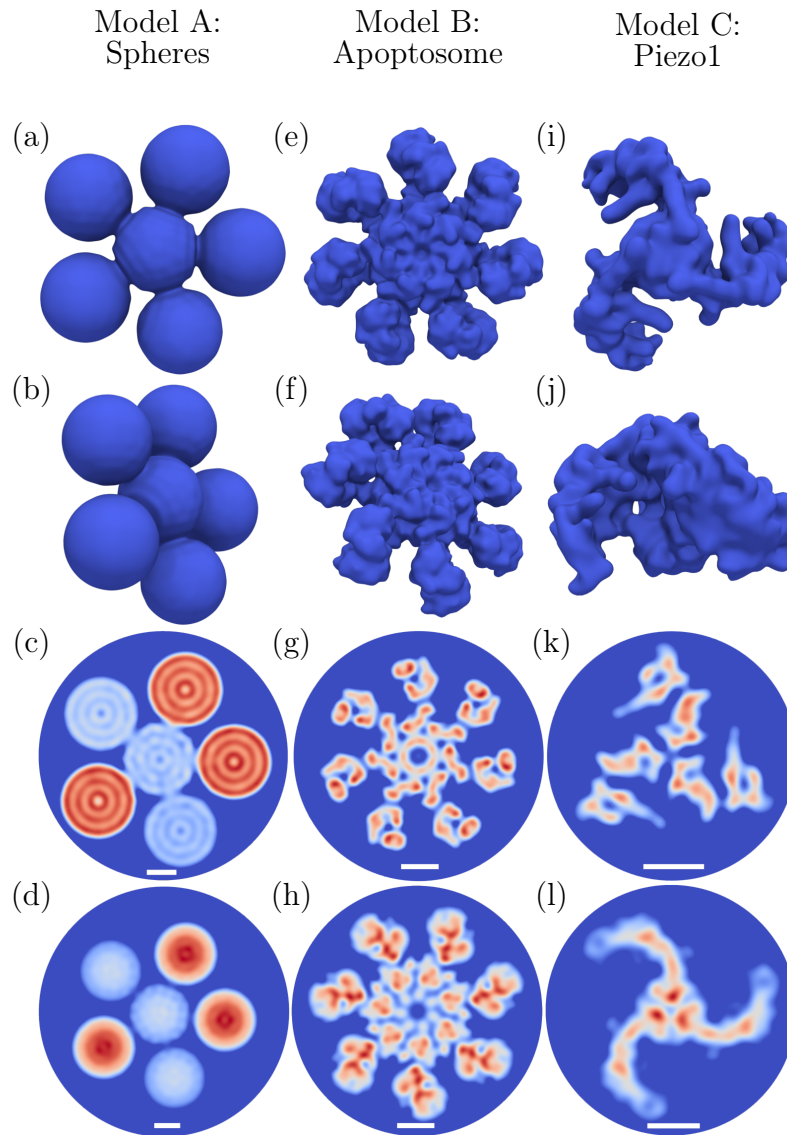


Figure 33: Averaged reconstructions using the 10-particle scattering datasets for all considered models. Similar to figures 26 and 30, the two upper rows display an isosurface of the 3D density profile, while the third consists of slices through these density profile and the last row corresponds to the averaged 2D reconstructions. The visible white scale bars again represent 5 nm.

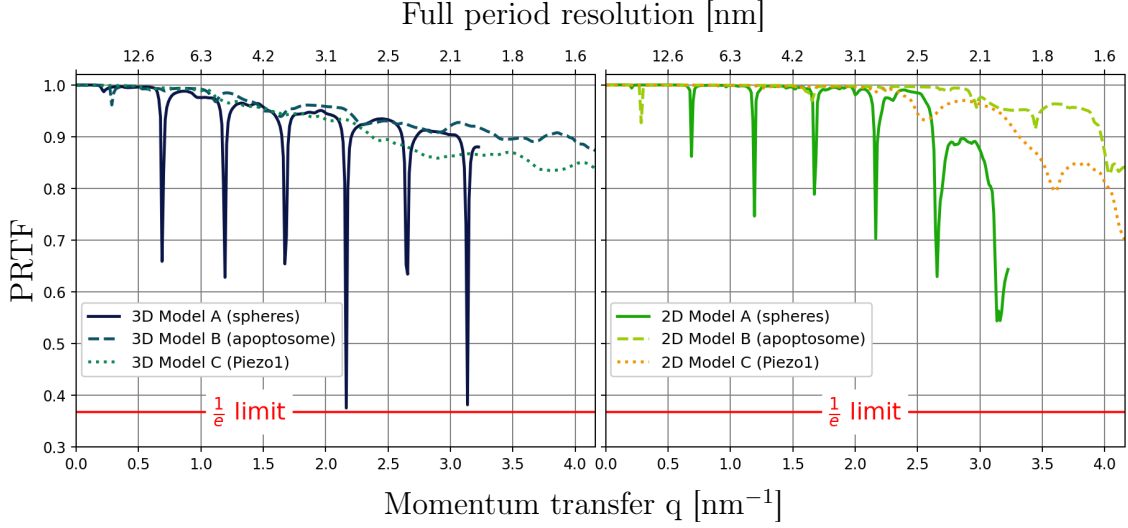


Figure 34: PRTF curves obtained for the averaged reconstructions produced from 10-particle diffraction data shown in figure 33. Similar to the single-particle case, the above PRTF curves indicate that the resolution of the obtained reconstructions is Fourier limited.

To test the sensitivity of reconstructions on errors in the assumed number of particles we performed a series of reconstructions based on the single-particle dataset of the pentagonal cluster of spheres (model A), while scaling the decomposition matrices $\tilde{\mathbf{V}}_l$ and $\tilde{\mathbf{v}}_n$ at $n = l = 0$ by different amounts. All other settings of the reconstruction workflow remained the same as for the single-particle case. The resulting averaged reconstructions can be seen in figure 35 and it becomes clear that the reconstructed densities are quite sensitive to changes in the relative scaling of invariants. An error in the estimated number of particles of $\pm 20\%$ ($N = 0.8, 1.2$) still preserves the shape of the final reconstructions

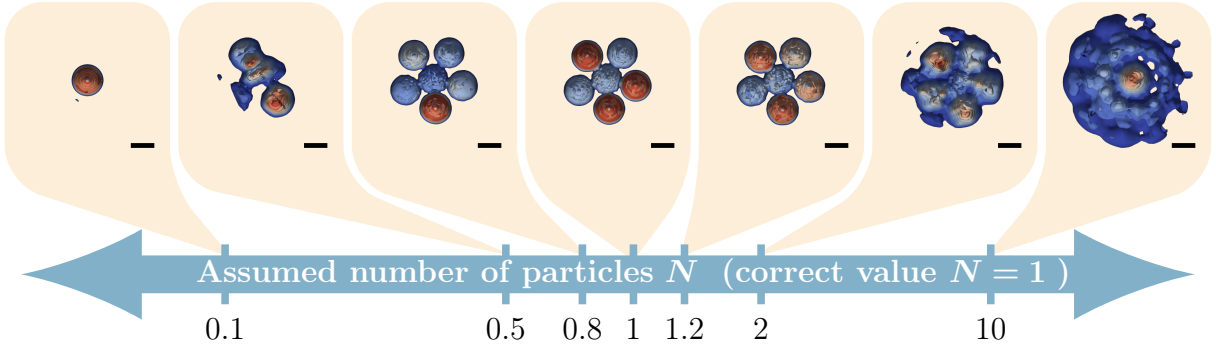


Figure 35: Averaged reconstructions from *single-particle* scattering data produced while assuming different numbers of particles N during phase retrieval. Each averaged reconstruction is the result of averaging over 50 independent reconstructions. All averages are visualized by cuts through 9 isosurfaces at 10%(deep blue) to 90%(deep red) of the maximal density. The black scale bars indicate a length of 10 nm on the plain that cuts the isosurfaces. Poorly reconstructed density variations are clearly visible in the averages at $N = 0.8$ and 1.2 .

but produces considerably different density distributions. One can also identify a general trend in the sense that an underestimation of the number of particles leads to density concentration in an area smaller than the considered particle, whereas an overestimation has the opposite effect. Overall, this shows that the correct estimation of the averages $\langle N \rangle$ and $\langle N^2 \rangle$, in the number of particles per diffraction pattern, is of fundamental importance for reconstructions based on multi-particle scattering datasets. In [21, Supplementary] a method was proposed that includes the relative scaling between the different invariants as free parameter in the phasing routine. For the given simulated dataset we could not successfully apply this approach. In our attempts, the number of particles did not converge to a preferred value across several reconstructions and could even cause runaway effects preventing convergence of the phasing routine. This might be connected to the fact that in our simulations we used a fixed number of particles, while the experimental dataset, used in [21], likely featured a fluctuating number of particles per diffraction pattern. Here we want to point at our theoretical analysis in section 2.5.3, which allowed us to gain new insights into the case of a fluctuating number of particles. As consequence of observation 2.19 we have seen, that the FXS invariants contain information about the number of particles in form of the square of its coefficient of variation, i.e. $\text{Var}(N)/\langle N \rangle^2$. Moreover, we could show that in cases where the probability distribution of the number of particles can be estimated to be a Poisson distribution⁴⁸ one can directly compute the missing scaling parameters, $\langle N \rangle$ and $\langle N^2 \rangle$, using equation (129). It still has to be seen whether this approach can be used in practice to determine $\langle N \rangle$ and $\langle N^2 \rangle$ with high enough accuracy, but it has the potential to eliminate these free parameters in FXS based reconstructions from multi-particle diffraction datasets.

5.1.2. Dependence on the harmonic cutoff

It is evident from the series expansions in equations (44) and (47) that the harmonic cutoff L , placed on the degree-2 invariants B_n and B_l , acts as an effective resolution limit for the obtainable single-particle intensity profile I . In order to test how this translates into changes on the averaged reconstructions we used the single-particle dataset for the human apoptosome complex (Model B) and performed reconstructions for different values of the cutoff degree L . Again, all other reconstruction and averaging parameter remained unchanged, as compared to the single-particle reconstructions shown in figure 30. The obtained structures and accompanying PRTF curves, displayed in figures 36 and 37, clearly indicate that the harmonic cutoff L also acts as an effective resolution bound on the averaged reconstructions. This is especially visible in the enlarged reconstruction areas visible in parts (g) to (l) of figure 36. It is interesting to note that for values below $L = 23$ we were not able to achieve averaged reconstructions that resemble the shape of the apoptosome complex.

⁴⁸A Poisson distribution in N is a good approximation if one can assume that the average number of particles is constant for each unit of volume and the positions of all particles are statistically independent.

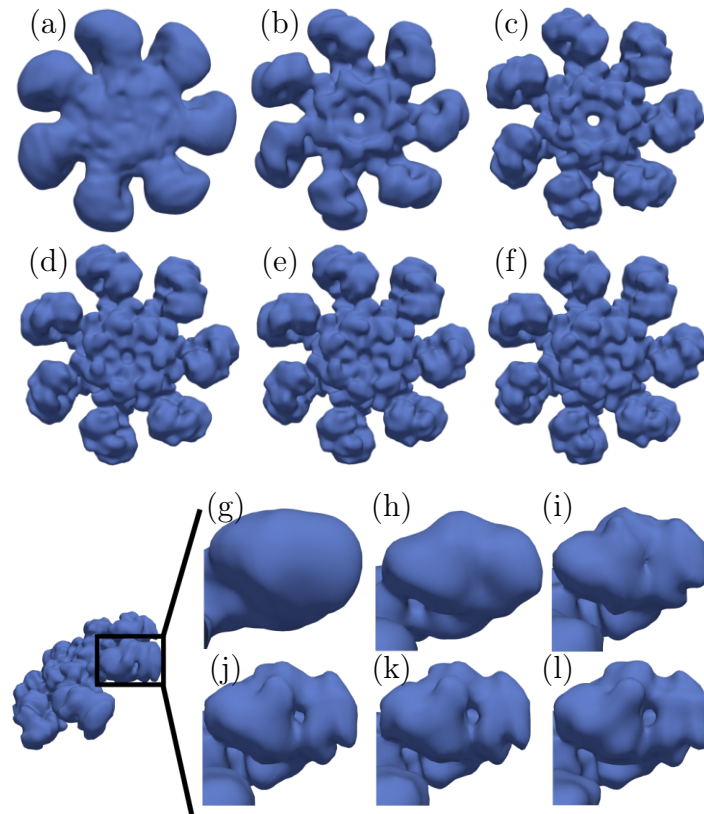


Figure 36: (a)-(f) Averaged 3D reconstructions of Model B (human apoptosome) determined from single-particle scattering data for $l_{max} = 23, 31, 39, 47, 63$ and 127 , correspondingly. (g)-(l) enlarged view of one of the seven “arms” of the apoptosome complex for each of the reconstructions shown in (a)-(f). All isosurfaces are taken at 15% of the maximal density of the respective reconstructions.

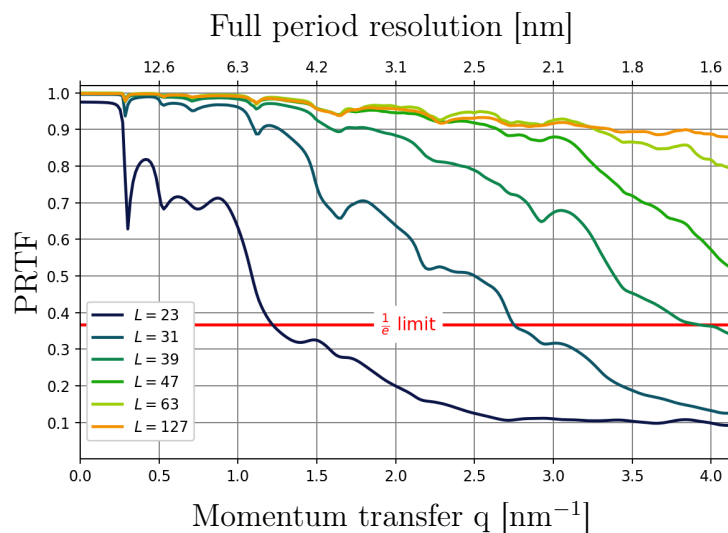


Figure 37: PRTF curves corresponding to the reconstructions in figure 36, showing a gradual decrease of resolution when restricting L to lower orders.

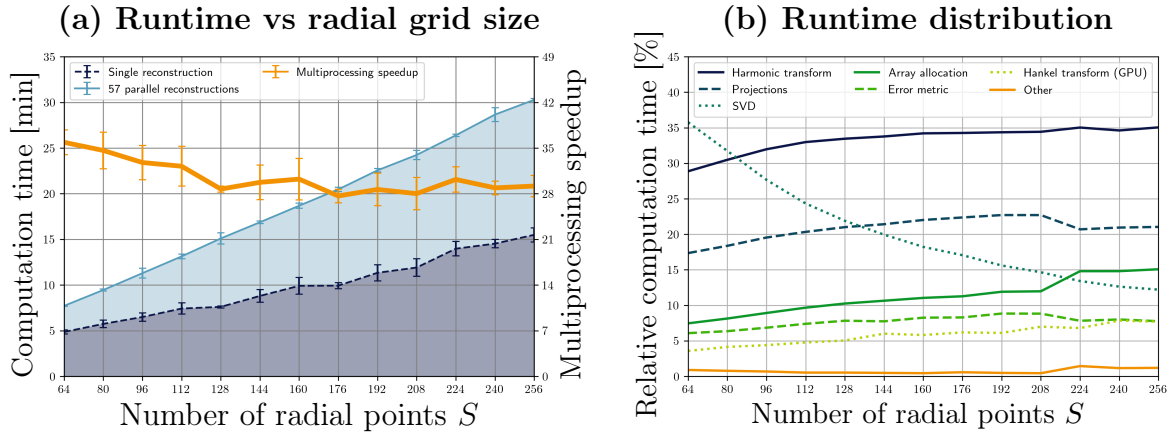


Figure 38: Performance of *xframe fxs reconstruct* for 3D reconstructions of Model A as a function of the radial grid size S . (a) Phasing runtime and multiprocessing speedup. The runtime for a single reconstruction t_1 is compared to the total runtime t_{57} for 57 reconstructions running in parallel. The multiprocessing speedup is determined as $57 \cdot t_1/t_{57}$. The results were averaged over 10 independent runs for single and parallel reconstructions, with the depicted error bars indicating the standard deviations in t_1 and t_{57} . (b) Average runtime distribution among different types of computations involved in the phasing loop are illustrated for one of the 57 reconstruction processes running in parallel. Most of the phasing time is spent in the categories *Harmonic transform* (spherical harmonic transforms), *SVD* [In the invariant projection P_{inv}], and *Projections* (reciprocal intensity projection and real-space projections, including HIO, ER and SW), and less in *Array allocation* (numpy methods *array* or *copy*), *Error metric* [calculating E_{real} , see equation (152b)], *Hankel transform (GPU)* [Hankel transforms (144) implemented on GPUs] and *Other* (computation time that is not associated with any other category above).

5.1.3. Performance of the phase retrieval routine

As final part of the discussion based on simulated diffraction data we will take a look at the computational performance of the phasing loop itself.⁴⁹ The following performance statistics were calculated on a single node running two AMD EPYC 7543 processors with a total of 64 physical CPU cores that access 512GB of RAM and two Nvidia RTX A6000 graphics cards with 48GB of memory each. Figure 38 displays a comparison between computation times for reconstructions of the six spheres structure (Model A) using 15 iterations of ($60 \times$ HIO, $1 \times$ SW, $40 \times$ ER) followed by a refinement stage of $200 \times$ ER steps. The harmonic cutoff was set to $L = 70$ for all considered reconstructions, which results in an angular grid of $N_\theta = 71$ polar and $N_\phi = 141$ azimuthal points (see section 3.4.2). The number of radial grid points was varied from $S = 64$ to $S = 256$ with a step size of 16. As it can be seen in figure 38 (a), the run-time of the presented algorithm depends linearly on the number of radial grid points, which is in agreement with the fact that all individual algorithm parts, except for the Hankel transforms, depend at most linear on the radial grid size. At the same time, this is a good indication that no computational bottlenecks in memory or compute units were reached for the specified parameter ranges. We observe an

⁴⁹Which is of course independent on the type of diffraction data.

approximately constant multiprocessing speedup of around 28 times, which corresponds to roughly 50% of the theoretically attainable speedup, that is equal to the number of reconstructions executed in parallel (57 in the given example). These speedups show that the multiprocessing scheme depicted in figure 25 works as intended and the unavoidable sequential access to individual GPUs is not breaking the CPU parallelization significantly. GPUs are currently exclusively used to compute the Hankel transforms (143)-(144), since their calculation would otherwise dominate the computation time. Moreover, the number of required computation steps for the Hankel transform depends quadratically on the number of radial grid points S . The overall linear increase in the computation time is a good indication that, within the tested radial grid sizes, the GPUs are able to compute each Hankel transform simultaneously at all considered radial grid points. The relative time fraction a phasing loop spends on GPU operations, i.e. Hankel transforms, can be seen in Fig. 38(b) and is for all radial grid sizes smaller than 8%. This low value presents a future upgrade path for the presented algorithm in which also the harmonic transform calculations, which currently are the most time consuming operations, could be performed on GPUs.

5.2. Reconstructions of PR772 from experimental XFEL data

The PR772 virus belongs to the *Tectiviridae* family and infects bacteria such as *Salmonella typhimurium*, which is a common cause of food poisoning. PR772 has an icosahedral capsid that is roughly 70 nm in diameter and encloses a lipid membrane, that contains the viral DNA [124]. As a member of the *Tectiviridae* family it injects its DNA into a host bacteria by restructuring its lipid membrane to form tubular structure that protrudes from one of the vertices of its icosahedral capsid and transports the viral DNA [125, 126].

In this section we will consider the two experiments *amo86615* [111] and *amo06516* [112]. Both of these experiments were conducted at the *Atomic Molecular Optics* (AMO) beamline [127] of the *Linac Coherent Light Source* (LCLS) at the *Stanford Linear Accelerator Center* (SLAC). The goal of these experiments was to develop the SPI technique in terms of the necessary experimental setup, as well as the associated data analysis. The collected datasets are therefore also perfectly suited to test FXS based reconstructions in the single-particle regime ($N = 1$). Table 4 summarizes key experimental parameters and information about the obtained datasets for *amo86615* and *amo06516*. In both experiments PR772 was aerosolized using a gas dynamic virtual nozzle [128, 129] and injected into the interaction region via an aerodynamic lens stack [4].

amo86615		amo06516	
Photon energy:	1.6 keV	Photon energy:	1.7 keV
Detector edge:	0.54 nm^{-1}	Detector edge:	1.12 nm^{-1}
Edge resolution:	11.6 nm	Edge resolution:	5.6 nm
Single-particle hits:	14,772	Single-particle hits:	9,033

Table 4: Experimental parameters for *amo86615* and *amo06516* taken from [111, 112]. The value *Detector edge* specifies the momentum-transfer value q_{max} , corresponding to a circle touching the edges of the recorded diffraction patterns. The *Edge resolution* is the corresponding full period resolution given by $2\pi/q_{\text{max}}$.

As a first step in the treatment of these datasets a particle size estimation was performed for each of the recorded single-particle hits. We followed a modified version of the estimation procedure described in [20]. The particle sizes were determined by fitting a spherical form factor,

$$I_{\text{spher}}(q) = A \left(\frac{\sin(qR) - qR \cos(qR)}{q^3} \right)^2, \quad (162)$$

to each azimuthally averaged diffraction pattern

$$I^M(q) = \frac{1}{2\pi} \int_0^{2\pi} d\phi I^M(q, \phi), \quad (163)$$

in the vicinity of its first minima. The fit parameters in equation (162) are the scaling parameter A and the radius of the corresponding sphere R . As described in [20] it is possible to use the obtained spherical radius R to estimate the outer diameter of an ideal icosahedral particle via

$$D_{\text{icos}} = 2^{5/6} \sqrt{5 + \sqrt{5}} \left(\frac{\pi}{5(3 + \sqrt{5})} \right)^{1/3} R \approx 2.36R. \quad (164)$$

This relation is obtained assuming that R describes a sphere whose volume is equivalent to that of a regular icosahedron. An example of such a fit can be seen in figure 39.

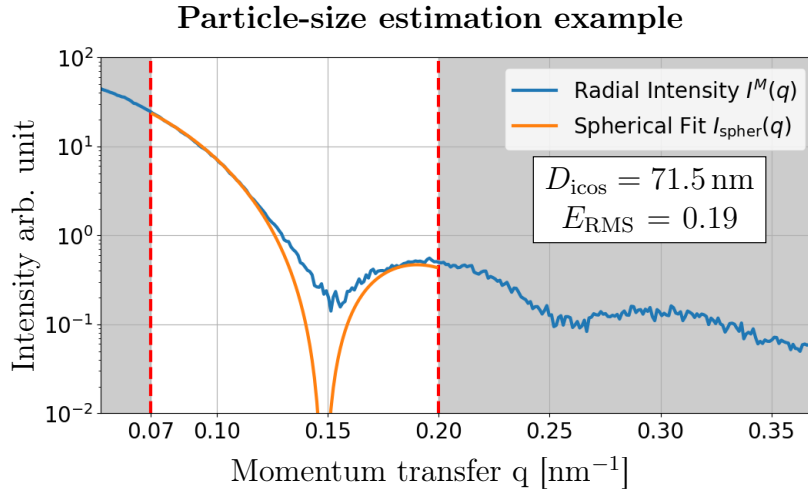


Figure 39: Example of fitting a spherical form factor (orange) to an azimuthally averaged intensity profile (blue) from the *amo86615* dataset, in the region of its first minima (dashed red lines). The estimated icosahedral diameter is 71.5 nm. All size estimates for the *amo86615* experiment were computed considering the momentum transfer region between 0.07 nm^{-1} and 0.2 nm^{-1} , whereas for *amo06516* the interval from 0.09 nm^{-1} to 0.2 nm^{-1} was considered.

In addition to the effective icosahedral diameter D_{icos} we compute the RMS error E_{RMS} for each fit, which is given by

$$E_{\text{RMS}}^2 = \frac{1}{q_2 - q_1} \int_{q_1}^{q_2} dq (I^M(q) - I_{\text{spher}}(q))^2. \quad (165)$$

Together with the total intensity I_{tot}^M of a diffraction pattern $I^M(q, \phi)$, the values of D_{icos} and E_{RMS} will be used as main parameters to further reduce and split the available diffraction data.

In the following we will focus individually on the two considered experiments and describe the diffraction pattern selection, the reconstruction workflow application as well as the obtained results.

5.2.1. Reconstructions for the AMO86615 experiment

For the *amo86615* experiment a final set of 5044 diffraction patterns were selected by restricting the total intensity I_{tot}^M to values greater than 80, in *analog-to-digital units* (ADU) per pixel, and the fit error E_{RMS} to values lower than 0.7. The corresponding histograms are shown in figure 40. All thresholds were selected to minimize noise in the computed degree-2 moments. Using the particle size histogram, given in figure 41, we divided the selected diffraction patterns into six size classes ranging from 67.5 nm to 72.5 nm in 1 nm steps, such that each part contains at least 300 patterns. In addition, we also simulated six sets of 10^5 diffraction patterns for ideal solid icosahedral particles, corresponding to the different size-parts, within the experimental momentum transfer range [see table 4]. Their purpose is to test potential deviations of the measured PR772 viruses from their ideal icosahedral symmetry. For each of the size-parts of the experimental and simulated datasets we computed the difference moments $\mathcal{M}_{\text{diff}}^2(q_1, q_2, n, n)$ from equation (134) according to our description in section 3.1. This was followed by the second step

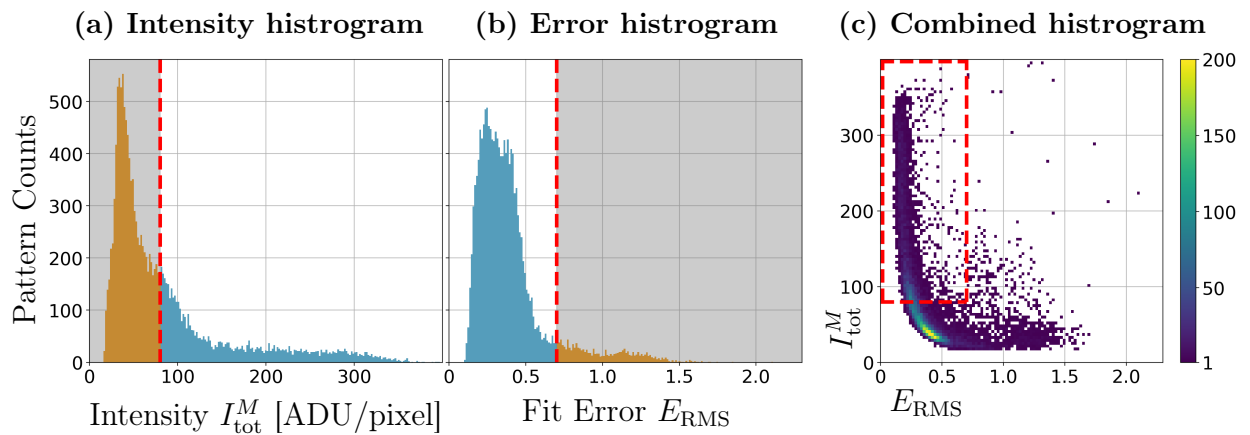


Figure 40: (a) Histogram of the total intensity I_{tot}^M of all single-particle hits. The dashed red line indicates the threshold value of $I_{\text{tot}}^M = 80$ [ADU/pixel]. The blue area of the histogram represents the diffraction patterns satisfying the threshold, while the shaded orange part corresponds to the excluded hits. (b) Histogram of the fit error E_{RMS} , where the threshold of $E_{\text{RMS}} = 0.7$ is again represented by the dashed red line. (c) Combined 2D histogram. The x-axis represents the error values E_{RMS} , the y-axis lists the total intensity I_{tot}^M and the color bar displays the number of diffraction patterns for each combination of intensity and error bins. The square of dashed red lines encloses the diffraction patterns that satisfy the constraints for E_{RMS} and I_{tot}^M . It can be seen that there is a clear correlation between high total intensities and low size estimation errors.

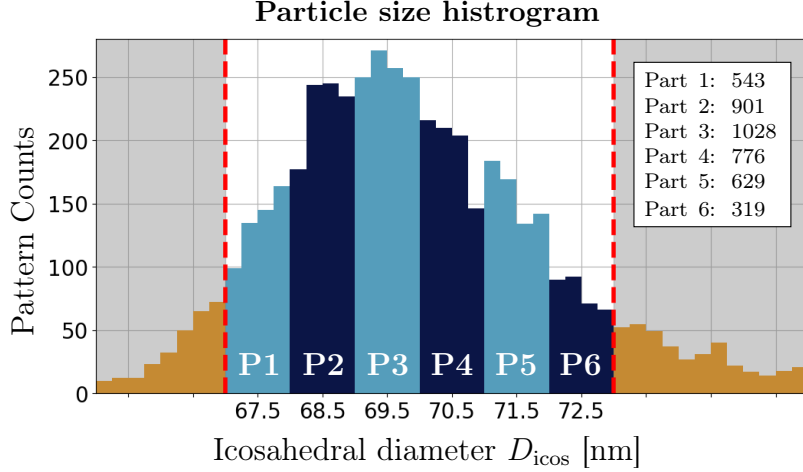


Figure 41: Particle size distribution histogram of the selected 5044 diffraction patterns. The six selected parts of the histogram are labeled by **P1** to **P6**. The corresponding numbers of patterns are given in the legend. Diffraction patterns that are located in the shaded areas are not contained in any of the six size-parts and will be neglected.

in our pipeline, the extraction and regularization of the invariants $B_l(q_1, q_2)$, using the command `xframe fxs extract`. The resulting moments and invariants for size-part P3 are shown in figure 42.

It can be seen that the experimental moments $\mathcal{M}_{\text{diff}}^2$ at harmonic degree $n = 12$ are dominated by noise which implies that the accessible invariants \mathbf{B}_l are limited to $l \leq 12$. There is a good agreement between the extracted invariants and their regularization given by $\tilde{\mathbf{V}}_l \tilde{\mathbf{V}}_l^\dagger$, as indicated by the error metrics. The sign boundaries do not show significant deviations and the error metric only spikes at zeros in \mathbf{B}_l or at noise polluted areas for higher harmonic degrees. White areas in $\tilde{\mathbf{V}}_l \tilde{\mathbf{V}}_l^\dagger$ correspond to masked momentum-transfer values and will not be used as constraints in the invariant projection P_{inv} during phase retrieval. Moreover, the differences between the experimentally observed invariants \mathbf{B}_l and their simulated counterparts $\mathbf{B}_l^{\text{sim}}$ are quite pronounced. This is especially visible in degrees $l = 2, 4, 8$, in which the experimental invariants attain absolute values that are roughly two orders of magnitude higher than their simulated counterparts. These comparatively high absolute values for $l = 2$, i.e. the lowest non-spherically symmetric contribution, hint at a possible elongation or squeezing of the particle shape in one coordinate direction over the other.

With access to the decomposition matrices $\tilde{\mathbf{V}}_l$ for all size-parts we were able to generate averaged reconstructions using the commands `xframe fxs reconstruct` and `xframe fxs average`. The same settings were used for the experimental and simulated datasets, as well as across all size-parts within them. For the initial density guess a spherically symmetric bump function was used

$$\rho_0(\mathbf{r}) = \begin{cases} e^{\frac{1}{2}r_{\text{max}}^2/(r_{\text{max}}^2-|\mathbf{r}|^2)} & |\mathbf{r}| \leq r_{\text{max}} \\ 0 & \text{otw.} \end{cases}, \quad (166)$$

that was multiplied with white noise and had a radius of $r_{\text{max}} = 35$ nm. The reconstruc-

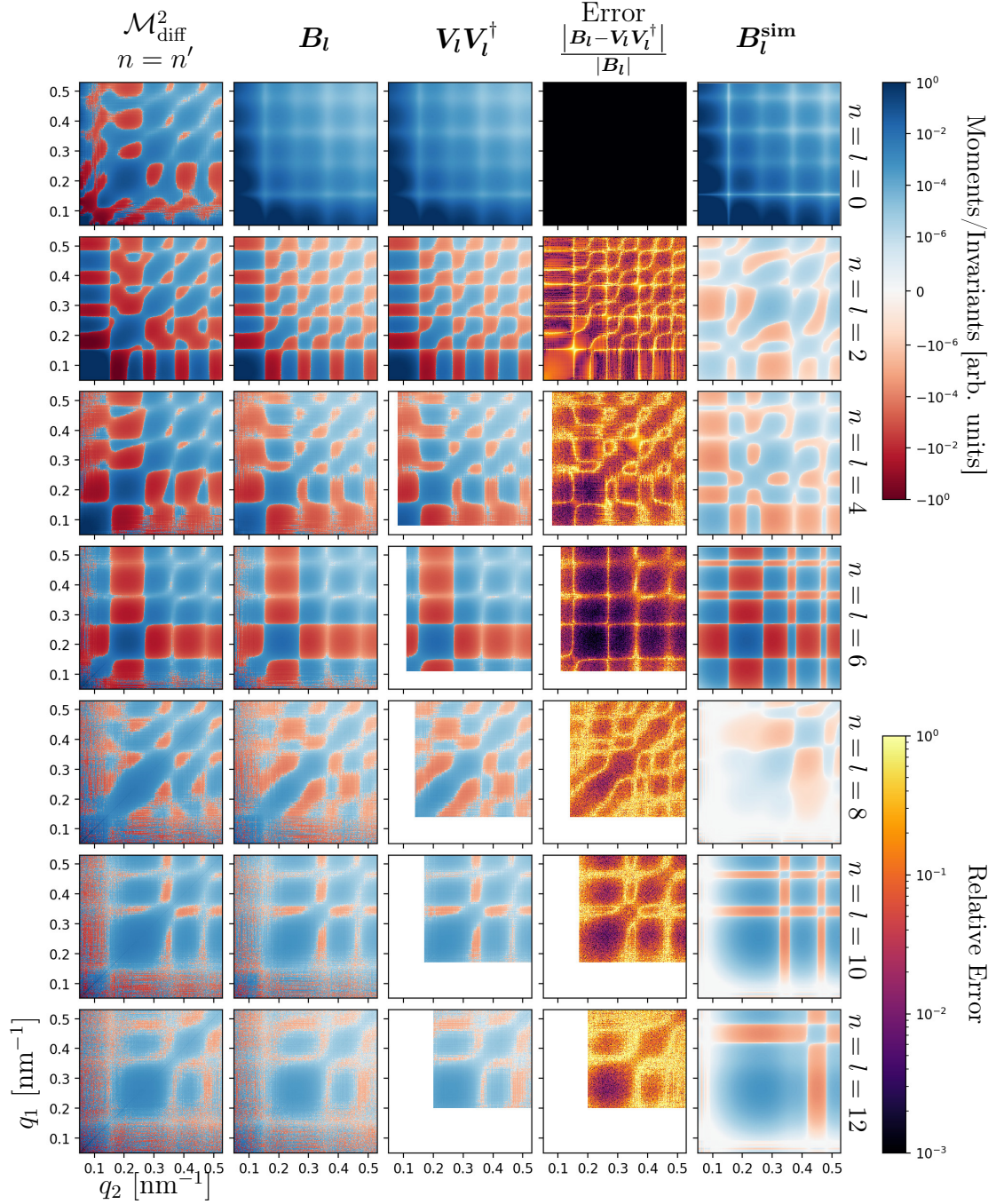


Figure 42: The five columns (from left to right) display the degree-2 moments $\mathcal{M}_{\text{diff}}^2(q_1, q_2, n, n)$ computed from experimental difference images, the corresponding extracted invariant matrices B_l , its regularized decomposition $\tilde{V}_l \tilde{V}_l^\dagger$, the relative error between B_l and $\tilde{V}_l \tilde{V}_l^\dagger$ and the invariants B_l^{sim} computed from the simulated diffraction data. Each row corresponds to a fixed even harmonic degree from $n = l = 0$ to $n = l = 12$. The invariants and moments are visualized on a symmetric logarithmic scale where blue areas indicate positive values and red areas negative values. In order to allow for a comparison between B_l , $\tilde{V}_l \tilde{V}_l^\dagger$, and B_l^{sim} , their values in all degrees have been normalized by the total median of B_0 , $V_0 V_0^\dagger$, and B_0^{sim} , respectively.

tion grid contained 256 radial grid points, 128 polar angles ϕ and 64 azimuthal angles θ , while restricting the used harmonic coefficients of the electron density $\rho(\mathbf{r})$ to spherical harmonic degrees $l \leq 12$. The phasing routine was again split into a main stage and a refinement stage. The former executed 10 blocks of $60 \times \text{HIO}$, followed by $1 \times \text{SW}$ and $40 \times \text{ER}$, while the refinement stage contained a single SW step followed by $100 \times \text{ER}$. During the entire phasing routine the HIO parameter was kept constant at $\beta = 1$. The shrink-wrap threshold was set to $\gamma = 0.07$, while its standard deviation σ followed a linear decay from initially $\sigma = 20 \text{ nm}$ to $\sigma = 10 \text{ nm}$. As an error metric the real space error E_{real} from equation (152b) was used. For each size-part a set of 112 reconstructions were computed. The reconstructions, both from experimental and simulated datasets, did not split into separate classes based on their error metric values, as has been observed in figure 29

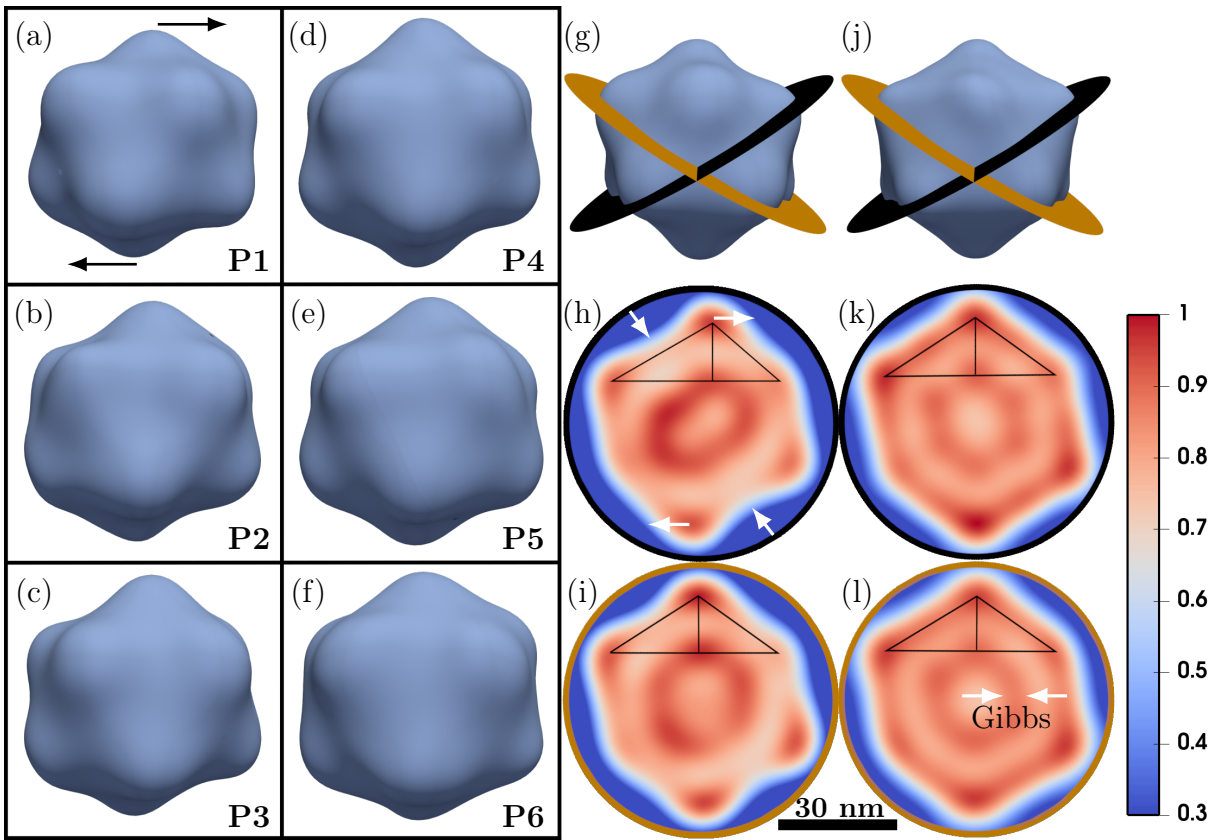


Figure 43: (a)-(f) Averaged reconstructions corresponding to the size parts P1 to P6 of the experimental dataset. (g) rotated and scaled version of (c) with indicated black and orange cut surfaces, whose density cuts are displayed in (h) and (i), respectively. (j) Averaged reconstruction from simulated diffraction patterns of an ideal solid icosahedron corresponding to size-part P3. Densities along the cut surfaces of the ideal icosahedron are visible in (k) and (l). The 30 nm scale bar is valid for the density cuts (h), (i), (k) and (l). All visible isosurfaces are taken at 30% of the maximal density value within each averaged reconstruction, respectively. The isosurfaces in (a)-(f) are displayed using the same field of view indicated by the black squares. One may notice, that the size of the reconstructed particle grows from (a) to (f). The black arrows in (a) indicate a shift of the upper and lower vertices with respect to an ideal icosahedron.

of the previous section. During alignment and averaging we therefore considered 100 reconstructions with the lowest error metric, for each size-part. The resulting averaged reconstructions are displayed in figure 43. As indicated by the degree-2 invariants, the reconstructions based on experimental data show deviations in the virus shape from its ideal icosahedral symmetry. A feature of this deviation is the relative shift of the upper and lower vertices in figure 43 (a), as indicated by the black arrows. This deviation is more pronounced for the lower size-parts, i.e. it decreases from (a) to (f) in figure 43. To investigate this further we considered the orange and black planes in (g) and (j), which are symmetry equivalent in an ideal icosahedron. This is nicely visible in the equivalence of cuts (k) and (l). While (i) is similar to these ideal cuts, (h) shows deviations from the cuts of the ideal icosahedral reconstruction. It has two density deficient boundary regions, that are marked by the diagonal white arrows. At the same time the upper and lower vertices in (h) are shifted horizontally in opposite directions, with respect to each other, as indicated by the horizontal arrows. This deviation is also visualized by the black triangles. Note that the vertical black line bisects the bottom hypotenuse in almost equal halves for cuts (i) (k) and (l), while in (h) the right part of the hypotenuse is shorter. The inner density rings, present in all cuts and marked by the white arrows in (l), are artifacts due to the Gibbs phenomenon and prevented an analysis of the interior density distributions. They are ultimately the result of the relatively low momentum transfer limit of the measured diffraction patterns, which corresponds to a full period resolution of 11.6 nm while the ring like artifacts have a width of roughly half of this resolution limit. The PRTF resolution metrics associated to the averaged reconstructions based on the experimental dataset are shown in figure 44. The obtained resolution for parts 1 to 3 is approximately given by 13 nm, with part 3 just barely touching the PRTF resolution limit of $1/e$, represented by the red horizontal line. In case of parts 4 to 6 the resolution is worse by one minima location and approximately limited to 18 nm. In total this compares favorably to [20], where a PRTF resolution of 17.7 nm was reported for the same dataset.

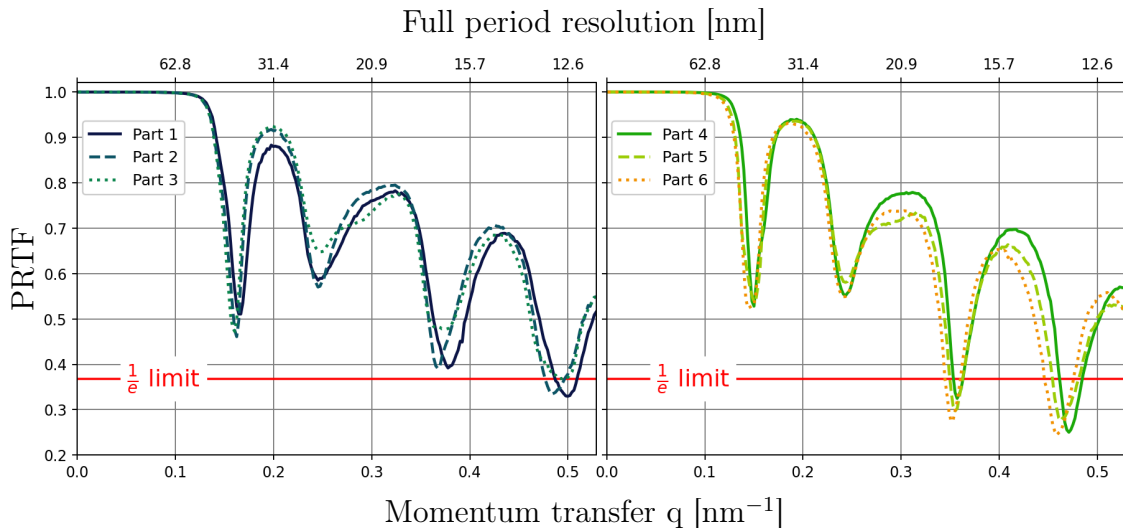


Figure 44: PRTF resolution metrics for the averaged reconstructions corresponding to size-parts 1 to 6 from the experimental dataset, displayed in (a)-(f) of figure 43.

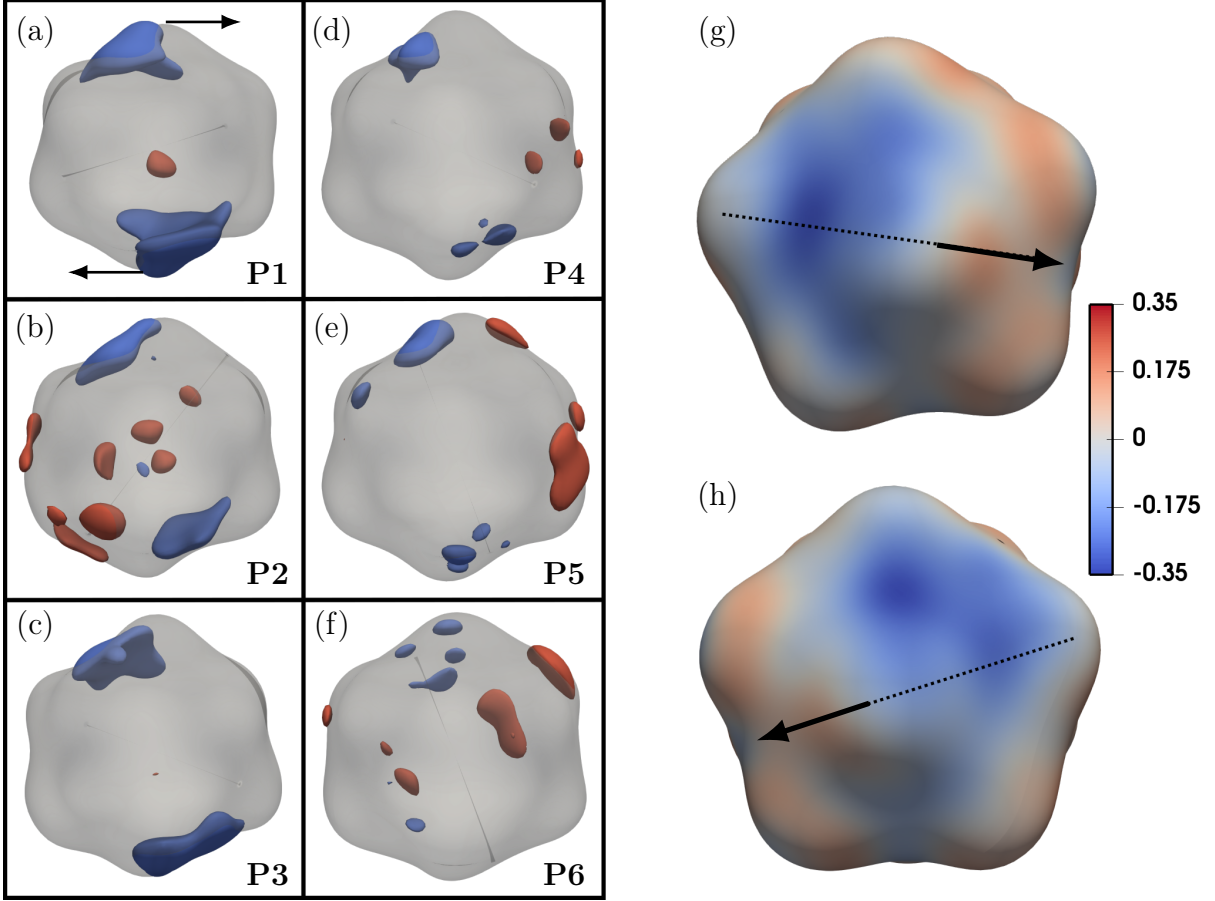


Figure 45: (a)-(f) Isosurfaces of ρ_{diff} that enclose areas of differences higher than 0.2 (red) and lower than -0.2 (blue). The images are created using the same view port as in (a)-(f) of figure 43 and the corresponding 30% isosurfaces are represented as opaque gray structures in this figure. (g) and (h) depict top and bottom views of the 30% isosurface of P3 given in (c) of figure 43. The value of ρ_{diff} on this surface is represented by colors. Blue areas denote missing density compared to an ideal icosahedron, i.e. negative ρ_{diff} . The dotted line and arrow indicate the relative shift direction of the top and bottom vertices.

To further characterize the observed deviations between the experimental reconstructions and those obtained from ideal icosahedral particles we computed their difference maps. For each size-part the averaged experimental reconstructions, as well as the averaged reconstruction from the simulated dataset, were normalized by their respective maximal density value and subsequently aligned using the alignment process described in section 3.5. After this, the averaged reconstruction based on the simulated dataset was subtracted from its experimental counterpart to form the final difference density ρ_{diff} , i.e. $\rho_{\text{diff}}(\mathbf{r}) = \rho_{\text{exp}}(\mathbf{r}) - \rho_{\text{sim}}(\mathbf{r})$. Graphical representations of $\rho_{\text{diff}}(\mathbf{r})$ can be found in figure 45. The approximate point symmetry in the difference maps, visible in (a) and (c) of figure 45, may hint towards the presence of the twin-image problem [130], which is a well known stagnation mode for iterative phase retrieval algorithms, in which the final reconstruction

is a mixture between the correct density and its point inverse. However, the structure and position of the blue parts in figure 45 (a)-(c) clearly show that the density deficient areas and the shift of the top and bottom vertices are the mayor differences between the experimentally observed virus capsid and its ideal icosahedral counterpart. While slight traces of the same deviation are also visible in (d) and (e) of figure 45, they can no longer be identified in (f), which corresponds to the largest size-part.

The observed differences may point towards a remodeling of the membrane and capsid of the virus, as PR772 is known to be sensitive to aerosolization [131, 132], or the onset of its DNA ejection process. Interestingly, similar features to the density deficient boundary regions and the shift of the top and bottom peak, as visible in figure 43 (h) (white arrows), were also observed in [9, Figure 7 (i)], which used SPI techniques (see section 1.5) to analyze the same diffraction dataset.

In summary, we could improve the previously obtained PRTF resolution limit from 17.7 nm [20] to 13 nm and provide clear evidence, that the measured PR772 virus capsids differ significantly from an ideal icosahedron. At the same time, we could verify that the presented workflow is able to produce successful reconstructions from a limited set of experimental diffraction patterns. This, in particular, includes our proposed extraction scheme for the degree-2 invariants, based on equation (113), as well as their regularization introduced in section 3.3.

5.2.2. Reconstructions for the AMO06516 experiment

The diffraction patterns of the *amo06515* experiment were recorded to about double the maximal momentum transfer value of the previously consider *amo86615* dataset, thereby offering the possibility of reduced Gibbs artifacts and higher reconstruction resolutions. Its downsides are, the overall worse data quality, visible from the diffraction pattern shown in figure 18 (b), and the lower number of measured single-particle hits.

The selection and division of recorded diffraction patterns into different size-parts was performed according to the methods, that have been described in the previous section

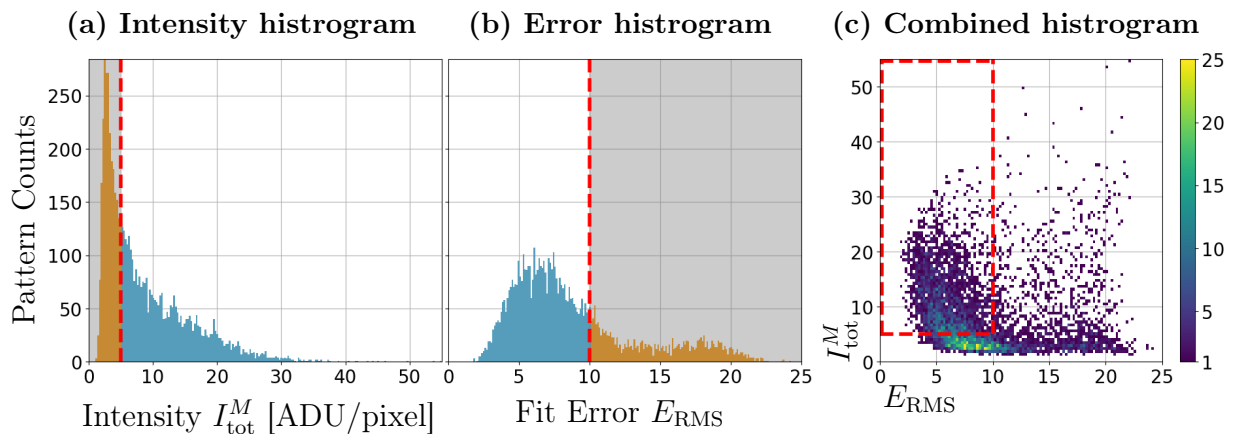


Figure 46: Same as figure 40 but for the *amo06516* dataset. (a) Histogram of the total intensity I_{tot}^M (b) Histogram of the size estimation fit error E_{RMS} . (c) Combined 2D histogram. The square of dashed red lines enclose the 2822 diffraction patterns satisfying $E_{RMS} < 10$ and $I_{tot}^M > 5$.

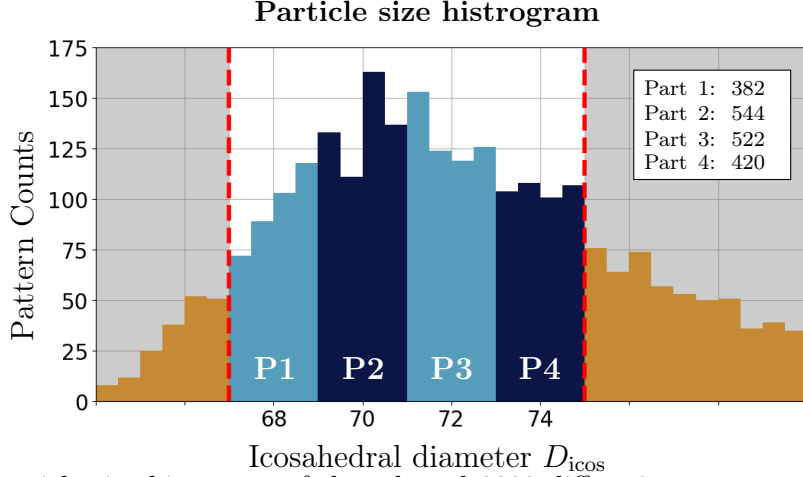


Figure 47: Particle size histogram of the selected 2822 diffraction patterns. We will consider the four size-parts labeled by **P1** to **P4**. Their corresponding number of contained patterns is given in the white box on the top right of the histogram.

and are based on thresholding the total intensity I_{tot}^M , the icosahedral diameter D_{icos} and the associated fit error E_{RMS} . As visible in figure 46, only those diffraction patterns were considered that have a total intensity higher than 5 [ADU/pixel] and a fit error lower than 10.

Comparing figure 46 with figure 40 for the *amo86615* experiment, shows that the correlation between high total intensities and low fit errors is weaker in the *amo06516* dataset and that it contains less diffraction patterns with low fit errors. Together this resulted in the selection of 2822 diffraction patterns. The corresponding particle size histogram is shown in figure 47 and was used to split the remaining patterns into 4 different size-parts.

Each part corresponds to a 2 nm range centered around an icosahedral diameter given by $D_{\text{icos}} = 68$ nm, 70 nm, 72 nm or 74 nm.

Following our workflow we performed the extraction and regularization step and obtained the degree-2 invariants for each of the four size-parts. The results for size-part P2 can be found in figure 48. Overall, the computed invariants have higher noise contributions than for the *amo86615* dataset, even at comparable momentum transfer values. This can also be observed by comparing the error values shown in figure 48 with the corresponding errors for the *amo86615* experiment, given in figure 42. After $n = 10$ the FXS moments for *amo06516* become noise dominated and the computation of degree-2 invariants \mathbf{B}_l is therefore limited to harmonic degrees lower or equal to 10, i.e. to those with $l \leq 10$. Note, that our proposed regularization scheme is still able to preserve the sign boundaries of \mathbf{B}_l and slightly reduces the noise level in harmonic degrees $l = 2, 6, 10$. In figure 42 we have seen that the absolute values of the invariants $\mathbf{B}_l^{\text{sim}}$, corresponding to the simulated ideal icosahedral particles, were highly suppressed in the harmonic degrees $l = 2, 4$ and 8 compared to those for $l = 6, 10$ and 12. This behavior was not present for the invariants from the *amo86615* dataset and figure 48 shows that it is also absent from \mathbf{B}_l for the *amo06516* dataset. In general, the moments $\mathcal{M}_{\text{diff}}^2(q_1, q_2, n, n)$ of both datasets are quite similar to each other, as can be seen in figure 49. On the level of the invariants

$\tilde{\mathbf{V}}_l \tilde{\mathbf{V}}_l^\dagger$ the similarity is still clearly visible but less pronounced. This is quite striking, given that the shown moments and invariants correspond to entirely different experiments and where generated from different spreads of particle sizes, as well as differing numbers of diffraction patterns. This is a clear indication for the validity of the obtained invariants.

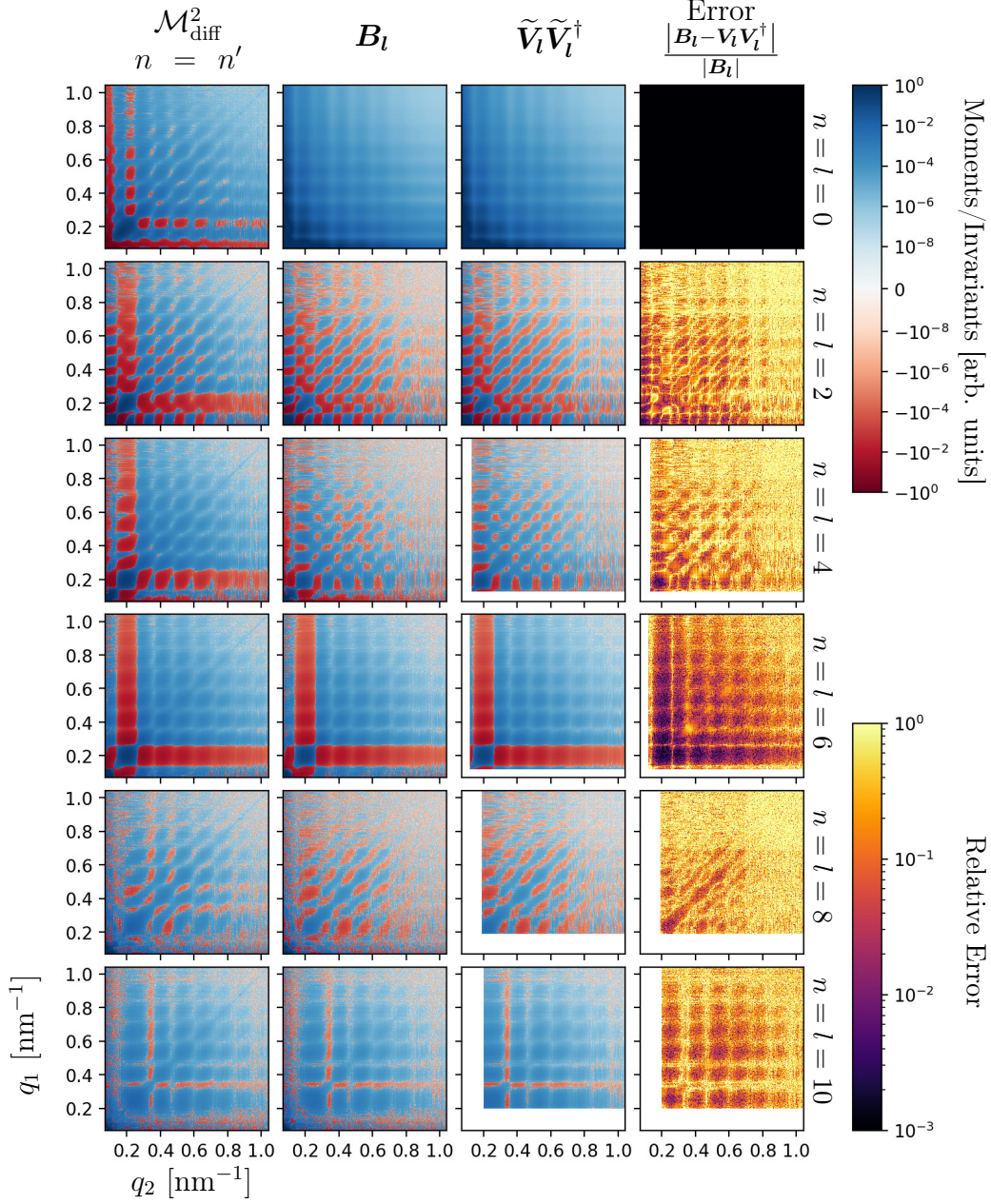


Figure 48: Degree-2 moments and invariants for size-part P2. The four columns (from left to right) display the degree-2 moments $\mathcal{M}_{\text{diff}}^2(q_1, q_2, n, n)$, the extracted invariant matrices \mathbf{B}_l , its regularized decomposition $\tilde{\mathbf{V}}_l \tilde{\mathbf{V}}_l^\dagger$ and the relative error between \mathbf{B}_l and $\tilde{\mathbf{V}}_l \tilde{\mathbf{V}}_l^\dagger$. Each row corresponds to a fixed even harmonic degree from $n = l = 0$ to $n = l = 10$. Similar to figure 42, the invariants and moments are visualized on a symmetric logarithmic scale where blue areas indicate positive values and red areas negative values.

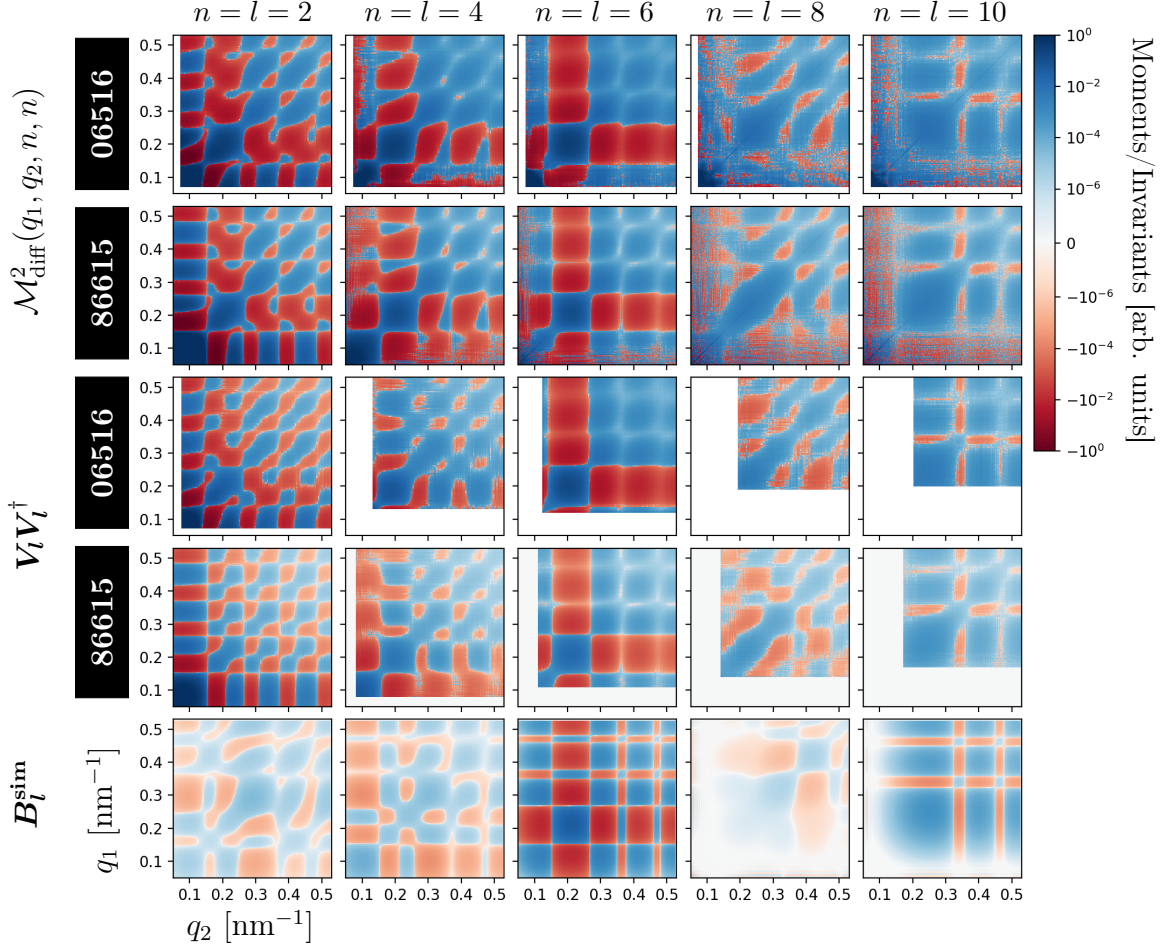


Figure 49: Comparison between the computed moments $\mathcal{M}_{\text{diff}}^2(q_1, q_2, n, n)$ and the invariants $\tilde{V}_l \tilde{V}_l^\dagger$ of size-part P3 for the *amo86615* experiment given in figure 42 and size part P2 for the *amo06516* experiment from figure 48. For reference the last row shows the invariants B_l^{sim} , that have been computed from simulated solid icosahedral particles.

In the following phasing step we employed the same settings as described in the previous section, with the exception that the invariant projection P_{inv} was limited to harmonic degrees $l \leq 10$ instead of $l \leq 12$. A total of 112 reconstructions were computed per size-part. The reconstructions did again not split into separate classes based on their final error metric values. For each size-part the 100 reconstructions with the lowest error metric values were used to generate the final averaged reconstruction, see figure 50. The associated PRTF resolution metrics, given in figure 51, indicate resolutions of approximately 18 nm for size-parts 1,2 and 4, while the resolution for part 3 is 14 nm.

A common feature of the reconstructions presented in figure 50 is a low density region near the upper vertex, see the black arrow in 50 (c). This region is similar to a more localized version of the blue density deficient volume, which is visible near the top vertex in figure 45 (a)-(c) for the *amo86615* experiment. It is interesting to note that the point symmetric behavior of this density deficient area is absent from the reconstructions for the

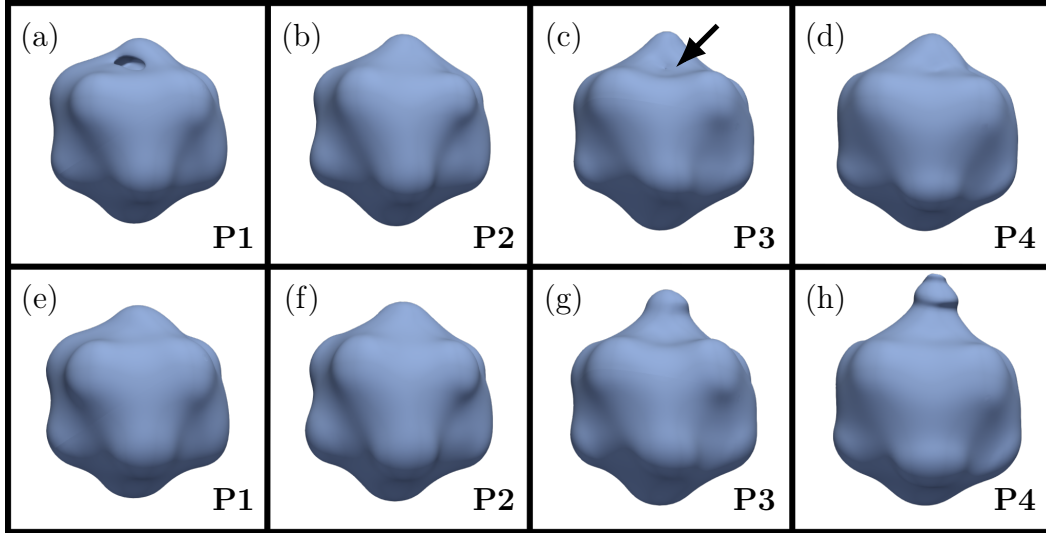


Figure 50: Isosurfaces of the size-parts **P1** to **P4** at 30% of their maximal density value (a)-(d) and at 20% of their maximal density (e)-(h), respectively. The field of view is the same for all plots and indicated by the black squares, which allows to compare feature sizes between the presented averages. All isosurfaces contain a dip near the upper vertex that is not present at other vertices. In (c) the position of this dip is indicated by the black arrow.

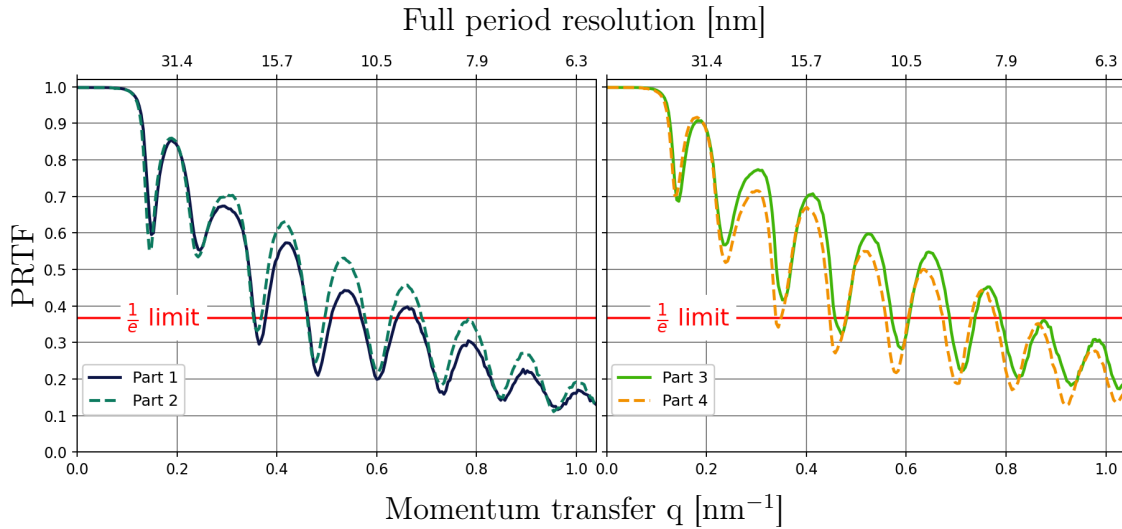


Figure 51: PRTF resolution metrics for the averaged reconstructions presented in figure 50.

amo06516 experiment. Together with the similarity of the extracted invariants, visible in figure 49, this is another hint towards the presence of the twin image problem [130] in the reconstruction step for the *amo86615* dataset. Another interesting feature of the reconstructions in figure 50 is the appearance of an extended density region at the upper vertex in the 20% surfaces (g) and (h). The diameter of this cylindrically shaped extension is approximately 15 nm. A possible explanation for its appearance, is that a portion of the viruses in the *amo06516* experiment have been imaged during their DNA ejection process,

in which they restructure their membrane to form a tubular extension that protrudes out of one of the vertices of the virus capsid [125, 126]. Since the final single-particle intensity represents an average over all observed virus structures one would expect the extended density region to be weighted by the relative number of viruses imaged during their ejection process which could explain its relatively low density value in the averaged reconstructions. In similarity to our discussion of the *amo86615* reconstructions we also considered density cuts along symmetry equivalent planes, which are shown in figure 52. Comparing the presented cuts to those of the *amo86615* experiment one immediately notices the reduced ring like artifacts inside of the virus capsid. It is clearly visible that the PR772 virus has a higher density capsid surrounding a lower density region inside of it. Moreover, the three symmetry equivalent cutting planes for all four size-parts are consistently different from each other. By “consistently different” we mean, that the three columns representing different size-parts in figure 52 show more similarities to each other, as indicated by the white dots and lines, than the rows which correspond to the different symmetry equivalent planes. This means that the observed virus structure deviates in a consistent way across all four size-parts from its ideal icosahedral symmetry. The elongated density region for size-parts P3 and P4 is visible in the black cuts (g) and (h) of figure 52 in the upper right vertex. It is interesting to see that the black cuts in (e) and (f) show an area of decreased density in the same region in which the elongation is visible for (g) and (h), further indicating that the corresponding vertex of the virus capsid is different from its other vertices.

In summary, the *amo06516* dataset allowed us to confirm the form of the degree-2 invariants that have been obtained from the *amo86615* experiment, see figure 49. It proved the capability of the presented workflow to handle significant amounts of noise as well as missing portions of diffraction patterns [visible in figure 18(b)]. The proposed regularization scheme for the degree-2 invariants was again able to preserve the sign boundaries and could even reduce the noise level for some harmonic degrees, as can be seen in figure 48. Despite of the, in part, lower resolution estimates the reconstructions of the *amo06516* experiment benefit from the higher momentum transfer limit, as can be seen in the reduced ring shaped Gibbs-artifacts in the density cuts of figure 52 compared to those in figure 43 (h) and (i). This allowed us to identify consistent deviations from the icosahedral symmetry across all considered size-parts as well as the special role of one of the vertices of the PR772 virus.

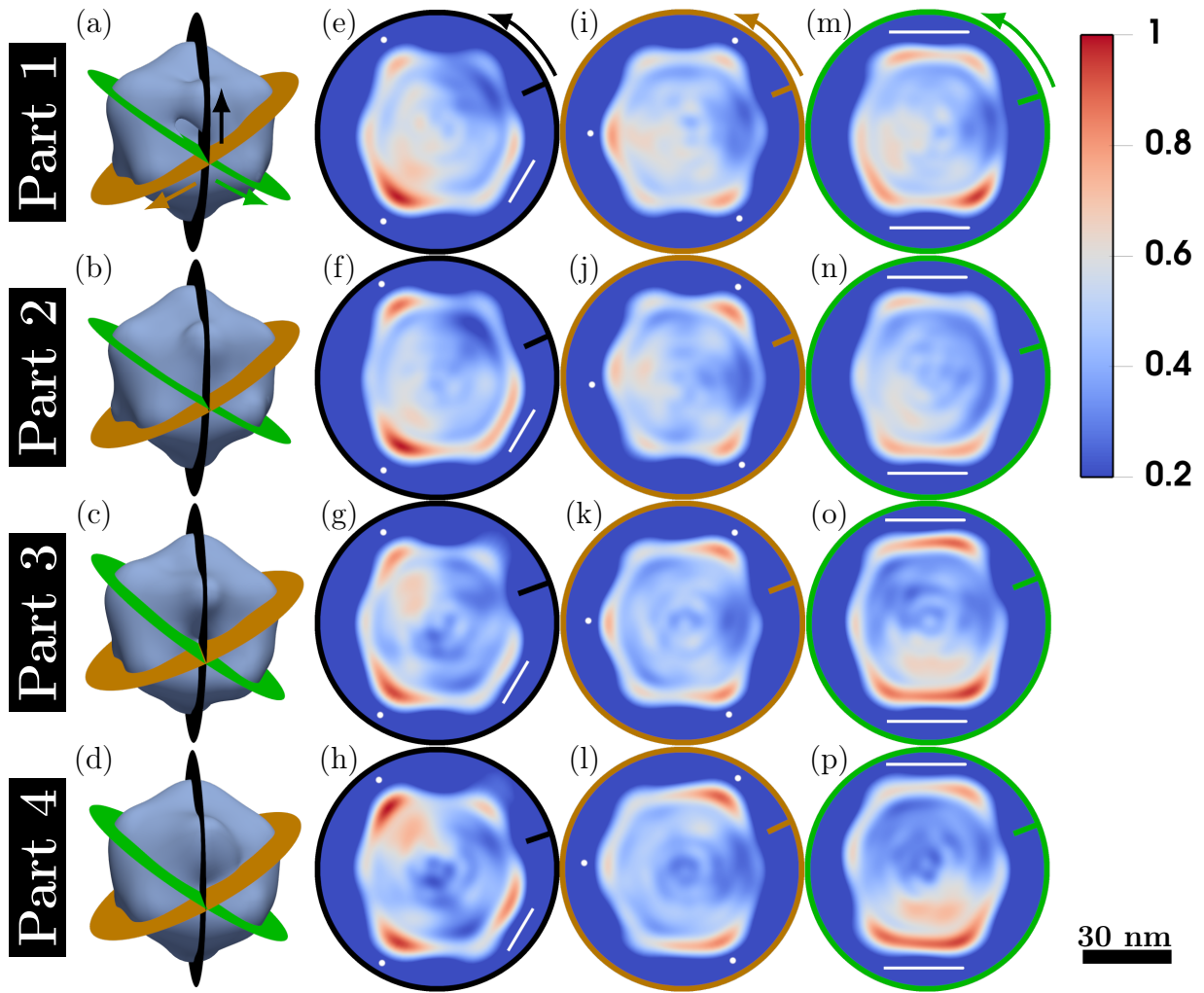


Figure 52: (a)-(d) Rotated versions of the 30% isosurfaces displayed in (a)-(d) of figure 50. The orientation of each reconstruction is such that the vertex pointing out of the image plane towards the viewer corresponds to the top most vertex in figure 50. (a)-(d) also display three symmetry equivalent cutting planes that intersect in a line going through the center of the dip in the isosurfaces, marked with an arrow in 50 (c). (e)-(p) density cuts along the symmetry planes visible in (a)-(d) that display density values higher than 20% of the maximal value for each size-part, respectively. (e)-(h) correspond to the black planes, (i)-(l) to the orange planes and (m)-(p) to the green planes. Each cut contains a line segment pointing from its boundary towards its center, which indicates the location of the intersection line between it and the other two planar cuts in each row. The colored arrows in (a), (e), (i) and (m) indicate the orientation of the density planes in the isosurface (a), starting from their visible intersection point. The orientations of the density planes of size-parts P2,P3 and P4 are the same as for size-part P1. The 30 nm scale bar in the bottom right is valid for all density cuts (e)-(p). The white dots and lines in (e)-(p) indicate high density features at the boundaries of the density cuts. These features are shared across different size parts for the same cutting plane, i.e. across (e)-(h),(i)-(l) and (m)-(p). The black planes (e) and (f) of size-parts 1 and 2 show a low density region in the vicinity of the upper right vertex. In (g) and (h) corresponding to size-parts 3 and 4 this lower density area is not visible instead this vertex now features an extended density region, also visible in (g) and (h) of figure 50.

6. FXS in the case of non-uniform orientational distributions

The application of FXS techniques is currently limited to systems of particles that follow a uniform rotational probability distribution. While it is still possible to simulate diffraction patterns for samples that follow non-uniform distributions and subsequently compute the FXS moments, all results about their connection to the single particle structure from sections 2.2 and 2.5.1 lose their validity. In practice the presence of nonuniform rotational distributions is not uncommon and most prominently includes pump-probe experiments, that are frequently conducted at XFELs [22, 25, 26, 133–135]. In such experiments one seeks to study dynamic processes in a sample, that have been triggered by irradiation with a laser field (pump-pulse). The measured quantities are scattering patterns that have been generated by interaction with an X-ray pulse (probe-pulse) whose time delay can be varied, with respect to the pump-pulse.

The presence of nonuniform rotational distributions in such experiments is caused by the orientation dependence of the interaction between the sample and the pump laser field [24, 136–138]. For example, consider the laser field to be linear polarized and resonant with an electronic transition of the molecules contained in a given sample. Under these conditions one finds, that the transition probability is dependent on the alignment between the laser polarization and the transition dipole-moment [24, 137]. The alignment of molecules in a laser field is in general not limited to the above setting and can also occur if the polarization of the laser field is elliptic or circular [138] and even under non-resonant conditions [24, 136]. At the same time it is known that the SAXS/WAXS intensity is sensitive to the orientational distribution of particles [22, 139–141] and Legendre polynomial based techniques have been proposed [142, 143] and employed to obtain structural information about individual excited particles [25, 26]. Since SAXS is contained in *fluctuation X-ray scattering* one may suspect that there should be an extension to the FXS formalism that captures non-uniform orientational distributions. In general there are two possible use cases of such an extension.

1. Given *a priori* knowledge about the orientational probability distributions, extract information about the single-particle structure.
2. Given *a priori* knowledge about the single-particle structure, extract information on their orientational probability distribution.

For the latter case note that, since we use scattered intensities to study real-space orientational probability distributions, the maximal amount of retrievable information is limited by the Friedel symmetry $I(\mathbf{q}) = I(-\mathbf{q})$, which does not allow to distinguish between a sample and its point-inverse.

In this section we will provide explicit formulas for the degree-1 and degree-2 moments of FXS for arbitrary orientational probability distributions. The key insight will be, that the dependence of the FXS moments on the probability distribution can be entirely formulated in terms of their discrete Fourier transforms on $SO(2)$ for the 2D case and $SO(3)$ in the 3D case. We will not only be able to give analytic results for specific

probability distributions, which can be found in section 6.4, but also a way to numerically handle arbitrary distributions.

Regarding the previously mentioned use cases we will be able to give the following partial answers in this chapter.

1. For 2D FXS the degree-2 invariants $B_n(q_1, q_2)$ can be extracted irrespective of the orientational probability distribution of the considered samples and one can apply the reconstruction workflow presented in section 3 to obtain the single-particle structure. In the converse case of a known structure, the measurement of a SAXS profile is enough to determine the orientational probability distribution over the rotation group $SO(2)$ upto point inversion symmetry.
2. In case of 3D FXS it will still be possible to determine the rotational probability distribution (now over $SO(3)$), upto point inversion, based on measurements of degree-1 moments (SAXS profiles), if the single-particle structure is known. In general it is, however, not possible to extract the degree-2 invariants $B_l(q_1, q_2)$. In special cases this might still be possible and the derived equations may serve as a starting point for the development of future reconstruction workflows.

A manuscript discussing these results is currently in preparation [144].

Perfect alignment (informal): An extreme example of the effect of a non-uniform rotational distribution on the moments \mathcal{M}^d , is given by the case of complete orientational alignment, i.e. the case in which the probability distribution is a delta distribution. For simplicity let us assume a single particle per sample. In this case each sample ρ^M consists of a particle that has to be in the unique rotation state around which the delta distribution is centered. The measured diffraction patterns I^M therefore simply correspond to the Ewald's sphere slice associated with this particular orientation state. This implies that all intensities in the definition of \mathcal{M}^d are constant with respect to the ensemble average and one finds

$$\mathcal{M}^d = \prod_{i=1}^d I^M. \quad (167)$$

Clearly higher moments with $d > 1$ do not contain any additional information and are also not given by sums over invariants under general particle rotations. In this example it is also clear that the degree-2 invariants $B_l(q_1, q_2)$, of 3D FXS, can not be extracted from the moments \mathcal{M}^d . The latter only contain information about a two-dimensional slice of the three-dimensional intensity profile while the invariants $B_l(q_1, q_2)$ hold genuine three-dimensional information, as has been discussed in section 2.3.

6.1. Rotational probability distributions and their characteristic functions

To set the stage let us first define what we mean by a rotational probability distribution. In the 2D case we are interested in probability distributions over the special orthogonal

group $\text{SO}(2)$ whose elements can be characterized by a single real number $0 \leq \alpha < 2\pi$ describing the rotation angle. As consequence one may think of $\text{SO}(2)$ as the unit circle and a probability distribution on this space is a positive real valued function $p(\alpha)$ such that⁵⁰

$$\frac{1}{2\pi} \int_{\text{SO}(2)} d\alpha p(\alpha) = \frac{1}{2\pi} \int_0^{2\pi} d\alpha p(\alpha) = 1 \quad (168)$$

and the probability of finding a rotation in the range $[a, b]$, i.e. a particle with the corresponding orientation, is given by

$$\frac{1}{2\pi} \int_a^b d\alpha p(\alpha).$$

Similarly, a probability distribution on $\text{SO}(3)$ is defined by a positive function $p(\omega) = p(\alpha, \beta, \gamma)$, where (α, β, γ) are Euler angles corresponding to the rotation $\omega \in \text{SO}(3)$, such that⁵¹

$$\frac{1}{8\pi^2} \int_{\text{SO}(3)} d\omega p(\omega) = \frac{1}{8\pi^2} \int_0^{2\pi} d\alpha \int_0^\pi d\beta \sin(\beta) \int_0^{2\pi} d\gamma p(\alpha, \beta, \gamma) = 1 \quad (169)$$

and the probability of finding a particle whose orientation state lies in a subset Q of $\text{SO}(3)$ is defined by

$$\frac{1}{8\pi^2} \int_Q d\omega p(\omega).$$

The average or expectation value of arbitrary functions $f(\alpha)$ and $f(\alpha, \beta, \gamma)$ under the above probability distributions then take the form

$$\langle f(\alpha) \rangle_{\text{SO}(2)} = \frac{1}{2\pi} \int_0^{2\pi} d\alpha p(\alpha) f(\alpha), \quad (170a)$$

$$\langle f(\alpha, \beta, \gamma) \rangle_{\text{SO}(3)} = \frac{1}{8\pi^2} \int_0^{2\pi} d\alpha \int_0^\pi d\beta \sin(\beta) \int_0^{2\pi} d\gamma p(\alpha, \beta, \gamma) f(\alpha, \beta, \gamma). \quad (170b)$$

In statistics there is a one to one correspondence between probability distributions of a real-valued random variable X and their characteristic functions, which are defined by the average

$$\langle e^{-iqX} \rangle_{\mathbb{R}} = \int_{-\infty}^{\infty} dx p_X(x) e^{-iqX},$$

i.e. by the Fourier transform of the associated probability density p_X . It is known that the concept of a characteristic function can be generalized to a large class of other probability spaces [145] including those defined over $\text{SO}(2)$ and $\text{SO}(3)$. The corresponding notions of Fourier “transforms” have already been introduced in section 1.7, via the Fourier series given in equations (44) and (53) for $\text{SO}(2)$ and $\text{SO}(3)$, respectively. In the context of

⁵⁰The factor of $1/(2\pi)$ is purely conventional and used to comply with the standard definition of the Fourier series, see equations (44) and (171).

⁵¹Similar to the 2D case the factor $1/(8\pi^2)$ is due to our convention for the Fourier series on $\text{SO}(3)$, see equations (53) and (172). In fact, $8\pi^2$ is the volume of $\text{SO}(3)$, i.e. $\int_{\text{SO}(3)} d\omega = 8\pi^2$.

characteristic functions we shall slightly alter our notation of the Fourier series coefficients to make their analogy to Fourier transforms of the probability density apparent. In the 2D case we shall write \widehat{p}_n for the characteristic function associated to $p(\alpha)$, that is

$$\widehat{p}_n = \frac{1}{2\pi} \int_0^{2\pi} d\alpha p(\alpha) e^{-in\alpha} = \left\langle e^{-in\alpha} \right\rangle_{\text{SO}(2)} \quad \text{with } n \in \mathbb{Z}. \quad (171)$$

It's analog over $\text{SO}(3)$ will be denoted by $\widehat{p}_{m,n}^l$ and is given by

$$\begin{aligned} \widehat{p}_{m,n}^l &= \frac{1}{8\pi^2} \int_0^{2\pi} d\alpha \int_0^\pi d\beta \sin(\beta) \int_0^{2\pi} d\gamma p(\alpha, \beta, \gamma) D_{mn}^l(\alpha, \beta, \gamma)^* \\ &= \left\langle D_{mn}^l(\alpha, \beta, \gamma)^* \right\rangle_{\text{SO}(3)}, \end{aligned} \quad (172)$$

where $l \in \mathbb{N}$ is a natural number and m, n are integers such that $-l \leq m, n \leq l$. Both of the above Fourier series coefficients can be efficiently computed. In the 2D case \widehat{p}_n is, up to a constant prefactor, given by the fast Fourier transform of a uniformly sampled version of the probability density $p(\alpha)$. For the computation of the coefficients $\widehat{p}_{m,n}^l$ a fast algorithm has been developed in [90].⁵² We have already used the latter indirectly to compute the rotation correlation, equation (155), in the alignment step of our reconstruction-workflow.

6.2. FXS moments for arbitrary orientational distributions

With the new rotational averages defined by equation (170) we are now able to derive explicit forms for the FXS moments \mathcal{M}_N^d under arbitrary orientational probability distributions. The first thing to note is that, without loss of generality, we can restrict our derivations to the single-particle moments \mathcal{M}^d . Their extension to the multiple-particle case is again given by observation 2.19. This is because the derivation of this result only depended on the statistical independence between rotations acting on different particles, but not on the uniformity of the corresponding probability distributions. In fact, we never explicitly computed any rotational averages in section 2.5.3. In the following we will restrict our discussion to degree-1 and degree-2 moments. Higher degree moments can however be obtained in complete analogy.

6.2.1. Two-dimensional case

degree-1: By their definition in equation (60) the moments $\mathcal{M}^1(q_1, \phi_1)$ have the form

$$\mathcal{M}^1(q_1, \phi_1) = \left\langle I^M(q_1, \phi_1) \right\rangle_M = \left\langle \mathbf{R}_\alpha I(q_1, \pi/2, \phi_1) \right\rangle_{\text{SO}(2)}. \quad (173)$$

where in the second equality we used that the scattered intensity of a single particle I is independent on its position in the interaction volume to reduce the average over M to the average over $\text{SO}(2)$ and that by definition 2.2 the measured diffraction patterns

⁵²A python version is provided by the package `pysofft`, available at <https://pypi.org/project/pysofft/>.

are obtained in the small-angle limit. Expanding the intensity profile $I(q_1, \pi/2, \phi_1)$, as function of the angle ϕ_1 , in a harmonic series and applying the rotation action over $\text{SO}(2)$ given in (57) yields

$$\begin{aligned}\mathcal{M}^1(q_1, \phi_1) &= \left\langle \sum_n \mathbf{R}_\alpha I_n(q_1) e^{in\phi_1} \right\rangle_{\text{SO}(2)} = \left\langle \sum_n I_n(q_1) e^{in\phi_1 - in\alpha} \right\rangle_{\text{SO}(2)} \\ &= \sum_n I_n(q_1) e^{in\phi_1} \langle e^{-in\alpha} \rangle_{\text{SO}(2)}\end{aligned}$$

Note that the remaining rotational average is precisely the characteristic function associated with the rotational probability distribution from equation (171) and we find

$$\mathcal{M}^1(q_1, \phi_1) = \sum_n I_n(q_1) e^{in\phi_1} \hat{p}_n \qquad \mathcal{M}^1(q_1, n_1) = I_n(q_1) \hat{p}_{n_1}$$

The given relation for $\mathcal{M}^1(q_1, n_1)$, the second definition of the FXS moments (61), are simply the Fourier coefficients of $\mathcal{M}^1(q_1, \phi_1)$ in ϕ_1 . Note that in contrast to the uniform case, presented in equations (99) and (78), the degree-1 moments can give access to intensity harmonic coefficients of arbitrary degree n , if the corresponding value of the characteristic function \hat{p}_n does not vanish. Stated differently, the anisotropic contributions to SAXS patterns, as observed for partially aligned systems of particles, are caused by the presence of higher harmonic coefficients of the single-particle intensity profile, which are weighted by the characteristic function of their orientational probability distribution. This statement will remain true for 3D FXS and explains the origin of anisotropic SAXS patterns, as e.g. observed in [25, 141].

degree-2: The derivation for higher degree moments is conceptually very similar. The important additional insight is, that products of rotation actions can be reduced to a single rotation action, i.e.

$$e^{-im_1\alpha} e^{-im_2\alpha} = e^{-i(m_1+m_2)\alpha}. \quad (174)$$

This seems quite trivial in the two-dimensional case but is actually tightly connected to the fact that functions of type $e^{in\alpha}$ form an orthonormal basis on the Hilbert space of all square integrable functions over $\text{SO}(2)$, which is what allows the formulation of a Fourier series. By extension one can directly conclude that a similar relation must also exist for basis functions of the Fourier series on $\text{SO}(3)$, which will enable the computation of higher degree moments in the 3D case.

For the degree-2 moments in 2D FXS we proceed as follows. Starting from their definition we express all occurring intensities via their harmonic series and apply the rotation action to obtain

$$\begin{aligned}\mathcal{M}^2(q_1, q_2, \phi_1, \phi_2) &= \left\langle \left(\sum_{m_1} \mathbf{R}_\alpha I_{m_1}(q_1) e^{im_1\phi_1} \right) \left(\sum_{m_2} \mathbf{R}_\alpha I_{m_2}(q_2) e^{im_2\phi_2} \right)^* \right\rangle_{\text{SO}(2)} \\ &= \sum_{m_1, m_2} I_{m_1}(q_1) I_{m_2}(q_2)^* e^{i(m_1\phi_1 - m_2\phi_2)} \langle e^{-i(m_1 - m_2)\alpha} \rangle_{\text{SO}(2)}.\end{aligned}$$

The remaining rotational average has again the form of a characteristic function and we can conclude

$$\begin{aligned}\mathcal{M}^2(q_1, q_2, \phi_1, \phi_2) &= \sum_{m_1, m_2} I_{m_1}(q_1) I_{m_2}(q_2)^* e^{i(m_1\phi_1 - m_2\phi_2)} \widehat{p}_{m_1 - m_2} \\ \mathcal{M}^2(q_1, q_2, n_1, n_2) &= I_{n_1}(q_1) I_{n_2}(q_2)^* \widehat{p}_{n_1 - n_2}\end{aligned}$$

6.2.2. Three-dimensional case

By swapping the Fourier series expansion with the expansion into spherical harmonics and replacing the rotation action of SO(2) by the action of SO(3), given in equation (56), we can compute concrete expressions for the FXS moments in the 3D case.

degree-1: We may now follow the same conceptual steps as for the 2D case in order to obtain an expression for the degree-1 moments. The 3D analog of equation (173) is

$$\mathcal{M}^1(q_1, \phi_1) = \langle I^M(q_1, \phi_1) \rangle_M = \langle \mathbf{R}_\omega I(q_1, \theta_\lambda(q_1), \phi_1) \rangle_{\text{SO}(3)},$$

where as usual $\theta_\lambda(q_1)$ describes the restriction on to the Ewald's sphere. We may now expand the intensity I in a spherical harmonic series and apply the rotation action to obtain

$$\begin{aligned}\mathcal{M}^1(q_1, \phi_1) &= \left\langle \sum_{l, m} \mathbf{R}_\omega I_m^l(q_1) Y_m^l(\theta_\lambda(q_1), \phi_1) \right\rangle_{\text{SO}(3)} = \left\langle \sum_{l, m, k} I_k^l(q_1) D_{m, k}^l(\omega)^* Y_m^l(\theta_\lambda(q_1), \phi_1) \right\rangle_{\text{SO}(3)} \\ &= \sum_{l, m, k} I_k^l(q_1) Y_m^l(\theta_\lambda(q_1), \phi_1) \langle D_{m, k}^l(\omega)^* \rangle_{\text{SO}(3)}.\end{aligned}$$

Like in 2D case one finds that the remaining rotational average has the form of a characteristic function, using its definition in equation (172) we find

$$\begin{aligned}\mathcal{M}^1(q_1, \phi_1) &= \sum_{l, m, k} I_k^l(q_1) Y_m^l(\theta_\lambda(q_1), \phi_1) \widehat{p}_{m, k}^l, \\ \mathcal{M}^1(q_1, n_1) &= \sum_{l, k} I_k^l(q_1) \widetilde{P}_l^{n_1}(\theta_\lambda(q_1)) \widehat{p}_{n_1, k}^l,\end{aligned}$$

where $\widetilde{P}_l^{n_1}$ are the scaled associated Legendre polynomials appearing in the definition of the spherical harmonics, see equation (46). It is interesting to note that $\mathcal{M}^1(q_1, \phi_1)$ has itself the form of a spherical harmonic series, i.e.

$$\mathcal{M}^1(q_1, \phi_1) = \sum_{l, m} \left(\sum_k I_k^l(q_1) \widehat{p}_{m, k}^l \right) Y_m^l(\theta_\lambda(q_1), \phi_1).$$

Comparing this result to the series expansion of the single-particle intensity $I(q, \theta, \phi) = \sum_{lm} I_m^l(q) Y_m^l(\theta, \phi)$ allows us to understand rotational averages purely on the level of

spherical harmonic coefficients. The rotational average under the probability distribution $p(\alpha, \beta, \gamma)$ acts on the level of harmonic coefficients via the following substitution rule

$$I_m^l(q_1) \longrightarrow \sum_{k=-l}^l I_k^l(q_1) \widehat{p}_{m,k}^l,$$

which can be thought of as the averaged version of the original rotation action given in equation (56). Another interesting observation is, that in the 3D case non-uniform orientational distribution may alter SAXS patterns non-trivially without introducing anisotropy. This occurs, if the characteristic function has the form $\widehat{p}_{m,k}^l = \delta_{m,0} \widehat{p}_{0,k}^l$. In section 6.4.3 we will see that this is for example the case for dipole transitions caused by a linear polarized pump pulse whose polarization axis is parallel to the propagation direction of the X-ray probe. This particular effect is well known and can also be observed in electron diffraction [146].

degree-2: As already mentioned in the 2D case, we shall need an analogue of equation (174) for the product of Wigner-D matrices $D_{m,n}^l(\omega)$, that from the orthogonal basis for the Fourier series on SO(3). Using the product formula given in equation (266) as well their symmetry relation with respect to complex conjugation from equation (268) we find

$$D_{m_1,k_1}^{l_1}(\omega)^* D_{m_2,k_2}^{l_2}(\omega) = (-1)^{m_2-k_2} \sum_{l=|l_1-l_2|}^{|l_1+l_2|} C_{m_1,-m_2}^{l_1,l_2,l} C_{k_1,-k_2}^{l_1,l_2,l} D_{(m_1-m_2),(k_1-k_2)}^l(\omega)^*, \quad (175)$$

where $C_{n_1,n_2}^{l_1,l_2,l}$ is our shorthand notation for the Clebsch-Gordan coefficients $\langle l_1 n_1 l_2 n_2 | l(n_1 + n_2) \rangle$, as introduced in equation (83b).

Now we may start our derivation as usual by expanding all intensities in their harmonic series and isolate the rotational average using the rotation action, that is

$$\begin{aligned} \mathcal{M}^2(q_1, q_2, \phi_1, \phi_2) &= \left\langle \left(\sum_{l_1, m_1} \mathbf{R}_\omega I_{m_1}^{l_1}(q_1) Y_{m_1}^{l_1}(\theta_\lambda(q_1), \phi_1) \right) \right. \\ &\quad \times \left. \left(\sum_{l_2, m_2} \mathbf{R}_\omega I_{m_2}^{l_2}(q_2)^* Y_{m_2}^{l_2}(\theta_\lambda(q_2), \phi_2)^* \right) \right\rangle_{\text{SO}(3)} \\ &= \sum_{\substack{l_1, m_1, k_1 \\ l_2, m_2, k_2}} I_{k_1}^{l_1}(q_1) I_{k_2}^{l_2}(q_2)^* Y_{m_1}^{l_1}(\theta_\lambda(q_1), \phi_1) Y_{m_2}^{l_2}(\theta_\lambda(q_2), \phi_2)^* \\ &\quad \times \langle D_{m_1, k_1}^{l_1}(\omega)^* D_{m_2, k_2}^{l_2}(\omega) \rangle_{\text{SO}(3)} \end{aligned}$$

The product formula from equation (175) now allows us to express the remaining average via the characteristic function of the rotational probability density, i.e.

$$\langle D_{m_1, k_1}^{l_1}(\omega)^* D_{m_2, k_2}^{l_2}(\omega) \rangle_{\text{SO}(3)} = (-1)^{m_2-k_2} \sum_{l=|l_1-l_2|}^{|l_1+l_2|} C_{m_1,-m_2}^{l_1,l_2,l} C_{k_1,-k_2}^{l_1,l_2,l} \widehat{p}_{(m_1-m_2),(k_1-k_2)}^l.$$

In analogy to equations (104) and (107) we may now introduce generalized versions of F^l , \tilde{F}_n^l and B_l via

$$K_{l_1, l_2} = \sqrt{2l_1 + 1} \sqrt{2l_2 + 1} \quad (176)$$

$$F_{m_1, m_2}^{l_1, l_2}(q_1, q_2, \phi_1, \phi_2) = K_{l_1, l_2}^{-1} Y_{m_1}^{l_1}(\theta_\lambda(q_1), \phi_1) Y_{m_2}^{l_2}(\theta_\lambda(q_2), \phi_2)^* \quad (177)$$

$$\tilde{F}_{n_1, n_2}^{l_1, l_2}(q_1, q_2) = K_{l_1, l_2}^{-1} \tilde{P}_{l_1}^{n_1}(\theta_\lambda(q_1)) \tilde{P}_{l_2}^{n_2}(\theta_\lambda(q_2)) \quad (178)$$

$$B_{m_1, m_2}^{l_1, l_2}(q_1, q_2) = K_{l_1, l_2} \sum_{k_1, k_2} I_{k_1}^{l_1}(q_1) I_{k_2}^{l_2}(q_2)^* (-1)^{m_2 - k_2} \\ \times \sum_l C_{m_1, -m_2}^{l_1, l_2, l} C_{k_1, -k_2}^{l_1, l_2, l} \hat{p}_{(m_1 - m_2), (k_1 - k_2)}^l. \quad (179)$$

Note, that these definitions are chosen such that for suitable parameters they coincide with their uniform expressions, i.e.

$$\tilde{F}_n^l(q_1, q_2) = \tilde{F}_{n, n}^{l, l}(q_1, q_2), \\ F_l(q_1, q_2, \phi_1 - \phi_2) = \sum_m F_{m, m}^{l, l}(q_1, q_2, \phi_1, \phi_2).$$

A derivation of the equivalence of $B_{m_1, m_2}^{l_1, l_2}(q_1, q_2)$ and $B_l(q_1, q_2)$ for a uniform probability distribution can be found in section 6.4. In summary, the above definitions allow us to represent the degree-2 moments for arbitrary rotational probability distribution as follows

$$\mathcal{M}^2(q_1, q_2, \phi_1, \phi_2) = \sum_{l_1, l_2, m_1, m_2} F_{m_1, m_2}^{l_1, l_2}(q_1, q_2, \phi_1, \phi_2) B_{m_1, m_2}^{l_1, l_2}(q_1, q_2), \\ \mathcal{M}^2(q_1, q_2, n_1, n_2) = \sum_{l_1, l_2} \tilde{F}_{n_1, n_2}^{l_1, l_2}(q_1, q_2) B_{n_1, n_2}^{l_1, l_2}(q_1, q_2).$$

Let us summarize our findings from this section as an observation

Observation 6.1 (FXS moments for arbitrary rotational distributions)

Consider the 2D and 3D cases of FXS as described in definitions 2.1 and 2.2, respectively. Instead of the [uniform distribution](#) assumption, let the individual particles in each sample ρ^M follow an arbitrary probability distributions $p(\alpha)$ (over $\text{SO}(2)$) in the 2D case or $p(\alpha, \beta, \gamma)$ (over $\text{SO}(3)$) for the 3D case. Consider \hat{p}_n and $\hat{p}_{m, n}^l$ to be the corresponding characteristic functions. The single particle moments of FXS for degree-1 and degree-2 are then given in the 2D case by

$$\mathcal{M}^1(q_1, \phi_1) = \sum_m I_m(q_1) e^{in\phi_1} \hat{p}_m, \quad (180a)$$

$$\mathcal{M}^1(q_1, n_1) = I_{n_1}(q_1) \hat{p}_{n_1}, \quad (180b)$$

$$\mathcal{M}^2(q_1, q_2, \phi_1, \phi_2) = \sum_{m_1, m_2} I_{m_1}(q_1) I_{m_2}(q_2)^* e^{i(m_1\phi_1 - m_2\phi_2)} \hat{p}_{m_1 - m_2}, \quad (180c)$$

$$\mathcal{M}^2(q_1, q_2, n_1, n_2) = I_{n_1}(q_1) I_{n_2}(q_2)^* \hat{p}_{n_1 - n_2} \quad (180d)$$

and for 3D FXS via

$$\mathcal{M}^1(q_1, \phi_1) = \sum_{l,m,k} I_k^l(q_1) Y_m^l(\theta_\lambda(q_1), \phi_1) \hat{p}_{m,k}^l, \quad (181a)$$

$$\mathcal{M}^1(q_1, n_1) = \sum_{l,k} I_k^l(q_1) \tilde{P}_l^{n_1}(\theta_\lambda(q_1)) \hat{p}_{n_1,k}^l, \quad (181b)$$

$$\mathcal{M}^2(q_1, q_2, \phi_1, \phi_2) = \sum_{l_1, l_2, m_1, m_2} F_{m_1, m_2}^{l_1, l_2}(q_1, q_2, \phi_1, \phi_2) B_{m_1, m_2}^{l_1, l_2}(q_1, q_2), \quad (181c)$$

$$\mathcal{M}^2(q_1, q_2, n_1, n_2) = \sum_{l_1, l_2} \tilde{F}_{n_1, n_2}^{l_1, l_2}(q_1, q_2) B_{n_1, n_2}^{l_1, l_2}(q_1, q_2), \quad (181d)$$

where the symbols $F_{m_1, m_2}^{l_1, l_2}$, $\tilde{F}_{n_1, n_2}^{l_1, l_2}$ and $B_{n_1, n_2}^{l_1, l_2}$ are defined in equations (176)-(179).

Remark 6.2 (Averaged angular cross-correlations) *As a direct consequence of observation 6.1 and equation (109), we can obtain explicit expressions for the harmonic coefficients of the averaged angular cross-correlation $\mathcal{C}_n(q_1, q_2)$ for arbitrary rotational probability distributions by choosing $n_1 = n_2 = n$ in equations (180d) or (181d).*

6.3. Consequences for FXS

With observation 6.1 at hand we are now able to characterize the two possible use cases mentioned at the beginning of this chapter in more detail. Let us again start our discussion for 2D FXS, where we can make the following statements.

1. Independent on the rotational probability distribution $p(\alpha)$ one may access the single-particle invariants $B_n(q_1, q_2)$ via

$$\mathcal{M}^2(q_1, q_2, n, n) = I_n(q_1) I_n(q_2)^* \hat{p}_{n-n} = B_n(q_1, q_2) \hat{p}_0 = B_n(q_1, q_2) \quad (182)$$

Consequently one may use the reconstruction workflow described in section 3, regardless of the probability distribution $p(\alpha)$.⁵³

2. If harmonic coefficients of the intensity $I(q_1, \pi/2, \phi)$ are known one may extract the values of the characteristic function from the degree-1 moments given in equation (180b), i.e.

$$\hat{p}_n = \frac{\mathcal{M}^1(q_1, n)}{I_n(q_1)} \quad (183)$$

The above equation can only be used for a given index n if $I_n(q_1)$ is not identically 0 for all parameter values q_1 . Since by Friedels symmetry $I_n = 0$ for all odd n we can at most recover \hat{p}_n for even indices. Computing the Fourier series with the even coefficients \hat{p}_n yields the symmetrized probability density $(p(\alpha) + p(\alpha + \pi))/2$.

⁵³Note that all probability distributions satisfy $\hat{p}_0 = 1$ by definition, see equation (168), since \hat{p}_0 corresponds to the probability of finding a particle in any arbitrary rotation state.

For the 3D case the situation is less favorable. In general it is not possible to extract the degree-2 invariants, even if the probability distribution $p(\alpha, \beta, \gamma)$ is known. At the beginning of this chapter we have seen this for the example of complete alignment. In equation (181d) this insight manifests itself via the dependence of the unknowns $B_{n_1, n_2}^{l_1, l_2}$ on the harmonic orders n_1 and n_2 which causes the linear system to be highly under determined. The situation becomes slightly simpler for $n_1 = n_2 = n$. In this case $\mathcal{M}^2(q_1, q_2, n, n)$ can be factored such that the unknowns do not depend on n , via

$$\mathcal{M}^2(q_1, q_2, n, n) = \mathcal{C}_n(q_1, q_2) = \sum_{l_1, l_2} \sum_{l=|l_1-l_2|}^{l_1+l_2} \tilde{F}_n^{l_1, l_2, l}(q_1, q_2) B_{l_1, l_2, l}(q_1, q_2)$$

with

$$\begin{aligned} \tilde{F}_n^{l_1, l_2, l}(q_1, q_2) &= (-1)^n C_{-n, n}^{l_1, l_2, l} \tilde{P}_{l_1}^n(q_1) \tilde{P}_{l_2}^n(q_2) \\ B_{l_1, l_2, l}(q_1, q_2) &= \sum_{k_1, k_2} I_{k_1}^{l_1}(q_1) I_{k_2}^{l_2}(q_2)^* (-1)^{-k_1} C_{-k_1, k_2}^{l_1, l_2, L} \hat{p}_{0, (k_2-k_1)}^L. \end{aligned}$$

However, for a given harmonic cutoff L , such that $l_1, l_2 \leq L$, there are still far more unknowns $B_{l_1, l_2, l}$ than equations \mathcal{C}_n . Whether the degree-2 invariants may be accessed for specific distributions other than the uniform one remains an open question. In section 6.4 we will give analytic expressions for several 3D probability distribution which may serve as a starting point for further investigations. Independent from this question one may use the derived equations in model based approaches, similar to [22], as efficient tool for the simulation of averaged angular correlations under arbitrary rotational distributions.

The statement that the rotational probability distribution $p(\alpha, \beta, \gamma)$ can be computed from the degree-1 observables, i.e. the averaged SAXS intensity, if the particle structure is known, remains true in the 3D setting. For any harmonic cutoff L and each fixed n (with $|n| \leq L$) equation (181b) is a system of S linear equations in at most $(L+1)^2$ unknown parameters $\hat{p}_{n, k}^l$, where S is the number of radial grid points. The matrix representation of this linear system for fixed n_1 is given by

$$(\mathbf{A}_{n_1})_{i, (l, k)} = I_k^l(q_i) \tilde{P}_l^{n_1}(\theta_\lambda(q_i)) \quad (184)$$

and we may restate equation (181b) in its matrix form via

$$\mathcal{M}^1 = \mathbf{A}_{n_1} \hat{\mathbf{p}}_{n_1} = \begin{bmatrix} I_{-n_1}^{n_1}(q_1) \tilde{P}_{n_1}^{n_1}(\theta_\lambda(q_1)) \cdots \cdots I_L^L(q_1) \tilde{P}_{n_1}^L(\theta_\lambda(q_1)) \\ \vdots \\ I_{-n_1}^{n_1}(q_S) \tilde{P}_{n_1}^{n_1}(\theta_\lambda(q_S)) \cdots \cdots I_L^L(q_S) \tilde{P}_{n_1}^L(\theta_\lambda(q_S)) \end{bmatrix} \begin{bmatrix} \hat{p}_{n_1, -n_1}^{n_1} \\ \vdots \\ \hat{p}_{n_1, L}^L \end{bmatrix}$$

Note that the number of pairs (l, k) is given by $\sum_{l=|n_1|}^L (2l+1) = (L+1)^2 - n_1^2$, which is exactly the number of independent parameters values of $\hat{p}_{n_1, k}^l$ for fixed n_1 and $l \leq L$. This implies, that as long as the number of radial grid points is large enough, i.e. $S \geq (L+1)^2$,

and $I_k^l(q_i)$ is such that the matrix \mathbf{A}_{n_1} has full rank, one may solve these linear systems using least squares methods. Note that the Friedel symmetry again implies that $I_m^l(q)$ are zero for odd l and we may retrieve the characteristic function $\widehat{p}_{m,k}^l$ only for even l . Using these coefficients in the Fourier series on $SO(3)$, equation (52), and its fast implementation given in [90], allows one to compute the symmetrized rotational probability density.

6.4. Analytic expressions of characteristic functions for selected distributions

For any given probability distribution on $SO(2)$ or $SO(3)$ it is always possible to compute the corresponding characteristic function numerically. In this chapter we will see that for selected distributions it is also possible to obtain analytic expressions for their characteristic functions. Initially we will revisit the case of a uniform probability distribution to observe how the generalized expressions for the FXS moments from section 6.2 reduce to the moments given in section 2.5.1. Similarly we shall revisit the case of complete alignment, which has been informally discussed at the beginning of chapter 6. After the treatment of these known cases we will define *effectively spherical* distributions, in which the probability of a particles rotation state only depends on the direction of a single vector inside the particle, e.g. the direction of its transition dipole moment. The last two cases for which we will be able to provide analytic expression for the characteristic functions are Gaussian distributions as well as analogues of distributions over the real line such as Cauchy and Laplace distributions.

6.4.1. Uniform distribution

The uniform probability distributions in the 2D and 3D cases are given by

$$p(\alpha) = 1, \quad (185a)$$

$$p(\alpha, \beta, \gamma) = 1. \quad (185b)$$

In the 2D case this results in the following form of the characteristic function

$$\widehat{p}_n = \frac{1}{2\pi} \int_0^{2\pi} d\alpha p(\alpha) e^{-in\theta} = \delta_{n,0}, \quad (186)$$

where $\delta_{n,0}$ is the Kronecker delta symbol. For the 3D case we similarly find

$$\begin{aligned} \widehat{p}_{n,k}^l &= \frac{1}{8\pi^2} \int_0^{2\pi} d\alpha \int_0^\pi d\beta \sin(\beta) \int_0^{2\pi} d\gamma p(\alpha, \beta, \gamma) D_{n,k}^l(\alpha, \beta, \gamma)^* \\ &= \frac{1}{8\pi^2} \int_0^{2\pi} d\alpha \int_0^\pi d\beta \sin(\beta) \int_0^{2\pi} d\gamma D_{n,k}^l(\alpha, \beta, \gamma)^*. \end{aligned}$$

Using the orthogonality relation of Wigner-D matrices, given by equation (264), in the special case of $D_{n',k'}^l = D_{0,0}^0 = 1$, allows us to compute the remaining integrals and conclude

$$\widehat{p}_{n,k}^l = \delta_{l,0} \delta_{n,0} \delta_{k,0}. \quad (187)$$

We may now use these characteristic functions to compute the corresponding FXS moments via observation 6.1. In the interest of brevity we shall only list the moments in their second form defined in equation (61). For the 2D case this implies

$$\begin{aligned}\mathcal{M}^1(q_1, n_1) &= \delta_{n_1,0} I_0(q_1) = \delta_{n_1,0} I^{\text{SAXS}}(q_1) \\ \mathcal{M}^2(q_1, q_2, n_1, n_2) &= \delta_{n_1, n_2} I_{n_1}(q_1) I_{n_2}(q_2)^*,\end{aligned}$$

which correspond to the degree-1 and degree-2 invariants presented in equations (78a) and (80a). For the degree-1 moments in 3D FXS we similarly find

$$\begin{aligned}\mathcal{M}^1(q_1, n_1) &= \sum_{l,k} I_k^l(q_1) \tilde{P}_l^{n_1}(\theta_\lambda(q_1)) \delta_{l,0} \delta_{n_1,0} \delta_{k,0} = \delta_{n_1,0} I_0^0(q_1) \tilde{P}_0^0(\theta_\lambda(q_1)) \\ &= \delta_{n_1,0} I^{\text{SAXS}}(q_1),\end{aligned}$$

which was already given in (103). Last but not least, the generalized coefficients $B_{n_1, n_2}^{l_1, l_2}$ of the degree-2 moments, given in equation (179), can be simplified via

$$\begin{aligned}B_{m_1, m_2}^{l_1, l_2}(q_1, q_2) &= K_{l_1, l_2} \sum_{k_1, k_2} I_{k_1}^{l_1}(q_1) I_{k_2}^{l_2}(q_2)^* (-1)^{m_2 - k_2} \\ &\quad \times \sum_l C_{m_1, -m_2}^{l_1, l_2, l} C_{k_1, -k_2}^{l_1, l_2, l} \delta_{l,0} \delta_{m_1, m_2} \delta_{k_1, k_2} \\ &= \delta_{m_1, m_2} K_{l_1, l_2} \sum_{k_1} I_{k_1}^{l_1}(q_1) I_{k_1}^{l_2}(q_2)^* (-1)^{m_1 - k_1} C_{m_1, -m_1}^{l_1, l_2, 0} C_{k_1, -k_1}^{l_1, l_2, 0}.\end{aligned}$$

Note that the Clebsch-Gordan coefficients of the form $C_{m_1, -m_1}^{l_1, l_2, 0}$ can be expressed directly [86, equations 3.16c and 3.23], via

$$C_{m, -m}^{l_1, l_2, 0} = \delta_{l_1, l_2} \frac{(-1)^{l_1 - m}}{\sqrt{2l_1 + 1}}.$$

Substituting this relation into our expression for $B_{m_1, m_2}^{l_1, l_2}(q_1, q_2)$ results in

$$B_{m_1, m_2}^{l_1, l_2}(q_1, q_2) = \delta_{l_1, l_2} \delta_{m_1, m_2} \sum_{k_1} I_{k_1}^{l_1}(q_1) I_{k_1}^{l_2}(q_2)^* = \delta_{l_1, l_2} \delta_{m_1, m_2} B_{l_1}(q_1, q_2),$$

which are the familiar degree-2 invariants from equation (80b).⁵⁴ Correspondingly we find that the degree-2 moments $\mathcal{M}^2(q_1, q_2, n_1, n_2)$ will take the same form as in equation (107).

6.4.2. Delta distribution (perfect alignment)

Coming from the completely delocalized uniform distribution we will now revisit the case of complete alignment, that has been discussed at the beginning of chapter 6. The corresponding rotational distributions are delta distributions, i.e.

$$\rho(\theta) = \delta(\theta), \quad (188)$$

$$\rho(\alpha, \beta, \gamma) = \delta(\alpha, \beta, \gamma). \quad (189)$$

⁵⁴The missing factor $\frac{1}{2l_1 + 1}$ is contained in the definition of $\tilde{F}_{m_1, m_2}^{l_1, l_2}(q_1, q_2)$ via K_{l_1, l_2} , see equations (176)-(179).

By the defining integral property of a delta distribution we directly find the corresponding characteristic functions to be

$$\widehat{p}_n = e^{-in0} = 1 \quad (190)$$

$$\widehat{p}_{n,k}^l = D_{n,k}^l(0, 0, 0) = \delta_{n,k} . \quad (191)$$

We expect to find, that the FXS moments simply correspond to products of the intensity slice $I(q, \theta_\lambda(q), \phi)$ given by the unique rotation state around which the delta distributions is centered, as observed in equation (167). In the 2D case this is directly evident from the generalized moments given in equations (180a) and (180c). The same is true for the degree-1 moment in the 3D formulation of FXS via equation (181a). It only remains to verify that the degree-2 moments in 3D FXS are given as product of intensity slices. Using the characteristic function from equation (191) in the definition of the generalized degree-2 invariants $B_{m_1, m_2}^{l_1, l_2}$ (179), results in

$$\begin{aligned} B_{m_1, m_2}^{l_1, l_2}(q_1, q_2) &= K_{l_1, l_2} \sum_{k_1, k_2} I_{k_1}^{l_1}(q_1) I_{k_2}^{l_2}(q_2)^* (-1)^{m_2 - k_2} \\ &\quad \times \delta_{(m_1 - m_2), (k_1 - k_2)} \sum_l C_{m_1, -m_2}^{l_1, l_2, l} C_{k_1, -k_2}^{l_1, l_2, l} . \end{aligned}$$

The remaining sum over a product of Clebsch-Gordan coefficients can be evaluated using the orthogonality relation given in equation (270) and yields

$$\begin{aligned} B_{m_1, m_2}^{l_1, l_2}(q_1, q_2) &= K_{l_1, l_2} \sum_{k_1, k_2} I_{k_1}^{l_1}(q_1) I_{k_2}^{l_2}(q_2)^* (-1)^{m_2 - k_2} \delta_{(m_1 - m_2), (k_1 - k_2)} \delta_{m_1, k_1} \\ &= K_{l_1, l_2} \sum_{k_1, k_2} I_{k_1}^{l_1}(q_1) I_{k_2}^{l_2}(q_2)^* (-1)^{m_2 - k_2} \delta_{m_2, k_2} \delta_{m_1, k_1} \\ &= K_{l_1, l_2} I_{m_1}^{l_1}(q_1) I_{m_2}^{l_2}(q_2)^* . \end{aligned}$$

This form of the degree-2 invariants forces the corresponding FXS moments \mathcal{M}^2 , see equation (181c), to factor into the expected product of Ewald's sphere slices of the scattered intensity, i.e.

$$\begin{aligned} \mathcal{M}^2(q_1, q_2, \phi_1, \phi_2) &= \sum_{l_1, l_2, m_1, m_2} F_{m_1, m_1}^{l_1, l_2}(q_1, q_2, \phi_1, \phi_2) K_{l_1, l_2} I_{m_1}^{l_1}(q_1) I_{m_1}^{l_2}(q_2)^* \\ &= \left(\sum_{l_1, m_1} Y_{m_1}^{l_1}(\theta_\lambda(q_1), \phi_1) I_{m_1}^{l_1}(q_1) \right) \left(\sum_{l_2, m_2} Y_{m_2}^{l_2}(\theta_\lambda(q_2), \phi_2)^* I_{m_2}^{l_2}(q_2)^* \right) \\ &= I(q_1, \theta_\lambda(q_1), \phi_1) I(q_2, \theta_\lambda(q_2), \phi_2) , \end{aligned}$$

which completes our derivation.

6.4.3. Effectively spherical distributions

An important case of probability distributions can be obtained by demanding that the probability of finding a molecule or any other three-dimensional object in a certain orientation only depends on a single direction (or vector) inside the molecule. This immediately

implies that we can describe its orientational probability density $\rho(\alpha, \beta, \gamma)$ as a function of α and β only. To see this let us denote the probability defining direction vector by \mathbf{m} and assume, without loss of generality, that in the default orientation \mathbf{m} points along the z direction (\mathbf{e}_z) of the coordinate system.⁵⁵ Any other rotational state of the given object is then specified by three Euler angles (α, β, γ) and the corresponding consecutive rotation $\mathbf{R}_{(\alpha, \beta, \gamma)}$ around the fixed coordinate axes Z, Y and Z axis. The direction of \mathbf{m} in state (α, β, γ) is therefore given by

$$\mathbf{m}(\alpha, \beta, \gamma) = \mathbf{R}_{(\alpha, \beta, \gamma)} \mathbf{e}_z = \mathbf{R}_{(\alpha, \beta, 0)} \mathbf{e}_z = \mathbf{m}(\alpha, \beta), \quad (192)$$

which only depends on α and β . The name *effectively spherical* reflects the fact that the rotational states of a single vector are in one-to-one correspondence to points on a sphere and we can interpret the Euler angles β and α as the azimuthal angle θ and polar angle ϕ of said sphere, in accordance with the usual convention of spherical coordinates. All effectively spherical probability densities $\rho(\alpha, \beta)$ have characteristic functions of the form

$$\hat{p}_{m,n}^l = \frac{1}{8\pi^2} \int_0^{2\pi} d\alpha \int_0^\pi d\beta \sin(\beta) \int_0^{2\pi} d\gamma p(\alpha, \beta) D_{mn}^l(\alpha, \beta, \gamma)^* = \delta_{n,0} \hat{p}_{m,0}^l \quad (193)$$

By formula (181b) the degree-1 moments of such a probability distribution are given by

$$\mathcal{M}^1(q_1, n_1) = \sum_{l,k} I_k^l(q_1) \tilde{P}_l^{n_1}(\theta_\lambda(q_1)) \delta_{k,0} \hat{p}_{n_1,0}^l = \sum_l I_0^l(q_1) \tilde{P}_l^{n_1}(\theta_\lambda(q_1)) \hat{p}_{n_1,0}^l \quad (194)$$

In the following we discuss a typical case, in which effectively spherical orientation distributions are observed.

Excitation by linear polarized light When considering electronic excitations by linear polarized light, the transition probability of a given molecule depends on the angle $\sphericalangle(\mathbf{m}, \boldsymbol{\epsilon})$ between the corresponding normalized transition dipole moment \mathbf{m} and the polarization direction $\boldsymbol{\epsilon}$ of the light[147, equation 15.4-6]. In order to keep the resulting equations simple we will assume that the polarization axis is parallel to the z -axis, i.e. $\boldsymbol{\epsilon} = \mathbf{e}_z$. In a corresponding pump-probe experiment this assumption demands that the polarization of the pump laser is parallel to the propagation direction of the X-ray probe pulse.⁵⁶ A visualization of this geometry can be found in figure 53. Under these assumptions we find the probability defining angle $\sphericalangle(\mathbf{m}(\alpha, \beta), \mathbf{e}_z)$ to be given by

$$\sphericalangle(\mathbf{m}(\alpha, \beta), \mathbf{e}_z) = \arccos(\langle \mathbf{m}, \mathbf{e}_z \rangle), \quad (195)$$

where $\langle \mathbf{m}, \mathbf{e}_z \rangle$ denotes the scalar product between \mathbf{m} and \mathbf{e}_z . Applying our general result for *effectively spherical* probability distributions from equation (192) results in

⁵⁵We choose the z direction because we follow the *zyz* convention for Euler angles as mentioned in section 1.7

⁵⁶This is because our description of the Ewald's sphere slice via the momentum-transfer dependence of the azimuthal angle $\theta_\lambda(q)$, as introduced in equation (12), is only valid if the X-ray probe pulse propagates along the z -axis.

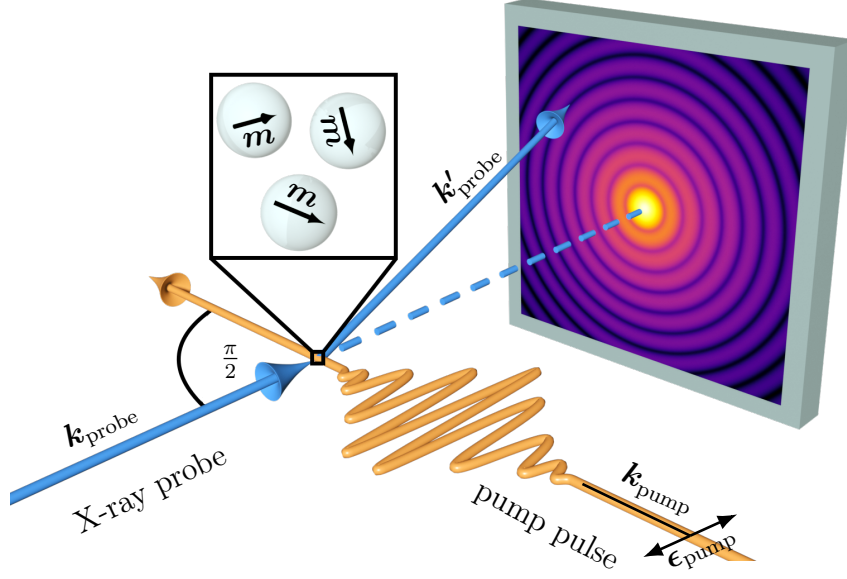


Figure 53: Pump-probe scattering geometry under the conditions that the X-ray probe pulse (blue) is orthogonal to pump pulse (orange) and the polarization ϵ_{pump} is parallel to the propagation direction $\mathbf{k}_{\text{probe}}$ of the probe pulse. The spheres in the inset represent particles in the interaction region, whose transition dipole moments \mathbf{m} are given by the black arrows.

$$\begin{aligned} \angle(\mathbf{m}(\alpha, \beta), \mathbf{e}_z) &= \arccos(\langle \mathbf{R}_{(\alpha, \beta, 0)} \mathbf{e}_z, \mathbf{e}_z \rangle) = \arccos(\langle \mathbf{R}_{(\alpha, 0, 0)} \mathbf{R}_{(0, \beta, 0)} \mathbf{e}_z, \mathbf{R}_{(\alpha, 0, 0)} \mathbf{e}_z \rangle) \\ &= \arccos(\langle \mathbf{R}_{(0, \beta, 0)} \mathbf{e}_z, \mathbf{e}_z \rangle) = \beta, \end{aligned} \quad (196)$$

where in the second step we used that $\mathbf{e}_z = \mathbf{R}_{(\alpha, 0, 0)} \mathbf{e}_z$ since a rotation around the z -axis does not change vectors pointing along the rotation axis. A visual representation of this derivation can be found in Figure 54.

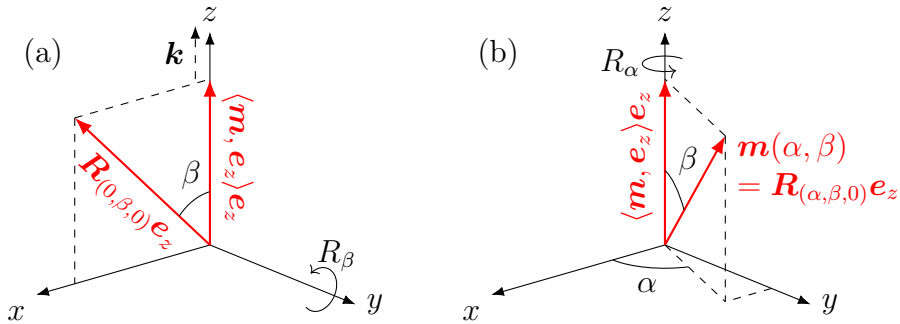


Figure 54: Visual representation of $\angle(\mathbf{m}(\alpha, \beta), \mathbf{e}_z) = \beta$. The transition dipole moment direction $\mathbf{m} = \mathbf{R}_{(\alpha, \beta, 0)} \mathbf{e}_z$ can be obtained by first applying a rotation $\mathbf{R}_{(0, \beta, 0)}$ around the y -axis to \mathbf{e}_z , shown in (a), followed by a rotation $\mathbf{R}_{(\alpha, 0, 0)}$ around the z -axis, as depicted in (b). From this it becomes clear that second rotation by α does not influence the angle between \mathbf{m} and the z -axis and that said angle is equal to β .

It has been shown that, considering single photon absorption, the orientational distributions of excited molecules follows a $\cos(\beta)^2$ distribution [142, 146]. Moreover in the case of multi-photon absorption a $\cos(\beta)^{2\eta}$ distribution was proposed [148]. The main feature of said distributions is that they are bimodal i.e. they have two maxima shifted by π with respect to each other. Another common bimodal distribution in statistics, is the Watson distribution [149], which is proportional to $e^{\kappa \cos(\beta)^2}$ for $\kappa > 0$. Under multiplication with their corresponding normalization constants the above mentioned probability distributions are given by

$$p(\eta; \alpha, \beta, \gamma) = K_{\cos} \cos(\beta)^{2\eta} \quad \text{with } K_{\cos} = 2\eta + 1, \quad (197)$$

$$p(\kappa; \alpha, \beta, \gamma) = K_W e^{\kappa \cos(\beta)^2} \quad \text{with } K_W = \frac{2}{\sqrt{\pi}} \frac{i\sqrt{\kappa}}{\operatorname{erf}(i\sqrt{\kappa})}, \quad (198)$$

where $\operatorname{erf}(x)$ denotes the error function. We will show that the corresponding characteristic functions are

$$\widehat{p}_{n,k}^l(\eta) = \begin{cases} K_{\cos} \frac{2^{l+1}(2\eta)!(\eta+\frac{l}{2}+1)!}{(\eta-\frac{l}{2})!(2\eta+l+2)!} & l \text{ even, } l \leq 2\eta, k = n = 0 \\ 0 & \text{otw.} \end{cases} \quad (199)$$

$$\widehat{p}_{n,k}^l(\kappa) = \begin{cases} K_W \sum_{m=0}^{\infty} \frac{\kappa^m}{m!} \frac{2^{l+1}(2m)!(m+\frac{l}{2}+1)!}{(m-\frac{l}{2})!(2m+l+2)!} & l \text{ even, } k = n = 0 \\ 0 & \text{otw.} \end{cases} \quad (200)$$

Let us first show that the normalization constants K_{\cos} and K_W are chosen correctly. For the cosine distribution we observe

$$\int_0^{2\pi} d\alpha \int_0^{\pi} d\beta \sin(\beta) \int_0^{2\pi} d\gamma \frac{K_{\cos}}{8\pi^2} \cos(\beta)^{2\eta} = \frac{K_{\cos}}{2} \int_{-1}^1 dx x^{2\eta} = \frac{K_{\cos}}{2\eta+1} = 1, \quad (201)$$

where as for the Watson distribution one finds

$$\int_0^{2\pi} d\alpha \int_0^{\pi} d\beta \sin(\beta) \int_0^{2\pi} d\gamma \frac{K_W}{8\pi^2} e^{\kappa \cos(\beta)^2} = \frac{K_W}{2} \int_{-1}^1 dx e^{\kappa x^2} \quad (202)$$

$$= \frac{K_W}{2} \frac{1}{i\sqrt{\kappa}} \int_{-i\sqrt{\kappa}}^{i\sqrt{\kappa}} dy e^{-y^2} = K_W \frac{1}{i\sqrt{\kappa}} \int_0^{i\sqrt{\kappa}} dy e^{-y^2} \quad (203)$$

$$= K_W \frac{\sqrt{\pi} \operatorname{erf}(i\sqrt{\kappa})}{2 i\sqrt{\kappa}} = 1. \quad (204)$$

Going back to the cosine case we may now compute its characteristic function as follows

$$\begin{aligned} \widehat{p}_{n,k}^l(\eta) &= \frac{K_{\cos}}{8\pi^2} \int_0^{2\pi} d\alpha \int_0^{\pi} d\beta \sin(\beta) \int_0^{2\pi} d\gamma \cos(\beta)^{2\eta} \underbrace{e^{i\alpha} d_{nk}^l(\beta) e^{ik\gamma}}_{=D_{nk}^l(\alpha,\beta,\gamma)^*} \\ &= \frac{K_{\cos}}{2} \delta_{k,0} \delta_{n,0} \int_0^{\pi} d\beta \sin(\beta) \cos(\beta)^{2\eta} P_l(\cos(\beta)) \end{aligned}$$

where in the last step we used the well known fact, that for $n = k = 0$ the small Wigner-d matrices are Legendre polynomials, see equation (269). The resulting integral can be further simplified by substituting $x = \cos(\beta)$ which yields

$$\widehat{p}_{n,k}^l(\eta) = \frac{K_{\cos}}{2} \delta_{n,0} \delta_{k,0} \int_{-1}^1 dx x^{2\eta} P_l(x). \quad (205)$$

Since the $P_l(x)$ is even for even l and odd otherwise we know that the integral in equation (205) is zero if l is odd, therefore we continue examining $\widehat{p}_{n,k}^{2l}$ only. Because the complete integrand is now even we may reduce the integral domain and obtain

$$\widehat{p}_{n,k}^{2l}(\eta) = K_{\cos} \delta_{n,0} \delta_{k,0} \int_0^1 dx x^{2\eta} P_{2l}(x). \quad (206)$$

The remaining integral is given in [150, equation 14.17.5]

$$\int_0^1 dx x^{2\eta} P_{2l}(x) = \frac{\Gamma(\eta + \frac{1}{2}) \Gamma(\eta + 1)}{2\Gamma(\eta - l + 1) \Gamma(\eta + l + \frac{3}{2})}$$

and simplifies under usage of the Gamma function relations [150, 5.4.1 and 5.5.5], i.e. $\Gamma(n + 1) = n!$ and $\Gamma(2z)\sqrt{\pi} = 2^{2z-1}\Gamma(z)\Gamma(z + \frac{1}{2})$, to

$$\begin{aligned} \int_0^1 dx x^{2\eta} P_{2l}(x) &= \frac{1}{2} \frac{\sqrt{\pi}}{2^{2\eta}} \frac{(2\eta)!}{(\eta - l)!} \frac{\Gamma(\eta + l + 2)}{\Gamma(\eta + l + \frac{3}{2}) \Gamma(\eta + l + 2)} \\ &= 2^{2l+1} \frac{(2\eta)!}{(\eta - l)!} \frac{(\eta + l + 1)!}{(2\eta + 2l + 2)!} \end{aligned} \quad (207)$$

which together with eq. (206) results in formula (199) for the characteristic function of the cosine distribution. Equation (200) for the characteristic function of a Watson distribution can be obtained as follows

$$\begin{aligned} \widehat{p}_{n,k}^l(\kappa) &= \frac{K_W}{8\pi^2} \int_0^{2\pi} d\alpha \int_0^\pi d\beta \sin(\beta) \int_0^{2\pi} d\gamma e^{\kappa \cos(\beta)^2} \underbrace{e^{i\alpha} d_{nk}^l(\beta) e^{i\kappa\gamma}}_{=D_{nk}^l(\alpha,\beta,\gamma)^*} \\ &= \frac{K_W}{2} \delta_{n,0} \delta_{k,0} \int_0^\pi d\beta \sin(\beta) e^{\kappa \cos(\beta)^2} P_l(\cos(\beta)) = \frac{K_W}{2} \delta_{n,0} \delta_{k,0} \int_{-1}^1 dx e^{\kappa x^2} P_l(x). \end{aligned}$$

Now, since $e^{\kappa x^2}$ is an even function the above integral is only nonzero if l is even as well. This allows us to write

$$\widehat{p}_{n,k}^{2l}(\kappa) = K_W \delta_{n,0} \delta_{k,0} \int_0^1 dx e^{\kappa x^2} P_{2l}(x) = K_W \delta_{n,0} \delta_{k,0} \sum_{m=0}^{\infty} \frac{\kappa^m}{m!} \int_0^1 dx x^{2m} P_{2l}(x).$$

The resulting integrals have already been computed in equation (207) and we finally obtain the characteristic function given in equation (200).

6.4.4. Gaussian distribution

On $SO(2)$ as well as on $SO(3)$ it is possible to define gaussian probability distributions such that they retain the essential properties of gaussian distributions on the real line including the central limit theorem⁵⁷. Their characteristic functions can be derived as a special case from the definition of gaussian distributions on compact Lie groups given in [145, equation 4.2.7], i.e.⁵⁸

$$\widehat{p}_n = e^{-\sigma^2 n^2} \quad \text{and} \quad \widehat{p}_{n,k}^l = e^{-\sigma^2 l(l+1)} \delta_{n,k}. \quad (208)$$

In the two dimensional case this definition coincides with what is known as wrapped Gaussian distribution [151, equation 3.5.65].

6.4.5. Analogs of distributions over \mathbb{R}

It may be of interest to find $SO(2)$ and $SO(3)$ analogs of common probability distributions given on the real line. A general answer can be given for distributions on $SO(2)$ using wrapped probability distributions [151, section 3.5.7]. Since $SO(2)$ is isomorphic to the circle group one may associate to each probability density $p(x)$ on the real line \mathbb{R} a distribution on $SO(2)$ by “wrapping” it around a circle, i.e.:

$$p_{SO(2)}(\alpha) = \sum_{k=-\infty}^{\infty} p(\alpha + 2\pi k) \quad (209)$$

These wrapped distributions have the property that their characteristic function is identical to the characteristic function of $p(x)$ [151, equation 3.5.59], that is

$$\widehat{p_{SO(2)_n}} = \int_{-\infty}^{\infty} dx p(x) e^{-inx} = \widehat{p_{\mathbb{R}}}(n). \quad (210)$$

For $SO(3)$ we can not give a general answer, but for many special cases such as Cauchy and Lorentz distributions analogs can be obtained by a process called subordination of probability distributions. In this process a known probability distribution, in our case a Gaussian distribution, is subordinated to obtain a new probability distribution. This process is known for probability distributions on \mathbb{R} (see [152, chapter 5] and [153, chapter 6]) as well as for probability distributions on arbitrary Lie groups (see [145, section 5.7]) and therefore allows us to find analogues of probability distributions that are connected to the Gaussian distribution given in equation (208).

⁵⁷In $SO(2)$ and $SO(3)$ the central limit theorem states that if $\omega_1, \dots, \omega_n$ are random rotations that are independently identically distributed and satisfy a set of general conditions [145, theorem 5.6.1], then the random variable given by the group product of all rotations $\omega_1 \cdot \dots \cdot \omega_n$ follows a Gaussian distribution in the limit of $n \rightarrow \infty$.

⁵⁸In the given reference equation one has to consider $t=1$. The representation of the identity rotation I_π for $SO(2)$ is given by $e^{-in0} = 1$ and similarly for $SO(3)$ via $D_{n,k}^l(0,0,0) = \delta_{n,k}$. Finally, the Casimir element κ_π of the Lie algebra $\mathfrak{so}(2)$ is n^2 while that of $\mathfrak{so}(3)$ is $l(l+1)$.

Let $p(x)$ be a probability distribution on \mathbb{R} , assume its characteristic function can be represented as follows

$$\widehat{p}_{\mathbb{R}}(t) = e^{-h(t^2)}, \quad \text{such that} \quad (-1)^i \frac{d^i}{ds^i} h(s) \leq 0 \quad \text{for all } i \text{ in } \mathbb{N} \quad (211)$$

In this case h is called a *Bernstein function* and the characteristic function $\widehat{p}_{n,k}^l$ of the probability distribution on $SO(3)$ corresponding to $p(x)$ is given by:

$$\widehat{p}_{n,k}^l = e^{-h(l(l+1))} \delta_{n,k}. \quad (212)$$

Let us now consider the example of Cauchy and Laplace distributions. For the Cauchy distribution centered at the origin we have :

$$\widehat{p}_{\mathbb{R}}(t) = e^{-\gamma|t|}, \quad \widehat{p}_n = e^{-\gamma|n|}, \quad \widehat{p}_{n,k}^l = e^{-\gamma\sqrt{l(l+1)}} \delta_{n,k}, \quad (213)$$

with the Bernstein function being $h(s) = \gamma\sqrt{s}$. Whereas, in case of the Laplace distribution centered at the origin one obtains.

$$\widehat{p}_{\mathbb{R}}(t) = \frac{1}{1+b^2t^2}, \quad \widehat{p}_n = \frac{1}{1+b^2n^2}, \quad \widehat{p}_{n,k}^l = \frac{1}{1-b^2l(l+1)} \delta_{n,k}, \quad (214)$$

where the Bernstein function is $h(s) = \ln(1+b^2s)$. Analogs of the above distributions centered at arbitrary rotations can be obtained using the shift theorem for Fourier transforms. In case of $SO(3)$ the shift theorem follows from the product rule [154, section 4.7.1]

$$D_{m,n}^l(\omega\omega_0) = \sum_k D_{m,k}^l(\omega) D_{k,n}^l(\omega_0), \quad (215)$$

where $\omega\omega_0$ denotes the combined rotation in which first a rotation by ω_0 and then one by ω is applied. With this, we find the characteristic function of a shifted rotational probability distribution $p'(\omega) = p(\omega\omega_0^{-1})$ to be given via

$$\begin{aligned} \frac{1}{8\pi^2} \int_{SO(3)} d\omega p(\omega\omega_0^{-1}) D_{m,n}^l(\omega)^* &= \int_{SO(3)} d\omega p(\omega) D_{m,n}^l(\omega\omega_0)^* \\ &= \int_{SO(3)} d\omega p(\omega) \sum_k D_{m,k}^l(\omega)^* D_{k,n}^l(\omega_0)^* \\ &= \sum_k \widehat{p}_{m,k}^l D_{k,n}^l(\omega_0)^*. \end{aligned}$$

Finally, we want to mention that the convolution theorem provides a powerful tool to derive characteristic functions of convolutions of probability distributions. In the case of $SO(3)$ the convolution theorem is a consequence of equation (215). Given two probability distributions $p(\omega)$ and $q(\omega)$ the characteristic function of their convolution $(p \star q)(\omega)$ is

defined by

$$\begin{aligned}
\widehat{p \star q}_{m,n}^l &= \int_{\text{SO}(3)} d\omega (p \star q)(\omega) D_{k,n}^l(\omega)^* \\
&= \int_{\text{SO}(3)} d\omega \left(\int_{\text{SO}(3)} d\omega_0 p(\omega\omega_0^{-1}) q(\omega_0) \right) D_{m,n}^l(\omega)^* \\
&= \int_{\text{SO}(3)} d\omega_0 \left(\int_{\text{SO}(3)} d\omega p(\omega\omega_0^{-1}) D_{m,n}^l(\omega)^* \right) q(\omega_0) \\
&= \int_{\text{SO}(3)} d\omega_0 \left(\sum_k \widehat{p}_{m,k}^l D_{k,n}^l(\omega_0)^* \right) q(\omega_0) \\
&= \sum_k \widehat{p}_{m,k}^l \widehat{q}_{k,n}^l
\end{aligned} \tag{216}$$

Consider the Voigt distribution which is the convolution of a Gaussian with a Cauchy distribution. Using the convolution theorem we know that its characteristic function is the product of characteristic functions for the individual distributions that is,

$$\widehat{p}_{\mathbb{R}}(t) = e^{-\gamma|t| - \sigma^2 t^2}, \quad \widehat{p}_n = e^{-\gamma|n| - \sigma^2 n^2}, \quad \widehat{p}_{n,k}^l = e^{-\gamma\sqrt{l(l+1)} - \sigma^2 l(l+1)} \delta_{n,k}. \tag{217}$$

on the real line, SO(2) and SO(3) respectively.

7. Summary

Theory of FXS

We proposed a generalized formulation of fluctuation X-ray scattering via definition 2.1, that also introduced a new version of the FXS moments in equations 61.

Starting from this definition we could identify connections to mathematical invariant theory, which allowed us to formulate general statements, see observations 2.3 and 2.12-2.14, on the type of information that FXS can retrieve about the single-particle intensity $I(\mathbf{q})$. This information comes in the form of rotational invariants, see equation (73) and section 2.2. Using the proposed version of the FXS moments we found a new method to extract the degree-2 invariants by solving the linear system given in equation (113) via back-substitution. Additionally, we were able to formulate the general connection between single-particle and multi-particle moments of arbitrary degree, while allowing the number of particles to be a random variable via observation 2.19. This insight was quite important for several theoretical results.

On one hand it allowed us to see that FXS contains information about the coefficient of variation in the number of particles, see equation (128). This could potentially remove the last remaining free parameters, in form of the statistical moments $\langle N^k \rangle$ in the number of particles, and allow direct computations of the single-particle moments from their scaled multi-particle counterparts, see equation (129).

On the other hand observation 2.19 also provided the single-particle to multi-particle connection in our extension of the FXS formalism to arbitrary rotational probability distributions, discussed in chapter 6. At the core of this extension lies the insight that the averaged rotation actions $\langle e^{-in\alpha} \rangle_{\text{SO}(2)}$ and $\langle D_{m,n}^l(\alpha, \beta, \gamma)^* \rangle_{\text{SO}(3)}$ have the form of characteristic functions and are connected to Fourier transforms of the rotational probability distributions on the rotation groups SO(2) and SO(3) for 2D and 3D FXS, respectively. This allowed us to obtain several interesting theoretical results. We found that the SAXS pattern $I^{\text{SAXS}}(\mathbf{q})$, thought of as the averaged 2D diffraction pattern $\langle I^M(q, \phi) \rangle$, contains the maximal amount of information about the rotational probability distribution. Specifically, with knowledge about the particle structure, one can retrieve the orientational probability distribution in both 2D and 3D FXS up to the limit posed by Friedel's symmetry (see equations (183) and (184)), i.e. up to the limitation posed by the point inversion symmetry in the scattering intensity $I(\mathbf{q})$. We also realized that for 2D FXS the degree-2 invariants can be computed without knowledge about the orientational probability distribution, see equation (182), therefore allowing structure determination under arbitrary orientational distributions. For 3D FXS the same does not hold, but we could still provide direct formulas that connect the degree-2 moments with the harmonic coefficients of the single-particle intensity $I_m^l(q)$ and the characteristic function of the orientational probability distribution, see observation 6.1. Finally, we have seen in section 6.4 that apart from numeric computations of the characteristic functions of arbitrary orientational probability distributions it is also possible to derive analytical results for selected distributions. Most notably, such distributions are relevant for pump-probe experiments on molecular solutions or aerosols at XFELs, see equation (199).

Single-particle reconstruction workflow

As part of this thesis we have developed and implemented an open source software suite *xFrame* for single-particle structure determination from *fluctuation X-ray scattering* data. It covers all necessary data processing steps, starting with the computation of the *averaged angular cross-correlation function* from diffraction patterns. It allows to extract and regularize the degree-2 invariants, perform phase retrieval and is able to align and average the obtained reconstructions.

The implemented workflow contains several novel approaches and insights. The regularization step, in which the extracted degree-2 invariants B_l and B_n are transformed into their decomposition representation $\tilde{\mathbf{V}}_l \tilde{\mathbf{V}}_l^\dagger$ and $\tilde{\mathbf{v}}_n \tilde{\mathbf{v}}_n^\dagger$, was extended to take their natural q -dependent decay into account and allows to minimize the phase difference between the invariants and their decompositions. We introduced a scheme by which one is able to partially mitigate the information loss that occurs due to masking in the regularization step, see equation (139).

The phasing routine itself crucially depends on Fourier transforms in spherical and polar coordinates, which need to be approximated. We investigated different approaches to their approximation via Hankel transforms and found that some of them converge to Riemann sum approximations, see appendix B, which prompted the use of the simple midpoint rule in the presented phasing routine. It was realized that artifacts due to the integral approximations can be reduced by adding a Fourier transform stabilization step to the phasing loop as described in equation (150). Since FXS uses rotation invariant information as phasing constraint, all obtained reconstructions differ in their rotation state and need to be aligned prior to the computation of an averaged reconstruction. For 2D FXS we identified an algebraic orientation determination algorithm that allows to rotationally align individual reconstructions without the need to select a reference.

All of the above mentioned steps and algorithms are now available as part of the *xFrame* python package which can be found at <https://github.com/European-XFEL/xFrame> and have been tested on simulated [23] and experimental datasets [122].

We demonstrated that the presented workflow is able to achieve Fourier limited reconstructions as well as its ability to perform single-particle structure recovery from multi-particle scattering patterns, if the number of particles is known [see section 5.1]. The presented reconstructions of the PR772 virus from diffraction data taken at the LCLS experiments *amo86615* and *amo06516* allowed us to confirm the robustness of the presented workflow to noise and missing diffraction data, as well as its ability to provide successful reconstructions from a limited amount of diffraction patterns. The similarity between the observed FXS moments and invariants from both experiments, visible in figure 49, indicates good reproducibility of the experimental results, which becomes especially obvious when comparing it, e.g. with results for a simulated solid icosahedral particle of comparable size. Our workflow could improve the previously obtained resolution estimates for MTIP reconstructions based on the *amo86615* experiment [20] and allowed us to identify deviations of the virus capsid from its ideal icosahedral symmetry. We could confirm the existence of deviations from the ideal capsid symmetry also for the *amo06516* dataset, where we found special features at a particular vertex of the virus capsid. Depending

on the considered size-part it either contained a density deficient area or showed a spike like extension, see figure 52 (e)-(h). Our experimental observations are in agreement with previous experimental XFEL studies on PR772, regarding deviations from the icosahedral symmetry [18, 20] and concerning the spike like extension [121]. They are also consistent with the low stability of the PR772 virion at varying temperatures, humidities, nebulization conditions [131, 132] and capsid remodeling mechanisms found in viruses belonging to the same family [125, 126].

Conclusions

In conclusion we have presented several new theoretical developments in *fluctuation X-ray scattering*. Most notably, the extension of FXS to cover arbitrary orientational probability distributions, which has potential applications in pump-probe experiments on molecular solutions and aerosols with an XFEL. We also implemented a complete single-particle reconstruction workflow based on FXS data, in form of the software suite *xFrame*. This workflow was successfully applied to experimental datasets and we hope that it will be useful for fellow scientists in the field of X-ray imaging.

Acknowledgments

I want to thank my wonderful wife and two daughters, to whom this thesis is dedicated. You always managed to put a smile on my face no matter the situation. Without your relentless support not a single page of this thesis would have been possible and I am very fortunate to share my life with you.

The second person I want to thank is Ruslan Kurta. Not only is he the best mentor I could have possibly hoped for when starting my PhD, the time and dedication he spent on our project is sheer unimaginable. I would have not been the scientist I am now without you. My gratitude also goes towards my supervisors Prof. Lichtenstein and Prof. Molodtsov for the trust they placed in me, their continued support as well as the reminders to finish soon, without which I would probably still be writing the introduction. Furthermore, I want to thank Nils Brouwer for fearlessly accepting to proofread large portions of my thesis, despite my terrible sense for orthography. Finally, I want to express my gratitude towards my fellow PhD students at the European XFEL. I am very fond of the time I spend at the European XFEL and to a large portion you are the ones responsible for this.

Befitting to the topic of this thesis let me close this section with an anecdote about an encounter by chance. While trying to figure out how to align 3D electron densities I stumbled over a paper by Peter Kostelec and Daniel Rockmore [90] that provided software for the computation of Fourier transforms on $SO(3)$, which was however nowhere available at the time. By pure luck I came into mail contact with Peter Kostelec who provided me a copy of his software. A version of which now forms the core of the 3D alignment routine in *xFrame*. Without his paper I would have never stumbled on Fourier transforms over rotation spaces and the ideas leading to the extension of FXS to cover arbitrary orientational distributions would have never come to my mind. For this I want to express my deep gratitude towards Peter Kostelec and by extension to all scientists on whose shoulders I stand.

A. Fluctuation X-ray scattering invariants and moments

A.1. Geometric interpretation of degree-2 invariants

In section 1.7 we have seen that the rotation action on harmonic coefficients given in equations (57) and (56) is a direct consequence of the rotation action on the corresponding expansion functions $e^{in\phi}$ and $Y_m^l(\theta, \phi)$.

$$\mathbf{R}_\alpha e^{in\phi} = e^{in(\phi-\alpha)} \quad \text{and} \quad \mathbf{R}_{(\alpha,\beta,\gamma)} Y_m^l(\theta, \phi) = \sum_{n=-l}^l Y_n^l(\theta, \phi) D_{nm}^l(\alpha, \beta, \gamma)^* .$$

The degree-2 invariants

$$B_n(q, q') = I_n(q) I_n(q')^* \quad \text{and} \quad B_l(q, q') = \sum_n I_n^l(q) I_n^l(q')^* ,$$

therefore have dual partner functions specified in terms of the expansion functions that have to share the property of being invariant under rotations.

$$\overline{B}_n(\phi, \phi') = e^{in\phi} e^{-in\phi'} = e^{in(\phi-\phi')} \quad \text{and} \quad \overline{B}_l(\phi, \theta, \phi', \theta') = \sum_n Y_n^l(\theta, \phi) Y_n^l(\theta', \phi')^* . \quad (218)$$

Rotating the intensity I simply means to apply the same rotation to both expansion functions in the these dual invariants (218). In the 2D case this results in

$$\mathbf{R}_\alpha \overline{B}_n(\phi, \phi') = \overline{B}_n(\mathbf{R}_{-\alpha}\phi, \mathbf{R}_{-\alpha}\phi') = e^{in(\phi-\alpha-\phi'+\alpha)} = \overline{B}_n(\phi, \phi') \quad (219)$$

and it is clear that $\overline{B}_n(\phi, \phi')$ is an invariant under the rotation action. Geometrically the parameter space of \overline{B}_n is given by the Cartesian product of two circles, each of which representing one of the angles ϕ and ϕ' . The Cartesian product of two circles can be visualized as a torus, see figure 55

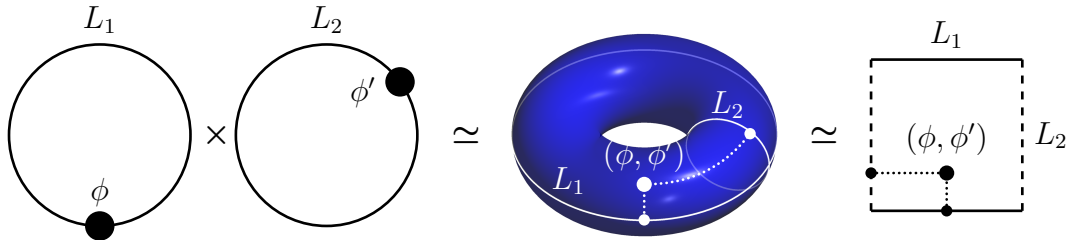


Figure 55: Different visualizations of the Cartesian product of two circles L_1 and L_2 . Selecting a point in the product space $L_1 \times L_2$, say (ϕ, ϕ') is the same as selecting a point on the surface of the torus (center) or a point in a square with periodic boundary conditions (right). The periodic boundary conditions in the square are such that dashed boundaries, corresponding to L_2 , are identified with each other and similarly for the solid boundaries representing L_1 .

In these graphical visualizations the rotation \mathbf{R}_α always acts by “rotating” the coordinate circles, which translates to

- (two circles) Rotating the circles L_1 and L_2 clockwise.
- (torus) Twisting the torus by rotating the L_1 and L_2 clockwise at the same time.
- (periodic square) Shifting the points in the square diagonally by shifting (the same as rotation due to periodic boundaries) the x and y coordinate axes corresponding to L_1 and L_2

A graphical representation of this can be found in figure 56. Functions invariant under

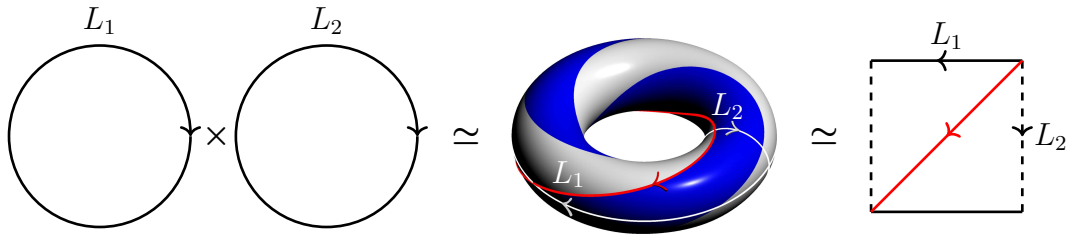


Figure 56: Rotation action on different representations of a Torus. Rotating the two circles L_1 and L_2 clockwise in the direction of the arrows causes all points on the torus to follow lines parallel to the red line. In its representation as square with periodic boundaries the corresponding shift of the coordinate axes cause all point inside the square to travel along lines parallel to the red diagonal.

rotations therefore have to remain constant along paths parallel to the red lines in figure 56. That this is exactly the case for all \overline{B}_n can be seen in figure 57.

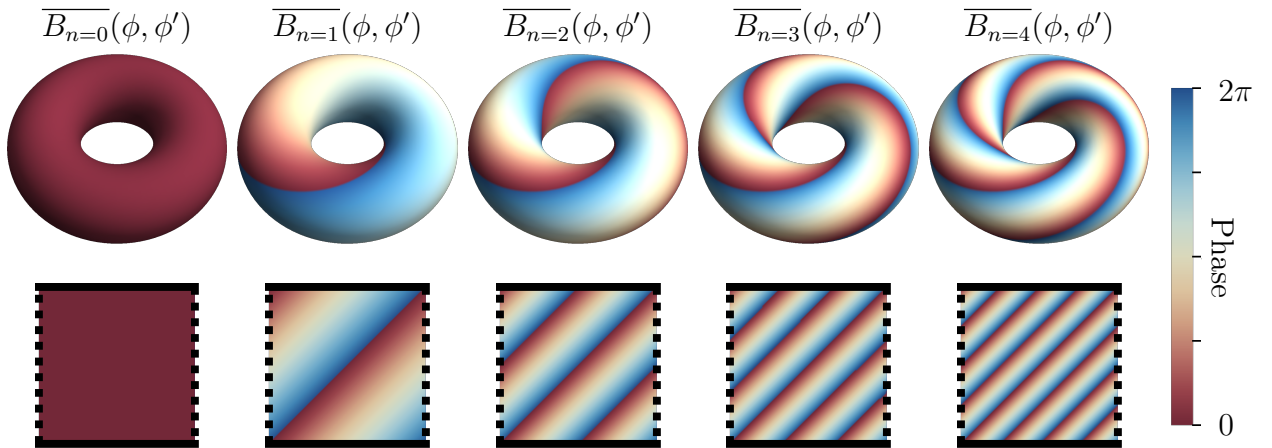


Figure 57: Values of the dual degree-2 invariants $\overline{B}_n(\phi, \phi') = e^{in(\phi-\phi')}$ for $n = 0, 1, 2, 3, 4$. Color represents the phase of the dual invariant. It can be seen that the values remain constant along the directions of the rotation action, i.e. that $\overline{B}_n(\phi, \phi')$ are invariant under rotations.

The rotation action in the 3D case is given by

$$\begin{aligned} \mathbf{R}_\omega \overline{B}_l(\phi, \theta, \phi', \theta') &= \overline{B}_l(\mathbf{R}_{\omega^{-1}}(\phi, \theta), \mathbf{R}_{\omega^{-1}}(\phi', \theta')) \\ &= \sum_{n=-l}^l \sum_m Y_m^l(\theta, \phi) D_{mn}^l(\omega)^* \sum_{m'} Y_{m'}^l(\theta, \phi)^* D_{m'n}^l(\omega), \end{aligned}$$

where ω denotes an element of $\text{SO}(3)$. General visualizations of the dual invariant, as in the two-dimensional case, are difficult since the parameter space of \overline{B}_l is the Cartesian product of two spheres and hence a curved four dimensional surface. If we however restrict our discussion to its rotational invariance only, then geometric interpretations are possible. Note, that in the two-dimensional case the sets of parameters connected by rotations, i.e. parallels to the red lines in figure 56, are loops and hence one dimensional subsets of the complete torus. And we have already seen that the rotational invariance of \overline{B}_n simply demands that it is constant on those one dimensional subsets. A particular simple choice of such a subspace of the torus is its main diagonal (in the square representation) given by points (ϕ, ϕ') such that $\phi = \phi'$. The corresponding “diagonal” in the three dimensional-case is characterized by $(\theta, \phi) = (\theta', \phi')$ on which the dual invariant is given by

$$\overline{B}_l(\phi, \theta, \phi, \theta) = \sum_{n=-l}^l Y_n^l(\theta, \phi) Y_n^l(\theta, \phi)^* = |Y_0^l|^2 + 2 \sum_{n=1}^l |Y_n^l(\theta, \phi)|^2, \quad (220)$$

where in the second equality we used that $Y_n^l(\theta, \phi)^* = (-1)^n Y_n^l(\theta, \phi)$. This subset is simply a sphere and the rotational invariance again demands that $\overline{B}_l(\phi, \theta, \phi, \theta)$ has to be constant under the rotation action for all points (θ, ϕ) on this sphere. Figure 58 visualizes this via parametric plots where the distance from the center of the coordinate system into the direction of (θ, ϕ) is given by the value of $\overline{B}_l(\phi, \theta, \phi, \theta)$. The parametric plot of a constant function is then simply a sphere and the rotational invariance translates into the statement that the sum of the parametric plots of the different $|Y_m^l|^2$, from equation (220), have to form a sphere.

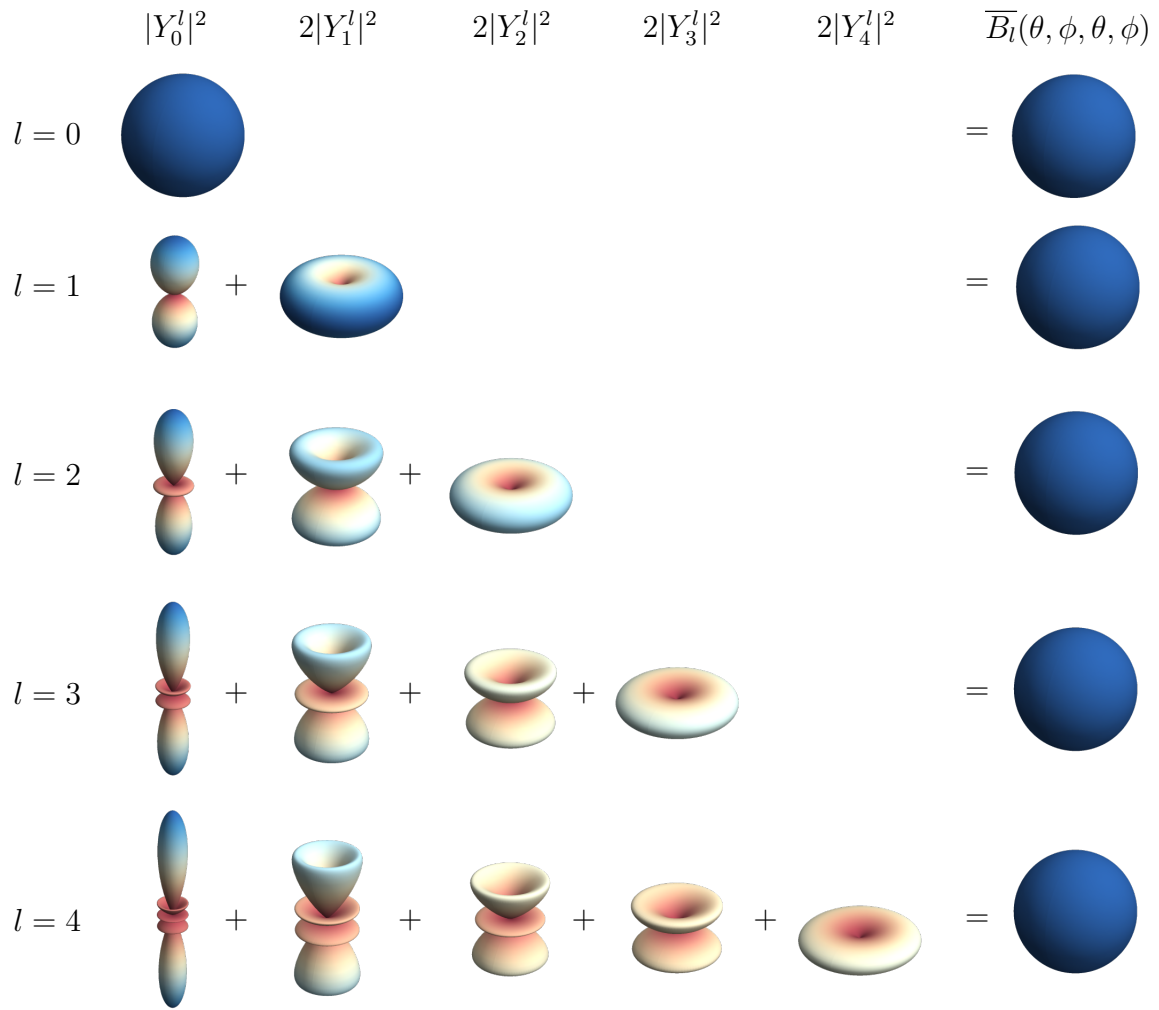


Figure 58: Parametric plots of the summands of the dual invariant $\overline{B}_l(\phi, \theta, \phi, \theta)$ as given in equation (220) for $l = 0, 1, 2, 3$ and 4. The color scale serves as an additional indication of the distance from the center, that is given by the value of $\overline{B}_l(\phi, \theta, \phi, \theta)$. Reddish points are close to the center while blue areas are further away. It can be seen that the different summands always add up to a sphere which shows the rotational invariance of $\overline{B}_l(\phi, \theta, \phi, \theta)$.

A.2. Proof of explicit form of degree-3 invariants

In this part of the appendix we will show that equations (83a) and (83b) are true. For convenience let us repeat the corresponding equations.

$$\begin{aligned}\mathcal{I}_{\text{SO}(2)}^3(q_1, q_2, q_3) &= \left\langle \mathbf{R}_\alpha I_{n_1}(q_1) I_{n_2}(q_2)^* I_{n_3}(q_3) \right\rangle_{\text{SO}(2)} = \delta_{n_2, (n_1+n_3)} I_{n_1+n_3}(q_2)^* I_{n_1}(q_1) I_{n_3}(q_3) \\ \mathcal{I}_{\text{SO}(3)}^3(q_1, q_2, q_3) &= \left\langle \mathbf{R}_\omega I_{m_1}^{l_1}(q_1) I_{m_2}^{l_2}(q_2)^* I_{m_3}^{l_3}(q_3) \right\rangle_{\text{SO}(3)} \\ &= \delta_{m_2, (m_1+m_3)} \frac{C_{m_1, m_3}^{l_1, l_3, l_2}}{2l_2 + 1} \sum_{n_1, n_3} I_{n_1+n_3}^{l_2}(q_2)^* I_{n_1}^{l_1}(q_1) I_{n_3}^{l_3}(q_3) C_{n_1, n_3}^{l_1, l_3, l_2}\end{aligned}$$

The two dimensional case is again a direct consequence of the rotation action given in equation (57) which can be used as follows

$$\begin{aligned}\left\langle \mathbf{R}_\alpha I_{n_1}(q_1) I_{n_2}(q_2)^* I_{n_3}(q_3) \right\rangle_{\text{SO}(2)} &= I_{n_1}(q_1) I_{n_2}(q_2)^* I_{n_3}(q_3) \left\langle e^{i(n_1-n_2+n_3)\alpha} \right\rangle_{\text{SO}(2)} \\ &= I_{n_1}(q_1) I_{n_2}(q_2)^* I_{n_3}(q_3) \frac{1}{2\pi} \int_0^{2\pi} d\alpha e^{i(n_1-n_2+n_3)\alpha} \\ &= \delta_{n_2, (n_1+n_3)} I_{n_1+n_3}(q_2)^* I_{n_1}(q_1) I_{n_3}(q_3)\end{aligned}$$

In the three-dimensional case we will for clarity suppress the summation ranges which yields

$$\begin{aligned}\left\langle \mathbf{R}_\omega I_{m_1}^{l_1}(q_1) I_{m_2}^{l_2}(q_2)^* I_{m_3}^{l_3}(q_3) \right\rangle_{\text{SO}(3)} \\ = \sum_{n_1, n_2, n_3} I_{n_1}^{l_1}(q_1) I_{n_2}^{l_2}(q_2)^* I_{n_3}^{l_3}(q_3) \left\langle D_{m_1 n_1}^{l_1}(\omega)^* D_{m_2 n_2}^{l_2}(\omega) D_{m_3 n_3}^{l_3}(\omega)^* \right\rangle_{\text{SO}(3)}.\end{aligned}$$

The remaining average in the Wigner-D matrices is directly proportional⁵⁹, to the well known triple integral relation given in equation (267) and we find

$$\begin{aligned}\left\langle \mathbf{R}_\omega I_{m_1}^{l_1}(q_1) I_{m_2}^{l_2}(q_2)^* I_{m_3}^{l_3}(q_3) \right\rangle_{\text{SO}(3)} \\ = \delta_{m_2, (m_1+m_3)} \frac{C_{m_1, m_3}^{l_1, l_3, l_2}}{2l_2 + 1} \sum_{n_1, n_3} I_{n_1+n_3}^{l_2}(q_2)^* I_{n_1}^{l_1}(q_1) I_{n_3}^{l_3}(q_3) C_{n_1, n_3}^{l_1, l_3, l_2}.\end{aligned}$$

⁵⁹With proportionality constant $\frac{1}{8\pi^2}$.

A.3. Proof of explicit form of the degree-3 moments

Let us now derive the explicit form of the degree-3 moments for the single-particle case ($N = 1$) given in equations 110 and 111, that is

$$\begin{aligned}\mathcal{M}^3(q_1, q_2, q_3, \phi_1, \phi_2, \phi_3) &= \sum_{l_1, l_2, l_3}^L F^{l_1, l_2, l_3}(q_1, q_2, q_3, \phi_1, \phi_2, \phi_3) B_{l_1, l_2, l_3}(q_1, q_2, q_3) \\ F^{l_1, l_2, l_3}(q_1, q_2, q_3, \phi_1, \phi_2, \phi_3) &= \sum_{m_1, m_3} \frac{2Y_{m_1+m_3}^{l_2}(\theta_\lambda(q_2), \phi_2)^*}{2l_2+1} \\ &\quad \times Y_{m_1}^{l_1}(\theta_\lambda(q_1), \phi_1) Y_{m_3}^{l_3}(\theta_\lambda(q_3), \phi_3) C_{m_1, m_3}^{l_1, l_3, l_2}\end{aligned}$$

and

$$\begin{aligned}\mathcal{M}^3(q_1, q_2, q_3, n_1, n_2, n_3) &= \delta_{n_2, n_1+n_3} \sum_{\substack{l_1 \geq |n_1|, l_3 \geq |n_3| \\ l_2 \geq |n_1+n_3|}}^L \tilde{F}_{n_1, n_3}^{l_1, l_2, l_3}(q_1, q_2, q_3) B_{l_1, l_2, l_3}(q_1, q_2, q_3) \\ \tilde{F}_{n_1, n_3}^{l_1, l_2, l_3}(q_1, q_2, q_3) &= \frac{2C_{n_1, n_3}^{l_1, l_3, l_2}}{2l_2+1} \tilde{P}_{l_1}^{|n_1|}(\theta_\lambda(q_1)) \tilde{P}_{l_2}^{|n_1+n_3|}(\theta_\lambda(q_2)) \tilde{P}_{l_3}^{|n_3|}(\theta_\lambda(q_3))\end{aligned}$$

where the invariants $B_{l_1, l_2, l_3}(q_1, q_2, q_3)$ are specified in equation (85) as

$$B_{l_1, l_2, l_3}(q_1, q_2, q_3) = \sum_{n_1, n_3} I_{n_1+n_3}^{l_2}(q_2)^* I_{n_1}^{l_1}(q_1) I_{n_3}^{l_3}(q_3) C_{n_1, n_3}^{l_1, l_3, l_2}$$

We shall start with the derivation of $\mathcal{M}^3(q_1, q_2, q_3, \phi_1, \phi_2, \phi_3)$. Expanding the scattering patterns I^M in the definition of \mathcal{M}^3 as spherical harmonic series in the single-particle harmonic coefficients I_m^l yields

$$\begin{aligned}\mathcal{M}^3(q_1, q_2, q_3, \phi_1, \phi_2, \phi_3) &= \langle I^M(q_1, \phi_1) I^M(q_2, \phi_2)^* I^M(q_3, \phi_3) \rangle_{\text{SO}(3)} \\ &= \sum_{\substack{l_1, l_2, l_3 \\ m_1, m_2, m_3}} \langle \mathbf{R}_\omega I_{m_1}^{l_1}(q_1) I_{m_2}^{l_2}(q_2)^* I_{m_3}^{l_3}(q_3) \rangle_{\text{SO}(3)} Y_{m_1}^{l_1}(\theta_\lambda(q_1), \phi_1) Y_{m_2}^{l_2}(\theta_\lambda(q_2), \phi_2)^* Y_{m_3}^{l_3}(\theta_\lambda(q_3), \phi_3) \\ &= \sum_{l_1, l_2, l_3} \sum_{n_1, n_3} I_{n_1+n_3}^{l_2}(q_2)^* I_{n_1}^{l_1}(q_1) I_{n_3}^{l_3}(q_3) C_{n_1, n_3}^{l_1, l_3, l_2} \\ &\quad \times \frac{2}{2l_2+1} \sum_{m_1, m_3} Y_{m_1}^{l_1}(\theta_\lambda(q_1), \phi_1) Y_{m_1+m_3}^{l_2}(\theta_\lambda(q_2), \phi_2)^* Y_{m_3}^{l_3}(\theta_\lambda(q_3), \phi_3) C_{m_1, m_3}^{l_1, l_3, l_2}\end{aligned}$$

, where in the last step we used the explicit form of the single-particle invariant $\langle \mathbf{R}_\omega I_{m_1}^{l_1}(q_1) I_{m_2}^{l_2}(q_2)^* I_{m_3}^{l_3}(q_3)^* \rangle_{\text{SO}(3)}$ given in equation (83b). Using our definitions of B_{l_1, l_2, l_3}

and F^{l_1, l_2, l_3} we directly obtain equation (110). Similarly one may find for $\mathcal{M}^3(q_1, q_2, q_3, n_1, n_2, n_3)$

$$\begin{aligned}
\mathcal{M}^3(q_1, q_2, q_3, n_1, n_2, n_3) &= \langle I_{n_1}^M(q_1, \phi_1) I_{n_2}^M(q_2, \phi_2)^* I_{n_3}^M(q_3, \phi_3) \rangle_{\text{SO}(3)} \\
&= \sum_{\substack{l_1, l_2, l_3 \\ m_1, m_2, m_3}} \langle I_{m_1}^{l_1}(q_1) I_{m_2}^{l_2}(q_2)^* I_{m_3}^{l_3}(q_3)^* \rangle_{\text{SO}(3)} \\
&\quad \times (Y_{m_1}^{l_1}(\theta_\lambda(q_1), \phi_1))_{n_1} (Y_{m_2}^{l_2}(\theta_\lambda(q_2), \phi_2)^*)_{n_2} (Y_{m_3}^{l_3}(\theta_\lambda(q_3), \phi_3))_{n_3}) \\
&= \sum_{l_1, l_2, l_3} \langle I_{n_1}^{l_1}(q_1) I_{n_2}^{l_2}(q_2)^* I_{n_3}^{l_3}(q_3) \rangle_{\text{SO}(3)} \tilde{P}_{l_1}^{n_1}(\theta_\lambda(q_1)) \tilde{P}_{l_2}^{n_2}(\theta_\lambda(q_2)) \tilde{P}_{l_3}^{n_3}(\theta_\lambda(q_3)) \\
&= \delta_{n_2, n_1 + n_3} \sum_{l_1, l_2, l_3} \sum_{m_1, m_3} I_{m_1 + m_3}^{l_2}(q_2)^* I_{m_1}^{l_1}(q_1) I_{m_3}^{l_3}(q_3) C_{m_1, m_3}^{l_1, l_3, l_2} \\
&\quad \times \frac{2C_{n_1, n_3}^{l_1, l_3, l_2}}{2l_2 + 1} \tilde{P}_{l_1}^{n_1}(\theta_\lambda(q_1)) \tilde{P}_{l_2}^{n_1 + n_3}(\theta_\lambda(q_2)) \tilde{P}_{l_3}^{n_3}(\theta_\lambda(q_3))
\end{aligned}$$

The third equality is due to equation (102), that links the Fourier coefficients of spherical harmonics Y_m^l to the functions \tilde{P}_l^n , which are proportional to associated Legendre polynomials. By substituting the definitions of B_{l_1, l_2, l_3} and $\tilde{F}_{n_1, n_3}^{l_1, l_2, l_3}$ into the last result one obtains equation (111).

A.4. Derivation of Observation 2.19

In observation 2.19 we stated that the multi-particle observables \mathcal{M}_N^d reduce to sums over their single particle versions \mathcal{M}^d and take the form

$$\mathcal{M}_N^d = \sum_{k=1}^d \left\langle \frac{N!}{(N-k)!} \right\rangle \sum_{(\mathbf{o}, \sigma) \in S_k^d} \prod_{p=1}^k \mathcal{M}_{\|\sigma}^{o_p},$$

where $(\mathbf{o}, \sigma) \in S_k^d$, with $\mathbf{o} = (o_1 \leq \dots \leq o_k)$, is given by our discussion of set partitions in section 2.5.3. Before continuing let us recall some of the shorthand notation that was used in the multi-particle discussion append it a little.

Notation	Description
$\sigma(p, a)$	Description of the p -th part of the set partition $(\mathbf{o}, \sigma) \in S_k^d$ via its associated permutation, see equation (116)
\mathcal{M}_N^d	Moments $\mathcal{M}_N^d(q_1, \dots, q_d, \phi_1, \dots, \phi_d)$ or $\mathcal{M}_N^d(q_1, \dots, q_d, n_1, \dots, n_d)$
$\mathcal{M}_{ i_1, \dots, i_o}^o$	Single-particle moment of same type as \mathcal{M}_N^d evaluated at the coordinate pairs i_1, \dots, i_o of \mathcal{M}_N^d .
$\mathcal{M}_{\ \sigma}^{o_p}$	Single-particle moment $\mathcal{M}_{ \sigma(p,1), \dots, \sigma(p, o_p)}^{o_p}$ whose coordinate indices correspond to the p -th part of the partition (\mathbf{o}, σ) applied to $\{1, \dots, d\}$.
$I_{j,i}^M$	$I_j^M(q_i, \phi_i)$ scattering contribution of the j -th particle evaluated at the i -th coordinate pair of \mathcal{M}_N^d
ω_j	Random variable describing the rotation state of the j -th particle in a sample.
N	Random variable describing the number of particles in a sample.
M	Statistical ensemble of samples, described by the random variables $\{N, \omega_1, \dots, \omega_N, \mathbf{x}_1, \dots, \mathbf{x}_N\}$.

The following discussion will not depend on the type of coordinate pairs (q_j, ϕ_j) or (q_j, n_j) , corresponding to the moments given by equation (60) or (61), and will be valid for both cases. This is also reflected in our shorthand notation, since $\mathcal{M}_{|i_1, \dots, i_o}^o$ only tracks the position of coordinate pairs but not their type. We will see that the derivation of equation 119 relies on the following assumptions made in definition 2.1

- The **dilute-limit** assumption.
- The **diffraction before destrucion** assumption that identifies the scattering amplitude $\widehat{\rho}^M$ as the Fourier transform of a sample ρ^M restricted to the Ewald's sphere.
- Part a) of the **nature of randomness** assumption, i.e. the statistical independence of the random variables.

The first assumptions allows us to approximate the scattered amplitude of a sample by the incoherent sum over the scattering contributions of its particles, i.e.

$$I^M(q, \phi) = \sum_{j=1}^N I_j^M(q, \phi) \quad \text{and therefore} \quad \mathcal{M}_N^d = \left\langle \prod_{i=1}^d \left(\sum_{j_i=1}^N I_{j_i, i}^M \right) \right\rangle_M$$

Using the second assumption one may see, using the Fourier shift theorem (18), that the intensity contribution of an individual particle is independent from its position. This allows us to substitute the ensemble average M with an average over the number of particles and rotations only, hence one finds

$$\mathcal{M}_N^d = \left\langle \sum_{j_1, \dots, j_d=1}^N \prod_{i=1}^d I_{j_i, i}^M \right\rangle_{N, \omega_1, \dots, \omega_N}$$

One of the issues with this equation is that the two types of random variables, N and ω_j , are tied to each other by the summation. In the next step we shall decouple them. First note that the *law of total expectation* [155, chapter 10 proposition 1.1 (a)] tells us that, given two random variables X and Y on the same ensemble M , the total expectation value (average) of X can be expressed using the conditional expectation value of X given that Y attains a specific value $y = Y$, i.e.

$$E[X] = E[E[X|Y]] \quad \text{or in our notation} \quad \langle X \rangle_M = \langle \langle X \rangle_{M, Y=y} \rangle_M$$

In our case Y is the number of particles and we therefore have

$$\mathcal{M}_N^d = \left\langle \left\langle \sum_{j_1, \dots, j_d=1}^N \prod_{i=1}^d I_{j_i, i}^M \right\rangle_{N=\eta, \omega_1, \dots, \omega_\eta} \right\rangle_{N, \omega_1, \dots, \omega_N}$$

Note, that by the statistical independence of N and ω_j , the inner average is simply the average over all possible rotation states $\omega_1, \dots, \omega_\eta$ for an arbitrary but fixed number of particles η . By the same reasoning one finds that the outer average reduces to a simple

average over the number of particles. If we denote the former average by $\mathcal{M}_{N=\eta}^d$ and let $P(\eta)$ be the probability of a sample consisting of η particles, we find

$$\mathcal{M}_N^d = \sum_{\eta=0}^{\infty} P(\eta) \mathcal{M}_{N=\eta}^d \quad (221)$$

With this we have reduced the problem of computing \mathcal{M}_N^d in general to the computation of $\mathcal{M}_{N=\eta}^d$ followed by an average over the number of particles. Since the summation indices in $\mathcal{M}_{N=\eta}^d$ do not depend on random variables anymore we may pull the sums out of the average, which yields

$$\mathcal{M}_{N=\eta}^d = \sum_{j_1, \dots, j_d=1}^{\eta} \left\langle \prod_{i=1}^d I_{j_i, i}^M \right\rangle_{\omega_1, \dots, \omega_{\eta}} \quad (222)$$

The statistical independence between rotations acting on different particles, i.e. between ω_s and $\omega_{s'}$ for $s \neq s'$, does allow us to reduce each summand to a product of single-particle averages, since only those intensities have to be averaged together that belong to the same particle. To formalize this, let k be the number of different particle indices within the summand tuple (j_1, \dots, j_d) and let i_1, \dots, i_k be the indices of these particles. Furthermore, let o_p be the number of times the i_p -th particle appears in (j_1, \dots, j_d) . In other words, each summand corresponds to a set partition $(\mathbf{o}, \sigma) = (o_1 \leq \dots \leq o_k)$ of the subscripts $(1, \dots, d)$, such that the particle indices j_i whose subscripts form a part of the set partition (\mathbf{o}, σ) are equal to each other. Moreover, all particle indices j_i corresponding to the p -th part of this partition are equal to i_p . Using the permutation representation of the set partition (\mathbf{o}, σ) allows us to describe the subscripts of the particle indices j_i belonging to the p -th part, via $(\sigma(p, 1), \dots, \sigma(p, o_p))$ and we find

$$\left\langle \prod_{i=1}^d I_{j_i, i}^M \right\rangle_{\omega_1, \dots, \omega_{\eta}} = \left\langle I_{i_1, \sigma(1,1)}^M \cdots I_{i_1, \sigma(1, o_1)}^M \right\rangle_{\omega_{i_1}} \cdots \left\langle I_{i_k, \sigma(k,1)}^M \cdots I_{i_k, \sigma(k, o_k)}^M \right\rangle_{\omega_{i_k}} \quad (223)$$

$$= \prod_{p=1}^k \mathcal{M}_{\sigma(p,1), \dots, \sigma(p, o_p)}^{o_p} = \prod_{p=1}^k \mathcal{M}_{\|\sigma}^{o_p}. \quad (224)$$

This implies that each summand is uniquely identified by a choice of k , a set partition $(\mathbf{o}, \sigma) \in S_k^d$ of a set with d elements into k parts and a choice of pairwise different particle indices i_1, \dots, i_k . Correspondingly we can write the sum in (222) as triple sum over the aforementioned parameters, i.e.

$$\mathcal{M}_{N=\eta}^d = \sum_{j_1, \dots, j_d=1}^{\eta} \left\langle \prod_{i=1}^d I_{j_i, i}^M \right\rangle_{\omega_1, \dots, \omega_{\eta}} = \sum_{k=1}^d \sum_{i_1 \neq \dots \neq i_k}^{\eta} \sum_{(\mathbf{o}, \sigma) \in S_k^d} \prod_{p=1}^k \mathcal{M}_{\|\sigma}^{o_p}. \quad (225)$$

Since the summands on the right hand side of (223) do not depend on the particle indices i_1, \dots, i_k we can directly evaluate their sum and find

$$\mathcal{M}_{N=\eta}^d = \sum_{k=1}^d \frac{\eta!}{(\eta - k)!} \sum_{(\mathbf{o}, \sigma) \in S_k^d} \prod_{p=1}^k \mathcal{M}_{\|\sigma}^{o_p}.$$

Combining this result with equation (221) finally yields the desired formula for the multi-particle observables, presented in observaiton 2.19.

B. Hankel transform approximations

In this appendix we consider different methods for approximating the continuous Hankel transforms in equations (141) and (142).

B.1. Expansion via orthogonal polynomials

One of the approaches to derive a discrete version of the Hankel transforms is to expand $\rho_m(r)$ or $\rho_m^l(r)$ using an orthogonal basis $\xi_i(r)$ of all square integrable functions on the interval $[0, R_{\max}]$, e.g. in the 2D case,

$$\rho_{m,i} = \int_0^{R_{\max}} \rho_m(r) \xi_i^*(r) dr, \quad (226a)$$

$$\rho_m(r) = \sum_{i=0}^{\infty} \rho_{m,i} \xi_i(r), \quad (226b)$$

where $\rho_{m,i}$ are the expansion coefficients. This allows one to shift the Hankel integration from $\rho_m(r)$ to the expansion functions $\xi_i(r)$, i.e. using equation (226b) in (141a) we get

$$\widehat{\rho}_m(q) = (-i)^m \sum_{i=0}^{\infty} \rho_{m,i} \int_0^{R_{\max}} \xi_i(r) J_m(qr) r dr. \quad (227)$$

The integral in equation (227) can be precomputed once, independently from the considered function $\rho_m(r)$, and then used for all subsequent Hankel transform computations. The remaining integral in (226a) in the determination of the expansion coefficients $\rho_{m,i}$ can then be approximated by using one of the available methods, e.g. the trapezoidal rule [19], or midpoint rule, to derive a discrete form of equations (141) and (142). Using the midpoint rule one can approximate equation (227) in the following general form

$$\widehat{\rho}_m(q_k) \approx A_m \sum_p \rho_m(r_p) w_m(k, p), \quad (228)$$

where A_m are some constants, $w_m(k, q)$ are quadrature weights defined by the integral in equation (227), and r_p and q_k are discrete coordinates in real and reciprocal space. Such an approach has been implemented in [19] using a cosine/sine series expansion. An example of the cosine/sine approach, using the midpoint rule to approximate the expansion coefficients, is presented in Appendix B.2. Alongside this thesis we also developed an approximation of the Hankel transforms that uses Zernike polynomials as the orthogonal basis functions $\xi_i(r)$. The advantage of the obtained expressions is that, in this case, the integral in (227) can be evaluated analytically [see Appendix B.3] and thus does not require numerical approximation as in the case of a cosine/sine series expansion [see Appendix B.2].

At the same time, analysis of expression (227) defined in terms of an arbitrary orthogonal basis $\xi_i(r)$ reveals further general aspects of such approximation schemes. By applying

the midpoint rule to approximate the integral in (226b) on a discrete grid as defined in 3.4.2, and substituting the result into (227) we obtain

$$\hat{\rho}_m(q) \approx (-i)^m \sum_{i=0}^{\infty} \frac{R_{\max}}{S} \sum_{p=0}^{S-1} \rho_m(r_p) \xi_i^*(r_p) \int_0^{R_{\max}} \tilde{J}_m(qr) \xi_i(r) dr, \quad (229)$$

where we denoted $\tilde{J}_m(qr) = J_m(qr)r$. Considering that $\tilde{J}_m(qr)$ is a real function, the integral in (229) defines, in fact, the complex conjugated coefficients $\tilde{J}_{m,i}^*(q)$ of expansion of $\tilde{J}_m(qr)$ in the basis $\xi_i(r)$, that is [see equation (226a)],

$$\tilde{J}_{m,i}^*(q) = \left[\int_0^{R_{\max}} \tilde{J}_m(qr) \xi_i^*(r) dr \right]^*. \quad (230)$$

Using the latter result in (229) and rearranging the terms we get

$$\hat{\rho}_m(q) \approx (-i)^m \frac{R_{\max}}{S} \sum_{p=0}^{S-1} \rho_m(r_p) \left[\sum_{i=0}^{\infty} \tilde{J}_{m,i}^*(q) \xi_i(r_p) \right]^*. \quad (231)$$

One may recognize, that the expression in square brackets is exactly the series expansion of $\tilde{J}_m(qr_p)$ in terms of $\xi_i(r_p)$ [see equation (226b)]. In the limit of infinite expansion orders ($i \rightarrow \infty$) such an approximation scheme is, therefore, independent of the chosen orthogonal basis ξ_i and results in the following expression

$$\hat{\rho}_m(q_k) \approx (-i)^m \frac{R_{\max}}{S} \sum_{p=0}^{S-1} \rho_m(r_p) J_m(q_k r_p) r_p. \quad (232)$$

Note that equation (232) corresponds exactly to simple numeric evaluation of the continuous Hankel transform using a Riemann sum in the integration bounds $[0, R_{\max}]$ [see equation (247) in Appendix B.4]. Similar derivations can be performed for the inverse Hankel transform, and also in the 3D case. This conclusion is supported numerically for the 3D case in Fig. S6 of the supporting information, where it is shown that the Zernike [equation (246)] and cosine/sine [equations (234)] weights approach the weights obtained by directly approximating the Hankel integrals using the midpoint rule [equation (144c)].

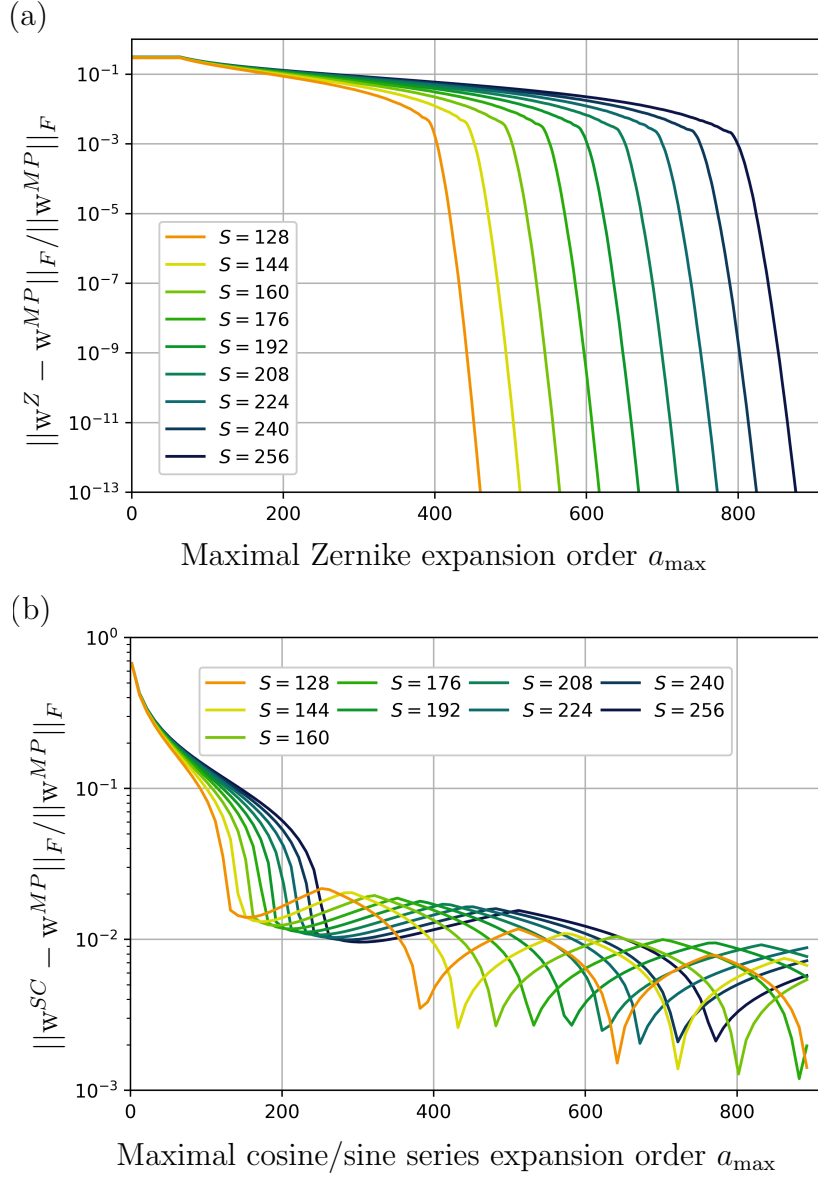


Figure 59: Relative difference, in Frobenius norm $\|\cdot\|_{F_q}$, between the weights $w^{MP} = w_n(p, k)$ generated from the midpoint rule [equation (143c)], and the weights (a) w^Z from Zernike series approximation [equation (245)], as well as (b) w^{SC} from cosine/sine series approximation [equations (233)], as function of the considered expansion cutoff a_{\max} . The Frobenius norm of $w_n(p, k)$ is given by $\sqrt{\sum_n^L \sum_{p,k}^S |w_n(p, k)|^2}$, and was computed upto a maximal harmonic degree of $L = 63$ and various radial grid sizes S specified in the figure legends. The difference between the quadrature weights obtained by different approximations decreases for arbitrary large a_{\max} .

B.2. Cosine/sine series expansion approximation

The quadrature weights given in [19] are determined by employing a cosine/sine series expansion of $\rho_m(r)$ or $\rho_m^l(r)$, and their reciprocal space counterparts. Using the sampling points defined section 3.4.2 and applying the midpoint rule for approximating the integrals, the weights for the 2D case take the following form for odd orders m

$$\begin{aligned} w_m(p, k) &= 2\pi^2 S \sum_{a=0}^{a_{\max}} \sin \left[\frac{\pi a(1+2p)}{2S} \right] \\ &\quad \times \int_0^1 \sin(\pi a x) J_m \left[\frac{\pi(1+2k)}{2} x \right] x dx, \end{aligned} \quad (233a)$$

and for even orders m ,

$$\begin{aligned} w_m(p, k) &= 2\pi^2 S \sum_{a=0}^{a_{\max}} c_a \cos \left[\frac{\pi a(1+2p)}{2S} \right] \\ &\quad \times \int_0^1 \cos(\pi a x) J_m \left[\frac{\pi(1+2k)}{2} x \right] x dx, \end{aligned} \quad (233b)$$

where a_{\max} defines the maximum expansion order in the cosine/sine series, $c_a = 1/2$ for $a = 0$, and $c_a = 1$ otherwise.

In the 3D case the weights for odd orders l are

$$\begin{aligned} w_l(p, k) &= 2\sqrt{2}\pi^2 \sqrt{\pi} S^2 \sum_{a=0}^{a_{\max}} \sin \left[\frac{\pi a(1+2p)}{2S} \right] \\ &\quad \times \int_0^1 \sin(\pi a x) j_l \left[\frac{\pi(1+2k)}{2} x \right] x^2 dx, \end{aligned} \quad (234a)$$

and for even orders l ,

$$\begin{aligned} w_l(p, k) &= 2\sqrt{2}\pi^2 \sqrt{\pi} S^2 \sum_{a=0}^{a_{\max}} c_a \cos \left[\frac{\pi a(1+2p)}{2S} \right] \\ &\quad \times \int_0^1 \cos(\pi a x) j_l \left[\frac{\pi(1+2k)}{2} x \right] x^2 dx. \end{aligned} \quad (234b)$$

The quadrature weights (233) and (234) can be directly used in forward transforms (143a) and (144a), respectively, while for the inverse transforms (143b) and (144b) the corresponding weight functions should be transposed with respect to p and k .

B.3. Zernike polynomials expansion approximation

Here we derive the quadrature weights $w_m(p, k)$ and $w_l(p, k)$ by employing the radial parts of the Zernike polynomials [156, 157] as the basis functions $\xi_i(r)$ in the expansion (226).

The radial parts $R_{D,a}^l(r)$ of the D -dimensional Zernike polynomials [158] can be defined using Jacobi polynomials $P_n^{(\alpha,\beta)}(x)$ as

$$R_{D,a}^h(r) = (-1)^{\frac{s-h}{2}} r^h P_n^{(\alpha,\beta)}(1-2r^2), \quad (235)$$

$$\alpha = h + \frac{D}{2} - 1, \quad \beta = 0, \quad n = \frac{s-h}{2}$$

for even $a-h$, and $R_{D,a}^h(r) = 0$ otherwise, where a and h are non-negative integers.

The radial polynomials $R_{D,a}^h(r)$ form a set of orthogonal polynomials on the interval $[0, 1]$, with the orthogonality condition given for an arbitrary h by

$$\int_0^1 R_{D,a}^h(r) R_{D,a'}^h(r) r^{D-1} dr = \frac{\delta_{a,a'}}{2a+D}. \quad (236)$$

This implies that any sufficiently smooth function $f(r)$, that is defined on a finite interval $[0, R_{\max}]$, has a series expansion in the polynomials $R_{D,a}^h(r)$, i.e.,

$$f(r) = \sum_{a=0}^{\infty} f_s R_{D,a}^h \left(\frac{r}{R_{\max}} \right), \quad (237a)$$

$$f_a = \frac{2s+D}{R_{\max}^D} \int_0^{R_{\max}} f(r) R_{D,a}^h \left(\frac{r}{R_{\max}} \right) r^{D-1} dr. \quad (237b)$$

The advantage of Zernike expansions is that the Hankel transform of $R_{D,a}^h$ can be evaluated exactly. In the 2D case ($D=2$) for $h=m$ one finds,

$$\int_0^1 R_{2,a}^m(r) J_m(qr) r dr = (-1)^{\frac{a-m}{2}} \frac{J_{a+1}(q)}{q}, \quad (238)$$

whereas in the 3D case ($D=3$) for $h=l$ we have,

$$\int_0^1 R_{3,a}^l(r) j_l(qr) r^2 dr = (-1)^{\frac{a-l}{2}} \frac{j_{a+1}(q)}{q}, \quad (239)$$

for $q \neq 0$. A proof of equation (238) can be found in Appendix VII of [157], and equation (239) is derived in this work in Appendix B.5. Since we are interested in approximating the Hankel transforms of a function defined on a finite interval $[0, R_{\max}]$, for an arbitrary positive R_{\max} , we use scaled versions of the integrals (238) and (239),

$$\int_0^{R_{\max}} R_{2,a}^m \left(\frac{r}{R_{\max}} \right) J_m(qr) r dr = (-1)^{\frac{a-m}{2}} \frac{J_{a+1}(qR_{\max})}{q} R_{\max}, \quad (240)$$

and

$$\int_0^{R_{\max}} R_{3,a}^l \left(\frac{r}{R_{\max}} \right) j_l(qr) r^2 dr = (-1)^{\frac{a-l}{2}} \frac{j_{a+1}(qR_{\max})}{q} R_{\max}^2. \quad (241)$$

Let us now consider the Hankel transform for the 2D case, as specified in equation (227), and obtain its discrete version in the form of equation (228). By considering the

expansion (237a) of $f(r) = \rho_m(r)$ up to the maximum order $s = s_{\max}$, with each expansion coefficient $\rho_{m,a}$ approximated using the midpoint rule, we can write

$$\begin{aligned}\widehat{\rho}_m(q) &= (-i)^m \int_0^{R_{\max}} \sum_{a=0}^{\infty} \rho_{m,a} R_{2,a}^m \left(\frac{r}{R_{\max}} \right) J_m(qr) r dr \\ &\approx (-i)^m \sum_{a=0}^{a_{\max}} \frac{2a+2}{SR_{\max}} \sum_{p=0}^{S-1} \rho_m(r_p) R_{2,a}^m \left(\frac{r_p}{R_{\max}} \right) r_p \\ &\quad \times \int_0^{R_{\max}} R_{2,a}^m \left(\frac{r}{R_{\max}} \right) J_m(qr) r dr.\end{aligned}\quad (242)$$

Since $\rho_m(r)$ is finitely supported, the integration range reduces from $[0, \infty)$ to $[0, R_{\max}]$. Note that equation (242) is already represented as a weighted sum with weights which are independent on the function $\rho_m(r)$. Using the integral relation from equation (240), we arrive at (for $q \neq 0$)

$$\begin{aligned}\widehat{\rho}_m(q) &\approx \frac{(-i)^m}{S} \sum_{p=0}^{S-1} \rho_m(r_p) \frac{r_p}{q} \sum_{a=0}^{a_{\max}} (-1)^{\frac{a-m}{2}} (2a+2) \\ &\quad \times R_{2,a}^m \left(\frac{r_p}{R_{\max}} \right) J_{a+1}(qR_{\max}).\end{aligned}\quad (243)$$

Considering the definitions in equation (146) we finally obtain the discrete version of the Hankel transform in the 2D case in the form of (228),

$$\widehat{\rho}_m(q_k) \approx \frac{(-i)^m}{Q_{\max}^2} \sum_{p=0}^{S-1} \rho_m(r_p) w_m(p, k),\quad (244)$$

with the quadrature weights determined as

$$\begin{aligned}w_m(p, k) &= \frac{\pi(1+2p)}{(1+2k)} \sum_{a=0}^{a_{\max}} (-1)^{\frac{a-m}{2}} (2a+2) \\ &\quad \times R_{2,a}^m \left(\frac{1+2p}{2S} \right) J_{a+1} \left[\frac{\pi(1+2k)}{2} \right].\end{aligned}\quad (245)$$

Following a similar procedure the Zernike weights for the 3D case can be specified as

$$\begin{aligned}w_l(p, k) &= \frac{\pi\sqrt{2\pi}}{2} \frac{(1+2p)^2}{(1+2k)} \sum_{a=0}^{a_{\max}} (-1)^{\frac{a-l}{2}} (2a+3) \\ &\quad \times R_{3,a}^l \left(\frac{1+2p}{2S} \right) j_{a+1} \left[\frac{\pi(1+2k)}{2} \right].\end{aligned}\quad (246)$$

The quadrature weights (245) and (246) can be directly used in the forward transforms (143a) and (144a), respectively, while for the inverse transforms (143b) and (144b) the corresponding weights are obtained by transposing $w_m(p, k)$ and $w_l(p, k)$ with respect to p and k .

B.4. Direct approximation of the Hankel integrals using the midpoint rule

Here we consider direct approximations of the Hankel transforms given in equations (141) and (142) with Riemann sums.

In the 2D case the integral in (141a) can be approximated using the midpoint rule as

$$\widehat{\rho}_m(q_k) \approx (-i)^m \frac{R_{\max}}{S} \sum_{p=0}^{S-1} \rho_m(r_p) J_m(q_k r_p) r_p. \quad (247)$$

Using the definitions in Appendix 3.4.2, we can present equation (247) in the form

$$\widehat{\rho}_m(q_k) \approx A_m \sum_{p=0}^{S-1} \rho_m(r_p) w_m(p, k), \quad (248)$$

where $A_m = \frac{(-i)^m}{Q_{\max}^2}$, and the quadrature weights $w_m(p, k)$ are given in equation (143c).

Similarly, in the 3D case the integral in (142a) can be approximated as

$$\widehat{\rho}_l(q_k) \approx A_l \sum_{p=0}^{S-1} \rho_l(r_p) w_l(p, k), \quad (249)$$

where $A_l = \frac{(-i)^l}{Q_{\max}^3}$, and the quadrature weights $w_l(p, k)$ are given in equation (144c). Approximations for the inverse Hankel transforms (141b) and (142b) can be obtained similar way, producing the discrete forward and inverse Hankel transforms given in equations (143) and (144).

B.5. Hankel transform of the radial part of the 3D Zernike polynomial

Here we provide a proof of equation (239) for the 3D Zernike polynomials, which closely follows the derivation of equation (238) given in [157]. We shall need the Rodrigues' formula for Jacobi polynomials $P_n^{(\alpha, \beta)}(z)$ and the series expansion of spherical Bessel functions $j_l(r)$, which can be obtained from 10.2.2, 10.47.3 and 18.5(ii) in [150]:

$$j_l(z) = \sqrt{\frac{\pi}{2z}} \sum_{p=0}^{\infty} \frac{(-1)^p}{p! \Gamma(p + l + \frac{3}{2})} \left(\frac{z}{2}\right)^{2p+l+\frac{1}{2}}, \quad (250)$$

$$P_n^{(\alpha, \beta)}(z) = \frac{(-1)^n}{2^n n!} (1-z)^{-\alpha} (1+z)^{-\beta} \times \left(\frac{d}{dz}\right)^n (1-z)^{\alpha+n} (1+z)^{\beta+n}, \quad (251)$$

where Γ denotes the gamma function, and $n!$ is the factorial of a non-negative integer number n .

By substituting $z = 1 - 2r^2$ in equation (251), and considering in equation (235) Jacobi polynomials for $\beta = 0$, the radial part of the Zernike polynomials for $D = 3$ yields

$$R_{3,s}^l(r) = \frac{(-1)^n}{n!} r^{-(\alpha+\frac{1}{2})} \left(\frac{d}{d(r^2)} \right)^n (r^2)^{\alpha+n} (1-r^2)^n, \quad (252)$$

with $\alpha = l+1/2$ and $n = (s-l)/2$. By expressing the spherical Bessel function in equation (250) in terms of the argument $z = qr$, and using equations (250) and (252) in the left hand side of equation (239) we find the following expansion for the integral,

$$\begin{aligned} \int_0^1 R_{3,s}^l(r) j_l(qr) r^2 dr &= \sqrt{\frac{\pi}{16}} \frac{(-1)^n}{n!} \sum_{p=0}^{\infty} \frac{(-1)^p}{p! \Gamma(p+\alpha+1)} \\ &\times \left(\frac{q}{2} \right)^{2p+\alpha-\frac{1}{2}} f(p, \alpha, n), \end{aligned} \quad (253)$$

with

$$f(p, \alpha, n) = 2 \int_0^1 (r^2)^{p+\frac{1}{2}} \left(\frac{d}{d(r^2)} \right)^n (r^2)^{\alpha+n} (1-r^2)^n dr. \quad (254)$$

The integral in (254) can be reformulated by introducing the variable $u = r^2$, which yields

$$f(p, \alpha, n) = \int_0^1 u^p \left(\frac{d}{du} \right)^n u^{\alpha+n} (1-u)^n du. \quad (255)$$

We shall now perform integration by parts in equation (255) for two cases, $p \geq n$ and $p < n$. Notice, that a single application of integration by parts results in

$$\begin{aligned} f(p, \alpha, n) &= \left(u^p \left(\frac{d}{du} \right)^{n-1} u^{\alpha+n} (1-u)^n \right) \Big|_0^1 \\ &\quad - p \int_0^1 u^{p-1} du \left(\frac{d}{du} \right)^{n-1} u^{\alpha+n} (1-u)^n \\ &= -p \int_0^1 u^{p-1} du \left(\frac{d}{du} \right)^{n-1} u^{\alpha+n} (1-u)^n, \end{aligned} \quad (256)$$

taking into account that $n-1 < n$ and $\alpha > 0$.

For $p \geq n$ we can then perform integration by parts n times in (255), that results in

$$f(p, \alpha, n) = (-1)^n \frac{p!}{(p-n)!} \int_0^1 u^{p+\alpha} (1-u)^n du. \quad (257)$$

One may recognize the remaining integral as the beta function [see 5.12.1 in [150]], which finally yields for $p \geq n$,

$$f(p, \alpha, n) = (-1)^n \frac{p!}{(p-n)!} \frac{\Gamma(p+\alpha+1)\Gamma(n+1)}{\Gamma(p+n+\alpha+2)}. \quad (258)$$

In the case of $p < n$, it is possible to perform integration by parts only p times in (255), that gives

$$f(p, \alpha, n) = (-1)^p p! \left(\left(\frac{d}{du} \right)^{n-p-1} u^{\alpha+n} (1-u)^n \right) \Big|_0^1 = 0. \quad (259)$$

Using equations (258) and (259) in (253), the latter can be rewritten as follows

$$\begin{aligned} \int_0^1 R_{3,a}^l(r) j_l(qr) r^2 dr &= (-1)^n \frac{1}{q} \sqrt{\frac{\pi}{2q}} \\ &\times \sum_{p=n}^{\infty} \frac{(-1)^{p-n}}{(p-n)! \Gamma(p-n+2n+\alpha+2)} \left(\frac{q}{2} \right)^{2(p-n)+2n+\alpha+1} \\ &= (-1)^n \frac{1}{q} \sqrt{\frac{\pi}{2q}} \sum_{k=0}^{\infty} \frac{(-1)^k}{k! \Gamma(k+(a+1)+\frac{3}{2})} \left(\frac{q}{2} \right)^{2k+(a+1)+\frac{1}{2}}, \end{aligned} \quad (260)$$

where in the last step we considered that $2n + \alpha = a + \frac{1}{2}$, and introduced a variable $k = p - n$. Note that the sum in equation (260), including the prefactor $\sqrt{\pi/(2q)}$, is precisely the series expansion of a spherical Bessel function $j_{a+1}(q)$ of the order $a + 1$ [see equation (250)]. This finally yields,

$$\int_0^1 R_{3,a}^l(r) j_l(qr) r^2 dr = (-1)^n \frac{j_{a+1}(q)}{q} = (-1)^{\frac{a-l}{2}} \frac{j_{a+1}(q)}{q}, \quad (261)$$

that completes the proof of equation (239).

List of orthogonality and symmetry relations

Spherical harmonics

Addition theorem for two vectors on the unit sphere \mathbf{r}_1 and \mathbf{r}_2 ,

$$\frac{1}{2l+1} \sum_{m=-l}^l Y_m^l(\mathbf{r}_1) Y_m^l(\mathbf{r}_2)^* = P^l(\langle \mathbf{r}_1, \mathbf{r}_2 \rangle), \quad (262)$$

where $\langle \mathbf{r}_1, \mathbf{r}_2 \rangle$ is the scalar product between \mathbf{r}_1 and \mathbf{r}_2 . If \mathbf{r}_1 and \mathbf{r}_2 are given in spherical coordinates one obtains

$$\begin{aligned} \frac{1}{2l+1} \sum_{m=-l}^l Y_m^l(\theta_1, \phi_1) Y_m^l(\theta_2, \phi_2)^* &= \frac{P^l(\cos(\theta_1) \sin(\theta_2) + \sin(\theta_1) \sin(\theta_2) \cos(\phi_1 - \phi_2))}{4\pi} \\ &= F^l(\theta_1, \theta_2, \phi_1 - \phi_2), \end{aligned} \quad (263)$$

where for convenience we introduced the function $F^l(\theta_1, \theta_2, \phi_1 - \phi_2)$.

Wigner D-matrices

Orthogonality over SO(3), complex conjugate of [86, equation 4.60],

$$\begin{aligned} \int_{\text{SO}(3)} d\omega D_{m,n}^l(\omega)^* D_{m',n'}^{l'}(\omega) \\ &= \int_0^{2\pi} d\alpha \int_0^\pi d\beta \sin(\beta) \int_0^{2\pi} d\gamma D_{m,n}^l(\alpha, \beta, \gamma)^* D_{m',n'}^{l'}(\alpha, \beta, \gamma) \\ &= \delta_{l,l'} \delta_{m,m'} \delta_{n,n'} \frac{8\pi^2}{2l+1}. \end{aligned} \quad (264)$$

Orthogonality over n and m , complex conjugate of [86, chapter 16],

$$\sum_{n=-l}^l D_{m,n}^l(\omega)^* D_{m',n}^l(\omega) = \delta_{m,m'} \quad \text{and} \quad \sum_{m=-l}^l D_{m,n}^l(\omega)^* D_{m,n'}^l(\omega) = \delta_{n,n'}. \quad (265)$$

The product formula for Wigner D-matrices is given by [86, equation 4.25]

$$D_{m,n}^l(\omega) D_{m',n'}^{l'}(\omega) = \sum_{L=|l-l'|}^{|l+l'|} C_{m,m'}^{l,l',L} C_{n,n'}^{l,l',L} D_{(m+m'),(n+n')}^L(\omega), \quad (266)$$

where the symbols of type $C_{m,m'}^{l,l',L}$ are a shorthand notation for the Clebsch-Gordan coefficients $\langle lm l'm' | L(m+m') \rangle$.

A direct consequence of the product formula together with the first orthogonality expression over SO(3) is the triple product integral relation, complex conjugate of [154, section 4.11 equation 5],

$$\int_{\text{SO}(3)} d\omega D_{M,N}^L(\omega) D_{m,n}^l(\omega)^* D_{m',n'}^{l'}(\omega)^* = \frac{8\pi^2}{2L+1} \delta_{M,(m+m')} \delta_{N,(n+n')} C_{m,m'}^{l,l',L} C_{n,n'}^{l,l',L}. \quad (267)$$

Symmetry under complex conjugation [86, equation 4.22]

$$D_{m,n}^l(\omega)^* = (-1)^{m-n} D_{-m,-n}^l(\omega) = D_{n,m}^l(\omega^{-1}). \quad (268)$$

In the special case of $m = n = 0$ the small Wigner-d matrices $d_{m,n}^l(\beta)$ from equation (51) reduce to [154, section 4.17 equation 2] Legendre polynomials

$$d_{0,0}^l(\beta) = P_l(\cos(\beta)). \quad (269)$$

Clebsch-Gordan coefficients

The Clebsch-Gordan coefficients satisfy the following orthogonality relation [86, equation 3.9]

$$\sum_{l=|l-l'|}^{l+l'} C_{n,n'-n}^{l,l',L} C_{k,k'-k}^{l,l',L} = \delta_{k,n} \delta_{n',k'}. \quad (270)$$

Own publications

- [22] R. P. Kurta et al., “Exploring fingerprints of ultrafast structural dynamics in molecular solutions with an x-ray laser”, *Phys. Chem. Chem. Phys.* **25**, 23417–23434 (2023).
- [23] T. B. Berberich, S. L. Molodtsov, and R. P. Kurta, “A workflow for single-particle structure determination via iterative phasing of rotational invariants in fluctuation X-ray scattering”, *Journal of Applied Crystallography* **57**, 324–343 (2024).
- [122] T. B. Berberich et al., “FXS based reconstructions of the PR772 virus”, in preparation.
- [144] T. B. Berberich et al., “Fluctuation X-ray scattering and arbitrary orientational distributions of particles”, in preparation.

References

- [1] Z. Kam, “Determination of macromolecular structure in solution by spatial correlation of scattering fluctuations”, *Macromolecules* **10**, 927–934 (1977).
- [2] Z. Kam, “The reconstruction of structure from electron micrographs of randomly oriented particles”, *J. Theor. Biol.* **82**, 15–39 (1980).
- [3] Z. Kam, M. H. J. Koch, and J. Bordas, “Fluctuation X-ray scattering from biological particles in frozen solution by using synchrotron radiation”, *Proc. Nati. Acad. Sci. USA* **78**, 3559–3562 (1981).
- [4] M. J. Bogan et al., “Single particle X-ray diffractive imaging”, *Nano Lett.* **8**, 310–316 (2008).
- [5] A. P. Mancuso et al., “Coherent imaging of biological samples with femtosecond pulses at the free-electron laser FLASH”, *New. J. Phys.* **12**, 035003 (2010).
- [6] M. M. Seibert et al., “Single mimivirus particles intercepted and imaged with an X-ray laser”, *Nature* **470**, 78–86 (2011).
- [7] M. F. Hantke et al., “High-throughput imaging of heterogeneous cell organelles with an X-ray laser”, *Nat. Photonics* **8**, 943–949 (2014).
- [8] T. Kimura et al., “Imaging live cell in micro-liquid enclosure by X-ray laser diffraction”, *Nat. Communications* **5**, 3052 (2014).
- [9] M. Rose et al., “Single-particle imaging without symmetry constraints at an X-ray free-electron laser”, *IUCrJ* **5**, 727–736 (2018).
- [10] T. Ekeberg et al., “Observation of a single protein by ultrafast X-ray diffraction”, *bioRxiv*, 2022.03. 09.483477 (2022).
- [11] J. Solem and G. Baldwin, “Microholography of living organisms”, *Science* **218**, 229–235 (1982).

- [12] R. Neutze et al., “Potential for biomolecular imaging with femtosecond X-ray pulses”, *Nature* **406**, 752 (2000).
- [13] K. J. Gaffney and H. N. Chapman, “Imaging atomic structure and dynamics with ultrafast X-ray scattering”, *Science* **316**, 1444–1448 (2007).
- [14] A. Aquila et al., “The linac coherent light source single particle imaging road map”, *Structural Dynamics* **2**, 041701 (2015).
- [15] T. Ekeberg et al., “Three-dimensional reconstruction of the giant mimivirus particle with an X-ray free-electron laser”, *Phys. Rev. Lett.* **114**, 098102 (2015).
- [16] H. N. Chapman, “X-ray free-electron lasers for the structure and dynamics of macromolecules”, *Annu. Rev. Biochem.* **88**, 35–58 (2019).
- [17] J. Bielecki, F. R. N. C. Maia, and A. P. Mancuso, “Perspectives on single particle imaging with x rays at the advent of high repetition rate X-ray free electron laser sources”, *Structural Dynamics* **7**, 040901 (2020).
- [18] D. Assalauova et al., “An advanced workflow for single-particle imaging with the limited data at an X-ray free-electron laser”, *IUCrJ* **7**, 1102–1113 (2020).
- [19] J. J. Donatelli, P. H. Zwart, and J. A. Sethian, “Iterative phasing for fluctuation X-ray scattering”, *PNAS* **112**, 10286–10291 (2015).
- [20] R. P. Kurta et al., “Correlations in scattered X-ray laser pulses reveal nanoscale structural features of viruses”, *Phys. Rev. Lett.* **119**, 158102 (2017).
- [21] K. Pande et al., “Ab initio structure determination from experimental fluctuation X-ray scattering data”, *PNAS* **115**, 11772–11777 (2018).
- [22] R. P. Kurta et al., “Exploring fingerprints of ultrafast structural dynamics in molecular solutions with an x-ray laser”, *Phys. Chem. Chem. Phys.* **25**, 23417–23434 (2023).
- [23] T. B. Berberich, S. L. Molodtsov, and R. P. Kurta, “A workflow for single-particle structure determination via iterative phasing of rotational invariants in fluctuation X-ray scattering”, *Journal of Applied Crystallography* **57**, 324–343 (2024).
- [24] H. Stapelfeldt and T. Seideman, “Colloquium: aligning molecules with strong laser pulses”, *Reviews of Modern Physics* **75**, 543 (2003).
- [25] E. Biasin et al., “Anisotropy enhanced x-ray scattering from solvated transition metal complexes”, *Journal of Synchrotron Radiation* **25**, 306–315 (2018).
- [26] K. Haldrup et al., “Ultrafast x-ray scattering measurements of coherent structural dynamics on the ground-state potential energy surface of a diplatinum molecule”, *Physical review letters* **122**, 063001 (2019).
- [27] J. Stöhr, *The nature of x-rays and their interactions with matter*, Springer Tracts in Modern Physics (Springer International Publishing, 2023).
- [28] J. Als-Nielsen and D. McMorrow, *Elements of modern x-ray physics* (Wiley, 2011).

- [29] E. J. Jaeschke et al., eds., *Synchrotron light sources and free-electron lasers: accelerator physics, instrumentation and science applications; Second edition*, Springer reference (Springer, Cham, 2020), (xxix, 2509 pages).
- [30] S. Weinberg, *The quantum theory of fields*, Quantum Theory of Fields, Vol. 2: Modern Applications v. 1 (Cambridge University Press, 1995).
- [31] V. Berestetskii, E. Lifshitz, and L. Pitaevskii, *Quantum electrodynamics: volume 4*, Course of theoretical physics (Elsevier Science, 1982).
- [32] M. Peskin and D. Schroeder, *An introduction to quantum field theory*, Frontiers in Physics (Avalon Publishing, 1995).
- [33] N.-T. D. Loh and V. Elser, “Reconstruction algorithm for single-particle diffraction imaging experiments”, *Phys. Rev. E* **80**, 026705 (2009).
- [34] M. Ladd and R. Palmer, *Structure determination by x-ray crystallography: analysis by x-rays and neutrons* (Springer US, 2014).
- [35] G. Friedel, “Sur les symétries cristallines que peut révéler la diffraction des rayons röntgen”, *CR Acad. Sci. Paris* **157**, 1533–1536 (1913).
- [36] E. M. Stein and G. Weiss, *Introduction to fourier analysis on euclidean spaces (pms-32), volume 32* (Princeton University Press, Princeton, 1972).
- [37] S. Yuan et al., “Changes in apaf-1 conformation that drive apoptosome assembly”, *Biochemistry* **52**, 2319–2327 (2013).
- [38] R. W. Gerchberg and W. O. Saxton, “A practical algorithm for the determination of phase from image and diffraction plane pictures”, *Optik* **35**, 227–246 (1972).
- [39] J. R. Fienup, “Reconstruction of an object from the modulus of its Fourier transform”, *Opt. Lett.* **3**, 27–29 (1978).
- [40] W. A. Hendrickson, “Determination of macromolecular structures from anomalous diffraction of synchrotron radiation”, *Science* **254**, 51–58 (1991).
- [41] G. Rhodes, *Crystallography made crystal clear: a guide for users of macromolecular models*, Complementary Science (Elsevier Science, 2010).
- [42] C. Giacovazzo and I. U. of Crystallography, *Phasing in crystallography: a modern perspective*, IUCr texts on crystallography (OUP Oxford, 2014).
- [43] J. R. Fienup, “Phase retrieval algorithms: a comparison”, *Appl. Opt.* **21**, 2758–2769 (1982).
- [44] J. R. Fienup, “Phase retrieval algorithms: a personal tour”, *Appl. Opt.* **52**, 45–56 (2013).
- [45] J. Spence, U. Weierstall, and M. Howells, “Coherence and sampling requirements for diffractive imaging”, *Ultramicroscopy* **101**, 149–152 (2004).
- [46] J. Miao, D. Sayre, and H. N. Chapman, “Phase retrieval from the magnitude of the fourier transforms of nonperiodic objects”, *J. Opt. Soc. Am. A* **15**, 1662–1669 (1998).

- [47] W. L. Briggs and H. Van Emden, *The DFT: an owner's manual for discrete Fourier transform* (Society for Industrial and Applied Mathematics, 1995).
- [48] H. N. Chapman et al., “High-resolution ab initio three-dimensional X-ray diffraction microscopy”, *J. Opt. Soc. Am. A* **23**, 1179–1200 (2006).
- [49] H. N. Chapman et al., “Femtosecond diffractive imaging with a soft-x-ray free-electron laser”, *Nature Physics* **2**, 839–843 (2006).
- [50] M. Carlsson and D. Gerosa, “On phase retrieval via matrix completion and the estimation of low rank psd matrices”, *Inverse Problems* **36**, 015006 (2019).
- [51] J. Guo, *X-rays in nanoscience: spectroscopy, spectromicroscopy, and scattering techniques* (John Wiley & Sons, 2010).
- [52] H. M. L. Faulkner and J. M. Rodenburg, “Movable aperture lensless transmission microscopy: a novel phase retrieval algorithm”, *Phys. Rev. Lett.* **93**, 023903 (2004).
- [53] J. M. Rodenburg, “Ptychography and related diffractive imaging methods”, *Advances in imaging and electron physics* **150**, 87–184 (2008).
- [54] A. M. Maiden and J. M. Rodenburg, “An improved ptychographical phase retrieval algorithm for diffractive imaging”, *Ultramicroscopy* **109**, 1256–1262 (2009).
- [55] S. Marchesini and D. Shapiro, *Coherent x-ray diffraction microscopy* (John Wiley & Sons, Ltd, 2010) Chap. 5, pp. 119–168.
- [56] P. Combettes, “The foundations of set theoretic estimation”, *Proceedings of the IEEE* **81**, 182–208 (1993).
- [57] H. H. Bauschke and J. M. Borwein, “On projection algorithms for solving convex feasibility problems”, *SIAM Review* **38**, 367–426 (1996).
- [58] S. Marchesini et al., “X-ray image reconstruction from a diffraction pattern alone”, *Phys. Rev. B* **68**, 10.1103/PhysRevB.68.140101 (2003).
- [59] V. Elser, “Phase retrieval by iterated projections”, *J. Opt. Soc. Am. A* **20**, 40–55 (2003).
- [60] D. R. Luke, “Relaxed averaged alternating reflections for diffraction imaging”, *Inverse Problems* **21**, 37 (2004).
- [61] Z. Wen et al., “Alternating direction methods for classical and ptychographic phase retrieval”, *Inverse Problems* **28**, 115010 (2012).
- [62] M. Pham et al., “Generalized proximal smoothing (gps) for phase retrieval”, *Opt. Express* **27**, 2792–2808 (2019).
- [63] E. J. Candès et al., “Phase retrieval via matrix completion”, *SIAM Journal on Imaging Sciences* **6**, 199–225 (2013).
- [64] H. H. Bauschke, P. L. Combettes, and D. R. Luke, “Phase retrieval, error reduction algorithm, and fienup variants: a view from convex optimization”, *JOSA A* **19**, 1334–1345 (2002).

- [65] N. Parikh and S. Boyd, *Proximal algorithms*, Foundations and Trends® in Optimization Series (Now Publishers, 2013).
- [66] A. Themelis and P. Patrinos, “Douglas–rachford splitting and admm for nonconvex optimization: tight convergence results”, *SIAM Journal on Optimization* **30**, 149–181 (2020).
- [67] P. Schmüser, M. Dohlus, and J. Rossbach, *Ultraviolet and soft x-ray free-electron lasers: introduction to physical principles, experimental results, technological challenges*, Springer Tracts in Modern Physics (Springer Berlin Heidelberg, 2008).
- [68] N. M. Kroll and W. A. McMullin, “Stimulated emission from relativistic electrons passing through a spatially periodic transverse magnetic field”, *Physical Review A* **17**, 300 (1978).
- [69] S. V. Milton et al., “Exponential gain and saturation of a self-amplified spontaneous emission free-electron laser”, *Science* **292**, 2037–2041 (2001).
- [70] Y. S. Derbenev, A. Kondratenko, and E. Saldin, “On the possibility of using a free electron laser for polarization of electrons in storage rings”, *Nuclear Instruments and Methods in Physics Research* **193**, 415–421 (1982).
- [71] P. Emma et al., “First lasing and operation of an ångström-wavelength free-electron laser”, *Nature Photonics* **4**, 641 (2010).
- [72] R. Abela et al., *XFEL: The European X-Ray Free-Electron Laser - Technical Design Report* (DESY, Hamburg, 2006), pp. 1–646.
- [73] P. Raimondi et al., “The extremely brilliant source storage ring of the european synchrotron radiation facility”, *Communications Physics* **6**, 82 (2023).
- [74] H.-D. Nuhn, *Linac Coherent Light Source (LCLS) Conceptual Design Report*, tech. rep. (SLAC National Accelerator Lab., Menlo Park, CA (United States), 2002).
- [75] T. Tschentscher et al., “Photon beam transport and scientific instruments at the European XFEL”, *Applied Sciences* **7**, 592 (2017).
- [76] T. Ishikawa et al., “A compact X-ray free-electron laser emitting in the sub-ångström region”, *Nature Photonics* **6**, 540 (2012).
- [77] I. S. Ko et al., “Construction and commissioning of PAL-XFEL facility”, *Applied Sciences* **7**, 479 (2017).
- [78] C. J. Milne et al., “SwissFEL: the Swiss X-ray free electron laser”, *Applied Sciences* **7**, 720 (2017).
- [79] B. Patterson et al., “Coherent science at the SwissFEL x-ray laser”, *New Journal of Physics* **12**, 035012 (2010).
- [80] W. Decking and T. Limberg, *European XFEL Post-TDR Description*, XFEL.EU Technical Note XFEL.EU TN-2013-004 (European XFEL, Hamburg, 2013), pp. 1–22.
- [81] H. Reddy et al., “X-ray diffraction imaging of coliphage PR772 at the Linac coherent light source”, *Scientific Data* **4**, 170079 (2017).

- [82] A. P. Dempster, N. M. Laird, and D. B. Rubin, “Maximum likelihood from incomplete data via the em algorithm”, *Journal of the royal statistical society: series B (methodological)* **39**, 1–22 (1977).
- [83] L. Feigin and D. Svergun, *Structure analysis by small-angle x-ray and neutron scattering* (Springer US, 2013).
- [84] B. Chaudhuri et al., eds., *Biological Small Angle Scattering: Techniques, Strategies and Tips*, Vol. 1009, *Advances in Experimental Medicine and Biology* (Springer, 2017), p. 268.
- [85] S. D. Vela and D. I. Svergun, “Methods, development and applications of small-angle X-ray scattering to characterize biological macromolecules in solution”, *Current Research in Structural Biology* **2**, 164–170 (2020).
- [86] M. Rose, *Elementary theory of angular momentum*, *Structure of matter series* (Wiley, 1957).
- [87] E. P. Wigner, *Group theory and its application to the quantum mechanics of atomic spectra*, Vol. 5, *Pure and Applied Physics* (Elsevier, 1959).
- [88] M. R. Sepanski, *Compact lie groups*, *Graduate Texts in Mathematics* (Springer New York, NY, 2006).
- [89] N. Zettili, *Quantum mechanics: concepts and applications* (Wiley, 2009).
- [90] P. J. Kostelec and D. N. Rockmore, “FFTs on the rotation group”, *J. Fourier Anal. Appl.* **14**, 145–179 (2008).
- [91] Y. R. Guo and R. MacKinnon, “Structure-based membrane dome mechanism for Piezo mechanosensitivity”, *eLife* **6**, edited by K. J. Swartz, e33660 (2017).
- [92] P. Wochner et al., “X-ray cross correlation analysis uncovers hidden local symmetries in disordered matter”, *Proc. Nat. Acad. Sci.* **106**, 11511–11514 (2009).
- [93] M. Altarelli, R. P. Kurta, and I. A. Vartanyants, “X-ray cross-correlation analysis and local symmetries of disordered systems: General theory”, *Phys. Rev. B* **82**, 104207 (2010).
- [94] R. P. Kurta et al., “X-ray cross-correlation analysis applied to disordered two-dimensional systems”, *Phys. Rev. B* **85**, 184204 (2012).
- [95] R. P. Kurta et al., “Solution of the phase problem for coherent scattering from a disordered system of identical particles”, *New J. Phys.* **15**, 013059 (2013).
- [96] B. von Ardenne, M. Mechelke, and H. Grubmüller, “Structure determination from single molecule x-ray scattering with three photons per image”, *Nat. Communications* **9**, 2375 (2018).
- [97] W. Zhao et al., “Structure determination using high-order spatial correlations in single-particle X-ray scattering”, *IUCrJ* **11**, 92–108 (2024).
- [98] A. V. Martin, “Orientational order of liquids and glasses *via* fluctuation diffraction”, *IUCrJ* **4**, 24–36 (2017).

- [99] D. K. Saldin et al., “Structure of isolated biomolecules obtained from ultrashort X-ray pulses: exploiting the symmetry of random orientations”, *Journal of Physics: Condensed Matter* **21**, 134014 (2009).
- [100] B. Pedrini et al., “Two-dimensional structure from random multiparticle x-ray scattering images using cross-correlations”, *Nat. Comm.* **4**, 1647 (2013).
- [101] A. S. Bandeira et al., “Estimation under group actions: recovering orbits from invariants”, *Applied and Computational Harmonic Analysis* **66**, 236–319 (2023).
- [102] A. Liu and A. Moitra, *Algorithms from invariants: smoothed analysis of orbit recovery over $SO(3)$* , 2022.
- [103] R. A. Horn and C. R. Johnson, *Matrix analysis*, 2nd ed. (Cambridge University Press, 2012).
- [104] S. Roman, *Advanced linear algebra*, Graduate Texts in Mathematics (Springer, 2007).
- [105] J. C. Gower and G. B. Dijkstra, *Procrustes problems*, Vol. 30, Oxford Statistical Science Series (Oxford University Press, 2004), p. 233.
- [106] P. R. Kommera et al., “GPU-accelerated multitiered iterative phasing algorithm for fluctuation X-ray scattering”, *J. Appl. Crystallogr.* **54**, 1179–1188 (2021).
- [107] T. Salditt, A. Egner, and D. Luke, *Nanoscale photonic imaging*, Topics in Applied Physics (Springer International Publishing, 2020).
- [108] W. Ford, *Numerical linear algebra with applications*, 1st ed. (Elsevier, 2015).
- [109] N. Schaeffer, “Efficient spherical harmonic transforms aimed at pseudospectral numerical simulations”, *Geochemistry, Geophysics, Geosystems* **14**, 751–758 (2013).
- [110] R. P. Stanley, *Enumerative combinatorics*, 2nd ed., Cambridge Studies in Advanced Mathematics (Cambridge University Press, 2011).
- [111] H. K. Reddy et al., “Coherent soft x-ray diffraction imaging of coliphage pr772 at the linac coherent light source”, *Scientific Data* **4**, 170079 (2017).
- [112] H. Li et al., “Diffraction data from aerosolized coliphage pr772 virus particles imaged with the linac coherent light source”, *Scientific Data* **7**, 404 (2020).
- [113] D. Padfield, “Masked object registration in the fourier domain”, *IEEE Trans Image Process* **21**, 2706–2718 (2011).
- [114] I. A. Zaluzhnyy et al., “Quantifying angular correlations between the atomic lattice and the superlattice of nanocrystals assembled with directional linking”, *Nano Lett.* **17**, 3511–3517 (2017).
- [115] C. R. Harris et al., “Array programming with NumPy”, *Nature* **585**, 357–362 (2020).
- [116] G. Bradski, “The OpenCV Library”, *Dr. Dobb’s Journal of Software Tools* (2000).
- [117] P. Virtanen et al., “SciPy 1.0: Fundamental algorithms for scientific computing in Python”, *Nat. Methods* **17**, 261–272 (2020).

- [118] W. Schroeder, K. Martin, and B. Lorensen, *The Visualization Toolkit: An object-oriented approach to 3D graphics* (Ingram, 2006).
- [119] N. The HDF Group, Q. Koziol, and U. O. of Science, *HDF5-Version 1.12.0*, Feb. 2020.
- [120] J. D. Hunter, “Matplotlib: A 2D graphics environment”, *Computing in Science & Engineering* **9**, 90–95 (2007).
- [121] A. Hosseinizadeh et al., “Conformational landscape of a virus by single-particle x-ray scattering”, *Nature Methods* **14**, 877–881 (2017).
- [122] T. B. Berberich et al., “FXS based reconstructions of the PR772 virus”, in preparation.
- [123] E. F. Pettersen et al., “UCSF Chimera—a visualization system for exploratory research and analysis”, *J. Comput. Chem.* **25**, 1605–1612 (2004).
- [124] H. K. Reddy et al., “Electron cryo-microscopy of bacteriophage PR772 reveals the elusive vertex complex and the capsid architecture”, *eLife* **8**, e48496 (2019).
- [125] B. Peralta et al., “Mechanism of membranous tunnelling nanotube formation in viral genome delivery”, *PLOS Biology* **11**, 1–15 (2013).
- [126] S. M. Caruso et al., “A novel genus of actinobacterial tectiviridae”, *Viruses* **11**, 1134, 10.3390/v11121134 (2019).
- [127] J. D. Bozek, “Amo instrumentation for the lcls x-ray fel”, *The European Physical Journal Special Topics* **169**, 129–132 (2009).
- [128] D. P. DePonte et al., “Gas dynamic virtual nozzle for generation of microscopic droplet streams”, *Journal of Physics D: Applied Physics* **41**, 195505 (2008).
- [129] R. Nazari et al., “3d printing of gas-dynamic virtual nozzles and optical characterization of high-speed microjets”, *Opt. Express* **28**, 21749–21765 (2020).
- [130] J. R. Fienup and C. C. Wackerman, “Phase-retrieval stagnation problems and solutions”, *J. Opt. Soc. Am. A* **3**, 1897–1907 (1986).
- [131] D. Verreault et al., “Resistance of aerosolized bacterial viruses to relative humidity and temperature”, *Applied and Environmental Microbiology* **81**, 7305–7311 (2015).
- [132] N. Turgeon et al., “Resistance of aerosolized bacterial viruses to four germicidal products”, *PLOS ONE* **11**, e0168815 (2016).
- [133] E. Biasin et al., “Direct observation of coherent femtosecond solvent reorganization coupled to intramolecular electron transfer”, *Nature chemistry* **13**, 343–349 (2021).
- [134] I. Inoue et al., “Observation of femtosecond x-ray interactions with matter using an x-ray–x-ray pump–probe scheme”, *Proceedings of the National Academy of Sciences* **113**, 1492–1497 (2016).
- [135] J. C. P. Koliyadu et al., “Pump–probe capabilities at the SPB/SFX instrument of the European XFEL”, *Journal of Synchrotron Radiation* **29**, 1273–1283 (2022).

- [136] B. Zon and B. Katsnelson, “Nonresonant scattering of intense light by a molecule”, *Zhurnal Eksperimental’noi i Teoreticheskoi Fiziki* **69**, 1166–1178 (1975).
- [137] M. J. Weida and C. S. Parmenter, “Aligning symmetric and asymmetric top molecules via single photon excitation”, *The Journal of Chemical Physics* **107**, 7138–7147 (1997).
- [138] C. T. L. Smeenk and P. B. Corkum, “Molecular alignment using circularly polarized laser pulses”, *Journal of Physics B: Atomic, Molecular and Optical Physics* **46**, 201001 (2013).
- [139] S. Stern et al., “Toward atomic resolution diffractive imaging of isolated molecules with x-ray free-electron lasers”, *Faraday Discuss.* **171**, 393–418 (2014).
- [140] T. Kierspel et al., “X-ray diffractive imaging of controlled gas-phase molecules: Toward imaging of dynamics in the molecular frame”, *The Journal of chemical physics* **152**, 084307 (2020).
- [141] K. M. Håkansson et al., “Hydrodynamic alignment and assembly of nanofibrils resulting in strong cellulose filaments”, *Nature communications* **5**, 4018 (2014).
- [142] J. S. Baskin and A. H. Zewail, “Oriented ensembles in ultrafast electron diffraction”, *ChemPhysChem: A European Journal of Chemical Physics and Physical Chemistry* **7**, 1562–1574 (2006).
- [143] U. Lorenz, K. B. Møller, and N. E. Henriksen, “On the interpretation of time-resolved anisotropic diffraction patterns”, *New Journal of Physics* **12**, 113022 (2010).
- [144] T. B. Berberich et al., “Fluctuation X-ray scattering and arbitrary orientational distributions of particles”, in preparation.
- [145] D. Applebaum, *Probability on compact lie groups*, Stochastic Modelling and Probability Theory (Springer, 2010).
- [146] J. S. Baskin and A. H. Zewail, “Ultrafast electron diffraction: oriented molecular structures in space and time”, *ChemPhysChem* **6**, 2261–2276 (2005).
- [147] L. Mandel and E. Wolf, *Optical coherence and quantum optics* (Cambridge University Press, 1995).
- [148] A. Natan et al., “Resolving multiphoton processes with high-order anisotropy ultrafast x-ray scattering”, *Faraday Discuss.* **228**, 123–138 (2021).
- [149] N. I. Fisher, T. Lewis, and B. J. J. Embleton, *Statistical analysis of spherical data* (Cambridge University Press, 1987).
- [150] *NIST Digital Library of Mathematical Functions*, <http://dlmf.nist.gov/>, Release 1.1.9 of 2023-03-15, F. W. J. Olver, A. B. Olde Daalhuis, D. W. Lozier, B. I. Schneider, R. F. Boisvert, C. W. Clark, B. R. Miller, B. V. Saunders, H. S. Cohl, and M. A. McClain, eds., 2023.
- [151] K. V. Mardia, *Directional statistics* (Wiley, Chichester u.a., 2000).
- [152] R. Schilling, R. Song, and Z. Vondracek, *Bernstein functions: theory and applications*, De Gruyter Studies in Mathematics (De Gruyter, 2012).

- [153] S. Ken-Iti, *Lévy processes and infinitely divisible distributions*, Cambridge studies in advanced mathematics (Cambridge University Press, 1999).
- [154] V. K. Khersonskii, A. N. Moskalev, and D. A. Varshalovich, *Quantum theory of angular momentum* (World Scientific Publishing Company, 1988).
- [155] A. Gut, *Probability: a graduate course*, Springer Texts in Statistics (Springer New York, 2013).
- [156] F. Zernike, “Beugungstheorie des Schneidenverfahrens und seiner verbesserten Form, der Phasenkontrastmethode”, *Physica* **1**, 689–704 (1934).
- [157] M. Born and E. Wolf, *Principles of Optics: 60th Anniversary Edition*, 7th ed. (Cambridge University Press, 2019).
- [158] F. Zernike and H. C. Brinkman, “Hypersphärische Funktionen und die in sphärischen Bereichen orthogonalen Polynome.”, *Proc. Akad. Wet. Amsterdam* **38**, 161–170 (1935).